NOTICE

The quality of this microform is heavily dependent upon the quality of the original thesis submitted for microfilming. Every effort has been made to ensure the highest quality of reproduction possible.

If pages are missing, contact the university which granted the degree.

Some pages may have indistinct print especially if the original pages were typed with a poor typewriter ribbon or if the university sent us an inferior photocopy.

Reproduction in full or in part of this microform is governed by the Canadian Copyright Act, R.S.C. 1970, c. C-30, and subsequent amendments.

AVIS

La qualité de cette microforme dépend grandement de la qualité de la thèse soumise au microfilmage. Nous avons tout fait pour assurer une qualité supérieure de reproduction.

S'il manque des pages, veuillez communiquer avec l'université qui a conféré le grade.

La qualité d'impression de certaines pages peut laisser à désirer, surtout si les pages originales ont été dactylographiées à l'aide d'un ruban usé ou si l'université nous a fait parvenir une photocopie de qualité inférieure.

La reproduction, même partielle, de cette microforme est soumise à la Loi canadienne sur le droit d'auteur, SRC 1970, c. C-30, et ses amendements subséquents.

Canada

JOINING OF SILICON NITRIDE-TO-SILICON NITRIDE AND TO MOLYBDENUM FOR HIGH-TEMPERATURE APPLICATIONS

by

Ali Mohammad Hadian

Department of Mining and Metallurgical Engineering
McGill University, Montreal
August, 1993

A thesis submitted to the
Faculty of Graduate Studies and Research
in partial fulfilment of
the requirement for the degree of
Doctor of Philosophy

ISBN 0-315-94628-8

Canada

To my parents and my family

ABSTRACT

The evolution of advanced ceramic materials over the past two decades has not been matched by improvements in ceramic joining science and technology, particularly for high temperature applications. Of the techniques being evaluated for joining ceramics, brazing has been found to be the simplest and most promising method of fabricating both ceramic/ceramic and ceramic/metal joints. A key factor in ceramic brazing is wetting of the ceramic by the filler metal.

This study deals with the application of brazing for the fabrication of Si_3N_4/Si_3N_4 and Si_3N_4/Mo joints using Ni-Cr-Si brazing alloys based on AWS BNi-5 (Ni-18Cr-19Si atom%). Thermodynamic calculations were performed to predict wetting at Si_3N_4/Ni-Cr-Si alloys interfaces. By using some simplifying assumptions and suitable scaling of the reaction, the model predicted that Ni-Cr-Si alloys with Ni/Cr=3.5 and X_{Si}<0.25 would react chemically with and wet Si_3N_4. Good agreement was found between the theoretical calculations and experimental results.

Brazing experiments were carried out to study the joinability of Si_3N_4 with various Ni-Cr-Si filler metals which had already shown good wetting characteristics on Si_3N_4. The Si_3N_4/Si_3N_4 joints formed with a 10 atom% Si brazing alloy exhibited the highest strength (≈120 MPa) which was mainly due to the presence of a CrN reaction layer at the ceramic/filler metal interface. The high temperature four-point bend strengths of Si_3N_4/Si_3N_4 joints were markedly higher than the room temperature values. A high strength of about 220 MPa was achieved when the joints were tested at 900°C.

From the results of the Si_3N_4/Mo joining experiments it was found that the joint quality and microstructure were strongly influenced by the composition of the filler metal and such brazing variables as time and temperature. Of all the Si_3N_4/Mo joints, those made with the S10 brazing alloy at 1300°C for 1 min. exhibited the highest strength of 55 MPa.

Finally, in all the cases, the shear strength of all the joints was found to be lower than their four-point bend values.

RÉSUMÉ

Au cours des deux dernières décénies, l'évolution des matériaux céramique de pointe n'a pas été suivie par la technologie en matière de joint, en particulier pour les applications à hautes températures. Parmi les techniques d'assemblage reconnues, le brasage s'avère être une methode simple et prometteuse pour l'élaboration de joints céramique/céramique et céramique/métal.

Cette étude porte sur l'utilisation des techniques de brasage pour la fabrication de joints Si_3N_4/Si_3N_4 and Si_3N_4/Mo utilisant des alliages de brasage Ni-Cr-Si (Ni-18Cr-19Si atom%, d'après AWS BNi-5). Un calcul thermodynamique fut effectué afin de prédire le mouillage à l'interface des systèmes Si_3N_4/Ni-Cr-Si. En utilisant des hypothèses simplifiées et en équilibrant de façon pertinente la réaction, le modèle a prédit que les alliages Ni-Cr-Si ayant une fraction Ni/Cr=3.5 et X_{Si}<0.25 réagiraient chimiquement avec Si_3N_4 et mouilleraient la céramique. Ceci fut confirmé par les résultats expérimentaux.

Des expériences de brasage ont été faites pour étudier la possibilité d'établir des joints entre Si_3N_4 et divers métaux d'apport de type Ni-Cr-Si, qui sont déjà reconnus pour avoir de bonnes charactéristiques de mouillage avec Si_3N_4. Les joints Si_3N_4/Si_3N_4 effectués avec un alliage de brasage contenant 10 at% Si ont été les plus résistants (~120 MPa); ceci principalement grâce à la présence d'une couche de réaction de CrN à l'interface céramique/métal d'apport. La résistance en flexion quatre-points des joints Si_3N_4/Si_3N_4 a été remarquablement plus élevée à haute température qu'à température ambiante; une valeur de 220 MPa a été atteinte lors d'essais à 900°C.

D'après les résultats des expériences sur les joints Si_3N_4/Mo, la qualité des joints et la microstructure sont fortement influencés par la composition du métal d'apport et de paramètres de brasage tels que le temps et la température. Parmi tous les joints Si_3N_4/Mo, ceux fait avec l'alliage de brasage S10 à 1300°C pendant 1 min. ont montré la plus haute résistance, soit 55 MPa.

Pour finir, dans tous les cas, les joints se sont avérés moins résistants en cisaillement qu'en flexion quatre-points.

ACKNOWLEDGEMENT

I would like to express my sincere gratitude to Professor R.A.L. Drew for his constant encouragement, expert guidance, and constructive criticism throughout the entire duration of the thesis, and also for providing me with the opportunity to combine my interests in metals and ceramics while here at McGill.

Special thanks go to Dr. K. Shanker, not only for his valuable comments during the preparation of this manuscript, but also for his readiness to discuss any problem, especially in the design of the equipment.

I would also like to thank Dr. M. Pugh and Dr. J. McDermid who assisted in many ways with their discussions.

Many thanks go to Professor W.T. Thompson (Royal Military College) and Professor F. Mucciardi for useful discussions on the thermodynamic aspects of this work.

Acknowledgments are due to the technical personnel of the department , in particular Ms. H. Campbell, and also to Mr. G. Poirier (Department of Geological Science) for his aid with the electron probe microanalyzer.

The author expresses his gratitude to Mr. M. Knoepfel and all the other machine shop personnel for their assistance and preparation of workpieces.

I would also like to thank all my colleagues, past and present, in the ceramics and composites group for providing a stimulating environment; they have been helpful in many ways. I am so much indebted to T. Lebeau for translation of the abstract into French.

The personal financial support of the Iranian Ministry of Culture and Higher Education through a Post-Graduate Scholarship is gratefully acknowledged. I would also like to thank Pratt and Whitney Canada and NSERC for the financial support for this project.

Last, but not least, I would like to thank my wife for her continuous sacrifices and encouragement and my children who were often neglected during the years it has taken me to satisfy my educational goal.

TABLE OF CONTENTS

LIST OF FIGURES

LIST OF TABLES

NOMENCLATURE

T	temperature (K)
R	gas constant (8.314 J $mol^{-1}K^{-1}$)
X_i	mole fraction of component i
n_i	total mole number of component i
a_i	activity of component i
H	enthalpy
S	entropy
G	Gibbs energy, energy release rate
G_i	molar Gibbs free energy of component i
G°_i	molar Gibbs free energy of component i in its standard state
$\overline{G}_i$	partial molar Gibbs free energy of component i in solution
ΔG	change in G due to a change in the state of the system
ΔG^M	integral molar Gibbs free energy change due to mixing of two or more components to form a solution
$\Delta G^{M,id}$	integral molar Gibbs free energy change due to mixing of two or more components to form an ideal solution
G^{xs}	integral excess molar Gibbs free energy of a solution ($\Delta G^M - \Delta G^{M,id}$)
Q	general state thermodynamic function
$\overline{Q}_i$	partial thermodynamic function of component i
α	coefficient of thermal expansion
E	Young's modulus of elasticity
A	surface area
V	molar volume
θ	contact angle
W	work of adhesion
γ_{sv}	solid-vapour surface energy
γ_{sl}	solid-liquid interfacial energy
γ_{lv}	liquid-vapour surface tension
Γ_i	adsorption coefficient of component i
Γ	toughness
μ_i	chemical coefficient of component i
[ ]	liquid solution
< >	pure solid
{ }	pure gaseous species

Chapter 1

Introduction

1.1 Advanced Ceramic Materials

Ceramics were one of the earliest durable products known to man before the advent of metals. The term "ceramics" comes from the Greek word "keramos" which includes a wide variety of inorganic materials. Today's definition is broader than the historic one. The definition adopted by the US National Academy of Science is, "an inorganic, non-metallic, material processed or consolidated at high temperature"[1]. In North America and Japan "ceramics" include glasses, while in Europe and many other countries "glasses" are distinguished from "ceramics" and can be defined as "non-crystalline solids with compositions comparable to the crystalline ceramics".

One of the systems of classification of ceramics is to divide them into two groups, traditional and advanced. The term "traditional" refers to those ceramic materials which have been used by primary industries and consumer market for many years, examples are, bricks, pottery, sanitary ware, dinnerware and thermal and electrical insulations. Advanced, structural or fine* ceramics refer to a broad group of high performance inorganic materials including oxides, and non-oxides such as carbides, nitrides, borides and the like. The former group includes alumina, zirconia,

---

* The term fine ceramics is used in Japan, because these materials are made from very fine powder with fine-grained microstructure.

magnesia, and other refractory oxides. In the non-oxide group are silicon carbide, silicon nitride, boron carbide, boron nitride, aluminum nitride, and other such compounds. Advanced ceramics are distinguished from traditional ceramics by their specialized properties and higher level of performance. They are also different from traditional ceramics by the sophisticated processing and composition control they require to achieve unique performance which influences the much higher cost over the traditional ceramics.[2]

The development of advanced ceramics is due to the use of new concepts of ceramic science, the discovery of new material compositions and manufacturing techniques to achieve desired properties, and to the technological demand for materials with unique properties.

High performance applications of advanced ceramics are due to their special properties over metallic materials such as hardness, corrosion and erosion resistance, mechanical strength at elevated temperature, magnetic properties, high melting or decomposition point, low density, low electrical and thermal conduction, and low coefficient of thermal expansion particularly in Si_3N_4 and SiC families which translate into superior thermal shock resistance (Table 1.1). However, there are some exceptions such as high thermal conductivity of beryllia and aluminum nitride or the refractory properties of molybdenum, tungsten and other refractory metals. Because of these special properties, advanced ceramic materials have potential use in a wide variety of applications ranging from heat and wear resistance parts to electronic, aerospace and defence, cutting tools, bioceramics, optical devices and particularly in heat engines[3,4](Fig. 1.1). The main parameter which currently limits the reliability of structural ceramics is the flaw population, introduced during processing. It has been demonstrated that this problem can be minimized by post sintering HIP (hot iso-pressing) treatment or colloidal methods for powder treatment and consolidation.[5]

Perhaps one of the major area of applications for structural ceramics lies in the field of aerospace and automotive engines[6,7,8,9]. The potential application

Table 1.1 Property comparisons for some ceramics and materials.[2,10,11]

Material	Melting Point °C	Density $g.cm^{-3}$	$\alpha x10^{-6}$ K^{-1}	Therm. Cond. $W\ m^{-1}K^{-1}$	Strength[b] 20°C	K_{Ic} $MPa.m^{1/2}$
Si_3N_4	1750-1900[a]	3.18	3.2	12-28	400-580	4-6
RBSN	"	2.7	2.8	3-6	200-350	2.5
α-SiC	2300-2500	3.2	4.8	50-100	450-520	3.0-3.5
Al_2O_3	2050	3.96	8.5	30-35	200-350	3.5-4.0
Cast iron	1300	7.3	10.5	45	150-250	20
Inconel 718[c]	1400	8.19	13.0	11.2	1290-1410	103

a; Decomposition temp. b; MOR for ceramics and tensile for metals
c; Ni/19Cr/18.5Fe/5Nb/3Mo/0.4Al/0.9Ti/0.04C wt%.

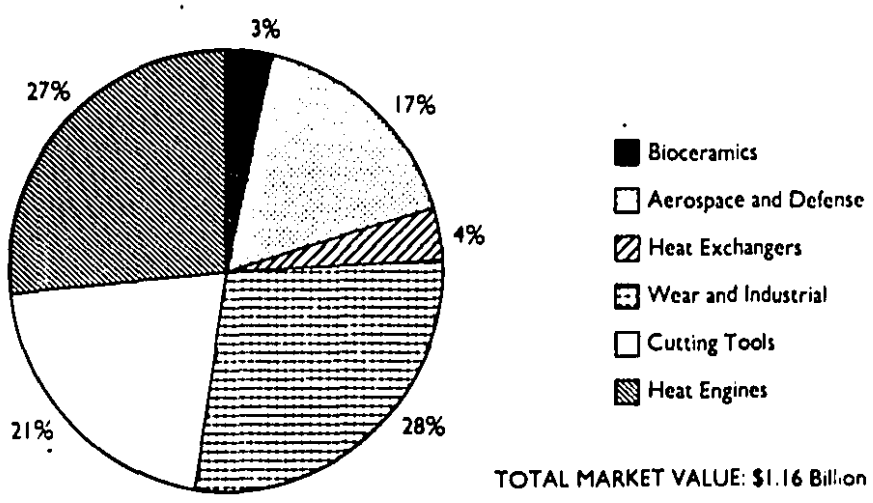

Figure 1.1 Advanced structures-ceramic market segments for 1995.[2]

in automotive engines can be divided into two groups: those for gas turbine engines and those for reciprocating engines (Fig. 1.2). Using ceramics in such systems results in increased operating temperatures, because of their strength and corrosion resistance at elevated temperatures. Functioning at higher temperature provides greater thermodynamic efficiency and, consequently, decreases fuel consumption. Moreover, in such systems as turbines or turbocharger rotors, where inertia is a critical consideration, ceramics may offer significant performance gain allowed by the decreased mass. The studies during the past decade have indicated that the use of ceramic components in an automotive gas turbine operating at ≈1300 °C would lower the fuel consumption to about 5.5 liter/100 Km[12]. Another study showed that the use of silicon nitride valves in a 5.8 L Chevrolet V-8 engine increased its power by 6 to 7%[13]. The primary interest of the aerospace industries in structural ceramics centres on their use in gas turbine engine[14]. Figure 1.3 shows the main ceramic components being considered for use in a helicopter gas turbine. Another motivation for developing ceramics for heat engine applications is the potential replacement of relatively expensive and strategic metals such as cobalt, chromium, niobium (columbium), nickel, manganese and tungsten[15]. Materials that may be affected by new developments in ceramic research are listed in Table 1.2. Current ceramic materials being evaluated for engine applications are silicon, nitrogen, and carbon which are inexpensive and available in abundant quantities.

Currently, consumption and shipments of advanced ceramic parts in the United States are in the range of $1 to $2 billion per year and is estimated to be about $10 billion by the year 2000[16], and that the market only for aircraft gas turbines could reach $3 billion by the first decade of 21th century[17]. The worldwide market has been proposed to grow to as much as $187 billion by the end of the century[17]. This rapid growth is due to the development of new applications and to the substitution of ceramics for alternative existing materials.

Although significant progress has been made in the processing and forming of monolithic ceramic components to improve their strength and toughness, these

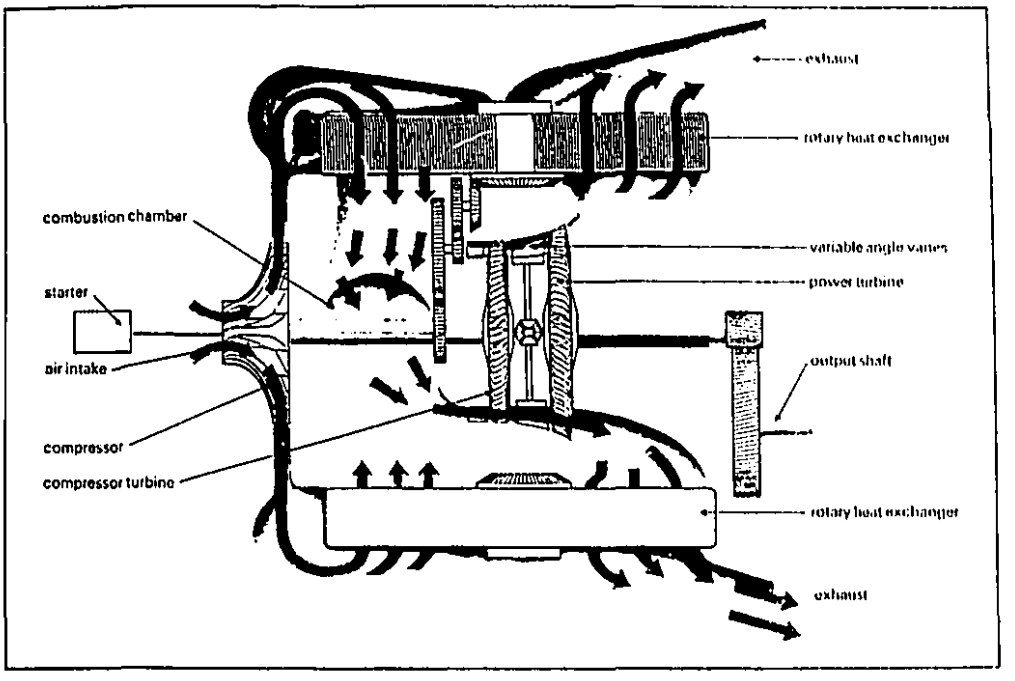

(a)

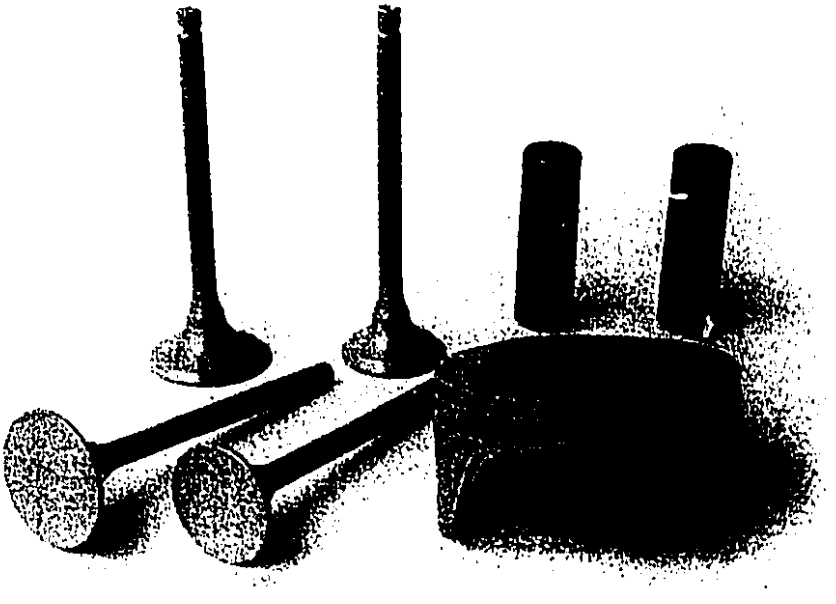

(b)

Figure 1.2 Simplified cross section of a 2S/350R gas turbine by Leyland[18](a), and (b) a set of ceramic components for a spark ignition engine[19].

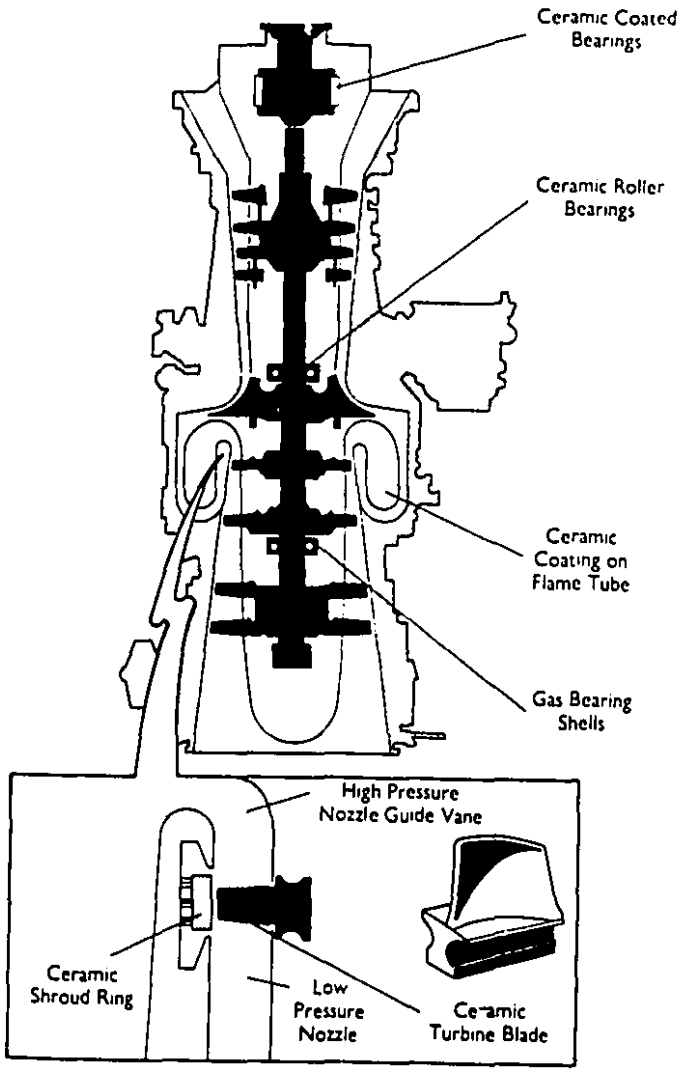

Figure 1.3 Ceramic helicopter gas turbine showing main ceramic components.[14]

materials are still far from exhibiting the advantageous ductility and toughness of metallic parts. Ceramic fibre reinforced/ceramic matrix composites and/or ceramic fibre reinforced/glass matrix (or glass-ceramic matrix) composites may present future alternatives to overcoming some of the mechanical property limitation. Also, developing joining techniques to reinforce ceramics by metallic components presents a major challenge to materials scientists.

Table 1.2 Some strategic materials for which ceramics could substitute.[15]

Material	Application where Ceramics May Replace the Material	Technological Barriers for Ceramics
Tungsten	Wear parts(bearings,nozzles) Cutting tools	Demonstration, scale up, cost Achieve hardness potential of Si_3N_4
Cobalt	Diesel combustion parts Turbocharger rotors heavy recovery systems	Demonstration, cost N/A N/A
Chromium	Heat engines Chemical ware Heat exchangers	Demonstration, properties, cost N/A Fabrication, performance, cost
Molybdenum	Heat recovery systems	N/A
Manganese	Heat engines	Demonstration, properties, cost
Titanium	Wear parts	Demonstration, scale-up, cost
Niobium	High-temperature applications	Fabrication, performance, demonstration

1.2 The Importance of Ceramic Joining

The promising role of structural ceramics in many useful devices and structures has in turn led to realization of the importance of developing ceramic joining techniques, which is perhaps one of the most important areas in the ceramic field for research and development[2,20,21,22].

The increasing demand for joining ceramics arises from:

a) Fabrication of ceramic components of complicated shape or large size in one piece can be very expensive and in some cases impractical, for the following reasons:

- Difficulties in processing steps and high cost of fabrication.
- High probability of destruction of entire pieces, even by a single flaw.
- Impossibility of reclaiming damaged parts.

• Difficulties in flaw detection for large parts.

There exist numerous methods by which complex-shaped engineering ceramic components may be formed, but each has its limitation. Difficulties with slip-casting (suspension-casting) or pressure-casting methods are shrinkage, mould release, lengthy drying cycle and particularly problems with shapes of varying cross section. Injection moulding appears to be a promising technique for mass production of ceramic components provided some existing problems can be solved. Accurate control of time, pressure, and temperature is required during forming, but injection moulding is amenable to producing components with both thin and thick sections, such as bladed rotors. However, difficulties with defects, binder removal from thick cross section without cracking, control of warpage, and lengthy debinding cycles are encountered[7,23].

These problems can be overcome by joining simpler and smaller components, which could be manufactured more easily. The simpler ceramic parts can be inspected individually before joining and those without the desired quality discarded. Furthermore, some applications may require ceramic materials of different properties to be joined.

b) In many cases, because of the limitation of ceramics resulting from poor impact properties and lack of tensile ductility, ceramic components functioning at high temperatures have to be attached to moving parts, mainly metals, which must withstand stresses or temperature gradients too great for ceramics. Another example of ceramic-metal bonding is joining metallic interconnects to ceramic substrate for microelectronic circuits.

Although the technology of ceramic joining has progressed steadily from late 1930's, currently it is not well developed, particularly for non-oxide ceramics, and extensive research efforts are being directed to better understanding the nature of adhesion at the interfaces, the relation between chemical bonding and mechanical stresses at the interface, and predicting reactions which occur during joining. This also includes the development of joining techniques to obtain reliable joints,

particularly when the joint is expected to be used at elevated temperature.

One of the most promising techniques for ceramic joining is high temperature brazing. This method is well suited for the fabrication of ceramic to metal joints and seals, and its status as the foremost method for making such joints has not been seriously threatened.[22,24,25,26]

This work deals specifically with the use of brazing technique for joining Si_3N_4 to Si_3N_4 and Si_3N_4 to Mo. Such aspects as the wettability of Si_3N_4 by the brazing filler metal as the basic requirement for brazing the candidate ceramic, the effect of brazing alloy composition and other brazing variables on joint quality and microstructure, and the influence of strength measurement methods on joint strength will be discussed.

Chapter 2

Literature Review

This chapter will briefly discuss the physical and chemical properties, manufacturing and applications of silicon nitride (Si_3N_4). A review of both ceramic-ceramic and ceramic-metal joining techniques will be given, with emphasis on available methods for joining silicon nitride. The problems, advantages and disadvantages of the brazing technique will be discussed. This chapter will also review various testing methods for measuring the joint strength and the relationship between them in evaluating ceramic joints.

2.1 SILICON NITRIDE

Of monolithic ceramics, Si_3N_4, because of the good combination of mechanical, thermal and thermo-mechanical properties is one of the most promising materials for high temperature structural applications[27,28,29]. Silicon nitride does not occur naturally and must therefore be synthesized[30]. Although it was initially accomplished in 1857 by Deville and Wöhlerand[31], its potential as a structural ceramic material has been explored only during the last two decades. In recent years significant progress has been made due to the improvement of Si_3N_4 starting powder and sophisticated consolidation techniques. So far, technological investigations have mainly been concentrated on two types of Si_3N_4: (a) dense Si_3N_4, which can be manufactured by hot-pressing(HPSN), sintering (SSN, SRBSN) or hot-isostatic pressing (HIPSN, HIPRBSN, HIPSSN, HIPSRBSN) and (b) porous Si_3N_4 produced by reaction-bonding of silicon powder compacts (RBSN). As a result of processing, the two forms of Si_3N_4 are different in density, resulting in different

mechanical, thermal and thermo-mechanical properties[32]. Silicon nitride has a high decomposition temperature and a high strength to density ratio compared to stainless steel[33]. Silicon nitride also exhibits excellent strength at elevated temperatures with a modulus of rupture (MOR) of ≈350 MPa at 1300°C[34]. The excellent resistance to corrosive environment and hot hardness of Si_3N_4 make it an ideal engineering ceramic for such applications as bearing and cutting tools[35,36], valves for diesel engines or turbine blades[37,38,39]. The main advantage of silicon nitride over other candidate materials (for heat engine applications), is its lower thermal expansion and moderate elastic modulus (Table 1.1), resulting in minimized stress development during severe thermal transients. The thermal shock resistance of silicon nitride is the critical characteristic which initially allowed Si_3N_4 to be a major candidate for heat engine applications. Figure 2.1 shows a comparison of the relative thermal shock resistance of Si_3N_4-based materials with other heat resistant materials. A strength measurement of turbo charger rotors made of Si_3N_4 and SiC at an exhaust gas temperature below 1050°C lead to the conclusion that Si_3N_4 and RBSN, in particular, feature a higher strength level and thus an increased reliability compared with silicon carbide[40].

The emphasis on Si_3N_4 is not only because of its structural properties, but also relates to the joinability of silicon nitride to itself and to other supporting metallic parts. Several Si_3N_4 components including glow plugs, hot plugs, rocker arm pads and the turbo charger rotors in commercial reciprocating engines are already in limited production. In spite of the above-mentioned advantage of Si_3N_4 over other ceramic materials being evaluated for heat engine applications, yet further investigations based on cost and performance are necessary to provide new comparisons.

2.1.1 The Structure of Silicon Nitride

Silicon nitride crystallizes in two forms, α and ß, with similar hexagonal crystal structure, but with different unit cell dimensions. The two forms of Si_3N_4

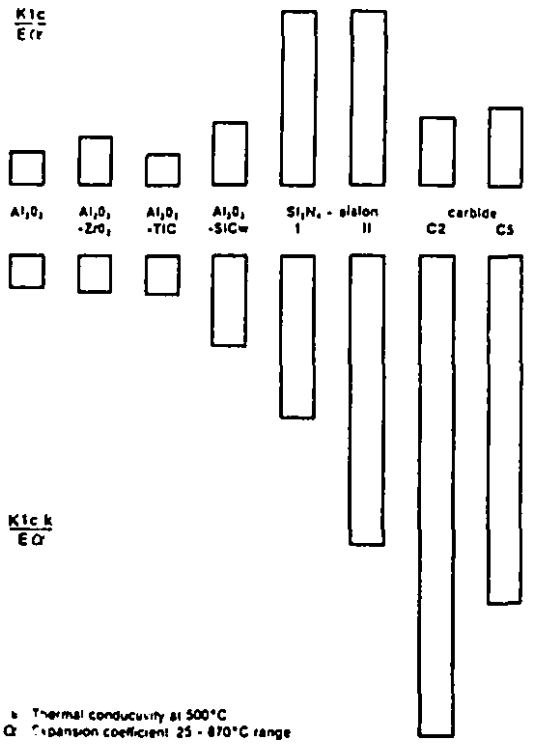

Figure 2.1 Comparison of the relative thermal shock resistance of Si_3N_4-based materials with oxides, ceramic matrix composites and WC-Co cemented carbides[41].

were identified for the first time by Vassiliou and Wild in 1957[42] and observed by Ruddlesden and Popper in 1958[43]. It was then established that the distance in the direction of the crystallographic *c* axis for α-Si_3N_4 is about twice as large as for the ß form (Table 2.1). In both α and ß-Si_3N_4 the silicon atoms are located in the centre of irregular nitrogen tetrahedra. Each nitrogen atom is shared between three tetrahedra so that each silicon atom has four nitrogen atom nearest neighbours and each nitrogen has three silicon atom nearest neighbours. (Figure 2.2). The Si_3N_4 unit cell of ß-phase is derived from the phenacite type structure (Be_2SiO_4) with the beryllium atoms being replaced by silicon and the oxygen atoms by nitrogen (Figure 2.3). The structure consists of Si_3N_4 layers which alternate in the sequence AB, forming hexagonal tunnels in the direction of the crystallographic *c*-axis. In the $Si_{12}N_{16}$ unit

Table 2.1 The Unit Cell Dimensions for Si_3N_4 (nm)[32].

AXIS	α-Si_3N_4	ß-Si_3N_4
a	0.775-0.777	0.759-0.761
c	0.516-0.569	0.271-0.292
c/a	≈ 0.70	≈ 0.37

cell of the α-phase, the layers known from the ß-structure alternate with mirror-inverted layers in the sequence ABCD, resulting in a *c*-direction lattice which is about twice as large as for the ß-modification. The hexagonal tunnels in the *c*-direction are not present in the α-phase[32].

The α-Si_3N_4 which is the major phase observed when silicon is nitrided at 1150-1350°C , given enough time and the proper means of mass transport, can be transformed to ß at around 1500°C, which is the more stable high-temperature form of Si_3N_4. The transformation, however, is reconstructive and can occur with

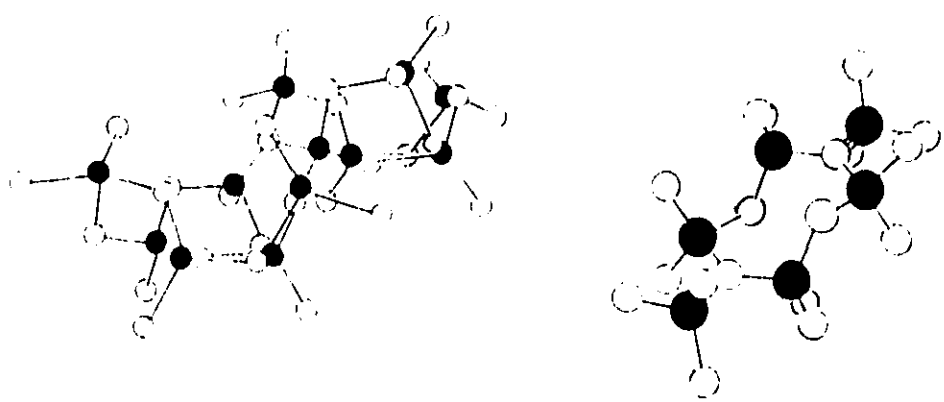

(a) (b)

Figure 2.2 Crystal Structure of a) α-Si_3N_4 and b) ß-Si_3N_4[34].

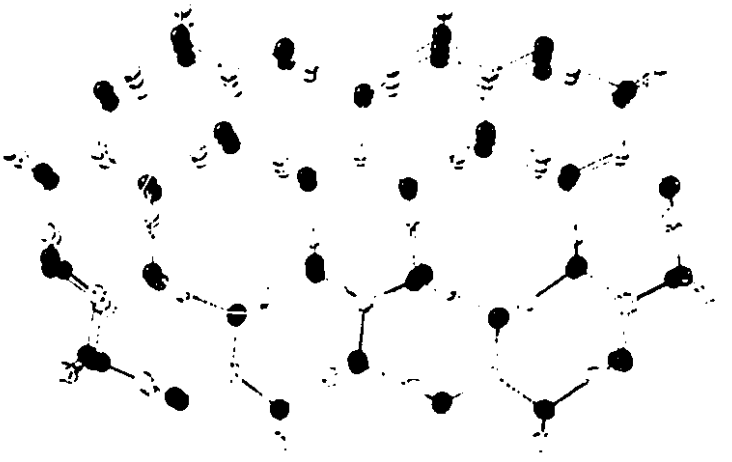

Figure 2.3 Ball Model of ß-Si_3N_4 Showing the Hexagonal Symmetry.[44]

solution-precipitation by means of a liquid phase. During transformation, α-Si_3N_4 grains dissolve in the liquid phase and reprecipitate as fibre-like grains. The intertwined structure of the acicular ß-Si_3N_4 grains is responsible for the high strength and toughness of Si_3N_4 products.

2.1.2 Powder Production and Processing of Si_3N_4 Ceramics

High purity silicon nitride powders can be synthesized by several methods, some of which have already been used for commercial production like carbothermal nitridation of SiO_2, direct nitridation of Si, the imide process and gas phase reaction[45]. The morphological characterization of Si_3N_4 powders including the fineness, particle shape, microstructure of particles and the powder agglomeration highly influence the compaction and sintering properties. These factors depend upon the method by which the powder is produced.

The direct nitridation of Si is an old and fairly simple method[46,47]. Si powders of 99 to 99.99% purity (less than 10 μm diameter) react with N_2 at 1473-1450°C in an atmosphere of NH_3, N_2/H_2 or N_2 to produce coarse Si_3N_4 powder[48].

In the imide process, silicon tetrachloride and ammonia react to produce a mixture of ammonium chloride (NH_4Cl) and so called silicon diimide ($Si(NH)_2$). The NH_4Cl is then washed out by liquid ammonia or thermal treatment in an inert gas stream at about 900°C. The remaining $Si(NH)_2$ will then be pyrolysed at 1200°C according to the following reaction:[49]

$$3Si(NH)_{2(s)} \rightarrow Si_3N_4 + 2NH_{3(g)} \qquad (2.1)$$

to produce amorphous Si_3N_4 powder.

In vapour phase reaction silicon tetrachloride and ammonia theoretically react at high temperature according to:[45]

$$3SiCl_4 + 4NH_3 \rightarrow Si_3N_4 + 12HCl \qquad (2.2)$$

practically, at 1050°C the gas phase reaction still will give silicon diimide which has to be calcined and crystallized as mentioned above. The carbothermal nitridation of silica seems to be a favourable method from an economical point of view for mass production of Si_3N_4 powder. The most important feature appears to be the abundance of high purity raw materials used, which are basically SiO_2, N_2 and a carbon-source[50]. The general form of the carbothermal reduction process where an oxide is reduced by carbon and then subsequently nitrided at 1350-1600°C can be described by the reaction:[50]

$$3\ SiO_{2(s)} + 6\ C_{(s)} + 2\ N_{2(g)} \rightarrow Si_3N_{4(s)} + 6\ CO_{(g)} \qquad (2.3)$$

Besides these industrially used methods, there are several synthesis methods such as plasma synthesis and laser-induced reactions which are only in development at present.

Because of high degree of covalent bonding, classical sintering is not applicable to produce pure dense Si_3N_4 ceramics. Consequently, alternative techniques have been developed, such as nitridation of silicon compacts or the addition of sintering aids to Si_3N_4 powder to create liquid-phase sintering with or

without the application of pressure to assist the sintering process.

The expression sintered (or pressureless sintered) silicon nitride usually refers to Si_3N_4 which has been densified with the help of additives (sintering aids) at atmospheric pressure. Below the sintering temperature (1650-1850°C), the additives react and melt to form a liquid phase. This liquid phase allows transport and rearrangement of the starting material at a greatly accelerated rate by a mechanism in which the starting α-Si_3N_4 particles dissolve into the liquid and the ß-Si_3N_4 phase is reprecipitated out as elongated interlocking grains[51]. Although many additives have been reported for densification of Si_3N_4, most studies have concentrated on the use of MgO, Y_2O_3, Al_2O_3 and AlN as sintering aids.

Since silicon nitride bodies with high density (≈ 95-99%) and very good strength (bend strength ≈ 400-1000 MPa) can be produced by pressureless sintering process, this is the preferred method for fabrication of complex-shaped components.

Hot pressing is analogous to sintering except that pressure and temperature are applied simultaneously. Most hot pressing is done in the range of 6.9 to 34.5 MPa at temperatures approximately half the absolute melting temperature of the material[52]. This process results in materials with higher final densities and fine grain size due to reduced densification temperature and increased contact stress between particles. Hot pressing permits reduction of the amount of sintering aid required to obtain full density. This can result in an order-of-magnitude improvement in high-temperature properties such as creep and stress rupture life[53]. The major limitation of hot pressing is shape capability. Non uniform cross section and intricate or contoured shapes are difficult and often impossible to be fabricated by conventional uniaxial techniques.

Another technique which combines good mechanical and thermo-mechanical properties of Si_3N_4 with the possibility of production complex-shaped components is hot-isostatic pressing (HIPping). During HIPping, high pressure (up to 300 MPa) is applied uniformly in all directions via an inert gas to consolidate a powder compact or to remove residual porosity from pre-sintered materials. During the past few

years special HIPping equipments have been developed to enable HIP densification at temperatures higher than 1700°C[32]. This method makes possible net shape forming because the pressure is equally applied from all directions. This also results in greater material uniformity by eliminating die wall friction effects and preferred orientation, resulting in higher strength and Weibull modulus. The HIP process is well suited to nitride ceramics, which decompose under normal pressure at lower than the melting temperature. In spite of the above mentioned advantages, HIPping is still a complex and costly alternative.

2.2 THE METAL MOLYBDENUM

Mo is a silver-white metal that is not found in pure form. It can be obtained principally from molybdenite (MoS_2). Wulfenite ($PbMoO_4$) and Powellite ($Ca(MoW)O_4$) are also minor commercial ores. Mo is also recovered as a by-product of Cu and W mining operations. The metal is prepared from the powder by the hydrogen reduction of purified molybdic trioxide or ammonium molybdate[54]. In most instances, Mo is consolidated from powder by compacting under pressure followed by sintering in the range from 1650 to 1900°C. Some Mo is consolidated by a vacuum arc furnace casting method in which a preformed electrode is melted by arc formation in a water-cooled mould [55].

Although Mo has been known for almost 200 years, its potential industrial uses date back only to the first decades of this century, and its significant consumption to the mid-thirties[56]. The importance of Mo was realized when the modern technologies of alloy production and the understanding of their properties were developed. Mo is a valuable alloying agent, as it contributes to the hardenability and toughness of quenched and tempered steels[57]. It also improves the strength of steel at high temperatures. Almost all ultra-high strength steels with minimum yield points up to 2000 MPa (≈300,000 psi) contain Mo in amounts from 0.25 to 8% [54]. Mo and its alloy are used for electrical and electronic parts, missile and aircraft parts, high-temperature furnace parts, thermocouples, nuclear energy applications,

corrosion-resistant equipment and metallizing. Mo, because of its low thermal expansion and high elastic modulus (Table 2.2), has found application as an interlayer in ceramic-to-metal joining. This layer would alleviate stresses generated by the thermal expansion mismatch between the ceramic and metal, resulting increased joint strength.

2.2.1 Oxidation and Corrosion Behaviour

Molybdenum oxides rapidly at elevated temperatures to the point of complete disintegration. The final product of the oxidation reaction is molybdenum trioxide (MoO_3), which is volatile and therefore is not a self-protective oxide. Below 500°C, a parabolic oxidation law is followed indicating some degree of self-protection. The oxidation of Mo is a two-step process with molybdenum dioxide (MoO2) as the internal oxide layer and molybdenum trioxide as the outer layer[58]. Above 500°C MoO_3 begins to volatilize and at 770°C it evaporates with same rate as it forms. At 996°C the oxidation rate is about 1400-2000 mg/cm^2 h. The rate increases with air pressure and falls when the pressure falls, particularly when the partial pressure of the oxygen falls in the corrosive gaseous mixture. For instance, the oxidation rate at 1135°C at an altitude of 5000 m is 100 times slower than at ground level under atmospheric pressure. Similarly the oxidation rate is lower in reducing atmospheres.

In summary, from the oxidation behaviour of Mo, it can be stated that Mo is not a suitable structural material for continued service at temperatures above 500°C in an oxidizing atmosphere, except for very short time service conditions. In contrast, it has been reported that, in oxygen-deficient combustion gases, Mo would have satisfactory high-temperature durability for combustion chambers or turbine blades. The corrosion rates in fuel-rich combustion mixtures at temperatures up to 1427°C are such that uncoated Mo appears feasible for applications in reducing atmosphere where engine life of less than 100 hour is acceptable[58,59]. Therefore, if Mo is to achieve its potential as a high-temperature structural material, it must

Table 2.2 Some Properties of Mo.[55]

Property	value
Atomic weight	95.94
Density	10.22 g/cm^3
Crystallography	b.c.c
Melting point	2610°C
Boiling point	5560°C
Coefficient of thermal expansion	5.3 to 6 μm/m.k (20 to 1000°C)
Coefficient of thermal conductivity	80 to 142 W/m.k (20 to 1500°C)
Electrical resistivity	52 to 620 nΩ (0 to 2000°C)
Hardness	≈250 HV (as-rolled at 20°C)
Elastic modulus	≈330 GPa (at 20°C)
Tensile strength	≈600 MPa (at 20°C)

be protected from oxidation by an adequate coating. Such oxidation resistance might be achieved through alloying or through the use of external coatings which would act as physical barrier between the Mo and O. Several types of protective coatings for Mo and its alloys are already in use. These includes, ceramic coatings, molybdenum disilicide coatings, sprayed metal and electroplated coatings[58]. It must be noted that the performance requirement for any coating system will vary depending on the operating conditions, i.e., time, temperature, gas composition, velocity and other

factors which will determine the durability and performance of a coating for a given application.

Mo has particularly good resistance to corrosion by mineral acids such as both aqueous and anhydrous HF. The corrosion rate of Mo in 25 to 50% HF at 100°C are 0.4 to 0.5 mm/yr in aerated acid, whereas, in the absence of air is so small as to be negligible[60]. It is also resistant to many liquid metals and to most molten glasses. In inert atmospheres, it is unaffected up to 1760°C by refractory oxides. Mo is relatively inert in hydrogen, ammonia, and nitrogen up to about 1100°C, but a superficial nitride case may be formed in ammonia or nitrogen[55].

2.2.2 The Brazing of Molybdenum

The low coefficient of thermal expansion of Mo (Table 2.2) allows this metal to be used as an interlayer in joining ceramics to metals to alleviate the residual stresses within the joint area caused by thermal expansion mismatch between the ceramic and metal (this will be discussed in detailed in § 2.3.1). In these systems the Mo interlayer is brazed to both ceramic and metal members. Therefore, all the arguments in brazing of Mo must be considered in these systems for a proper joint design.

The property which is of importance in any discussion on joining Mo is its ductility. In common with other refractory metals, Mo, because of its body-centred cubic (bcc) structure exhibits a change from ductile to brittle behaviour on cooling below a certain temperature; the ductile to brittle transition temperature. This temperature is not fixed and varies with strain rate, alloying additions, impurities, heat treatment and method of fabrication[61]. The transition temperature for pure Mo is 150 - 260°C[62], thus, Mo is brittle at room temperature and must be handled carefully to avoid damage. Also, this metal should be brazed in a stress -free condition. Another factor which influences the strength and ductility of Mo is the microstructural changes that occur when the recrystallization temperature is exceeded. The recrystallization temperature range for Mo is 1150 - 1200°C and can

be increased through alloying. For example the recrystallization temperature of Mo-0.5Ti-0.7Zr is about 1470°C, and the stress-rupture strength of this alloy at elevated temperatures (980 to 1100°C) is several times that of unalloyed Mo. In some applications, brazing performed below the recrystallization range using low melting temperature filler metals. Other applications for high temperature services require filler metals with melting temperature above the recrystallization temperature. In this case the joint must be designed with the loss in mechanical properties associated with recrystallization. The low coefficient of thermal expansion should be considered in the joint design especially when Mo is brazed to other metals which may have expansion coefficient three or four times higher than that of the Mo. Usually joint clearance in the range of 50 to 125 μm at the brazing temperature are suitable. Thermal conductivity is important in brazing Mo. The coefficient of thermal conductivity of Mo is high at room temperature and drops as the temperature is increased (Table 2.2). The high coefficient of thermal conductivity allows rapid heating and a minimum of time at the temperature, thereby minimizing the danger of uneven heating.

2.2.3 Brazing Atmosphere and Equipment

The brazing environment is of importance because of the reactivity of Mo with O, N and C and the effect of these elements on the mechanical properties of the metal. As mentioned previously, the surfaces of Mo to be exposed to O at high temperatures must be protected from oxidation. Since the coating layer would alter the wetting of the metal by brazing filler metal, for such service conditions, the brazing filler metal must be compatible with both the base metal and the coating. The solvation of N at temperatures above 1100°C and its severe influence on mechanical properties of Mo must be taken into account as well. Mo forms carbides in the presence of minute quantities of carbon. Thus, the brazing atmosphere must contain minimal amounts of O_2, N_2, CO and CO_2 when brazing uncoated Mo. Torches, controlled-atmosphere furnaces, vacuum furnaces, induction and resistance

heating equipments can be used to braze Mo. Oxyacetylene torch brazing can be accomplished with Ag and Cu-based braze filler metals and an appropriate flux[62]. In terms of fixturing, graphite should not be used to position the metal during brazing. Outgassed ceramic materials, Ta and W can be used as brazing fixtures[62,63].

2.2.4 High Temperature Filler Metals

Many pure metals and alloys have been used to braze Mo for high temperature applications. Mo can be brazed with Au, Pd, Pt, Ni, reactive metals, Ni-based filler metals and refractory metal-based alloys [62,63]. Mo samples brazed with Inconel as the brazing alloy showed a braze-shear strength of approximately 130 MPa at 980°C[63]. It has been demonstrated that Mo joints made with Ti-65V, pure V, V-50Mo and MoB-50MoC are as strong or stronger than the base metal at elevated temperature. Mo-0.5Ti Mo base metal has been successfully brazed using two binary braze metal, V-35Nb and Ti-30V at 1870 and 1650°C respectively[62]. Ti-25Cr-13Ni braze filler metal, with a brazing temperature of 1870°C, has produced joints with ≈168 MPa shear strength at 1100°C[62].

2.3 CERAMIC-CERAMIC AND CERAMIC-METAL JOINING

The literature on ceramic joining is extensive and a discussion of all the materials is beyond the scope of this thesis. In this section a survey of ceramic-ceramic and ceramic-metal joining for both oxide and nonoxide ceramics, with emphasis on joining silicon nitride, will be given. Methods of joining ceramics, problems of ceramic joining, and methods by which the strength of ceramic joints are measured will be discussed.

2.3.1 Joining Theory

A completely acceptable theory for bonding ceramics has not been developed. Most of the information available is empirical in nature, describing observations of

investigators concerning the nature of the bonding materials and interfaces under a specific set of experimental conditions. The large number of variables involved and the complexity of ceramic structure provide significant difficulties in the development of a satisfactory predictive theory of bonding ceramics.

Ceramic-to-ceramic or to metal bonding is the result of chemical and/or mechanical interaction between the materials. The chemical interaction may result in either the formation of new compounds at the interface or the development of weaker adhesion resulting from the formation of secondary bonding forces[64].

In spite of the absence of a general theory for bonding ceramics, two theories for adherence of metals to ceramics have emerged over the last three decades. One is known as the "glass migration theory" and the other as the "chemical reaction theory". The former theory, proposed by Cole and Sommer[65] in 1961, suggests that the glassy phase present in the grain boundaries of impure ceramics, migrates by capillary action into the sintered metal layer, producing a bond. This theory describes bonding using the refractory metallizing technique. However, the basic theory for this system is applicable to other metal-to-ceramic systems. The criticism of the glass migration theory, in spite of its successes in explaining certain procedures, is two fold. First it leaves out many examples where no glassy phase is present, before, during, or after bonding. For instance, it fails to explain the relatively high adherence of a pure Mo metallizing layer to single crystals or to alumina ceramics i.e. with no glassy phase or low impurity content. Second, it leaves unanswered the question why the metal adheres to the glassy phase[66].

Many researchers have focused on importance of the role of chemical bonding at ceramic metal interface. They have shown that the chemical bonding between the ceramic and the metal is achieved through the formation of an intimate, atomic contact interface or reaction to reach chemical equilibrium at the interface[67]. Discussion on chemical bonding will be given in detail in Chapter 3.

2.3.2 Methods of Joining Ceramics

Many different techniques have been developed for joining ceramics to ceramics and to metals. Most of the published information relating to techniques for joining ceramics mainly describe the results of development work rather than proven production process. The classification of joining techniques is somewhat arbitrary and can be done in different ways[68,69,70,71,72,73]. Here we will divide the joining methods into three major techniques[70]:

• **Mechanical joining** - used in both traditional and new applications such as the tying-in of furnace roof refractories with metal hooks or dogbones. Press and shrink fitting is another type of mechanical joining which is widely used in mass production processes.

• **Direct bonding** - achieved by pressing together very flat mating surfaces to achieve diffusion bonding, as in the joining of sapphire to Nb during the fabrication of high-pressure sodium lamps. Experimental studies of fusion welding using electron beam, laser, and imaging arc techniques have also met with some success for high melting point systems.

• **Indirect bonding** - the most common method of achieving high integrity joints using a wide range of intermediate bonding materials such as organic adhesives, glasses or glass-ceramics, soldering, welding, and brazing with or without pretreatment of the ceramic surfaces to render them wettable.

Irrespective of the joining process, the achievement of successful joints depends on the[70]:

- intimate contact between the workpieces and conversion of these contacting surfaces into an automatically bonded interface, and the ability of this interface to accommodate thermal expansion mismatch stresses generated during cooling after

fabrication or temperature changes in operational conditions.

- the joining process should cause minimal chemical and mechanical degradation of the base materials.

Of the above joining techniques, attention will be given to those processes that permit the achievement of strong joints by direct bonding and indirect bonding for high temperature applications. Low temperature techniques such as soldering and adhesive joining will not be discussed. Since fusion welding is usually impractical because of marked differences in the refractoriness of the workpiece materials and problems with some ceramics (BN, SiC,Si_3N_4) which sublime or decompose before melting will not be discussed.

Mechanical fastening has a limitation because it requires three- dimensional design and it cannot produce a plane-to-plane bond structure. Furthermore, it is quite difficult to build up a large-scale joined component by mechanical fastening.

2.3.2.1 Direct Bonding

Direct bonding is analogous to solid state or diffusion bonding. The literature contains many reports which have used this method for bonding metals such as Al, Pb, Cr, Zn, Cu, Ni, Fe, Pt, and refractory metals such as Nb and W to oxide and nonoxide ceramics. Solid state bonding can follow contact without any apparent need for bulk interactions. Achievement of the minimum contact and bonding for a specific application depends on the selection of not only the materials, but also fabrication parameters, such as surface roughness and cleanness, environment, pressure, time, and temperature[70]. Solid state bonding of ceramics to metals can be carried out directly or with the use of an interlayer material to promote bonding at the ceramic/metal interface.

Solid state reaction bonding procedures have the following characteristics[74]:

- Bonding temperatures lie below the melting point of the lowest melting component

in the system (generally the metal), usually about 50 to 98% of the melting point in degrees absolute.

- Bond formation is carried out in air, argon or vacuum.

- Clamping pressures from 0.5 to 100 MPa are used, to ensure good physical contact at the interface during bonding.

- Bonding times vary from a few second to about 3 hours.

- The surface of the ceramic to be bonded must be polished to a finish approaching optical flatness for the maximum bond strength.

Solid state bonding can be approached in two ways. The first involves the use of considerable applied pressure, >7 MPa, which act as a significant driving force in the sintering kinetics. The second way is to use much lower pressures only to maintain contact and alignment during bonding.

Usually, increasing the fabrication time or pressure improves contact and bond quality, but as shown in Figure 2.4 the influence of temperature has been reported to be of greater importance[75,76]. On the other hand the high temperature employed increases the magnitude of the CTE (coefficient of thermal expansion) mismatch stresses, often resulting in fracture of the ceramic[77]. Therefore it is very difficult to bond ceramics to metals directly. Thus, when applications at high temperatures are considered, it is indispensable to develop a bonding method on such materials with a proper design that be able to accommodate the stresses generated during cooling after fabrication. Unfortunately, the need to exert pressure in diffusion bonding causes most joints to be of the face seal type, which is not well suited for accommodating mismatches[70]. It has been found that the use of a soft material layer inserted between the ceramic and metal members

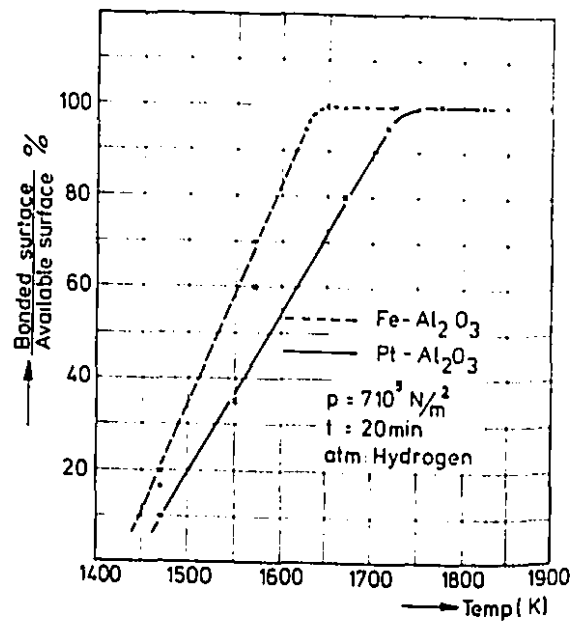

Figure 2.4 Influence of fabrication temperature of diffusion-bonded area of Al_2O_3 at constant pressure and time.[76]

can overcome or mitigate the effect of some of these practical problems [75,78,79]. Another approach is the use of either a metal interlayer (usually refractory metals) whose coefficient of thermal expansion is between the ceramic and the metal[80] to minimizing the CTE mismatch between the ceramic and metal or by placing a number of layers between the metal and ceramic; the difference in alpha between each layer should be minimized to alleviate the interfacial stress. As shown in Figure 2.5 the CTE mismatch is reduced by incorporating layers of different compositions and closely matched values; the interfacial stress is reduced if the layers are properly designed. This technique which is also known as composite interlayer method has been successfully used in many investigations[81,82]. Eaton and Novak[80] employed this method for the fabrication of a graded gas-path sealing as shrouding in the turbine section of an aircraft gas turbine engine. The top layer

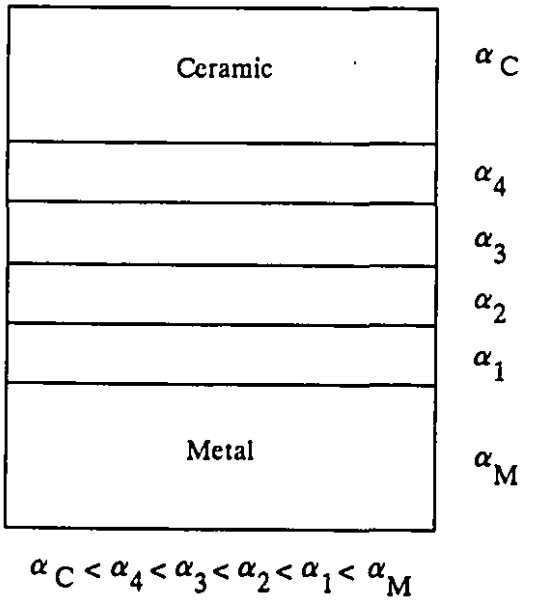

Figure 2.5 Graded alpha (α) attachment technique designed to reduce the α mismatch between ceramics and metals.[67]

material was stabilized zirconia and a series of ceramics (mullite, zirconia, alumina, spinel, and ceria)/CoCrAlY were used for the intermediate layer compositions. Alumina/CoCrAlY intermediate layer material exhibited desirable dimensional and oxidation stability which showed an as-fabricated four-point bend strength of 58 MPa and 111 MPa after 36 hour of oxidation at 1093°C. This joining method was employed by Suganuma *et al.*[80, 82] to form AlN-Mo, TiN-Mo, and BN-Mo joints by HIPping at 1620°C for 30 min. under 3 GPa pressure. The interlayer of each couple contained 60 vol% of the ceramic phase to be bonded and 40 vol% of Mo powder.

Various ceramics have been diffusion bonded to metals and alloys. Klomp[76] studied the bonding of Pt, Fe, Ni, Cu, Al, and Pb to pure alumina. The Pt-alumina joints bonded at 1550°C under 3.1 MPa pressure for 100s showed a bond strength of 250 MPa. Ruhle *et al.*[83]studied the bonding mechanism between the Nb and alumina by introducing line-shaped defects on single or polycrystal Nb. Those Nb crystals were then diffusion bonded to alumina. They found that bonding occurred

primarily in the area of close contact between Nb and alumina.

Yamada and co-workers[84] studied diffusion bonding of SiC and Si_3N_4 to Nimonic 80 (Ni-20Cr-3Fe-2.3Ti-1.4Al-2Co wt%) using Ni, W and Cu interlayers with different thicknesses. They found that the residual thermal stress in the ceramic part of the composite was extremely low and that the composite had a tensile strength of more than 95 MPa at room temperature.

The disadvantages of hot-press bonding are that the process is complex and expensive, that proper alignment of the parts is difficult, and the components frequently fracture or deform while being joined.

2.3.2.2 Indirect Bonding Processes

Indirect bonding of ceramics includes those techniques in which a liquid medium is responsible for bonding. Liquid phase bonding using molten metals or glasses has been widely used to create ceramic/ceramic and ceramic/metal joints. Of all the liquid phase joining techniques, brazing is uniquely suited to the fabrication of ceramic joints and seals and its status as the foremost method of making such joints has not been seriously threatened. The advantages of brazing can be summarized as follows[85]:

- Brazing is a simple and flexible process which can use existing equipment, therefore requires little capital investment and can be readily adapted to mass-production operations.

- Large or complex assemblies can be joined in a single step operation and in a stress-free condition especially with respect to ceramic-to-metal joining[86].

- Joint members of different thicknesses can be brazed to each other.

- Using brazing filler metals with different melting temperatures, additional

assemblies can be joined to a partially completed structure.

- Through proper joint design, brazed joints require little or no finishing.
- Joints can be brazed for a wide range of service conditions by proper selection of the filler metal.

The main limitation of brazing for joining ceramics is finding proper braze compositions that meet all the desirable properties. In fact the brazing filler metal is the key material for brazing ceramics. The following criteria must be met for a brazing filler metal to achieve the joining requirements particularly for high-temperature applications:

1) the filler metal must wet the parent materials of interest especially the ceramic.
2) the filler metal and/or brazing process should cause minimal degradation of the base material(s).
3) it should be chemically compatible with the base material(s) to avoid formation of low melting intermetallics or undesirable phases at the interface(s).
4) the filler metal must be ductile to accommodate CTE mismatch stresses at the ceramic/filler metal interface generated during cool-down from brazing temperature.
5) relatively strong bonds must be formed that will survive not only potential thermal stresses but also service conditions.
6) it is also important that the brazing filler metal be able to withstand high service temperatures and severe chemical environments.
7) the filler metal should not blush over the ceramic or the metal member.
8) the filler metal should have a low vapour pressure, particularly for vacuum brazing.
9) good fluidity.
10) an appropriate melting point for intended application.

Of the above mentioned requirements, wetting of ceramic is the basic and most important requirement for the filler metal. The aspects of wetting will be discussed in detail in Chapter 3. Briefly, Most braze filler metals do not wet ceramics easily. To promote wetting, either the surfaces of ceramics must be treated by metallizing or the braze compositions should contain active elements such as Ti or Zr.

Indirect brazing of ceramics involves metallizing the surface to be joined by such processes as the "Mo-Mn process" followed by brazing, the metal hydride powder process, and the metal vapour coating process followed by brazing. The Mo-Mn process is by far the most commonly employed[87,88]. It consists of spraying (or brushing) the ceramic with a mixture of Mo and Mn powders suspended in an organic carrier. The coating is sintered to the ceramic in a wet hydrogen atmosphere. This coating is electrically conductive, and Cu (or another metal) is electroplated onto the coated area. The metallized and plated ceramic is then brazed, usually in a controlled atmosphere furnace. It is evident that, although the ceramic may be stable to high temperatures, its use at high temperatures is limited by the presence of the lower melting plating material[89]. The active hydride process is essentially a single-step process in which hydride reduction and brazing proceeds simultaneously. The ceramic surface is coated with Ti (or Zr) hydride and the coating is fired. The hydride dissociates at about 900°C and a residue of pure metal remains. The Ti (or Zr) thereupon bonds by reaction with the ceramic and subsequently the metallized ceramic with the filler metal. Even though the process is considered a one-step process, the hydride process has been replaced by the active metal process[85,89].

Another metallizing method which can be used for metallizing oxide ceramics is "direct copper method". In this process a thin Cu sheet is placed on the surface of the ceramic and heated in air to about 1100°C. The oxidized surface of Cu adheres strongly to the ceramic and the free surface is cleaned up and can be brazed or soldered to metal[71].

Many other alloys and compounds have been studied for metallizing ceramics surfaces. Naka *et al.*[90] used amorphous Cu-Ti alloy for metallizing Si_3N_4. The metallized surface was then Ni-electroplated and joined to carbon steel using Ag-Cu filler metal.

Metal vapour coating of ceramics includes chemical and physical vapour deposition. For active metals the latter proves feasible[91]. Several variations of physical vapour deposition have been used to coat reactive metals. They include, sublimation and evaporation, sputtering, and ion plating. Hommands and co-workers[91] investigated the Ti coating of alumina and zirconia ceramics using plasma ion bombarding. Although this method produces coatings generally with superior adhesion, the process is not as widely used commercially as other physical deposition methods. Vacuum evaporation method was used by Santella[92] for coating Si_3N_4 with Ti. This study showed that a 1 μm-thick layer of Ti improves wetting of Si_3N_4 by Ag-Cu, Au-Ni, and Au-Ni-Pd alloys.

Direct metallization of Si_3N_4 has been developed by the Toshiba Co[71]. The process consists of decomposition of Si_3N_4 at the surface of substrate to elemental silicon and nitrogen gas under vacuum at high temperature according to the equation:

$$Si_3N_4 \rightarrow 3Si + 2N_2 \qquad (2.4)$$

The decomposition process depends on both temperature and nitrogen partial pressure. In this process Ni powder is introduced onto the surface prior to vacuum heat treatment at about 1200°C. In the Ni-Si system a eutectic forms at 20 at%Si and 1150°C between Ni and Si which allows for complete wetting.

The above mentioned metallizing methods, particularly the Mo-Mn process have been developed to a high degree of reliability, but all the processes are time consuming and require extensive process control. Joining ceramics to metals using or alloys containing active elements has been investigated since 1940[93]. It is a one-step joining process and it is less sensitive to process variables than the Mo-Mn

process. There are several methods of the active metal brazing. One method involves cladding of a sheet of Ti by two sheets of the conventional brazing alloys[79]. Another method uses titanium hydride powder mixed with Ag powder (also Cu, Au, etc.) and the mixture is applied as a paint onto a ceramic surface. Then a metal member is placed in contact and the assembly heated to about 1000°C under dry hydrogen[93]. However, the most economical method utilizes a filler metal where an active element forms a true alloy with the base filler metal. Most of the developed active filler metals centre on Cu-Ag containing various Ti additions with or without the addition of third elements[94,95,96]. In spite of extensive investigations on active metal brazing and fabrication of strong joints, this process may result in consistent properties of the joints[79,93] and is also limited to low temperature applications.

2.3.2.3 Miscellaneous Joining Techniques

In addition to previously mentioned techniques, several other methods have been developed for joining ceramics. Most of those processes in fact are not distinct methods, but a combination of conventional joining methods with novel techniques to improve the joint quality; some of which include:

• **Squeeze brazing**: developed by Suganuma[97], is a new joining process for bonding ceramics to ceramics and ceramics to metals. This process utilizes squeeze casting. A brazing material is squeezed into the interface channel to be brazed and is solidified under a high pressure ranging from 10-100 MPa. Using pure Al as a filler metal, this method can produces high-strength alumina-alumina and silicon nitride-silicon nitride joints.

• **Microwave joining**: the concept of microwave joining is basically the same as solid state bonding except that electromagnetic energy is used to heat the materials. Microwave processing has been applied for drying, melting, calcining, firing and

sintering. The current emphasis is on sintering. The first report on microwave joining dates back to 1985. The interested reader will find a coverage in the article by Palaith and Silberglitt[98]. Although at an early stage of development, microwave joining has the potential as a cost-effective method for joining both oxide and non-oxide ceramics[98].

• **Ion bombardment:** the N^+ion bombardment of Si_3N_4 surface has shown improvement in the adhesion property of films of reactive elements like Ti and Zr. The increase in peel and tensile strength of the coating to ceramic bond is believed to be a result of atom mixing caused by the ion bombardment[71].

• **Carbon flux metallization:** it has been demonstrated that a thin layer of carbon on the surface of a wide range of structural ceramics enhances the wettability of the surface by a Cu-35%Mn type braze, improving joint strength[71].

• **Coating by hot isostatic pressing:** HIPping has been used as a means of coating metals with ceramics. Many ceramics such as TaC, TiC, AlN, TiN, and Al_2O_3 have been coated onto stainless steel. The novelty of the process is the simultaneous sintering and bonding to the metal[71].

2.3.3 Problems of Joining Ceramics

Fundamental problems of joining ceramics arise from the fact that all types of ceramic joining create interfaces across which there are discontinuities in material properties. Even diffusion-bonding of two single crystals in ultra high vacuum likely involves some degree of structural discontinuity at the interface[72]. Other practical joining methods like brazing exhibits other types of discontinuities. They are chemical, mechanical, and thermo-mechanical mismatches. The study of the nature of these discontinuities and learning how to control and to manipulate the properties of the interface for the intended application is the objective of ceramic

joining engineering. Thus, the degree of joint reliability and performance is determined by how well those mismatches are identified and accommodated.

Depending on the joining method and application, these discontinuities exhibit themselves in different ways. The following are some of the material properties that may change suddenly at an interface between a ceramics and a metal[73]:

• Crystallographic: generally there is a lattice mismatch between a ceramic-metal joint.

• Thermodynamic: in general, two materials at an interface will not be in thermodynamic equilibrium and they will tend to react at the sealing temperature to form interfacial reaction products.

• Mechanical: there can be a variation in elastic modulus across an interface.

• Thermo-mechanical: there will be a difference in the coefficient of thermal expansion (CTE) across an interface.

Crystallographic: It is widely recognized that the crystallographic structure of an interface determines to a great extent the physical, chemical and mechanical properties of the interface. Theoretical work on the microstructure of ceramic-metal interfaces is still in its infancy, in particular if chemical reactions have to be taken into account[99].

The optimum interface properties are achieved if certain crystallographic planes of the ceramic and of the metal, including those of the reaction products, form a coherent interface that involves little or no elastic strain. Theoretical works stress the significance of the planar atom density on the interface energy. This seems to be supported by observations on non-reactive ceramic-metal systems where the densest metal and ceramic planes coincide[99].

Experimental investigations on the crystallographic relationship between α-SiC single crystal and a Ti-foil revealed a lattice matching in the *c*-direction between SiC and Ti_3SiC_2. As shown schematically in Figure 2.6 every seventh (0002) plane (5.278 nm) of SiC coincides well with every sixth (0002) plane (5.288 nm) of Ti_3SiC_2 [100]. Other examples of the study of orientation relation between the phases at ceramic-metal interface include the work of Morozumi *et al.*[101] and Iseki *et al.*[102]. The complexity of the phase relations increases greatly in going from binary to ternary and multi-components systems where various reaction products are formed at the ceramic-metal interface.

Thermodynamic: In joining ceramics to metals, particularly when using brazing technique, the chemistry of the ceramic-metal system plays a significant role. The

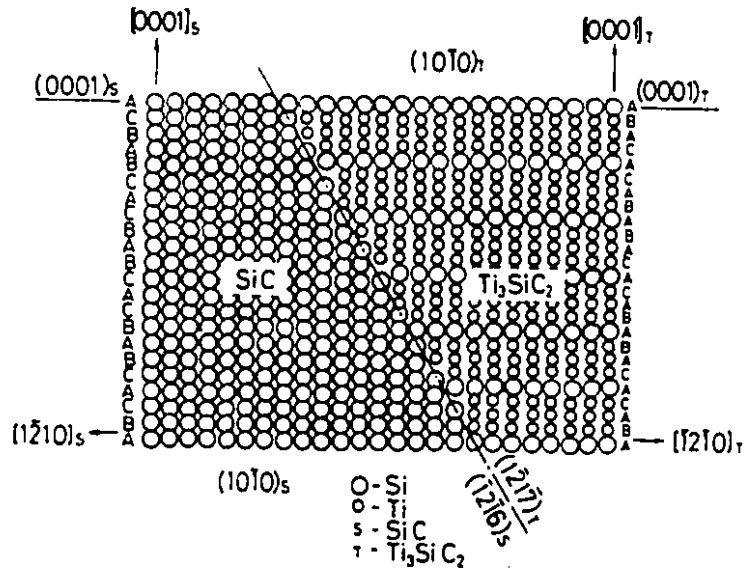

Figure 2.6 Schematic lattice matching between SiC and Ti_3SiC_2 in $(10\bar{1}0)$ plane section.[100]

interaction of ceramic with the metal will determine both the optimum process conditions for the bond formation and the properties of the joint. It is therefore of extreme importance to determine the conditions for chemical reactions to take place at a ceramic-metal interface from the thermodynamics point of view. This will provide information to properly design the ceramic-metal joining system.

Mechanical and thermo-mechanical: One of the major problems in ceramic-metal joining is the development of residual stresses at the interface as the material is cooled down from the bonding temperature to room temperature. These residual stresses reduce the strength of the bonded material, and in some cases lead to joint failure during or after the joining process.

The primary source of residual stresses is the CTE mismatch between joining materials, i.e. ceramics and metals. This is also, to a lesser degree due to the mismatch of elastic properties of the individual materials and the plastic flow of the metallic members. Careful design along with proper selection of joining materials for intended applications can alleviate the residual stresses developed during joining.

The interfacial stress (σ), in a ceramic/metal joint consisting of two parallel ceramic metal rods of the same length and cross-sectio. al areas which are fixed at one end and are restrained from moving at the other end (Fig. 2.7), and assuming that fully elastic conditions can be determined using the relation[103]:

$$\sigma = \Delta\alpha \Delta T \frac{E_M E_C}{E_M + E_C} \tag{2.5}$$

where E_M and E_C are the elastic moduli of the metal and ceramic rods respectively. $\Delta\alpha$ is the thermal expansion mismatch between the metal and ceramic rod ($\Delta\alpha = \alpha_M - \alpha_C$), and $\Delta T = T_2 - T_1$ is the temperature change. When the thermal stress in the metal rod exceeds its yield strength, the following equation will determine the thermal stress[103]:

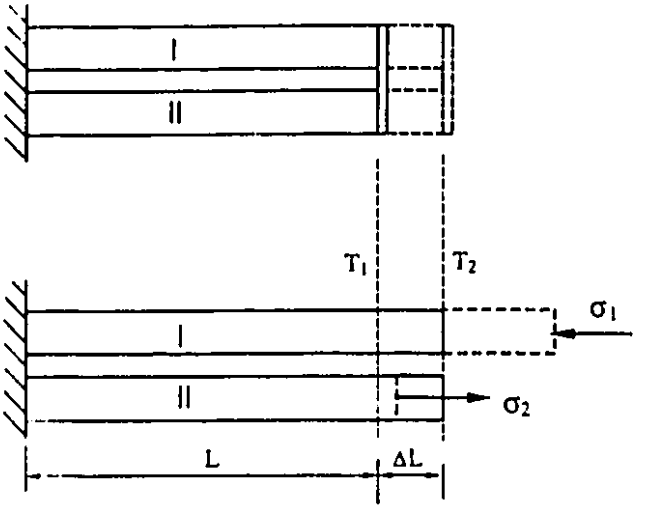

Figure 2.7 One dimensional model for ceramic/metal joint (the metal rod is I and the ceramic rod is II; temperature change from T_1 to T_2).[103]

$$\sigma=\sigma_{My}+(E_{Mp}\Delta\alpha\Delta T) \tag{2.6}$$

where E_{Mp} is the linear strain hardening coefficient and σ_{My} is the yield strength of the metal (linear elastic-linear plastic conditions are assumed). Equation 2.5 shows the dominant effect of CTE mismatch on the cool-down stress level when a high yield strength metal is employed and Eq. 2.6 indicates the role of yield stress of a soft interlayer such as Cu on the thermal stress[103].

There have been many useful analytical investigations on the stresses around a bonded joint of different materials. Analytical modelling has been found to be a useful tool in ceramic joining science. Initially it allows insight into some of the mechanics of the bonding process that the material scientists cannot see, such as residual stress. Secondly, it can predict that in what ceramic/metal combinations, in terms of shape, size and materials properties, the residual stresses are at lowest values.

Hsueh and Evans[104] carried out the theoretical stress analysis for simple shapes of metal/ceramic bonded strips. Dalgleish *et al.*[105] analyzed the stresses

at the interface of ceramic/metal bonded materials in order to estimate of the bond strength. The effect of a transient thermal load on an interfacial edge crack and centre crack between a ceramic-metal bond was investigated by Kokini[106]. Other useful studies have been reported as well[107,108].

Many attempts have been directed towards the use of the finite element method (FEM) to investigate the residual stresses developed at the joint area of dissimilar materials[109,110,111,112]. Using FEM, accurate stress analysis is obtained in very complex geometries, but without very precise explanation of the fundamental mechanisms of deformation. Analytical solutions on the other hand, show the direct effect of each individual parameter, but they are restricted to very simple geometries.

Irrespective of the method being utilized for stress analysis, two key factors must be taken into account:

• plastic deformation: all successful ceramic-metal joints comprise of some form of plastic flow in the metallic constituents which results in relaxation of residual stresses.

• variation of properties of joining materials: undoubtly, the mechanical and thermo-mechanical properties (elastic modulus, shear modulus, Poisson's ratio, and thermal expansion) of nearly all the materials are functions of temperature. Thermal expansion usually increases but elastic and shear moduli decrease as temperature increases.

It is therefore of great importance to consider these factors in evaluation of cool-down stresses, since it will determine the accuracy of calculations and also will prevent the estimated stress values from not exceeding the stresses present in the actual joints.

Suganoma *et al.*[113] calculated the stress distribution and maximum residual stresses in Si_3N_4-Steel joints and found that the tensile stress appears in the area

near the free surface. The maximum tensile stress is shown in Figure 2.8 as arrows and it shows why the cracks always grow to form a domelike failure path in ceramics. Figure 2.8 also shows that the metal is under tensile stress while the ceramic is under compression. In another report by the same authors[114], they investigated the residual stresses when an alumina ceramic is bonded to steel with three pure metals and one cermet as interlayers. The Nb interlayer with the same thermal expansion as Al was found to be the most effective material in reducing the internal stresses from ≈940 MPa (The maximum stress without using interlayer) to about 125 MPa when a 2 mm thick Nb interlayer was inserted between the ceramic and the metal. In both studies all physical constants were assumed to be independent of temperature and plastic deformation in the metallic constituents was ignored.

The investigation of Yada and Koguchi[115]regarding the use FEM for estimation of internal stresses in modeled Al_2O_3-Cu joints allowed for plastic deformation of Cu when it was bonded to alumina at 800°C. The variation of

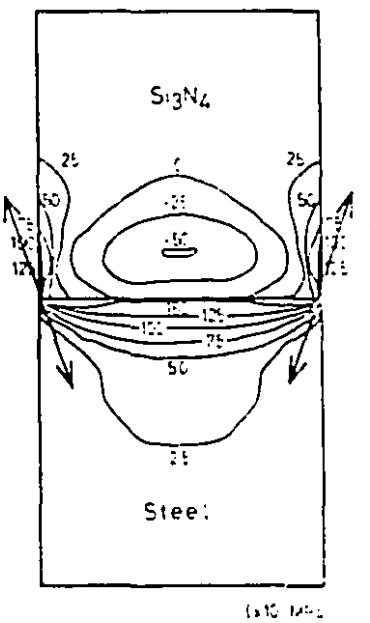

Figure 2.8 Contour map of internal stress. Arrows represent maximum tensile stress appearing in silicon nitride.[113]

mechanical and thermo-mechanical properties of Cu and alumina with temperature was taken into account as well. Another useful FEM calculation on magnitude and distribution of thermal stresses in Si_3N_4-steel joints using Cu, Kovar, Mo, and W interlayers was reported by Zhou *et al.*[116]. The FEM analysis took into account the plastic flow and variation of mechanical properties of the interlayers. The results of the study strongly suggested that selection of optimum interlayer materials depends not only on thermal expansion, but also on the thickness of the interlayer and on the change of interlayer mechanical properties.

The investigation of Tanaka *et al.*[117] when brazing alumina to steel using double Mo-Cu interlayer showed that the mode of cracking in the ceramic depends on the thickness of the Mo interlayer.

As shown schematically in Figure 2.9 when the Mo is thin, it cannot accommodate the shrinkage deformation of the Cu and steel; the thermal expansion coefficient α_C of the ceramic is smaller than that α_M of the metal and the ceramic is subjected to tensile stress and cracks at the edge. On the other hand when the Mo is thick, it completely constrains the shrinkage deformation of the Cu; since the $\alpha_{Mo} < \alpha_{alumina}$, the ceramic attempts to shrink more than the Mo and the relation $\alpha_C > \alpha_M$ holds; tensile stress acts on the core of the ceramic and cracks the ceramic longitudinally at the core.

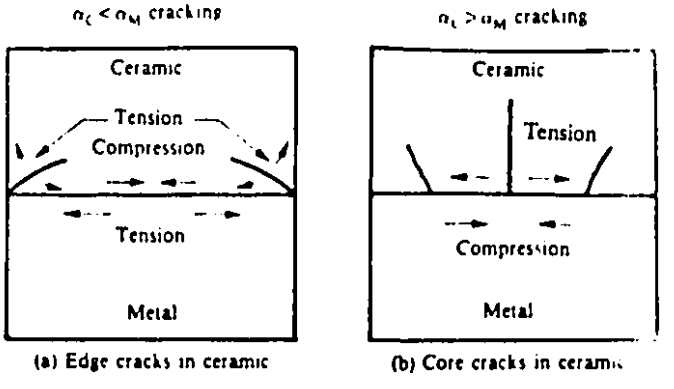

Figure 2.9 Schematic illustration of thermal stress in joint interface and mode of cracking due to difference of thermal expansion coefficient.[117]

2.3.4 Joining of Oxide Ceramics

Most of the early investigations on joining ceramics centred around joining of oxide ceramics, specifically brazing Al_2O_3 to metals with low melting temperature metals such as Cu or Ag for low temperature applications.

In general oxide ceramics are more difficult to wet than carbides. The problem of bonding to a ceramic oxide surface is usually met by applying a thin adherent coating to the ceramic or using filler metals containing active elements[118]. Many metals and alloys have been used for joining alumina either by solid-state reaction and diffusion bonding or by liquid-phase bonding with or without pre-surface treatment. Ti-containing braze filler metals are the most widely used alloys for joining alumina ceramics.

Refractory metals such as Nb and Mo, because of their low coefficient of thermal expansion have been extensively used directly or as interlayers in Al_2O_3-metal joining.

A study on solid-state bonding (under conditions of 100 MPa and 1300 or 1400 °C for 30 min.) between Al_2O_3 and steel using Nb interlayer and Nb/Mo laminated layer was performed by Suganuma and co-workers[80, 82]. They examined the effect of interlayers on both bonding strength and the resistance to thermal cycling for Al_2O_3/steel joints. They showed that the joints with a Nb/Mo layer bonded at 1440°C had the highest strength with the best resistance to thermal cycling.

Another study[101] on solid-state bonding of Al_2O_3 to Nb showed that the fairly high bond strength of a Al_2O_3-Nb interface might be attributed to the formation of a thin NbO_x layer, which had grown epitaxially on the Al_2O_3 surface after considering lattice matching between Al_2O_3 and NbO_x phases.

Bonding of Cu to Al_2O_3 seems to require a thin layer of O on the surface of Cu prior to bonding in order for $CuAlO_2$ or $CuAl_2O_4$ to form[119] . Okamoto and Naka[120] studied the joining of low carbon steel to alumina ceramics using Cu filler metal in a slightly oxidizing atmosphere. They found that in the low carbon steel/alumina joint, the intermediary compound $FeAl_2O_4$ between Cu and alumina

provides the essential role in joining steel to alumina. To promote wetting and bonding of alumina, amorphous $Cu_{50}Ti_{50}$ filler metal was developed by Naka *et al.*[118]. This brazing alloy was then used for joining alumina to Kovar (Fe-29%Ni-17%Co) alloy that possesses similar thermal expansion characteristics as alumina ceramics. They reported a maximum room temperature shear strength value of 170 MPa for the joints brazed at 1150°C for 30 min. Longer brazing time resulted in lowering the joint strength. Another investigation by the same authors[121] indicated that the formation of a titanium oxide on the Al_2O_3 surface was attributable to the strong joining between alumina and the Cu-Ti filler metal.

There have been many reports on joining Al_2O_3 ceramics to other pure metals such as Pt, Fe, Ni, Al, and Pb[75,76,78,122]. In the investigation of Sakata and co-workers[123], samples of diffusion-bonded Al_2O_3-Fe were prepared using either FeO or Fe-FeO composite interlayers.

There exist extensive investigations concerning the bonding mechanisms and characteristics of Al_2O_3-metal joints using the active Ag-Cu eutectic alloys (i.e. Cusil-ABA, Incusil-ABA, and Ticusil)[86,91,94,95]. More references are found in the book by Schwartz[67]. These alloys exhibit good wetting and bonding behaviour with Al_2O_3 ceramics. The ductility of these alloys will permit the metal to yield below the fracture strength of the ceramic, minimizing CTE mismatches. Active brazing alloys based on Ag-Cu with addition of Sn to reduce the Ti level have been studied for brazing alumina and zirconia ceramics[124]. More details on the role of Ti for enhancing wettability of ceramics will be given in the following chapter.

Of other oxide ceramics, zirconia (ZrO_2) ceramics, because of their transformation toughening abilities, which gives higher fracture toughness, have been the subject of many investigations for engine applications and joining[125]. PSZ (partially stabilized zirconia), the toughest known ceramic, is being investigated for uncooled diesel engine application because of its insulating capability, high strength, and toughness.[91,126,127]

Joining of zirconia-based ceramics have been investigated using different

brazing alloys. Rathner and Green[128] studied the brazing of yttria-tetragonal zirconia polycrystal (Y-TZP) to itself with pure Al and an Al-5.8 wt% Zr alloy. The specimens brazed with Al-Zr alloy exhibited higher joint strength due to the formation of needlelike Al_3Zr precipitates which can aid in strengthening of the joint. Joining of partially stabilized zirconia to nodular cast iron was accomplished by Hammond *et al.*[91] using Ag-30Cu-10Sn (AWS A5.8) brazing alloy. They fabricated the joints using a new process, termed "the active substrate process", rather than by the usual active metal approach. The process utilizes a Ti transition piece to minimize strain on the ceramic side. This process was then employed by Santella *et al.*[129] for joining the same materials. Moorhead[127] developed a broad range of experimental filler metals that will braze MgO- and Y_2O_3-stabilized PSZ. Two of the alloy systems studied, Ag-30Cu-21Ti and Cu-20Au-18Ti at%, produced ceramic-ceramic brazements with room temperature flexural strengths greater than 100 MPa.

Bonding between PSZ and two types of metals, Incoloy 909 and SAE 8620 as the shaft materials for turbocharger rotors applications was studied by DeLuca and Swain[130]. The cyclical fatigue test results showed that the attachments are stable up to 650°C.

2.3.5 Joining of Si-Based Ceramics

Joining of silicon-based ceramics such as silicon carbide and silicon nitride have been the subject of many recent investigations for structural use in hot machinery such as gas turbines. Several approaches have been taken to join these materials either to themselves or to other metallic members, but not all of them have been successful, particularly for high-temperature applications.

It is expected that the development of suitable joining techniques, particularly for joining these materials to metals, will be of great importance for the full realization of such structural applications.

2.3.5.1 Joining of Silicon Carbide Ceramics

Joining of SiC ceramics has been investigated using both solid state and liquid phase bonding techniques. Solid-state bonding of SiC has been practiced by direct joining or by the use of a joining vehicle. SiC-SiC joints formed by pressing two SiC blocks at 1500-1600°C using a Ni-active metal (or hydride) powder mixtures as a bond layer showed a shear strength of about 100 MPa[131]. Another example of solid-state bonding of SiC with foils of Ti or Zr at 1500°C or at 1000°C for Al/Ti/Al foils was reported by Morizumi *et al.*[100] They achieved a maximum room-temperature bend strength of 300 MPa for the joints bonded with Ti interlayer. In another study a thin (10 μm) double layer of Ti and Si was used as a bond layer for joining SiC[132]. Ti and Si layers were sputtered onto the faces to be joined. Bonding was performed using a HIPping process at 1800°C and 30 MPa for 60 min. in an inert atmosphere. The joint's four-point bend strength was measured at room-temperature and 1000°C. The mean strength value of the specimens broken at room-temperature was approximately 76 MPa, whereas it was almost 209 MPa for the samples broken at 1000°C. Reaction between SiC and some transition metals has been reported by some investigators[133,134,135,136]. Most of these studies have focused on reaction products formed rather than forming joints. The work of Choi *et al.*[137] have led to the conclusion that SiC reacts with transition metals (Ti, Cr, Fe, Ni) at all temperatures between 700-900°C under condition of inert atmosphere since SiC is dissociated into Si and C.

There have been studies on bonding mechanism between SiC and Ni-or Fe-based alloys[138,139]. The four-point bend strength of these joints have been reported to be about 60 MPa. A very real problem has been reported when SiC is in close contact with a Ni-based (Ni-20Cr-10Al at%) alloy in hot machinery[139]. This problem, which is due to the presence of liquid phases at 900°C, can be overcome by the use of barrier coatings to minimize undesirable reactions. Such barrier coatings are necessary if SiC ceramics in contact with Ni-based alloys are to be used above 700°C[139]. Apart from the severe reaction, another difficulty in joining

SiC to Ni and Fe or their alloys is the great CTE mismatch, which leads to stresses so large that may make the two parts uncouple. Schiepers *et al.* investigated the use of a Cu foil (25 and 50 μm thick) barrier[140]. They found no reaction between SiC and Ni or Fe. They also concluded that the Cu foil seemed to cope with the thermal expansion mismatch.

Brazing of SiC ceramics due to the simplicity of the technique and other previously mentioned advantages over solid-state bonding appears to be an industrially practical method for fabrication such joints. In the low temperature brazing of SiC, metals and alloys such as Al[102], Cu[141], and Ag- and Au-based alloys with or without active element additions are generally used as the brazing filler metal[142,143,144,145]. Other compounds such as SiB_6, Al_4C_3, and $MoSi_2$ have been studied for brazing SiC[146]. Using Fe or Ni- based brazing alloys, joints suitable for high temperature applications can be formed. Again, control of reaction between SiC and brazing alloy constituents is of great importance to avoid formation of undesirable reaction products. McDermid *et al.*[147,148] developed a thermodynamic approach to the high-temperature brazing of SiC-SiC and Nb-SiC using Ni-based brazing alloys. Through the use of the thermodynamic model, they designed appropriate brazing alloy compositions to optimize the reaction between SiC and the filler metal. The four-point bend strength of SiC-SiC joints was reported to be as high as 100 MPa.

Reaction at the interface between pressureless sintered SiC or reaction sintered SiC and Al at 1100°C was studied by Iseki *et al.*[142] The room temperature four-point bend strengths were about 240 and 110 MPa for the joints of pressureless sintered SiC and of reaction sintered SiC, respectively. They concluded that this difference in joints strength is closely related to a reaction between SiC and Al. In the case of reaction sintered silicon carbide, free Si and Al form a continuous liquid phase with some cracks at the front of Al-penetrated region in RBSC. The presence of cracks explains the lower strength for RBSC/Al joints. Another study showed that in the case of joining of RBSC (which contained 10wt% free Si) to stainless steel

using an active Ag-Cu brazing alloy, it was necessary to add more Ti (up to 18 wt%) to the brazing filler metal to induce wetting. The low, 40 MPa shear strength of these joints was due to the formation of Cu-Ti and Si-Ti compounds which made the brazing filler metal brittle[142].

2.3.5.2 Joining of Silicon Nitride Ceramics

The unique properties of Si_3N_4 make it attractive for many advanced structural applications and was described in Chapter 1. In many instances the application of Si_3N_4 is associated with joining this material to metallic components or to itself to fabricate complex assemblies. Despite the obvious importance of Si_3N_4 in many high temperature engineering applications, there have been few systematic studies of Si_3N_4-Si_3N_4 and Si_3N_4-metal bonding.

A number of joining techniques such as hot-press reaction and interdiffusion bonding, surface treatment joints (CVD, surface oxidation), metallization joining, joining using glass or ceramic compounds, and brazing have been utilized for bonding Si_3N_4 ceramics. Ideally any method for joining Si_3N_4 to itself should produce a bond at least as strong and as chemically resistant as the base materials. However, it has proved difficult to achieve this in practice. Although there are reports available on the fabrication of high strength Si_3N_4 joints, almost all of them have either concentrated on low temperature brazing processes or have employed hot-pressing which is complex and expensive and is only applicable to simple geometries.

Of all the joining methods which have been developed for bonding Si_3N_4 , brazing is under active development. The advantages of this technique was remarked on in § 2.3.2.2, because it is a relatively easy and inexpensive process suitable for mass production. An example is that, NTK Ceramics is producing about 10,000 automotive turbo charger rotors per month (as of mid-1988) for Nissan Motor Co. that consist of a Si_3N_4 rotor brazed to a stainless-steel shaft[149]. The main limitations of brazing are refractoriness of the bonded assembly and in some cases low joint strength and reliability[150]. Proper selection of filler metal, along with

a correct joint design and an appropriate brazing procedure can minimize these limitations.

In choosing the filler material to be used to form an interface or bond layer between the solid components, both chemical and mechanical compatibility with the components to be joined must be considered. A reasonable match in coefficient of thermal expansion and Young's modulus is required to minimize interface stresses. While wetting of Si_3N_4 by filler metal is the basic requirement in brazing, most metals and alloys do not wet this material. There exist numbers of approaches for treating the surface of Si_3N_4 to make it wettable; the most commonly used is the Mo-Mn process. Brazing Si_3N_4 using active filler metals, particularly based on Ag-Cu alloys has been extensively investigated. The following points are suggested in designing active brazing filler metals[151]:

1. The selected active element should have a high free energy of reaction with the ceramic, and strong segregation at the ceramic-metal interface.
2. The lower limit of active element content in the brazing filler metal should ensure a good wetting of ceramic by the brazing filler metal, while the upper limit should be such that there is no brittle dispersed phase in the brazing filler metal.
3. The brazing temperature and time should be sufficient to ensure interface reaction of the brazing filler metal with the ceramic.

Extensive work concerning the bonding mechanisms and characteristics of Si_3N_4/Si_3N_4 and Si_3N_4/metal joints using the active Ag-Cu filler metals has been done at Sandia National Laboratory (Albuquerque, New Mexico) and by other groups. Reactions between Si_3N_4 and Ag-Cu-Ti braze alloys (Cusil-ABA and Ticusil) have been studied by Loehman *et al.*[152], Braw and Loehman[153], Tomsia *et al.*[154], and Johnson[155]. It was found that the reaction zone contained TiN and titanium silicides. In another study, a layer of orthorhombic Ti-Si-Cu-N compound was identified between the TiN and the Si_3N_4 substrate[156].

Mechanical properties of the Si_3N_4/Si_3N_4 brazed joints using Ag-Cu active

filler metals have been evaluated in many studies. High strength values of between 300 to 770 MPa (depending on joint thickness) are reported by Loehman and co-workers[152]. In another study a joint strength of 490 MPa was reported[151].

Application of Ag-Cu active filler metals in brazing Si_3N_4 to metals has been reported in some investigations[116,157]. Zhou *et al.*[116] examined the joining of Si_3N_4 to mild steel using an active brazing method combined with the insertion of Mo, W, Cu, or Kovar interlayers to lessen interfacial stress. They found that the use of low yielding/high thermal expansivity Cu interlayers is more effective in reduction of thermal stresses than the use of low thermal expansivity Mo and W interlayers. However, due to the low melting point of Cu, the application of such joints is limited to low temperatures.

The oxidation behaviour of Si_3N_4 joints brazed with a series of active brazing filler metals at 600°C was studied by Kapoor and Eagar[158]. Their study revealed formation of a nonprotective oxide on the alloys: Cu-10Sn-10Ti, Ag-Cu eutectic + 5% Ti and Ag-Cu eutectic + 5% Zr. This indicates the poor oxidation resistance of active-metal brazing alloys. To enhance oxidation resistance they add Al, Si, or Ni to the base alloys. The addition of Si caused a significant loss in wettability. However, a protective scale was formed by the addition of Al.

Application of active Cu alloys in brazing of Si_3N_4 has been investigated by Naka *et al.*[159]. They used amorphous Cu-Ti alloys for brazing both Si_3N_4 to Si_3N_4 and Si_3N_4 to pure metals and alloys such as Cu, Fe, Invar, Kovar, or SUS 304 alloy. They obtained a maximum shear strength value of 313 MPa for Si_3N_4 joints using $Cu_{66}Ti_{34}$ filler which was higher than that of Si_3N_4 joints using other Cu-Ti fillers at a brazing temperature of 1100°C. It was also found that the strength of Si_3N_4 joints using $Cu_{50}Ti_{50}$ filler decreased from 176 MPa to about 19 MPa with increasing brazing time from 30 min. to 2 hour. The authors studied the effect of brazing temperature on Si_3N_4 joints made with the same filler metal[160]. At constant brazing time of 30 min., the shear strength of Si_3N_4-Si_3N_4 joints exhibited a maximum value of 180 MPa at 1100°C and the strength decreased markedly to 14

MPa at 1200°C. The above results show the influence of brazing variables such as brazing time and temperature on joint strength which is one of the main goals in ceramic joining. Thus, the achievement of reliable ceramic brazements depends on how adequately these parameters are being controlled.

The elevated temperature fracture shear strength of the Si_3N_4 joints made with $Cu_{50}Ti_{50}$ filler increased to 199 MPa at 100°C and gradually decreased to 106 MPa at 700 °C[159]. During brazing Si_3N_4 to metals with $Cu_{50}Ti_{50}$ filler, Fe, Cu, Co etc. diffused into the filler from the metals. In joining of Cu, large amounts of Co dissolved in the Cu-Ti filler and Ti in the filler diffused into Cu. All of the ceramic-metal joints made in this study were affected and cracked by the thermal stresses which arose from the difference in mechanical and thermo-mechanical properties between Si_3N_4 and metals (or alloys) during cooling from the bonding temperature. Besides, poor ductility of the filler did not allow for alleviation of thermal stresses.

Another example of joining Si_3N_4 to metal using active Cu filler metals was reported by Tanaka *et al.*[117] They used Cu-34Ti at% filler metal for joining Si_3N_4 to Co. The report has mainly concentrated on reaction products between the filler and the base materials. The assessment of mechanical strength of the joints was not addressed in the report, but the joint microstructure indicated cracking at the ceramic-metal interface. Joining of Si_3N_4 using active element coating of the ceramic surface followed by brazing or solid state bonding has also been investigated[92,161].

Among the pure metals being evaluated for joining silicon nitride ceramics, particular attention has been paid to the potential of Al as a braze metal. Al possesses two properties; firstly aluminum bonds strongly with Si_3N_4. The bond strength sometimes approaches the strength of silicon nitride[162]. Secondly, Al is a soft metal which relaxes the stress arising from the CTE mismatch between ceramic and metal during the joining process[163]. Wetting of Si_3N_4 by Al is usually not as good as active filler metals[164]; oxidizing the silicon nitride surface can improve the wettability[165]. Despite the formation of strong bond between

Al and Si_3N_4, the low melting point of Al limits the application of such joints to be below 500°C. Although pure Al is often used to join Si_3N_4, some researchers focused on joining using Al-Cu and Al-Ti alloys[166,167].

Reaction between Al and silicon nitride has been studied using both analytical transmission electron microscopy and X-ray diffraction. In the study of interface chemistry of thin Al film deposited on Si_3N_4 surface, an interfacial AlN like layer was observed[168]. Naka *et al.*[169] found that two reaction phases, an AlN-type sialon and an amorphous phase of alumina were formed at the interface between pressureless-sintered silicon nitride and liquid Al at 1200°C. In the investigations of Ning *et al.*[170,171] formation of ß'-sialon and an amorphous alumina layer containing silicon was reported. Recently Ning and co-workers[172] analyzed the brazed interface between Al and HIPped additive-free silicon nitride. Bonding was conducted at a low temperature of 800°C for 5 hour or at a high temperature of 1200°C for 30 min. in a vacuum of 1.3 MPa. In reviewing the work of these authors and other researchers, it can be concluded that ß'-sialon and silica-alumina oxides are formed at low temperature, while ß'-sialon, AlN-type sialon, aluminum nitride, silicon and the silica-alumina oxides are formed at higher temperatures.

The application of pure Al as a filler for brazing Si_3N_4 to metals and alloys has also been studied[173,174,175]. The strength of Si_3N_4-Invar alloy joints was measured between 150 and 200 MPa[175]. The room-temperature tensile strength of solid-state bonded Si_3N_4/Nimonic 80 alloy joints varied from 1 to 15 MPa depending on the bonding atmosphere and surface condition of the ceramic[176].

The application of Ni-based brazing alloys in the formation of Si_3N_4 brazements has been very scarce. Heat and corrosion resistance properties of these alloys make them a major candidate as a bonding medium in ceramic joining for high-temperature applications. Nearly all the available reports on the use of Ni-based alloys for joining silicon nitride ceramics centre around solid-state bonding rather than brazing.

Because of the high reactivity of Ni and Cr with Si_3N_4, alloys containing

these elements have been employed in joining. Interaction of Si_3N_4 with Ni and/or Cr in the solid state has been investigated at different temperatures and environments [177,178,179,180].

Nakamura and Peteves[181] studied the solid-state bonding of hot-pressed silicon nitride using aa Ni-20Cr wt% alloy at 1000-1350°C under uniaxial pressure in the range of 50 to 100 MPa. The average four-point bend strength was about 300 MPa. However, they found a large scatter in strength due to the formation of interfacial pores. The major interfacial reaction products were found to be Cr nitrides. The oxidation resistance of the joints was excellent up to 800°C in air.

Peteves *et al.*[182] also used Ni-20Cr wt% alloy foil for diffusion bonding of silicon nitride at 1150°C by applying 100 MPa for 1 hour in an Ar atmosphere or at 1200°C in vacuum. The reaction of Si_3N_4 with the alloy produced an interfacial CrN layer which was assumed to be responsible for strong bonding between the ceramic and the metal foil. In the case of joining uncoated Si_3N_4 under argon atmosphere, bonding strength was 309 MPa, while Cr-coated samples exhibited a joint strength of 384 MPa. For the ceramic specimens joined in vacuum, a strength of <100 MPa was reported.

Another example of using Ni-Cr alloys in joining Si_3N_4 ceramics is provided by the investigation of Mehan *et al.*[183] on solid-state bonding of Si_3N_4 and SiC using Ni-20Cr-10Al at% alloy. The study revealed that Si_3N_4 reacts to some extent with the alloy producing AlN, Ni and Cr silicides and probably a chromium nitride. SiC reacted with the alloy to a significantly higher degree than silicon nitride ceramic, because of the dependence of the Si_3N_4/metal reaction on the partial pressure of N_2.

The investigation of Bennett and Houlton[184] provides information on the interaction between silicon nitride and several Fe, Ni, and Mo-based alloys. The primary solid-solid interaction between Si_3N_4 and the alloys at 800 to 1100°C in an inert gas atmosphere involved the reaction of Cr, Fe and/or Ni with the nitride to form a silicide, which also contained dissolved nitrogen.

An example of using pure Ni as an interlayer in joining Si_3N_4 to type 405 steel is provided by Suganuma *et al.*[185] It was found that severe reaction took place between the metal and the ceramic which damaged the Si_3N_4 side near the interface. It then reduced the bond strength significantly. Diffusion of Si from the Si_3N_4 side to the Ni side was also observed.

One of the common features of all of the above mentioned studies is that, Ni-based alloys containing such elements as Cr, Fe, Al, etc. react with Si and N (supplied by the decomposition of Si_3N_4) to produce nitrides and silicides. The degree of reactions which sometimes results in excessive degradation of the ceramic is determined by the alloy composition and bonding conditions. Therefore, the achievement of successful joints strongly depends on optimization of both the alloy composition and joining variables such as temperature, time, and environment. In perhaps one of the best studies yet reported, McDermid[147, 148] employed solution thermodynamics for designing Ni-Cr-Si alloys as brazing filler metals for joining SiC to SiC and to Nb.

2.3.6 Joint Strength Measurement

A key factor in any joining process, from the standpoint of both design and reliability, is the mechanical strength of the resultant interface. A variety of methods for testing have been developed, including tensile, shear, three- and four-point bend strength, and peel tests. Different methods have different features and the best test method is that which simulates the intended application of the joint[79].

The major requirements for any testing method to evaluate the mechanical properties of the ceramic-ceramic or ceramic-metal joints are:

- The method should lead to accurate and consistent results.
- The method should be able to evaluate effects of processing variables on the joint properties.
- The results of the tests should provide meaningful engineering parameters that can be utilized for designing the ceramic-ceramic and ceramic-metal joints.

The strength of ceramic joints is not normally characterized by tensile testing because of difficulties in fabrication of test specimens and the requirement of extremely good alignment of the load train during testing. Any misalignment introduces a bending moment, which results in uncertainty in the tensile strength measurement.

The peel test is a useful method for evaluating the adhesion of a thin metal strip bonded to a ceramic substrate. However the result of the peel test cannot be translated into meaningful engineering parameters for designing ceramic-metal joints[79].

Joints can be evaluated in terms of fracture toughness, as well as strength, and such evaluation offers the possibility of determining whether the material properties or processing defects act to limit the joint strength[186,187,188].

In the case of designing a joint to be employed under shear loading, the shear test will provide information on shear strength of the joint. Figure 2.10 schematically illustrates three types of shear tests on brazed joints. In type (a), a hold-down load (F_H) which applies a compressive force on the joint is required. The problem with type (b) is that, the joint is under compressive stresses due to the shrink-fit nature of the metal ring. Type (c) which consists of a double-brazed specimen has found to provide more accurate information than the two former types[79]. However, this method is very sensitive to instrumental misalignment. Type (d), which was utilized in the present study, is a fairly simple method for measuring the shear strength of a single joint, but care should be taken to avoid excess holding force which will affect the accuracy of the results.

Although shear testing has been used for evaluation of joints strength in many investigations, the strength of ceramics and ceramic joints is normally characterized by four-point and three-point bending or flexure test. This is also known as the "modulus of rupture" test, but this expression is passing out of usage. Although in both three and four -point bending the bonded interface is under maximum tensile stress, the four-point bending is preferred since a greater area of material is under

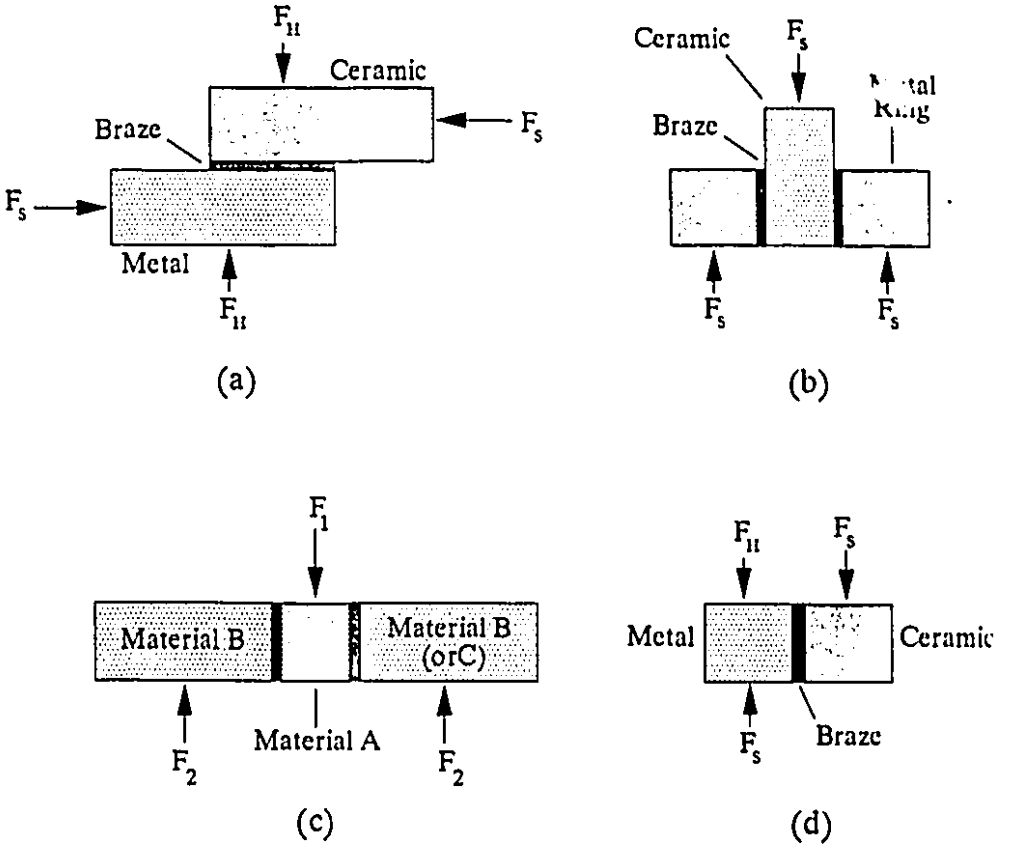

Figure 2.10 Schematic representation of different types of shear testing on ceramic/metal brazed joints.

maximum tensile stress. This provides more consistent and reliable results than the three-point bending test. Since the joints area is usually associated with different types of defects, the strength of nominally identical samples have frequently a considerable spread. The most commonly used method of characterizing the spread of strength is to apply Weibull statistical theory[189].

Although the flexure test appears to be the most promising technique for measuring the strength of advanced ceramics as well as bond strength in ceramic joints, unfortunately there is no a suitable universal standard method for this test.

Specimen sizes including specimen length and cross-section vary. Fixture sizes and configurations, load geometry, fixture bearings and loading speed vary as well. The size of test specimens can have a significant influence on the results because of the statistical nature of the fracture in brittle materials[190]. Generally, as the size of the test specimen increases, the probability of encountering a critical-sized flaw that will initiate failure will increase, resulting in a lower strength. Consequently, the compatibility and reproducibility of data are poor. Direct comparison of test data from different studies should only be done when each researcher has used the same identical specimen size and geometry.

The most widespread accepted standard flexure test in the United States is the MIL-STD-1942A "Flexure Strength of High-Performance Ceramics at Ambient Temperature". The American Society for Testing and Materials (ASTM) has recently created ASTM Standard C 1161 (1991), which is based on the MIL-STD[191].

Chapter 3

Theory of Wetting and Adhesion

Wetting at ceramic-metal interfaces is becoming increasingly important with the progress in liquid phase ceramic joining science and technology[192,193]. Wetting determines the degree to which molten metals will react with ceramics, since metals are known to wet ceramics essentially by chemical bond formation[194]. The main factors which control wetting are: the properties of the surfaces and internal boundaries of ceramic materials, the reactivity of metals with ceramics, and the surrounding atmospheres.

This chapter will briefly discuss the solid surfaces with emphasis on ceramic materials, the surface and interfacial energies in solid-liquid systems, and chemical wetting and spreading. In addition, previous studies on the interaction of metals with ceramics will be briefly reviewed. However, it is not intended here to cover and discuss the large literature of surface science in any finite way, but rather to point out some topics of practical importance for this study.

3.1 Surfaces and Interfaces

The term "surface" is usually applied to the area between a condensed phase (solid or liquid) and a gas phase, while "interface" is normally applied to systems involving two condensed phases. The type of interfaces possible can be summarized

in a formal way in terms of the three states of matter; solid, liquid, and gas as: solid-gas, solid-liquid, solid-solid, liquid-gas, and liquid-liquid interfaces. The unique characters of surfaces and surface-related phenomena arise from the fact that atoms and molecules at surfaces and interfaces possess energies and reactivities significantly different from those of the same species in a bulk or solution situation, due to their special environment. As illustrated in Figure 3.1(a) a unit (an atom or molecule) of a substance in a bulk phase possesses a uniform force field due to its interaction with neighbouring units. If the bulk phase is detached by a distance H along a plane close to the unit of question, it can be seen that the forces acting on the unit are no longer uniform (Figure 3.1b). Since the unit is now in a different environment relative to those in the bulk, its total free energy must change. In this

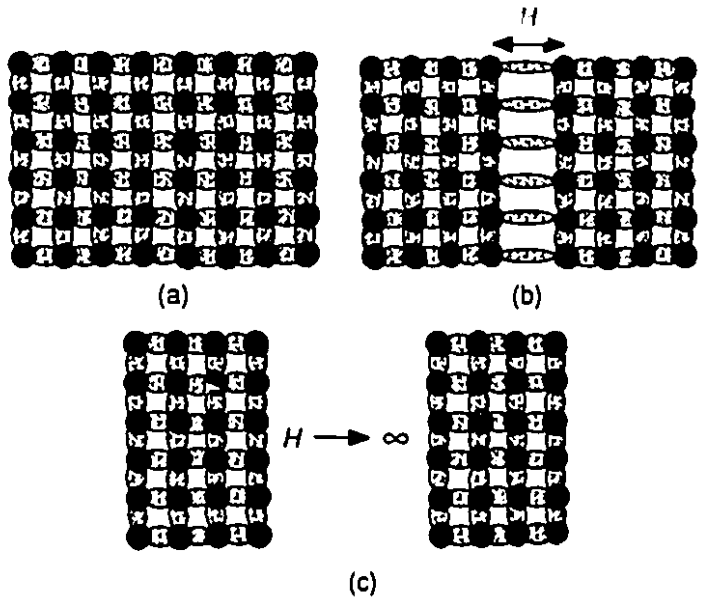

Figure 3.1 Schematic representation of changes in interatomic or intermolecular forces during formation of a new surface: (a) equilibrium position of bulk units; (b) at separation distance H, when the surface units continue to interact, but to a reduced extent; (c) at separation distance of infinity when the surface units interact only with adjacent bulk units, giving rise to the existence of an excess surface energy.[195]

case, since the interactions in the bulk phase produce a net lowering of the free energy of the unit, the removal of those interactions by the formation of a new surface results in an increase in the free energy of the unit at or near the surface.[195] Therefore when talking about interfacial energy, what is meant and measured by experiment is the "interfacial free energy", γ.

The total free energy of a system containing an interface of area A and free energy γ per unit area is given by:[196]

$$G=G^{\circ}+A\gamma \tag{3.1}$$

where G° is the free energy of the system assuming that all material in the system has the properties of the bulk, and γ is therefore the excess free energy. It is also the work that must be done at constant T and P to create unit area of interest.

Consider a hypothetical system consisting of a liquid film that fills a frame having a sliding side (Figure 3.2). The material of the frame is such that the interfacial tension between it and the liquid is zero. It is found that a force F per unit length must be applied to maintain the moving side in position. If the moving side slides for a small distance so that the total area of the film is increased by dA, the work required to do so will be FdA. This work is used to increase the free energy

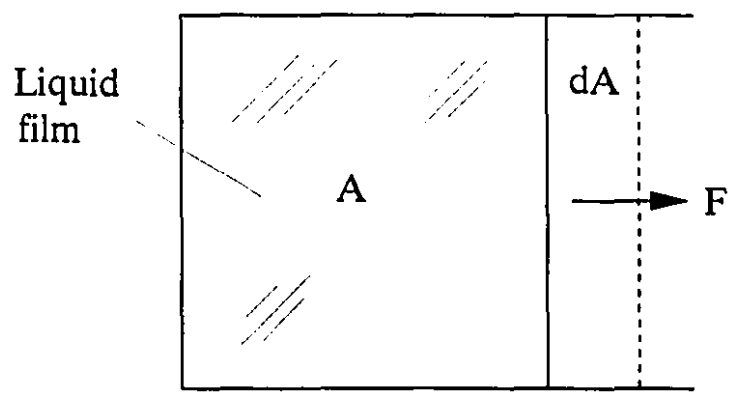

Figure 3.2 A liquid film with surface energy γ on a frame with a sliding side[196].

of the system by dG. From Equation 3.1:

$$dG=\gamma\, dA+A d\gamma \tag{3.2}$$

equating this with FdA gives:

$$F=\gamma+A\frac{d\gamma}{dA} \tag{3.3}$$

in the case of a liquid film the surface energy is independent of the area of the interface and $d\gamma/dA = 0$. This leads to the well-known result

$$F=\gamma \tag{3.4}$$

i.e., a surface with a free energy γ Jm^{-2} exerts a surface tension of γ Nm^{-1}.

3.2 Solid Surfaces

A solid is by definition a phase of matter that is rigid and resists stress. A solid surface represents the discontinuity of the bulk structure; the resulting distortion and change in coordination number of the atoms at the surface causes a higher free energy over a corresponding plane and number of atoms in the bulk. Therefore, a solid surface must be characterized by some surface free energy terms. However, such free energy for solids cannot be characterized using the capillary and related methods so useful in the study of fluid surfaces. Compared to the liquid surfaces, solids surfaces are in many ways much more difficult to treat from a theoretical point of view and also more difficult to quantify in certain aspects. We usually think of a solid form to be in stable thermodynamic equilibrium, which is not normally the case. If solid geometries were the minimum energy configuration, then such processes as annealing and sintering would not be possible. It can be seen, within a normal time scale, that the newly formed surface of a liquid rapidly undergoes plastic flow to take up an equilibrium configuration to maintain an uniform surface density. The same is not true for a solid surface and the nature of

a solid surface with some exceptions which depends on the exact nature of the surface and environmental conditions, will be determined as much by its history as by equilibrium thermodynamics or surface tension forces. Therefore the solid surfaces are likely to have a considerable range of values of surface free energy, varying from region to region on surface. It also depends on atomic arrangement on the solid surface. Thus in the case of interfaces involving solids, it is not immediately obvious that γ in Equation 3.2 is independent of area, then $d\gamma/dA \neq 0$ and surface free energy and surface tension will not be identical.

3.2.1 The Surface Energy of a Solid

Let us consider a solid surface in which the surface tension is resolved into two directions at right angles denoted as γ^1 and γ^2 in Figure 3.3. For an anisotropic solid, if the area is increased in two directions by dA_1 and dA_2, then the total increase in available energy is given by the work done against the stress γ^1 and γ^2. Thus, at constant temperature (T), volume (V), and the number of moles of the solid (n):[197]

$$d(AF^S)_{T,V,n}=\gamma^1 dA_1+\gamma^2 dA_2 \tag{3.5}$$

where F^S denotes the available energy per unit area. If $\gamma^1=\gamma^2=\gamma$ then

$$\gamma=\frac{d(AF^S)_{T,V,n}}{dA}=F^S+A[\frac{dA^S}{dA}]_{T,V,n} \tag{3.6}$$

in the case of a solid, however, $dF^S/dA \neq 0$ as a general rule, in fact it would be so for an ideal crystal-like surface. Therefore, F^S and γ will be different from their equilibrium values and different from each other[197].Thus only if the surface achieved some uniform equilibrium state would $F^S=\gamma$ or

$$F^S=A\gamma \tag{3.7}$$

where A is the area occupied by one mole of material on the surface. For numerical

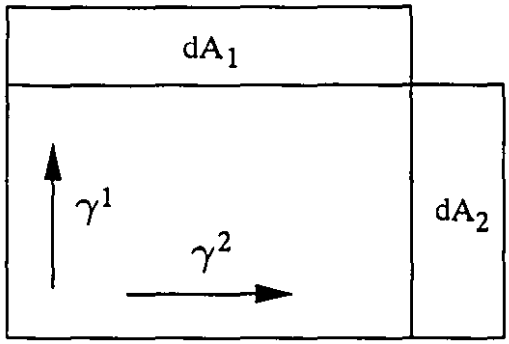

Figure 3.3 Resolution of the surface tensions of an anisotropic solid in two directions.[197]

evaluation of the molar surface quantities, an estimate is made of the molar surface area (A) by assuming spreading of a mole of atoms into a monolayer for which:[198,199]

$$A = mN^{1/3}V^{2/3} \tag{3.8}$$

where N is the Avogadro's number, V is the molar volume of the substrate, and m is the fraction of nearest-neighbour atoms lying in an adjacent layer, and therefore, m is a function of local surface structure. Assuming the volume occupied by surface is zero, then, the Helmholtz surface energy and Gibbs surface energy would be equal. Thus

$$G^{S} = A\gamma \tag{3.9}$$

3.2.2 Wetting of Solids by Molten Metals

Contact between a metal melt and the surface of a high melting solid substance or material occurs in many physical phenomena and some important technological processes. They include the processes of crystal nucleation and growth from the metal melt, various metallurgical processes such as casting, moulding of steel and alloys, soldering, brazing, welding, processes of powder metallurgy by

liquid-phase sintering or liquid metal infiltration of a porous ceramic.

The contact sy tems under consideration are usually characterized by the development of interphase surfaces, a highly dispersed state of the solid phase, cavities, channels and space of small cross-section (capillaries) present in the solid phase. In such systems as the process advances, the velocity and the direction, as well as the properties of the product obtained, depend on the state and properties of the interface, the degree of wettability of the solid phase by the liquid melt and the contact adhesion strength.

Measuring the degree of wettability of solid body surfaces by liquid metals makes it possible to determine the energetic parameter of interaction between the pair of substances, i.e., the work of adhesion. For systems with a rather low degree of interaction (solid bodies which are insoluble in the liquid metal and nonwettable by it) it is practically impossible to obtain such characteristics by any other method (e.g calorimetry). The method of measuring wettability for such purposes becomes the only one.

3.2.3 General Laws of the Wetting of Solids by Liquids

When a drop of liquid is brought into contact with a flat solid surface, the final or equilibrium shape taken up by the drop conforms to the minimum total surface and interfacial energies that exist in the system. These energies can be defined as γ_{sv}, the solid surface energy, γ_{lv} the liquid surface tension and γ_{sl} the solid-liquid interfacial energy. If γ_{lv} is high the liquid tends to form a ball having minimum surface area and if γ_{sv} is high the liquid tends to wet or spread over the solid surface to eliminate this high energy (Figure 3.4).

The main thermodynamic relationship of the wetting theory are the well known equations for wetting angle (Θ) and the work of adhesion (W_a):

$$\gamma_{sv}-\gamma_{sl}=\gamma_{lv}\cos\theta \qquad (3.10)$$

and

$$W_a=\gamma_{lv}(1+\cos\theta) \tag{3.11}$$

Both of the above equations were proposed in 1804 by T. Young without rigorous proof[200]. These equations were then obtained theoretically by different methods ranging from the mechanical equilibration of forces at the three-phase boundary (Figure 3.4) to the use of thermodynamic concepts (A list of useful references can be found in Ref. 200). One of the proofs of Young's equation from energy considerations has been that, if a small change in area takes place in a system with liquid-vapour interface of area A_{lv}, solid-vapour area of A_{sv}, and a solid-liquid interface of area A_{sl}, then the free energy of system will change as:[201]

$$dG=\gamma_{lv}dA_{lv}+\gamma_{sv}dA_{sv}+\gamma_{sl}dA_{sl} \tag{3.12}$$

if only the drop slides, then

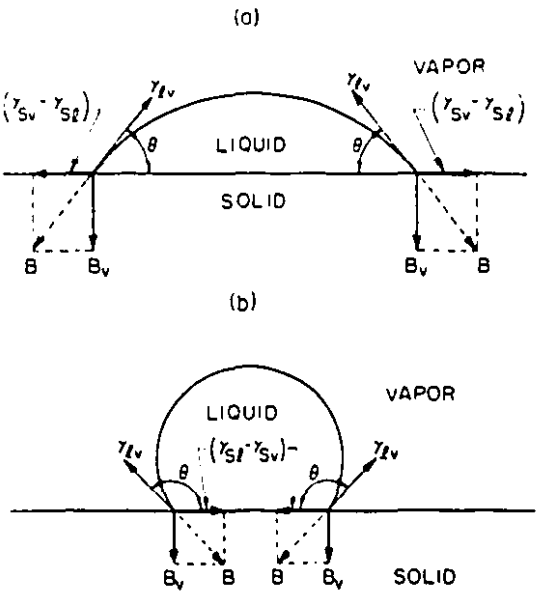

Figure 3.4 The contact angle Θ of a) wetting and b)non-wetting the solid surface by the liquids.[211]

$$dA_{sl}=-dA_{sv} \tag{3.13}$$

assuming that

$$dA_{lv}=\cos\theta dA_{sl} \tag{3.14}$$

combining equation (3.12), (3.13), and (3.14), we obtain

$$dG=\gamma_{lv}\cos\theta dA_{sl}-\gamma_{sv}dA_{sl}+\gamma_{sl}dA_{sl} \tag{3.15}$$

Since at equilibrium dG=0, this relation gives Young's equation. The Young's equation has also been verified by comparing the experimental values of the work of adhesion[200]. These values can be obtained experimentally by measuring critical angles of the solid surface, i.e. the angle (α) at which a liquid drop with the mass m and radius r begins to roll down from the solid surface such that W_a may be obtained according to the formula:

$$W_a=\frac{mg\ \sin\alpha}{2r} \tag{3.16}$$

These values have been compared with the experimental data for the contact angle and the liquid surface tension. Satisfactory correspondence of the value of the adhesion work on wetting various solid bodies by different liquids confirms the essential correctness of Eq. 3.11. Equation 3.10 can be readily obtained from equation 3.11 using the Dupré equation which is expressed as:

$$W_a=\gamma_{sv}+\gamma_{lv}-\gamma_{sl} \tag{3.17}$$

That is why the correction of Equation 3.11 confirms the validity of Equation 3.10.

The meaning of the term "wetting" of a solid by a liquid is only a matter of definition. The most convenient procedure would be to describe the degree of

wetting in terms of contact angle "θ". One definition is to relate a contact angle of value zero to complete wetting or spreading, and a finite value of contact angle to an incomplete wetting system. Another definition is to describe initial wetting and nonwetting in terms of θ. A value of $\theta<90^{\circ}$ represents initial wetting and a wetting angle of $\theta>90^{\circ}$ is considered as initial nonwetting[202,203].

Wetting can be classified into two broad categories a) physical wetting, and b) chemical wetting. In physical wetting, the attractive energy required for wetting is provided by reversible physical forces such as those of Van der Waals. In chemical wetting, a reaction occurs at the solid-liquid interface and the resultant chemical forces are responsible for wetting. The basic difference between the two types of forces which are of significance here, is their magnitude. The bond energies of physical (Van der Waals) forces are functions or units of a cal/mol. The energies of chemical interaction equal tens and hundreds of cal/mol. For systems with physical wetting the degree of wetting can be connected to physical properties of contacting materials, while in the case of chemical wetting it is necessary to take into account such chemical variables in the system as the chemical affinity of atoms from different phases, the reaction equilibrium contact, the free energy of formation of compounds, etc..

Under nonreactive conditions, wetting represented by a steady-state contact angle, Θ, always occurs when $\gamma_{sv}>\gamma_{sl}>\gamma_{lv}$. This configuration is typical of a liquid glass drop on a metal substrate[204]. Also under nonreactive conditions, nonwetting occurs when $\gamma_{sv}<\gamma_{sl}<\gamma_{lv}$. This configuration in many cases conforms to a liquid metal drop on a ceramic surface. Therefore wetting can be defined as the reduction of γ_{sv} by the liquid and the driving force for wetting is thus $(\gamma_{sv}-\gamma_{sl})$ which is acting on the periphery of the liquid drop. It has been stated that in the absence of a reaction, the driving force for wetting never exceeds γ_{lv} and spreading or extension of the liquid drop does not occur[204]. When a reaction occurs between a solid and a liquid, the free energy of reaction per unit interfacial area and unit time enhances the driving force for wetting. This condition can be expressed by the following

inequality:[204]

$$\gamma_{sv}-(\gamma_{sl}+\frac{-dG_R}{dA.dt})\rightarrow\gamma_{lv}\cos\theta \qquad (3.18)$$

In this case whether γ_{sv} is greater than γ_{lv} or not, the enhanced driving force for wetting by a reaction exceeds γ_{lv} and spreading occurs.

3.3 Measurement of Wetting Angle and Surface Energy

The angle of contact between a solid and a liquid can be determined with a number of methods. The sessile drop method is often used to evaluate the experimental contact angle (Θ). This method has some advantages which are of great importance when working with molten metals. These are the simplicity of the method, the simple shape of the solid body, and the need for small quantity of both solid and liquid phase (the liquid quantity may be less than 10 mg). This method also does not require direct access to the sample during measurement, and therefore it can be done in a closed apparatus. The main disadvantage of the method is its sensitivity to the local atmosphere around the drop leading to a non-stable shape of the liquid surface as it accumulates contaminants and impurities. This problem is severe for reactive metals whose surfaces are more likely to oxidize. Nevertheless, this disadvantage can be eliminated by carrying out the test in a highly controlled atmosphere and using high purity materials.

Surface energy, as mentioned earlier, is the work to expand surface area and related to interatomic forces. Thus material properties such as heat of fusion or evaporation, hardness, elastic modulus, and melting temperature can provide a rough estimation of surface energies of solids[196,205]. Although there is no perfect model, several theoretical methods have been introduced for the estimation of surface energy of solid metals[206,207]. Data for surface energy of ceramics are less readily available, some values have been tabulated[208] and/or being experimentally or theoretically calculated[209,210].

3.4 Wetting in Equilibrium and Nonequilibrium Systems

As mentioned previously, the degree of wetting of a solid by a liquid in a solid-liquid-vapour system is characterized by the condition of thermodynamic equilibrium. The system can be either under thermodynamic equilibrium or not over a large period of time. In wetting studies at elevated temperatures, the phases of a system are not often at chemical equilibrium. Examples are some systems containing molten metals as a liquid phase which can react intensively with the solid phase. It has been suggested that under chemical nonequilibrium conditions interfacial reactions or diffusion of a component from one bulk phase to the other results in the lowering of the corresponding interfacial tensions. Naidich[200] has classified various equilibrium and nonequilibrium systems and has analyzed the wetting phenomena in each type of system. Pask *et al.*[211] studied the correlation between the degree of wetting and interfacial chemical reaction or corresponding interfacial tension under both equilibrium and nonequilibrium conditions.

a) Wetting under equilibrium conditions

In equilibrium systems, where the contacting solid and liquid phases are in thermodynamic equilibrium, the chemical potential of each component, and the temperature and pressure of each phase are the same[200]. The total difference of the free energy of a solid-liquid-vapour system (Fig. 3.4) neglecting the effect of gravitational field (at constant pressure and temperature and assuming that the effect of curvature on the pressure is negligible and interfacial tensions are independent of orientation) can be expressed as:[211]

$$dG=\sum_i \mu_i^s dn_i^s+\sum_i \mu_i^l dn_i^l+\sum_i \mu_i^v dn_i^v+\gamma_{sl}dA_{sl}+\gamma_{sv}dA_{sv}+\gamma_{lv}dA_{lv}$$
$$+\sum_{\alpha\beta}\left[\sum_i \frac{\partial G^{\alpha\beta}}{\partial n_i^{\alpha}}dn_i^{\alpha}+\sum_i \frac{\partial G^{\alpha\beta}}{\partial n_i^{\beta}}dn_i^{\beta}+\sum_i \frac{\partial G^{\alpha\beta}}{\partial n_i^{\alpha\beta}}dn_i^{\alpha\beta}\right] \qquad (3.19)$$

where:

α and ß= designated phases

αß= interfacial phase

μ_i= the chemical potential of component i in the designated phase

n_i= the total number of moles of component i in the designated phase (obtained by multiplying the concentration of component i in the homogeneous region of the phase by its volume, i.e, $C_i^{\alpha}V^{\alpha}$).

G= total free energy of designated phase (obtained by multiplying the free energy of a unit volume in the homogeneous region of the phases by the volume of the corresponding phase, i.e., $g^{\alpha}V^{\alpha}$)

A= interfacial area

If we split Equation 3.19 into two parts, at total thermodynamic equilibrium, when dG=0; then since the variation of mass is independent of variation of area, the first part (Eq. 3.20) which outlines the condition of mechanical equilibrium becomes zero

$$\gamma_{sl}dA_{sl}+\gamma_{sv}dA_{sv}+\gamma_{lv}dA_{lv}=0 \tag{3.20}$$

and the second part (Eq. 3.21) which represents the chemical equilibrium in the system becomes zero as well and γ will have a static value:[211]

$$dG=\sum_i \mu_i^s dn_i^s+\sum_i \mu_i^l dn_i^l+\sum_i \mu_i^v dn_i^v+\sum_{\alpha ß}$$
$$\left[\sum_i \frac{\partial G^{\alpha ß}}{\partial n_i^{\alpha}}dn_i^{\alpha}+\sum_i \frac{\partial G^{\alpha ß}}{\partial n_i^{ß}}dn_i^{ß}+\sum_i \frac{\partial G^{\alpha ß}}{\partial n_i^{\alpha ß}}dn_i^{\alpha ß}\right]=0 \tag{3.21}$$

Now, if it is assumed that the system is under chemical equilibrium (i.e., Eq. 3.21 is equal to zero), and the liquid is a small sphere (due to negligible gravitational effects), then a solid-liquid interface will form between the drop and the flat rigid solid surface if:[211]

$$\Delta G=\Delta\int_{sl}\gamma_{sl}dA_{sl}+\Delta\int_{sv}\gamma_{sv}dA_{sv}+\Delta\int_{lv}\gamma_{lv}dA_{lv}<0 \qquad (3.22)$$

this condition provides a driving force for the solid-liquid interface to be increased and Eq. 3.22 will be satisfied. Therefore in a nonreactive system the final configuration of the liquid drop is only determined by mechanical equilibrium and the free energy changes for the system are only associated with changes in the interfacial areas[211]. It should be mentioned that in the absence of chemical reactions no spreading will be observed in sessile drop experiments[212]. Several progressive configurations of the drop geometry and the change in the interfacial area of the solid-liquid and liquid-vapour as a function of contact angle (Θ) are shown in Figure 3.5. This Figure shows that the liquid-vapour interfacial area decreases from 180° to 90° and then increases as the contact angle decreases to 0°, whereas the solid-liquid interface increases continuously[211]. Noting that $dA_{sl}=-dA_{sv}$, Eq. 3.22 can be simplified into:

$$\Delta G=\Delta\int_{sl}(\gamma_{sl}-\gamma_{sv})dA_{sl}+\Delta\int_{lv}\gamma_{lv}dA_{lv} \qquad (3.23)$$

or

$$\frac{dG}{dh}=(\gamma_{sl}-\gamma_{sv})\frac{dA_{sl}}{dh}+\gamma_{lv}\frac{dA_{lv}}{dh} \qquad (3.24)$$

which represents the free energy change in terms of variation of the drop height. The value of dG/dh in Eq 3.24 will determine the drop shape. If dg/dh <0 the solid-liquid interface will continue to form and the contact angle will continue to decrease. When a balance is achieved between the two terms of the Eq. 3.24, dG/dh becomes zero which conforms to the minimum energy configuration in the system[211]. For instance, when $\gamma_{sv}>\gamma_{sl}>\gamma_{lv}$ the contact angle is always acute; and when $\gamma_{sv}<\gamma_{sl}<\gamma_{lv}$ the contact angle is always obtuse. When $\gamma_{sv}-\gamma_{sl}>\gamma_{lv}$, an equilibrium contact angle is not obtained since the reduction of free energy on wetting the rigid solid is greater than its increase due to the extension of the liquid

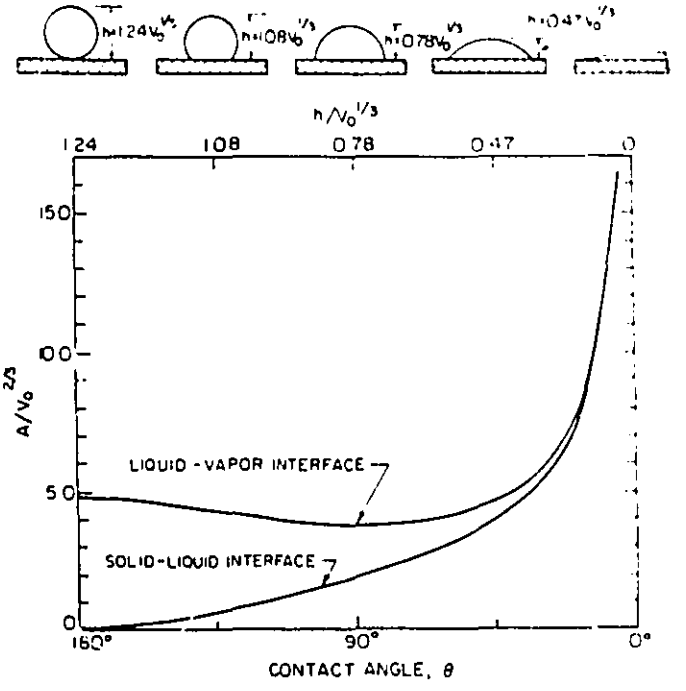

Figure 3.5 Variation of the solid-liquid and the liquid-vapour interfacial areas vs. contact angle (Θ), or the height of the drop (h). V_0 is the volume of the liquid drop[211].

surface; then a dynamic spreading continues as long as the bulk liquid is available [211]. A reduction of the total surface energy of the solid by liquid ($\gamma_{sv}>\gamma_{sl}$) is defined as wetting and a condition of $\gamma_{sl}>\gamma_{sv}$ is defined as nonwetting of the solid. Thus, γ_{sv} - γ_{sl} can be considered as the driving force for wetting[211]. Under chemical equilibrium conditions, the formation of a true interface can be considered to be analogous to the formation of a solution. It indicates formation of an interfacial structure whose interfacial energy (γ_{sl}) is between γ_{sv} and γ_{lv}. However, the degree of chemical bonding or minimization of structural discontinuity across the interface will determine the magnitude of γ_{sl}. Thus γ_{sl} becomes smaller with increasing chemical bonding at the interface. For $\gamma_{lv}>\gamma_{sv}$, then γ_{sl} approaches γ_{sv} with the development of chemical bonding, resulting in a limiting contact angle of 90°. For

$\gamma_{sv}>\gamma_{lv}$, then γ_{sl} approaches γ_{lv}. The maximum reduction of γ_{sv} by the liquid is by the amount equal to γ_{lv} resulting in a zero contact angle as long as $\gamma_{sv} - \gamma_{lv} \geq \gamma_{lv}$ as can be seen from Eq. 3.10. If $\gamma_{sl}>\gamma_{sv}$ and γ_{lv}, a true interface has not formed and if $\gamma_{sl}< \gamma_{sv}$ and γ_{lv}, a transient condition involving chemical reaction exists[211].

3.4.2 Wetting Under Nonequilibrium Conditions

When the condition of chemical equilibrium presented in Eq. 3.19 is not satisfied throughout the system, the phases of solid, liquid and vapour will react with each other to achieve a state of equilibrium. Under nonequilibrium conditions, the value of interfacial energies and thus the contact angle will be continuously changing[211],. The driving force for the irreversible phenomena is the decrease of the total free energy $G=G^{\alpha}+ G^{\beta}+ G^{\alpha\beta}$.[213]

The simplest phenomena developing after formation of the interface is adsorption (no mass transfer across the interface when the bulk phases are at equilibrium) by diffusion of components from the bulk phases to the interface. During this process, the interfacial energy γ_{sl} decreases with time towards its equilibrium value (curve 1 in Fig. 3.6). In case of chemical reactions, mass transfer or absorption occurs across the interface. Such transformations involve a much larger decrease of the free energy of the system than simple adsorption[211,213]. The initial decrease in the free energy of the system at the first instant of formation of the interface is caused by decrease in the free energy of the interfacial region ($G^{\alpha\beta}$) while G^{α} and G^{β} remain unchanged. The decrease in $G^{\alpha\beta}$ will then attribute to the decrease of $\gamma^{\alpha\beta}$ (or in the case of solid-liquid interface, γ_{sl} according to the following equation:[211,213]

$$\gamma=\frac{G^{\alpha\beta}}{A}-\sum_i \Gamma_i \mu_i^{\alpha\beta} \qquad (3.25)$$

where, Γ_i is adsorption of component i. This decrease can be quite high if the enthalpy change associated with the interface interaction is large (curve 2 in Fig.

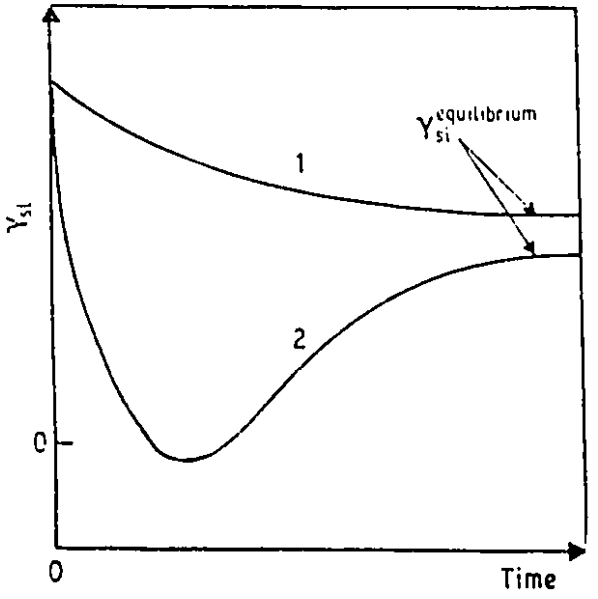

Figure 3.6 Variation of the interfacial energy γ_{sl} with time in nonequilibrium condition: Curve 1, pure adsorption; Curve 2, reaction between the two phases.[213]

3.6). This interaction increases linearly with the difference between the chemical potentials of the components in the two phases[213]. The dynamic value of γ_{sl} can even become negative[211].

When the transformation proceeds in the bulk phases, the difference between the chemical potential in the two phases and the strength of the interaction at the interface will decrease ($G^{\alpha\beta}$ increases, meaning that $G^{\alpha} + G^{\beta}$ decreases more than G). Thus, γ_{sl} increases gradually towards its equilibrium value (Fig. 3.6), which is always positive since the interface is always less stable than the bulk phases[213]. The time required to reach the minimum of γ_{sl} will depend upon the kinetics of diffusion of the components in the bulk phase. Therefore it depends very much on temperature.

In practice, quasi-equilibrium often occurs due to the presence of a thin diffusion barrier (such as an oxide layer) at the interface limiting the contact between the two bulk phases.

If we consider a solid-liquid-vapour system (Fig. 3.4) assuming that the solid-vapour and liquid-vapour are under chemical equilibrium conditions, but not the solid-liquid, several types of reactions may occur between the solid and the liquid. These reactions can be classified into two categories:[211]

i) only the solid is not saturated with some or all of the components of the liquid

ii) only the liquid is not saturated with some or all of the components of the solid

iii) both phases are not saturated with respect to the other

and

iv) a compound forms at the interface.

Figure 3.7 illustrates schematically several dynamic stages of the first type of the reaction. At time t_0 there exists a quasi-chemical equilibrium in the system involving no solid-liquid interfacial reaction (Fig. 3.7a). Young's equation can then be expressed only in terms of the initial dynamic surface tension. As the reaction proceeds at the interface, γ_{sl} changes with time to $\gamma_{sl}=\gamma_{sl}^0 + \Delta g_{sl}$ (Δg_{sl} is the interfacial free energy change due to the free energy of the reaction)[211].

Figure 3.7(b,c,d) shows the situation where the growth rate of the reaction product (or the diffusion rate of the reacting compounds) is slower than the spreading rate of the liquid. The case when the diffusion rate of the reacting solid are greater than the flow rate of the liquid is illustrated in Figure 3.7 (b',c',d). It should be noted that in stage (b) the periphery of the drop is in contact with unreacted solid. Whereas, in stage b', because of relatively faster growth rate of the reacted solid, the liquid at the periphery of the drop is in contact with reacted solid.[211]

Several dynamic stages are associated with a reaction of type (ii), where the liquid is not saturated with respect to the solid, are shown in Figure 3.8. At time t_0, Young's equation can be used to express the condition of mechanical equilibrium in terms of the dynamic interfacial energies. After the initial reaction, the composition

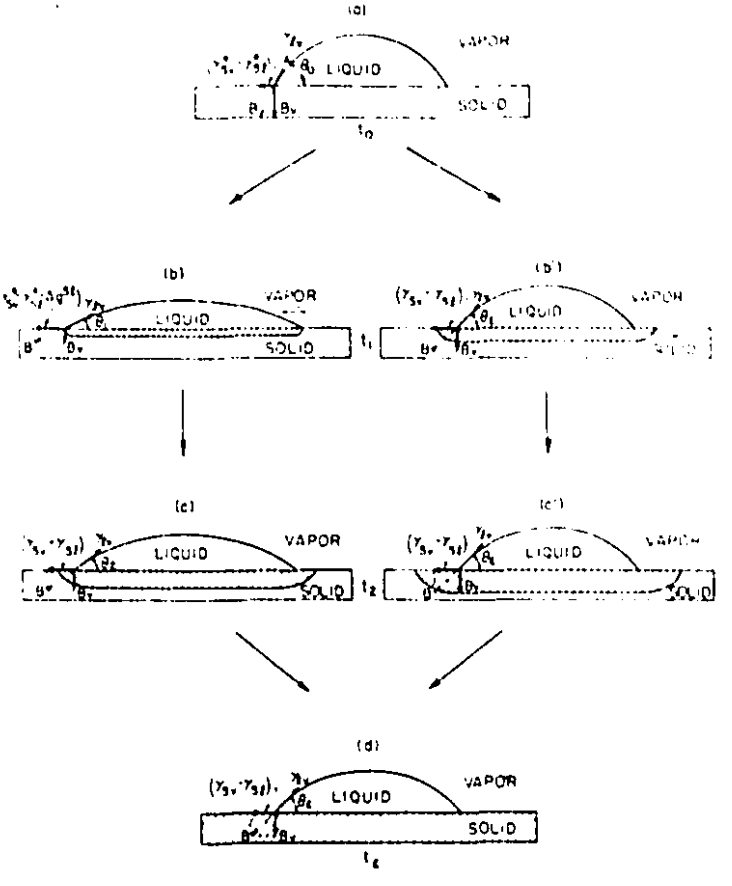

Figure 3.7 Schematic representation of the various dynamic stages of sessile drop when the initial solid is not saturated with some or all of the components of the liquid. The path abcd corresponds to the case where the growth rate of the reaction is slower than the flow rate of the liquid drop; and path ab'c'd corresponds to the case where the growth rate of the reaction products is faster than the flow rate of the liquid drop.[211]

of the liquid at the drop periphery will rapidly approach its equilibrium value, resulting in a decrease of γ_{sl}^{0} and γ_{lv}^{0} because of the free energy contribution of the reaction. Then, these parameters will rapidly approach their static value. Thus, during the initial stages of the reaction an immediate lowering of contact angle may be observed which is rapidly followed by the drop pulling back to an equilibrium contact angle. In the case of fast diffusion rate and high-viscosity of the liquid, the initial spreading will not be observed [211]. A type (iii) reaction may have similar

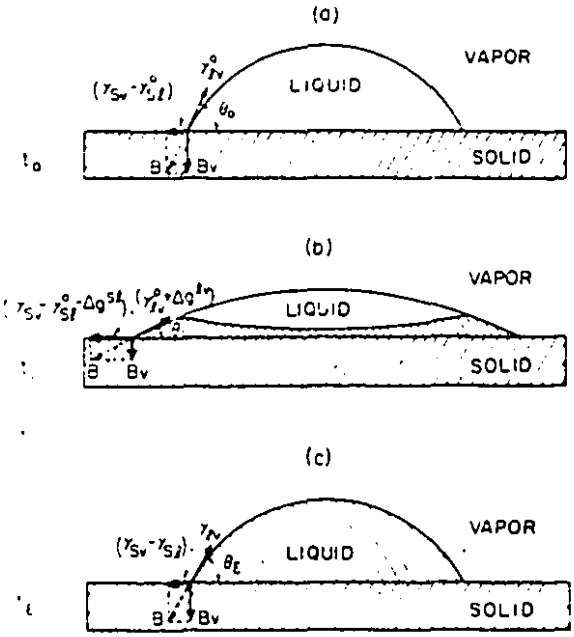

Figure 3.8 Schematic representation of the dynamic stages of a sessile drop when the initial liquid is not saturated with some or all of the components of the solid.[211]

behaviour of either type (i) or type (ii) configuration, depending on which material is saturated with respect to the other. The type (iv) which is associated with formation as a compound at the interface is expected to have the same behaviour as the type (i) reaction. However the analysis in this case could be more complicated, especially if the compound isolates the liquid from direct contact with the reacting solid[211]. With a reaction at the interface the magnitude of γ_{sl} will be smaller due to the existence of strong chemical bonds instead of weak Van der Waals bonds. In this case, the discontinuity will be less severe due to the presence of electronic continuity across the interface. With a reaction at interface, wetting and adhesion may be enhanced. In this case the work of adhesion Eq. 3.11 becomes:[72]

$$W_{ad}=\gamma_{lv}(1+\cos\theta)+\gamma_{ss}-C\Delta G_R \qquad (3.26)$$

where γ^{ss} is the interfacial energy between the solid and the reaction layer, ΔG_R

is the free energy of interfacial compound, and C is a constant related to the moles of product formed by unit increase in the liquid-solid contact area.

3.5 Wetting of Ceramics by Liquid Metals

Ceramics can be characterized by ionicity or covalency of their lattices with closed stable electronic configurations or atoms, and strong saturated interatomic bonding. Interaction of liquid metals with this type of solid bodies is possible only with partial or complete dissociation of interatomic bonding in the solid bodies. This can usually explain poor wettability of ceramics by molten metals. In ionic bodies such as oxide ceramics, the surface is formed by anions, and their interaction with liquid metals is mainly determined by the interaction with the solid body anions[200]. On the basis of intensive studies, it has been stated that, wettability of an oxide by a metal and adhesion in such a system depends on the affinity of the liquid metal for oxygen[200]. This is indicated by the variation in the thermodynamic potential of metal oxide formation. Chemically reactive metals which are prone to oxidation such as titanium, zirconium, aluminum, silicon, manganese and lithium (either pure or in the form of alloys) spread completely over certain oxide surfaces such as Al_2O_3, BeO, SiO_2, and MgO.

Covalent solids such as diamond, graphite, silicon nitride and carbide, boron nitride, and boron carbide are characterized by closed stable electron configurations of atoms with high strength interatomic bonds. Wettability in liquid metal-covalent solids systems is possible only by chemical reaction at the interface at the expense of bond dissociation in the solid phase. Therefore the metal in order to wet a covalent solid, should possess high chemical affinity for the solid phase atoms. For instance, transition metals such as Ti, Ta, W, Fe, etc., either in a pure form or in the form of additives, show considerable adhesion activity on contact with graphite or diamond. Wettability in such systems is determined by chemical interaction, carbide formation, or dissolution of the solid in the liquid at the interface.[200]

Several attempts have been made to calculate wettability in terms of bonding

interactions in various metal-ceramic systems. Kingery and Humenik[214] suggested a correlation of wetting behaviour for oxide ceramics with ceramic- melt reactivity. It was then employed by McDonald & Eberhart[215]. They performed wetting experiments between alumina and several kinds of pure metals and reported a linear relationship between the work of adhesion and the free energy change of the formation of the metal oxides as illustrated in Figure 3.9.

Metallizing the ceramics surfaces has been widely used to promote wetting at metal-solid oxide interfaces[216]. In many processes, Mo is employed for metallizing alumina, where the grains are held together by a glassy binder phase[216]. The Mo is applied to the surface of the ceramic in the form of powder often mixed with, Mn, Ti, or MnO_2 and fired in a reducing atmosphere. The glassy phase from alumina then migrates into the powder under capillary forces and bonds the particles to each other and to the alumina surface to produce a wettable surface layer. In the case of pure alumina and oxides without a glassy bonding phase, it is necessary to add glasses to the metallizing mixture.[216]

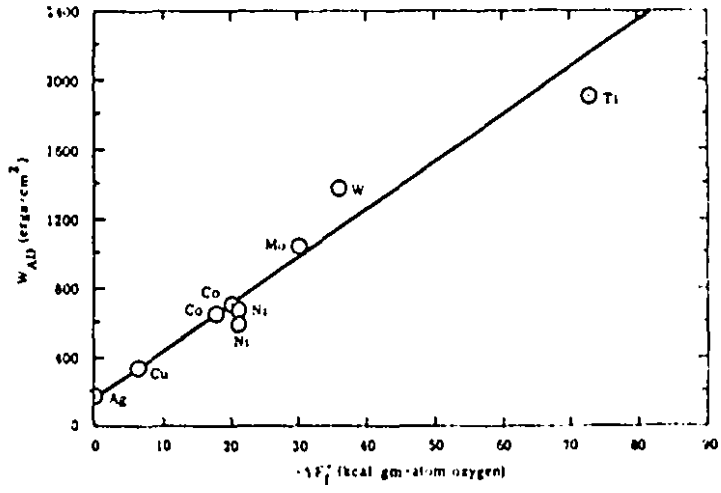

Figure 3.9 Work of adhesion on Al_2O_3 vs standard free energy of oxide formation for various liquid metals under vacuum.[215]

Other methods of metallizing oxide and non-oxide ceramic surfaces are electroplating and various vapour deposition processes. Probably the most common deposition process is TiH_2 activation In this process the hydride, in the form of powder, is applied to the surface and dissociates at 350-550°C to form a wettable Ti coating[216]. Although the metallized layer ensures wettability of the ceramic by the filler metal and brazing of metals to such surfaces is a relatively straightforward process, it is a costly and time consuming process.

Another method of enhancing wettability at a ceramic-metal interface is changing the chemistry of the ceramic surface by the addition of active metals to the braze. Simple brazing alloys are binary Ti alloys such as Cu-Ti, Ni-Ti, Co-Ti, and Al-Ti[217,218], with optimized concentration of Ti to prevent further increase in brittleness of the filler metals. However, the influence of a third alloying element on the concentration of the active element should be considered. Furthermore the optimum alloying composition range must be determined from the mechanical properties of the braze in addition to its wettability. Nicholas and co-workers showed the effect of the addition of a third element on wetting of alumina by Cu-Sn-Ti alloys at 1150°C[219]. They showed that alumina can be wetted by Cu-8 at% Ti in vacuum but if is alloyed with 11 at% Sn, the Ti concentration is reduced to 3.5 at%. Therefore, as shown in Figure 3.10, there is a trade-off between the Ti and the Sn level. Similar effects are achieved by alloying Cu-Ti with In and to a lesser extent with Al, Au, or Ag, but not with Ga or Ni. It has been suggested that the most effective additives are those with low Ti solubility and low surface energy. Since the activity of Ti is high in a saturated liquid, alloying additions that decrease the Ti solubility will increase the activity of a given concentration. Furthermore, if the ternary addition decreases the surface energy of the liquid, the actual wetting will be improved.

Complex reactions can occur at a ceramic-active metal braze interface. However, for some systems these reactions can be analyzed using some simplifying assumptions. Generally, Ti can dissolve considerable quantities of O and form a family

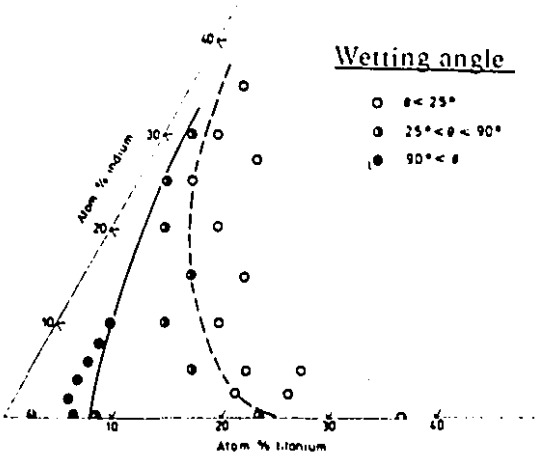

Figure 3.10 Influence of composition on wetting of alumina by Cu-Sn-Ti alloys at 1150°C[219].

of oxides. The stoichiometry and stability of these products is determined by temperature and activity level (a). Thus several oxide products might be formed by reaction between alloys containing Ti and less or similarly stable ceramics such as alumina[216]. If these products are assumed to be stoichiometric titanium oxide, respecting free energy data, it has, for example, been concluded that alloys with $a_{Ti}>4x10^{-4}$ at 1127°C (1400 K) can form TiO_2, or TiO_2-Al_2O_3 mixed oxide, by reaction with alumina:[216]

$$3[Ti]+Al_2O_3 \rightarrow 3TiO+2[Al] \qquad (3.27)$$

where the square brackets indicate solutes. The direction of reaction is determined by $a_{[Al]}$ and $a_{[Ti]}$. Depending on the temperature and the alloy composition, the reaction product could be either TiO or Ti_2O_3.[216]

Although many active alloying elements have been considered in many brazing alloys, Ti is the most commonly used active metal added to Ag-Cu eutectic in concentration of 5 to 10 wt% Ti.

3.6 Wetting of Silicon Nitride

It has been reported that most pure metals do not wet silicon nitride and exhibit poor bonding[220](Al being an exception). An addition of 3% Ti in Cu improves the bonding. Ti additions are more effective in providing low contact angle in Al-28% Cu alloys. With the addition of 2% Ti a thin double layer of TiN and a titanium silicide form at the interface which promotes wetting without formation of coarse Cu-Ti intermetallics in the bulk of the alloy[220]. The wetting angle is also influenced by the partial pressure of surrounding gaseous species. The work of Naka *et al*[221] indicates that Al definitely wets Si_3N_4. They found that the work of adhesion of Al on Si_3N_4 increases significantly with increasing temperature. The contact angle between silicon nitride and molten Si decreases with decreasing oxygen partial pressure, due to the increase in surface energy of the solid[210]. The observation of Li *et al*[222] indicates that at very low oxygen partial pressure in the region of about 10^{-19} Pa complete wetting can be achieved at 1450°C. There are data cited by Allen and Kingery[192] for the wettability of silicon nitride by Sn and Sn-Ti alloy over a wide range of temperature (800-1470°C). In the case of using pure Sn, wetting angles are 154 to 140° under H_2 atmosphere or 168 to 29° under vacuum. Addition of Ti markedly reduces the contact angle. From surface tension and contact angle measurements, they made estimates of the solid-liquid interfacial energy and the surface energy of silicon nitride. The sessile drop technique was used to investigate the wetting of silicon nitride in vacuum by a series of intermetallic compounds ($TiAl_3$, $TiSi_2$, TiNi, $TiNi_3$, $TiCr_2$, Cr_3Si_2, Fe_2Al_5, FeSi, Fe_2Si_5, CoSi, $CoSi_3$, NiAl, Ni_2Si), by Si, and by a Ni super alloy (713LC)*, within the range 1200 to 1600°C[223]. Very low contact angles (<40°) were given by $CoSi_3$, $TiSi_2$ and Si while the remaining silicides wet silicon nitride to lesser extent (60-80°) and $NiSi_2$ did not wet at all (Θ=108° at 1450°C). Aluminides gave moderate wetting (≈75°)

* Nominal analysis: N,12.5Cr-6.1Al-0.8Ti-4.2Mo-2.2Nb-0.1C-o.1Zr-2.5 max Fe wt%.

while Ti containing compounds gave moderate to good wetting (66 to <40°). A contact angle of <40° was reported for the Ni alloy (713LC) at 1400°C[223]. There exists a patented work on the wetting of Si_3N_4 with an alloy comprising Ni-7.5 Ti-2.5 Si wt%, which has shown good wetting characteristics with the ceramic[224].

Chapter 4

Objectives

The main objective of this study was to braze Si_3N_4 to Si_3N_4 and to Mo for high temperature applications (above 800°C), using Ni-Cr-Si brazing alloys based on a commercially available filler metal AWS BNi-5. Since wetting is a basic requirement in the brazing technique, another objective of this work involves a fundamental study of the wetting behaviour of the ceramic by the filler metals, through a thermodynamic and experimental modelling of wetting at the ceramic/filler metal interface. The results of this part of the study will then be applied to designing suitable Ni-Cr-Si brazing alloys for forming Si_3N_4/Si_3N_4 and Si_3N_4/Mo joints.

The following are other objectives of this work:

- Study the interfacial reactions in both Si_3N_4/Ni-Cr-Si/Si_3N_4 and Si_3N_4/Ni-Cr-Si/Mo joints.

- Study the influence of such process variables as the filler metal composition and brazing time and temperature on joint quality and microstructure and define the optimum parameters for obtaining strong joints.

- Evaluate the joint strength using both shear and four-point bend tests and

a comparison between the tests results.

• Carry out high temperature four-point bend tests, up to 900°C, to evaluate the effect of temperature on the CTE mismatch stress relaxation and also to assess the mechanical and chemical stability of the joints at elevated temperatures.

Chapter 5

Experimental

5.1 Experimental Materials

The experimental materials for all of the joining experiments consisted of pure Mo (99.95%), pressureless sintered silicon nitride, and a commercially available nickel-based brazing alloy, AWS* BNi-5 as the base filler metal. The BNi-5 filler metal will be referred hereafter, according to its Si content as "S19" (Table 5.1).

The Mo was supplied by AESAR** in the form of a 50x50x12 mm^3 plate.The silicon nitride was manufactured in house in the form of 9x6x80 mm^3 bars, further manufacturing procedures will be discussed later in this chapter. The S19 (BNi-5) brazing alloy used was supplied by Wall Colmonoy Corporation in the form of atomized powder (-200 mesh). Other forms such as plastic bonded sheets or transfer tapes were made of the same alloy powder processed with a binder in the form of thin sheets of certain thicknesses. Extensive effort was directed to produce S19 ribbons using melt spinning techniques, but the products were so brittle that they were not suitable for joining experiments. The chemical compositions and some

---

* American Welding Society

** AESAR Catalog No. 10048

Table 5.1 Physical Characteristics of S19 (BNi-5) Brazing Alloy.

Nominal Composition	Ni-18.87Cr-18.76 Si atom% (0.06C max)
Specific Gravity	7.65 g cm^{-3}
Solidus-Liquidus	1080°C-1135°C
Suggested Brazing Temp.	1150°C to 1200°C

Adopted from Wall Colmonoy Corporation technical data sheets No. 2.1 1 & 2.1.7.

physical properties of S19 (BNi-5) are given in Table 5.1. This brazing alloy is ideal for joining components used in high temperature and high stress applications. Its oxidation resistance is among the best, high service temperature filler metals and it exhibits good flow characteristics during brazing for 0.025 to 0.1 mm clearance joints. In fact the main reasons for selecting S19 as the experimental filler metal were its high melting temperature and chemical compatibility in terms of the concentration of Ni and Cr and the reactivity of these elements with Si_3N_4.

5.1.1 Chemical Analysis of Experimental Brazing Alloy

In order to confirm the chemical composition of the brazing alloy provided by the supplier, the compositional analysis of S19 filler metal was performed using atomic absorption and energy dispersive spectroscopy (EDS). The sample for EDS analysis was prepared by melting S19 powder in a BN crucible under inert atmosphere, followed by slow cooling and polishing the resultant solid sample. The results of EDS analysis as well as atomic absorption are given in Table 5.2.

Table 5.2 Chemical Analysis of S19 (BNi-5) Brazing Alloy.

Method of Analysis	composition atom% Ni	Cr	Si
EDS	62.50±0.35	18.43±0.29	19.02±0.31
Atomic Absorption	62.65	18.4	18.95

Several other brazing alloys based on S19, with some compositional modification, were used during the course of this study. They were composed of Ni-Cr-Si with the same Ni/Cr ratio, but different Si contents. The alloys were made through the addition of either Si powder (in the case of fabricating alloys having >19 at%Si) or a Ni-20 wt%Cr alloy to the commercial S19 in the required quantity followed by intimate mixing to obtain a uniform powder dispersion. In order to conform to the alloy compositions, a sample of each alloy was melted, solidified, and analyzed with an accuracy of ± 0.3 atom%, using the energy dispersive spectroscopy (EDS) technique. Table 5.3 shows the chemical compositions of these alloys. The designations presented in this Table will be used throughout the rest of the text.

5.1.2 Fabrication of Ceramic Samples

The silicon nitride samples used for both the wetting and joining experiments were fabricated in house using slip casting, followed by pressureless sintering. Due to its simplicity, slip casting is well suited for the fabrication of test samples and the production of a small number of individual shapes since the cost of plaster moulds is low. The basic steps of fabricating silicon nitride samples are illustrated in Figure 5.1. The additive composition for the silicon nitride was Si_3N_4-1.72 AlN-4.56 Y_2O_3-4.97 Al_2O_3 wt%[225]. The properties of the starting silicon nitride powder as well as of the other sintering aid powders are given in Table 5.4. The

Table 5.3 Chemical Analysis of Modified Brazing Alloys.

Designation	Composition (atom%)		
	Ni	Cr	Si
S10	69.61	20.35	10.04
S15	65.54	19.5	14.96
S25	58.34	16.66	25.0
S30	54.45	15.55	30.0

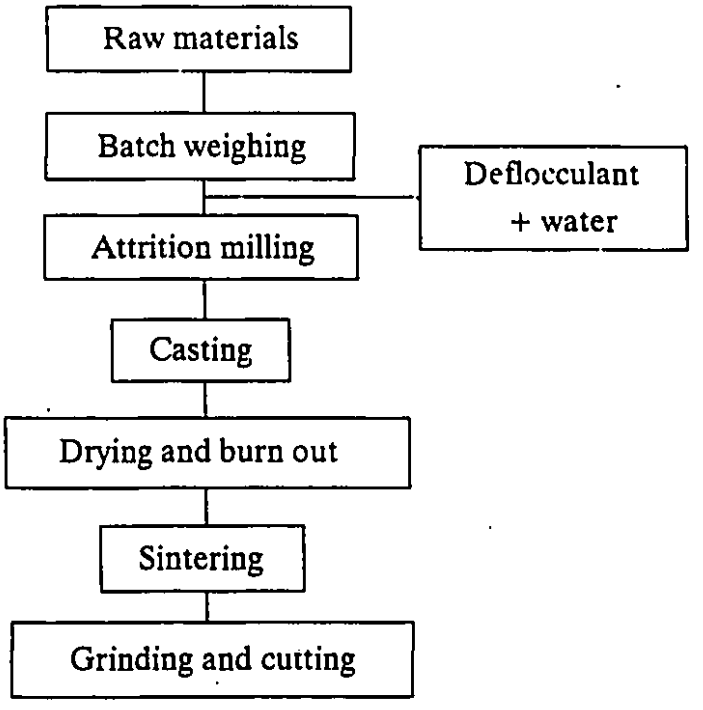

Figure 5.1 Basic steps in fabrication of Si_3N_4 samples.

Table 5.4 Characteristics of Starting Powders.

Commercial Brand	Company	Particle Size (μm)	O_2 Content	Crystal Phase
Si_3N_4 SN-E-10	UBE	0.1-0.3	1.39	α-hex
AlN Grade C	H.C.Starck	0.5	2.64	Hexagonal
Al_2O_3 HPA-0.5	Ceralox	0.3	47.06	α-Al_2O_3
Y_2O_3 Y5603	Molycorp	0.1-0.2	21.26	Cubic

powders were carefully weighed and mixed with liquid (which consisted of distilled water + 1 vol% deflocculant) with a ratio of 2:1 solid to liquid.

The deflocculating agent used was a commercially available polymer dispersant, Darvan C*, which is an aqueous solution of ammonium salt of a polyelectrolyte. The mixture was then attrition milled for 30 min. at 250 RPM using Si_3N_4 media to minimize contamination during milling. After milling, the slurry was sieved and poured into a porous plaster of Paris mould. As the mould adsorbed water from the contact areas, solid silicon nitride bars were built up. The solid pieces were then removed from the mould, dried at 500°C for 3 hours to remove the organic deflocculant and remaining water, and sintered at 1750°C for 2 hours. Sintering took place in a graphite element, vacuum furnace under a slight nitrogen overpressure (0.1 MPa). The density of sintered bars was measured according to ASTM C373-82[226], and was 3.17±0.02 g cm^{-3} which is almost 97% of theoretical density. The surfaces of the sintered bars were then ground using a 240 grit diamond grinding wheel on a surface grinding machine.

5.1.3 Strength Testing and Microstructure of Experimental Ceramic

Since the strength of ceramic is crucial for further joint strength evaluation, flexure strength tests were performed on sintered silicon nitride samples. According to MIL-STD-1942A[191] specimens having approximate dimensions of 3x4x45 mm^3 were prepared and both the tensile and comprehensive faces were longitudinally ground using a 240 grit diamond surface grinding wheel. The edges of the samples to be exposed to tensile stresses were bevelled. Specimens were then placed in a four-point modulus of rupture (MOR) jig (Fig. 5.2) with outer and inner spans of 40mm and 20mm respectively, and tested at room temperature on an universal testing machine ** with a cross head speed of 0.5 mm $min.^{-1}$.

---

* P.T. Vanderblit Co, Norwalk, CT, USA

** Instron Model 1362

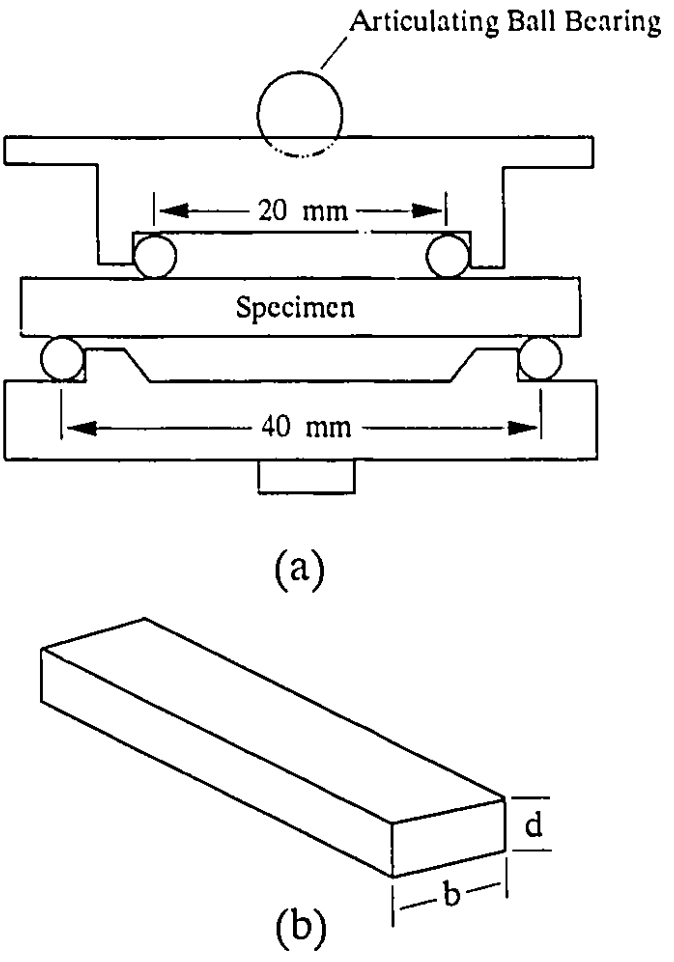

Figure 5.2 Modulus of rupture jig (a) and sample (b).

The MOR value for a rectangular sample can be calculated by:

$$MOR = \frac{3Fa}{bd^2} \tag{4.1}$$

where: F= fracture force (N)

a= distance between inner and outer span

b= the width of specimen

d= thickness of specimen

The mean MOR value for a total of twelve tested samples was 600±30 MPa. In order to provide a measure of the degree of reliability, the Weibull modulus "m" was calculated from the slope of the plot of ln ln $(1/1-P_f)$ against ln MOR, where:

$$P_f=\frac{n}{1+N} \tag{4.2}$$

n=ranking of the samples

N=total number of samples

The Weibull modulus is an indication of the reliability of ceramic products (a value of m >10 is considered good). As illustrated in Figure 5.3, the Weibull modulus

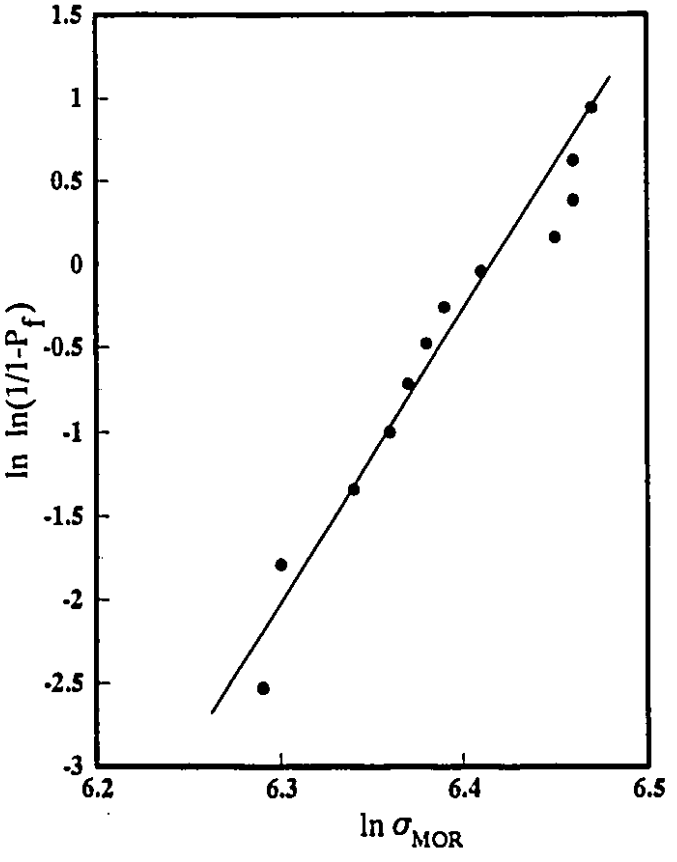

Figure 5.3 Weibull plot of the experimental Si_3N_4 MOR data.

was calculated to be 15.8 and the characteristic strength (σ_0) to be 620 MPa. Although the mean strength value obtained for sintered silicon nitride samples is lower compared to commercially available HIPped products[227], it is still expected to be much higher than the joint strengths.

The XRD pattern taken from the silicon nitride samples confirmed that the $\alpha \rightarrow$ ß transformation was completed.

5.2 Experimental Equipment

The main experimental apparatus used in this study consisted of a high-temperature furnace suitable for sintering the Si_3N_4 samples, a brazing furnace and a sessile-drop furnace.

5-2-1 Sintering Furnace

The sintering furnace was essentially a horizontal controlled atmosphere graphite element resistance furnace. Its 30x30x40 cm^3 chamber was insulated from the water-cooled body by graphite fibre insulation. The elements were connected to a 50 kVA power supply. A type C thermocouple (W5%Re vs W26%Re) monitored the temperature. The furnace temperature was regulated by a controller connected to a silicon control rectifier (SCR). A rotary pump evacuated the furnace to a vacuum of 15 Pa ($1.5x10^{-4}$ atm). In order to be assured of the experimental temperature, the furnace was calibrated frequently by melting pure metals such as copper and nickel. This was done by heating up the furnace until the metal melted and then comparing the reading temperature with the melting point of the metal. The calibration accuracy was estimated to be ±5°C. This furnace was mainly used for sintering Si_3N_4 samples under a N_2 atmosphere.

5.2.2 Brazing Furnace

A graphite element vacuum furnace was used for all the brazing experiments. As shown in Fig. 5.4, the furnace consisted of a cylindrical graphite heating element

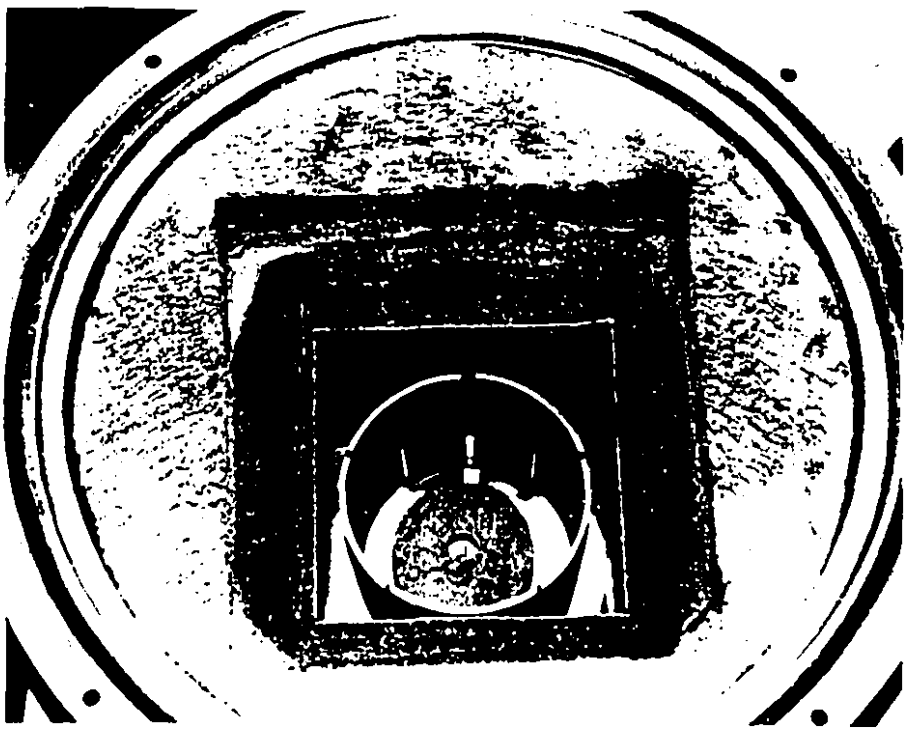

Figure 5.4 Experimental brazing furnace.

having approximate dimensions of 110 mm inner diameter, 127 mm height, and 4 mm thickness, connected to a 15 kVA power supply. The hot zone was insulated from the water-cooled body by fibre graphite insulations. The temperature cycle was controlled by an Omega Model CN-2041 microprocessor based programmable controller connected to a SCR power control unit. A rotary pump evacuated the furnace to a vacuum of 5 Pa ($5x10^{-5}$ atm). The temperature was monitored using a type C thermocouple. The furnace was frequently calibrated in the same manner as outlined in the previous section. The calibration accuracy was estimated to be ±5°C.

5.2.3 Sessile-drop Furnace

The sessile-drop furnace was essentially a horizontal tube furnace, consisting of a 60 cm long alumina tube having 26 mm inner diameter (Fig. 5.5). The hot zone

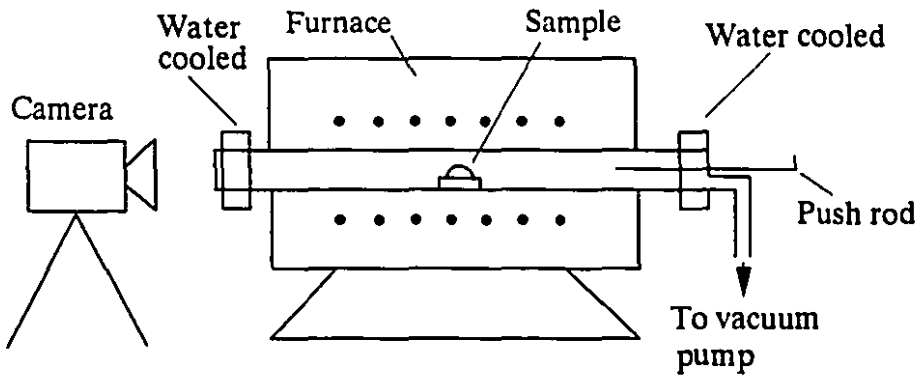

Figure 5.5 Experimental sessile-drop furnace.

inside the tube was almost 10 cm long. The furnace could be heated up to 1250°C and a vacuum of 2 Pa could be obtained using a rotary pump. The temperature was monitored using a type K thermocouple with ±5°C accuracy. The temperature cycle was controlled using an Omega CN8600 process controller. A water-cooled quartz window was fitted on one end of the alumina tube for direct viewing of the substrate. An optical system was arranged in front of the window to take photographs of the drops at temperature. The furnace configuration allowed for rapid (if desired) or slow heating and cooling. In the case of rapid heating, the sample holder along with the Si_3N_4 substrate was pushed by a vacuum tight push rod from the cold zone inside the tube to the hot zone, and vice versa for fast cooling. The furnace could be run under inert gas if desired.

5.3 Wetting Experiments

In order to assess the wetting of the experimental brazing alloy on Si_3N_4, wetting experiments were performed using the sessile-drop technique. Wetting specimens were blocks of 9x9x6 mm^3 Si_3N_4. The 9x9 mm^2 surfaces to be examined were ground and polished to a 1μm surface finish (using the same procedure as § 5.6.1) and degreased ultrasonically with acetone prior to the experiments. A small amount of brazing powder (≈0.05 gr.) was mixed with distilled water to form a paste

and placed on the Si_3N_4 surface. The substrate was then positioned in the cold zone of the tube furnace and after evacuation the sample was slowly pushed to the hot zone of the furnace. The heating rate was estimated to be about 100°C min^{-1} to 500°C and about 200°C $min.^{-1}$ to the experimental temperature (1220°C). After the ailoy started to melt, photographs were taken of the drop every minute for wetting angle measurement.

5.4 Brazing Experiments

The experimental brazing specimens consisted of blocks of Si_3N_4 and/or Mo having approximate dimensions of 9x9x6 mm^3. The Si_3N_4 blocks were cut from the sintered bars and the 9x9 mm^2 faces to be joined were polished to a 1 μm finish. The brazing alloys in quantities sufficient to form a layer of 100 μm thick upon solidification were mixed with a water-based gel suspending agent (Nicrobraz Cement-S supplied by Wall Colmonoy Corporation) to provide a means of applying the filler metal in an easy-to-use thixotropic paste. The paste was applied on the polished 9x9mm^2 Si_3N_4 surfaces and another polished block of Si_3N_4 or Mo was placed on top of it. The samples were then placed in a BN brazing jig to ensure alignment during the brazing procedure. The assembly was then placed in the vacuum furnace for brazing. Depending on the brazing temperature and cooling rate, different brazing cycles were used. A typical brazing cycle is illustrated in Figure 5.6, and essentially consisted of heating up the furnace at the rate of 20°C min^{-1} to the brazing temperature, holding for the desired time, and cooling to room temperature. The cooling rate varied from 10°C $min.^{-1}$ to as low as 3°C $min.^{-1}$ depending on the brazing cycle. The purpose of allowing the joints to be cooled very slowly was to let the filler metal deform plastically to alleviate the thermal stresses developed within the joint area and to avoid thermal shock to the ceramic. In some cases joint annealing was performed by holding the brazed samples at 900 °C for 30 to 60 min. followed by slow cooling to room temperature. After cooling, the samples were removed from the furnace and prepared for further examinations.

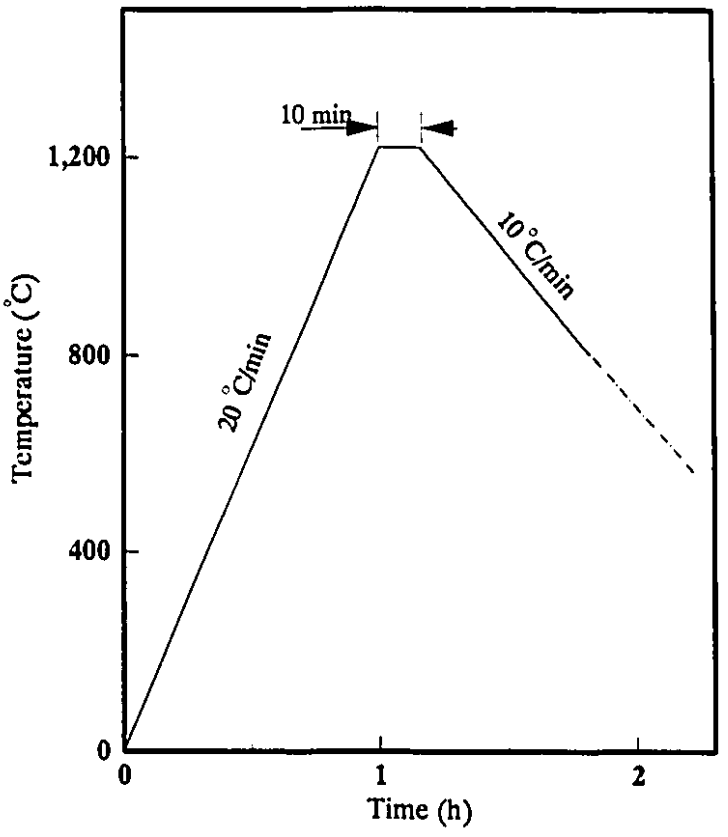

Figure 5.6 Typical brazing cycle used for joining Si_3N_4 to Si_3N_4.

5.5 Joint Strength Measurement

The interfacial strength of both Si_3N_4-Si_3N_4 and Mo-Si_3N_4 joints was determined by both four-point bending and fracture shear loading using two types of double-brazed and single brazed shearing jigs. Initially a double-brazed shearing jig, by which the mechanical properties of two joints could be tested in a single test was developed. The loading principles were similar to those which had already been used by Mizuhara *et al*[228], with some modifications in order to improve the assembly alignment and load distribution, which allowed viewing the test specimen.

As illustrated in Figure 5.7b the double-brazed shearing samples consisted of three blocks of Si_3N_4 and/or Mo having dimensions of 20x9x6 mm^3 (side blocks) and

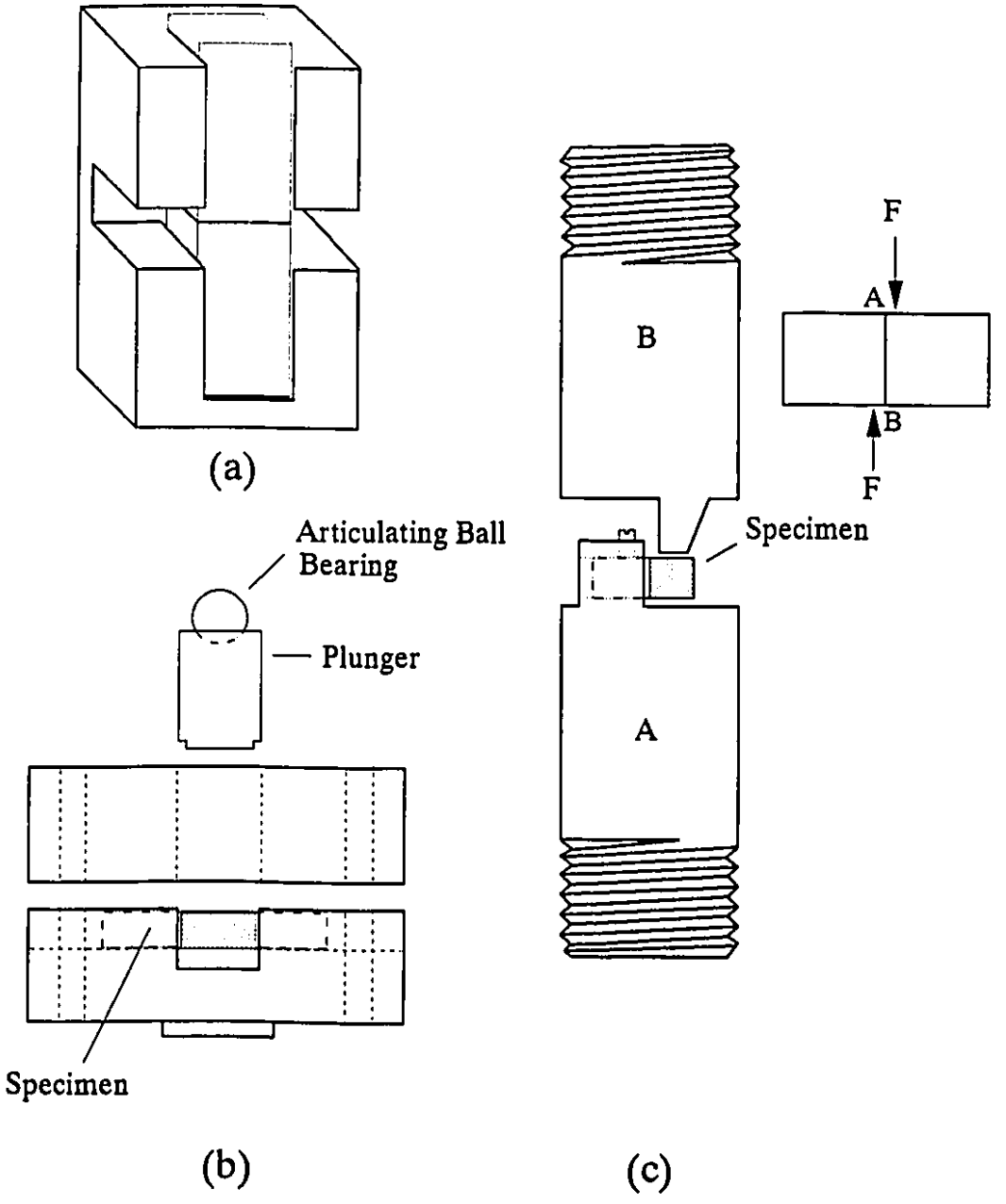

Figure 5.7 a) BN jig used for brazing MOR and double-brazed shearing samples, b) arrangement for double and c) single-shearing test.

9x9x6 mm^3 (centre blocks). The side blocks were Si_3N_4 in all the cases and the centre blocks were either Mo, in case of evaluation of ceramic-metal joint strength, or Si_3N_4 for ceramic-ceramic joint strength measurement. These blocks were butt-joined together from the 9x6 mm^2 faces which had been polished and degreased prior to joining. A specially designed BN fixture (Fig. 5.7a) was used to ensure proper alignment of the blocks during the brazing procedure. The brazing cycle, the form of the filler metal applied, and the brazing equipment were all the same as used for fabrication of the experimental joints. Brazed samples were then surface ground to produce parallel sides of the samples in the same way mentioned previously for the experimental MOR specimens. They were then placed in the bottom part of the jig in such a way that the centre block was located on the top of the groove, which provided for free movement of the fractured sample. After carefully placing the specimen, the top part was attached to the bottom part using four screws. These screws applied a slight pressure to prevent any bending moment and specimen movement during testing. A loading plunger was then introduced into the cavity of the upper part of the jig. The contact area between the bottom of the plunger and specimen could be viewed and controlled accurately to guarantee that the applied load was over the entire area of centre block. The assembly was then placed in the Instron testing machine. A steel ball was located between the top of the plunger and the loading bar to avoid bending moments. The plunger pushed the centre block under a crosshead speed of 0.5 mm min^{-1} against the two end blocks. The specimens were loaded until fracture occurred in both joints with the load-displacement curves being obtained on a chart recorder. The shear strength was calculated as:

$$S=\frac{P_{max}}{2A} \qquad (4.3)$$

where: S= the shear strength (MPa)

P_{max}= the fracture load in the test (N)

A= the specimen cross section area (mm^2)

In order to evaluate the applicability of the double-brazed shearing test, a series of Si_3N_4-Si_3N_4 and Mo-Si_3N_4 brazed joints using Cusil-ABA brazing alloy were made and tested; the results of these tests are presented in Appendix IV.

Because of some problems observed with the use of the double-brazed shearing test (discussed in Chapter 7), a single-brazed shearing jig was designed and used for the remainder of the shear strength evaluations. As shown schematically in Figure 5.7c, the test assembly consisted of two blocks with threaded heads that could be screwed onto the load frames which were attached to the load cell and actuator of the testing machine. A gap of 0.7 mm was left between the two blocks. The shear specimens were essentially the same size as the experimental brazing samples. They were surface ground using a 240 grit surface grinding wheel to ensure that the sides to be exposed to shear loading were parallel. Samples were then fitted into block A (referred to as the holding block) by two screws in such a way that the joint interface was situated right at the gap (in the case of ceramic-metal joints, the metal side was placed in block A and the load was applied on the ceramic side). The specimens were loaded at the same cross-head speed (0.5 mm $min.^{-1}$) until fracture occurred. The shear strength of the interfaces could then be obtained from the load-displacement curve recorder.

The four-point bend strength of ceramic-ceramic and ceramic- metal joints was measured according to MIL-STD-1942A[191]. In order to evaluate the high-temperature strength of ceramic-ceramic joints, the four-point bending test was carried out at 500, 700, and 900°C using the same testing machine which was equipped with a vertical type 1600-VTF (Split)* tube furnace. The temperature cycle was controlled by a Eurotherm Model 810 controller in conjunction with a type B (Pt 6% Rh vs Pt 30% Rh) thermocouple. After placing the sample in a silicon

* CM furnace, Inc., Bloomfield, NJ.

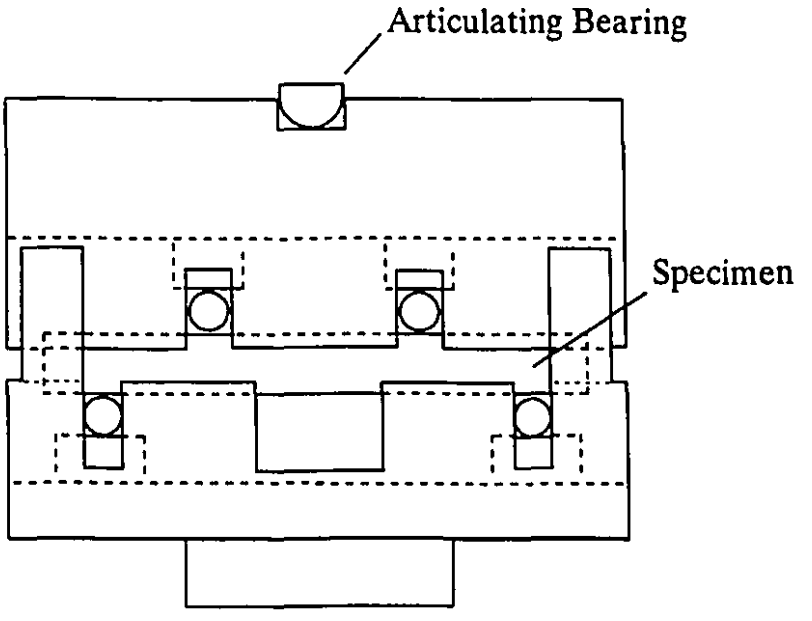

Inner Span= 20 mm

Outer Span= 40 mm

Figure 5.8 Schematic illustration of the SiC MOR jig.

carbide bending jig (Figure 5.8), the furnace was heated up slowly at a rate of 15°C min.$^{-1}$ to prevent thermal shock to both the jig and sample. In order to be assured of the experimental temperature, another type B thermocouple was placed near the specimen. The specimen was held at the desired temperature for more than 5 min. before fracture test.

5.6 Analysis

5.6.1 Scanning Electron Microscopy

All of the microstructural examination was performed using a JEOL JSM-840A, a high-resolution scanning electron microscope (SEM). The JSM-840 was equipped with an energy dispersive spectroscopy unit, permitting micro-chemical

elemental analysis (see below). The microscope was operated at 20 kV accelerating voltage during all the investigation.

Samples examined on the SEM were either the fracture surfaces of samples or polished experimental joints. In the case of chemical analysis, the brazed specimens were mounted using a cold-setting epoxy resin and sectioned perpendicular to the joint area using a diamond cut-off wheel (LECO CM-15 cut-off machine). The resultant surfaces were polished using a Leco VP-150 VARI/POL automatic polisher equipped with an AP-50 load controller. The polishing procedure consisted of grinding the samples using 240 and 600 grit diamond grinding discs followed by polishing using 15, 6, and finally 1μm diamond pastes on nylon polishing cloths. In order to prevent a negative charge build up on the specimen surfaces, all SEM samples were either Au-Pd* or C** coated prior to examination. Carbon coating was performed when characteristic X-ray analysis was required.

5.6.2 Microchemical Analysis

All the compositional analysis within the braze layer was performed with wavelength dispersive X-ray spectroscopy (WDS) using an electron probe microanalyzer (EPMA) unit (CAMEBAX, Cameca, Courbevoie, France). The examinations were carried out at an accelerating voltage of 15 kV using a beam current of 20 nA and a beam size of 2 μm. The standards consisted of pure Ni (Ni-K_α), Cr (Cr-K_α), Mo (Mo-L_α), and SiO_2(Si-K_α), Al_2O_3 (Al-K_α) and Drake & Weill No.2 ***(Y-L_α). N was analyzed by difference. The program resident in the WDS system employed the PAP[229] correction method for converting the sample intensities to quantitative concentrations.

The overall composition of the braze layer or any other structure of interest

---

* ANATECH Hummer IV sputtering system

** EDWARDS E306A coating system

*** 3.21Y-3.66La-16.25Al-12.68Si-18.11Ca-3.41Ce-3.79Pr-38.89O wt%

was determined by the area analysis method. Using this type of analysis, the area shown on the microscope screen was analyzed. Spot analysis was performed to analyze individual phases within the braze layer or at the interfaces, which were too small for area analysis. In any case, whether for spot or area analysis, ten different locations of the same phase or structure were analyzed to enhance the degree of accuracy. Elemental line profiles across the joint were taken in steps of 1 μm. The X-ray elemental dot mapping within the joints area using the EPMA spectrometers was performed when appropriate.

Besides the EPMA, the JEOL-840A in conjunction with a microcomputer-based energy dispersive X-ray spectroscopy (EDS) analysis unit was used for microchemical analysis of the light elements (i.e. N) free phases. The X-ray detector (Tracor Northern TN-96-606E31513) was mounted with an incline of 60° to the column axis, providing a higher take-off angle to increase the collection efficiency and to minimize the magnitude of the absorption factor[230]. Among the programs resident in the EDS system, a quantitative analysis program called "SQ" was used for this study. This program employs the ZAF[230] (atomic number, absorption, fluorescence) correction method to determine the composition of an unknown material and compares it with the known composition of internal standards resident in the data-base of the unit. All examinations were carried out under a working distance of 39 mm and a detector slide position of 75 mm. An operating voltage of 20 kV was selected as a compromise between minimum beam penetration and maximum signal intensity.

5.6.3 X-ray Diffraction

X-ray diffraction was used for the qualitative phase analysis. All XRD patterns were obtained using a Phillips X-ray automatic powder diffraction diffractometer with a goniometer and a scan range from 15° to 80°. The monochromatic CuKα radiation was generated by passing the X-ray beam through a Ni filter, using an American Instrument X-ray generator with an accelerating voltage of 40

kV and a beam current of 20 mA with both voltage and emission stability of better than 0.1% for ±10% line voltage variation. The system was linked to a Phillips APD 1700 computer (Digital-Micro PDP-11) for acquiring and storing the data. The samples were step-scanned at the rate of $1^{\circ}min.^{-1}$. The phases presented in the pattern were identified by comparing with the JCPDS-XRD reference patterns available on the computer.

Because of the small concentration of interfacial phases and joint thicknesses, XRD of the joint cross-sections was difficult to perform. Instead, the method was employed for qualitative phase analysis of the sample fracture surfaces.

5.7 Thermodynamic Analysis

The Facility for the Analysis of Chemical Thermodynamics (F*A*C*T) system was employed for the thermodynamic calculations when necessary. F*A*C*T is a mainframe computer program and consists of several program modules. The system has its own databases consisting of the thermodynamic properties of over 3800 stoichiometric compounds and a number of binary solutions.[231]

Chapter 6

Wetting at the Si_3N_4/Ni-Cr-Si Brazing Alloy Interface

This chapter discusses the results of the thermodynamic calculations for predicting wetting at the Si_3N_4/Ni-Cr-Si filler metal interface and its application to designing a Ni-Cr-Si alloying system which will adequately wet Si_3N_4.

6.1 Thermodynamic Calculation of Wetting at Si_3N_4/Ni-Cr-Si Alloy Interface.

In this section, thermodynamic calculations to predict wetting at Si_3N_4/Ni-Cr-Si system will be presented. The composition of the brazing alloy used for the calculations was based on S19 (BNi-5), with approximate composition of 63Ni-18Cr-19Si atom%. For all other alloy compositions the ratio of Ni/Cr was assumed to be fixed at 3.5 (the same as S19) and only the Si content of the alloys was varied. This assumption allows the Ni and Cr content of each alloy composition to be calculated knowing the Si level. The reasons for this assumption will be outlined later. All the alloys in contact with Si_3N_4 were supposed to be in the liquid state.

6.1.1 Wetting Model

As mentioned previously in Chapter 3, wetting occurs at the ceramic/metal interface as a result of chemical bond formation between the ceramic surface and

the liquid metal. When a reaction occurs, the free energy of reaction per unit interfacial area and unit time enhances the driving force for wetting. The simplest reaction is the solution of one phase by the other to form an immediate equilibrium saturation at the interface and then its continuation into the bulk in order to reach the lowest free energy state. In a solution reaction when the liquid phase is unsaturated with respect to the ceramic, its composition will change while the ceramic composition will remain unchanged. The free energy change for this solution reaction can then be used to predict wetting affinity.

In order to achieve realistic results from the wetting model all the process conditions must be properly taken into account. These parameters are temperature, amount and composition of reacting materials, as well as the reaction environment. Accordingly, several constraints and assumptions must be incorporated in order to simplify the calculations.

For the purpose of Gibbs energy evaluation in the system, including Si_3N_4 in contact with the liquid alloy consisting of Ni, Cr, and Si, it was assumed that a given quantity of alloy reacts with Si_3N_4 at 1220°C (1493K). This condition is shown schematically in Figure 6.1. The selection of this temperature allows for the Ni-Cr-Si alloy compositions used to be in the liquid state. The assumption was made after examination of the liquidus surface of the Ni-Cr-Si system proposed by Lugscheider *et al.*[232], the investigations of Ansara *et al.*[233] and Guard and Smith[234]. It was also assumed that the reaction between the ceramic and liquid alloy occurred under isobaric and isothermal conditions. This assumption was made because

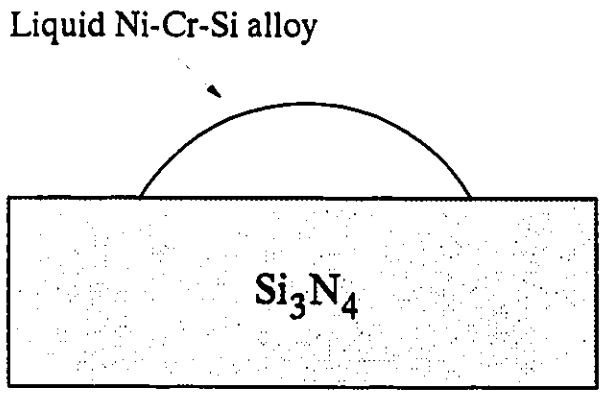

Figure 6.1 Schematic illustration of Si_3N_4/liquid metal wetting system.

the heat evolved during the reaction does not significantly affect the temperature of the system. The N_2 partial pressure in the system is extremely important since this parameter will determine the free energy change during the decomposition of Si_3N_4 and consequently the Gibbs energy change of the wetting system being modeled. It was assumed that the wetting reactions occurred under a N_2 partial pressure of 15 Pa. Another important factor is the quantity of both liquid alloy and silicon nitride available to react with each other. In the present calculations, it has been assumed that 0.001 mol of alloy will react with a layer of 2 μm of Si_3N_4. Considering the molar weight of S19 ($\approx$51.6 g mol^{-1}) this is almost equal to 0.05 g, which is nearly equivalent to the amount of alloy required to form a liquid metal droplet on the solid substrate in the sessile-drop experiments. The 2 μm thickness of Si_3N_4 reacting with the alloy was chosen because previous studies of wetting in ceramic/metal systems had shown the presence of reaction layers with 1 to 5 μm thickness at the interface [219,235].With respect to the assumed depth of the reaction in Si_3N_4 and the area over which the alloy will spread, a value of 10^{-6} mol of Si_3N_4 was calculated to react with the alloys. The effect of the variation of this value on Gibbs energy calculations will be discussed later.

Another assumption to simplify the computation was that all of the starting Ni-Cr-Si alloys reacting with Si_3N_4 lie within the ternary Ni-Cr-Si composition triangle along the line shown in Figure 6.2. This line represents all the compositions having fixed Ni/Cr ratio of 3.5. This greatly reduces the number of calculations involved for the further determination of the Gibbs energy change in the ternary Ni-Cr-Si system.

The above assumptions can be summarized as follows:

1- The reaction between 10^{-6} mol Si_3N_4 and 10^{-3} mol liquid Ni-Cr-Si alloy takes place under isobaric and isothermal conditions at 1493 K and 15 Pa N_2 pressure.

2- The Si liberated as a result of the decomposition of the Si_3N_4 dissolves in the liquid alloy and the N_2 escapes into the environment.

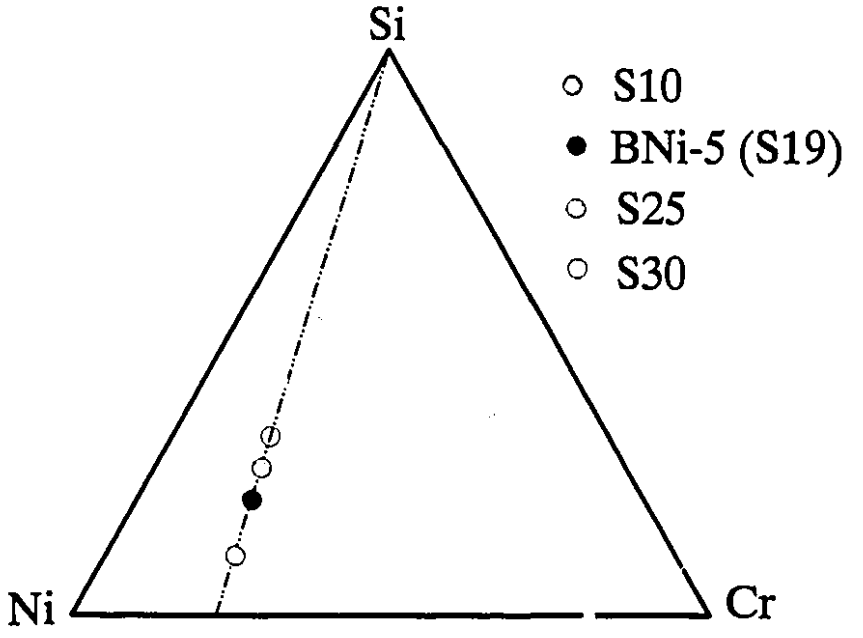

Figure 6.2 The path of the alloy compositions within the Ni-Cr-Si ternary system used in the thermodynamic calculations.

3- Since there are no sources or sinks for Ni and Cr in the system, the ratio of Ni/Cr in product alloy will remain fixed at 3.5.

The appropriate chemical equation, for which the Gibbs energy must be found, is as follows:

$$\langle Si_3N_4 \rangle + \{Ni\text{-}Cr\text{-}Si\}_{L_1} \rightarrow \{Ni\text{-}Cr\text{-}Si\}_{L_2} + (N_2) \qquad (6.1)$$

This unbalanced equation indicates that the liquid alloy with composition L_1 reacts with solid Si_3N_4 to produce a new liquid of composition L_2 and N_2 gas. The reasons for assuming that the liberated N_2 will escape into the environment without any reaction with the Ni and Cr are:

1. N_2 is insoluble in and does not react with Ni at temperatures up to 1400°C to form a stable nitride[236] (the free energy of formation of Ni_3N is about 10 kJ/mol

at 1473 K).

2. In the Cr-N system in the absence of external N_2 pressure (even if it is as low as 1 Pa) no chromium nitride will form above 1000°C.[178]

In order to obtain the corresponding Gibbs energy equation, the chemical equation (Eq. 6.1) should be broken up as follows:

$$y\langle Si_3N_4\rangle \rightarrow 3y\ \langle Si\rangle + 2y\ (N_2) \qquad \Delta G_1 \tag{6.2}$$

$$3y\ \langle Si\rangle \rightarrow 3y\ (Si) \qquad \Delta G_2 \tag{6.3}$$

$$z\left\{\frac{1-x}{1.28}Ni/\frac{1-x}{4.5}Cr/xSi\right\}_{L_1} + 3y(Si) \rightarrow z+3y\left\{\frac{z(1-x)}{1.28(z+3y)}Ni/\frac{z(1-x)}{4.5(z+3y)}Cr/\frac{zx+3y}{z+3y}Si\right\}_{L_2} \qquad \Delta G_3 \tag{6.4}$$

Equation 6.2 indicates the decomposition of Si_3N_4 into solid Si and N_2 gas and Eq. 6.3 represents the fusion of solid Si. Eq. 6.4 illustrates the dissolution of Si into the initial Ni-Cr-Si alloy with composition L_1 to form the new composition L_2.

The corresponding Gibbs energy equations for the system will be the sum of ΔG_1, ΔG_2, and ΔG_3:

$$\Delta G_r = \Delta G_1 + \Delta G_2 + \Delta G_3 \tag{6.5}$$

The free energy change ΔG_r, represents the energy released or required when Si_3N_4 reacts with the liquid alloy. A negative ΔG_r indicates a spontaneous reaction and, hence, wetting. The reaction will continue until thermodynamic equilibrium is reached, i.e., $\Delta G_r = 0$. In order to predict the sign and magnitude of ΔG_r, numerical values of ΔG_1, ΔG_2 and ΔG_3 need to be calculated.

The Gibbs free-energy change ΔG_1 for the reaction presented in Eq. 6.2 can be calculated using the relation shown in Eq. 6.6:

$$\Delta G_1 = \Delta G^\circ + RT \ln \frac{P_{N_2}^2 \cdot a_{Si}^3}{a_{Si_3N_4}} \qquad (6.6)$$

where ΔG° is the standard Gibbs free energy change for the decomposition of Si_3N_4 in the bulk. The activity of the liberated Si (a_{Si}) in Eq. 6.6 should be unity. Since the Si_3N_4 used in the wetting experiments contained about 10% additives, a value of 0.9 was used for the activity of Si_3N_4 in the calculations.

The explanation presented in Eq. 6.6 does not account for the fact that the liquid alloy is in contact with the surface of the Si_3N_4, the free energy change of formation or the decomposition of which is different from the bulk. The value of the free energy change for the decomposition of Si_3N_4 on the surface would be less positive than ΔG° because the atoms on the surface are missing half their nearest neighbours and , thus, are loosely bound to each other compared to the atoms in the bulk. Consequently, less energy is required to liberate atoms at the surface. It is therefore expected that some metals will react with the ceramic surface even when a bulk reaction is not thermodynamically achievable. The concept of free energy of surface formation defined as ΔG^{surf} was first used by Chidambaram *et al.*[237] for predicting the wetting tendencies of various metals on α- Al_2O_3 surfaces.

As mentioned previously in § 3.2.1, the Gibbs excess surface energy is defined as:

$$G^{xs} = A\gamma \qquad (6.7)$$

where γ is the surface energy and:

$$A = mN^{1/3}V_m^{2/3} \qquad (6.8)$$

where V_m is the molar volume, N is Avogadro's number, and m is the fraction of nearest-neighbour atoms lying in an adjacent layer. The Si_3N_4 structure consists of

SiN_4 tetrahedra joined by sharing N corners so that each N is common to three tetrahedra (Figure 2.2). Therefore, each N atom is shared between three tetrahedra so that each Si atom has four N atom nearest neighbours and each nitrogen has three Si atoms nearest neighbours. If we assume that the Si_3N_4 crystal cleaves along the plane where the Si atoms are located*, one out of four Si-N bonds will break. Therefore, a value of 1/4 was used for *m* in the calculations. The surface energy of Si_3N_4 was taken from the investigation of Barsoum and Ownby[238] . They reported a value of 1150 mJ m^{-2} at 1200°C.

The G^{xs} quantifies in Gibbsian terms for excess energy associated with the surface phase with respect to the bulk phase. Therefore in terms of the dissociation energy:

$$\Delta G^{surf} = \Delta G^{\circ} - G^{xs} \tag{6.9}$$

where $\Delta G^{\circ}$is the energy required for decomposition of Si_3N_4 in the bulk phase. Eq. 6.9 suggests that the surface phase requires less energy than the bulk phase by G^{xs} to dissociate[237].

Taking into account G^{surf}, ΔG_1 will be written as:

$$\Delta G_1 = (\Delta G^{\circ} - G^{xs}) + RT\ln\frac{p_{N_2}^{2}.a^{3}Si}{a_{Si_3N_4}} \tag{6.10}$$

ΔG_2 represents the free energy change for the fusion of Si and is readily available from tabulated data. Now, the last term to be calculated is ΔG_3 which is the corresponding free energy change of Eq. 6.4. Physically, this equation represents the free energy change in a system containing ternary Ni-Cr-Si alloy as a result of the addition of Si. Thus, the free energy change for the reaction shown in Eq. 6.4 (ΔG_3) is:

---

* This assumption compares well with alumina ceramic with an hcp structure in which cleavage occurs along the basal plane where the oxygen atoms are situated.

$$\Delta G_3 = G_{(Ni-Cr-Si)_{L_2}} - (G_{(Ni-Cr-Si)_{L_1}} + G_{Si}) \tag{6.11}$$

it is therefore necessary to calculate the free energy change due to the formation of ternary Ni-Cr-Si solutions with two different compositions of L_1 and L_2.

For any A-B-C ternary solution, the molar free energy of formation is given as:[239]

$$\Delta G^M = RT(X_A \ln a_A + X_B \ln a_B + X_C \ln a_C) \tag{6.12}$$

The components in an ideal Raoultian solution, obey the relationship:

$$a_i = X_i \tag{6.13}$$

thus for an ideal A-B-C ternary solution:

$$\Delta G^{M,id} = RT(X_A \ln X_A + X_B \ln X_B + X_C \ln X_C) \tag{6.14}$$

For a nonideal solution which does not obey Raoult's law, the relationship a_i=X_i does not hold. In this case:

$$a_i = \gamma_i X_i \tag{6.15}$$

where γ_i is the activity coefficient*. Thus for a nonideal solution:

$$\Delta G^M = \Delta G^{M,id.} + RT\,(X_A \ln \gamma_A + X_B \ln \gamma_B + X_C \ln \gamma_C) \tag{6.16}$$

The properties of a nonideal solution (i.e., a regular solution) are best

---

* A knowledge of the variation of γ_i with composition and temperature is of central importance in solution thermodynamics, since the value of γ_i is required for the determination of a_i, which in turn is required for the determination of ΔG^M.

examined through the concept of excess functions. The excess value of an extensive thermodynamic solution property is simply the difference between its actual value and the value it would have when the solution is ideal[239]. Thus Eq. 6.16 can be written as:

$$\Delta G^{M} = \Delta G^{M,id.} + G^{xs} \tag{6.17}$$

where G^{xs} is the excess molar free energy of the solution.

It is thus seen that the excess free energy of the solution is required for determining the free energy of formation of a nonideal solution. Relatively little data concerning the thermodynamic properties of ternary solutions are available. This is due mainly to the fact that obtaining ternary properties requires excessive numbers of experiments. However, the thermodynamic properties of most of the binary solutions are available, and some methods have been developed to obtain the thermodynamic properties of ternary solutions from the data of binary systems. These methods generally attempt to obtain ternary activity coefficients or excess free energy data by means of the application of the ternary Gibbs-Duhem equation (Appendix I)

The two most notable equations for determining the excess free energy of ternary systems from the data of binary solutions are Toop's and Kohler's equations[240](the details of derivation of these equations from the Gibbs-Duhem equation are given in Appendix I). Toop's equation is expressed as:

$$G^{XS}_{ABC} = \left[\frac{X_A}{1-X_B}G^{XS}_{AB} + \frac{X_C}{1-X_B}G^{XS}_{BC}\right]_{X_B} + (1-X_B)^2\left[G^{XS}_{AC}\right]_{\frac{X_A}{X_C}} \tag{6.18}$$

and Kohler's equation is written as:

$$G_{ABC}^{XS} = (1-X_C)^2 \left[G_{AB}^{XS}\right]_{\frac{X_A}{X_B}} + (1-X_B)^2 \left[G_{AC}^{XS}\right]_{\frac{X_A}{X_C}} + (1-X_A)^2 \left[G_{BC}^{XS}\right]_{\frac{X_B}{X_C}} \quad (6.19)$$

The definition and location of the terms in Equations 6.18 and 6.19 are given in Figure 6.3. Although these equations have been written for G^{XS}, they may also be applied in the calculation of ΔH and S^{XS} in an obvious manner.

The Toop and Kohler equations have been successfully used for the calculation of ternary thermodynamic properties from binary data. A list of the relevant literature can be found in the extensive review of Ansara[241].

Substituting Ni, Si, and Cr for A, B, and C respectively in Equations 6.14, 6.18 and 6.19, the Equation 6.17 for ternary Ni-Cr-Si using Toop's equation (Eq.6.18) for calculating G^{xs} yields:

$$\Delta G_{Ni-Cr-Si}^{M} = RT(X_{Ni}\ln X_{Ni} + X_{Si}\ln X_{Si} + X_{Cr}\ln X_{Cr}) + \left[\frac{X_{Ni}}{1-X_{Si}} G_{Ni-Si}^{XS} + \frac{X_{Cr}}{1-X_{Si}} G_{Si-Cr}^{XS}\right]_{X_{Si}} + (1-X_{Si})^2 \left[G_{Ni-Cr}^{XS}\right]_{\frac{X_{Ni}}{X_{Cr}}} \quad (6.20)$$

and using Kohler's equation G^{XS} can be written as:

$$\Delta G_{Ni-Cr-Si}^{M} = RT(X_{Ni}\ln X_{Ni} + X_{Si}\ln X_{Si} + X_{Cr}\ln X_{Cr}) + (1-X_{Cr})^2 \left[G_{Ni-Si}^{XS}\right]_{\frac{X_{Ni}}{X_{Si}}} + (1-X_{Si})^2 \left[G_{Ni-Cr}^{XS}\right]_{\frac{X_{Ni}}{X_{Cr}}} + (1-X_{Ni})^2 \left[G_{Si-Cr}^{XS}\right]_{\frac{X_{Si}}{X_{Cr}}} \quad (6.21)$$

Using Equations 6.5, 6.10, and 6.11 with respect to Equations 6.20 and 6.21

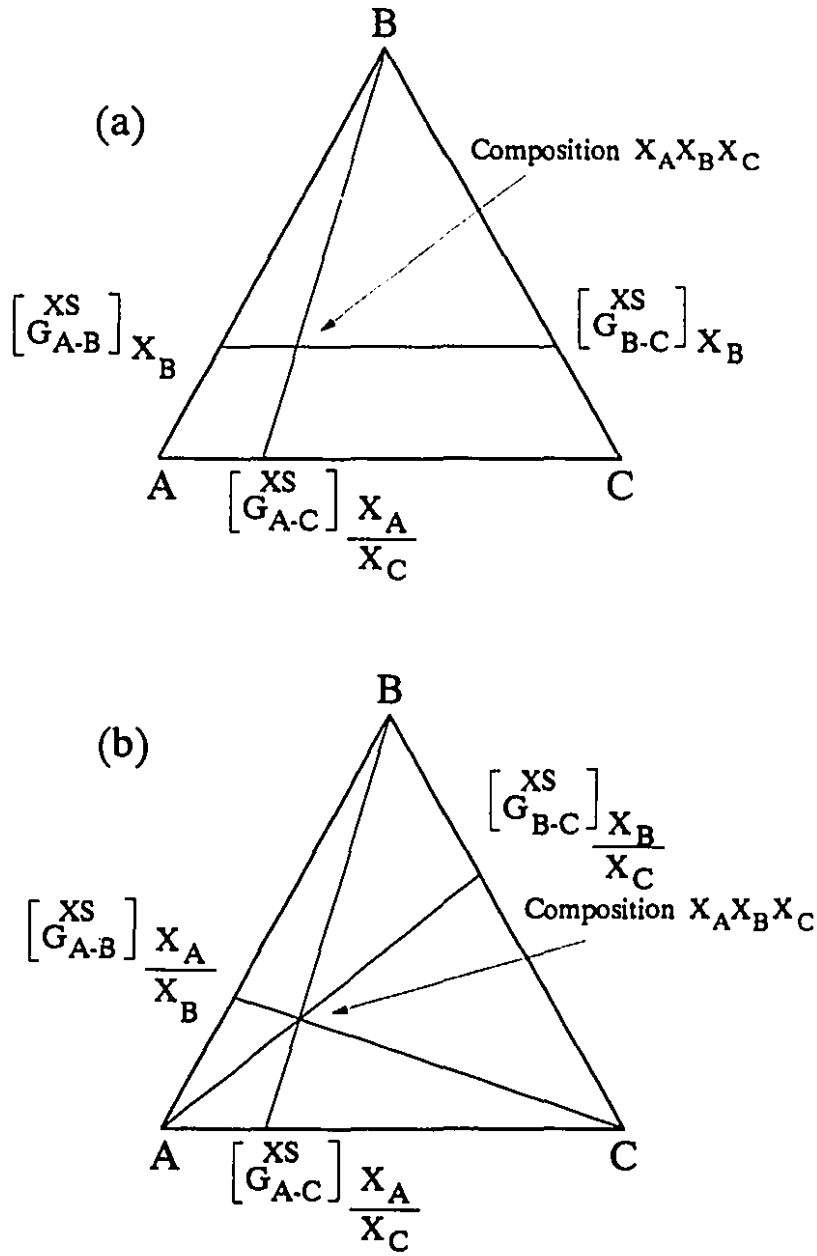

Figure 6.3 Illustration of the binary terms used in application of the (a) Toop, and (b) Kohler equations.[240]

the corresponding Gibbs energy change for Equation 6.4 was computed for $0.05 \leq X_{Si} \leq 0.95$ at intervals of $X_{Si}=0.05$. The thermodynamic data used through the computation together with the relevant literature references are presented in Table 6.1. From the Table, it can be seen that no ternary thermodynamic data were used in the calculations of the ternary Ni-Cr-Si system. In the case of the binary Ni-Cr system, G^{XS} was directly taken from the data in the literature, whereas, G^{XS} of the Ni-Si and Cr-Si systems for both the Toop and Kohler equations was calculated from the data of H^M and S^{XS} of those systems. It should be mentioned that the data for all the binary systems concerned are for the liquid alloys only and the standard state is the pure elemental liquid.

The standard Gibbs free energy change of decomposition of Si_3N_4 is given by:[242]

$$\Delta G^{\circ}_T = 740{,}568 + 24.09\ T\ logT - 402.9\ T \qquad J\ mol^{-1} \tag{6.22}$$

and the free energy change associated with the fusion of Si is:[243]

$$\Delta G_{Si_{s\rightarrow l}} = 50{,}530 - 29.99T \qquad J\ mol^{-1} \tag{6.23}$$

The corresponding Gibbs free energy change for Equation 6.4 as a function of X_{Si} in the starting alloy is presented in Figure 6.4. The program used to generate

Table 6.1 Thermodynamic data used in the modelling of the Si_3N_4/Ni-Cr-Si wetting system.

System	H^M ($Jmol^{-1}$)	S^{XS} ($Jmol^{-1}K^{-1}$)	G^{XS} ($Jmol^{-1}$)
Cr-Ni[244,245]	----	----	$-X_{Ni}X_{Cr}8368$
Cr-Si[246,247]	$X_{Cr}X_{Si}(177842X^2_{Si}$ $-223000X_{Si}-36400)$	$X_{Cr}X_{Si}(28.73-$ $26.56X_{Si})$	----
Ni-Si[248]	$-X_{Ni}X_{Si}(X_{Ni}259994$ $+X_{Si}133888)$	$-X_{Ni}X_{Si}(X_{Ni}62.01$ $+X_{Si}22.01)$	----

this figure along with a sample of the calculations is given in Appendix II.

An examination of Figure 6.4 will show that $\Delta G_r=0$ for $X_{Si}=0.255$ in the curve generated using Toop's equation and a value of $X_{Si}=0.24$ results in $\Delta G_r=0$ when using Kohler's equation. Thus, the Toop equation predicted that the Ni-Cr-Si

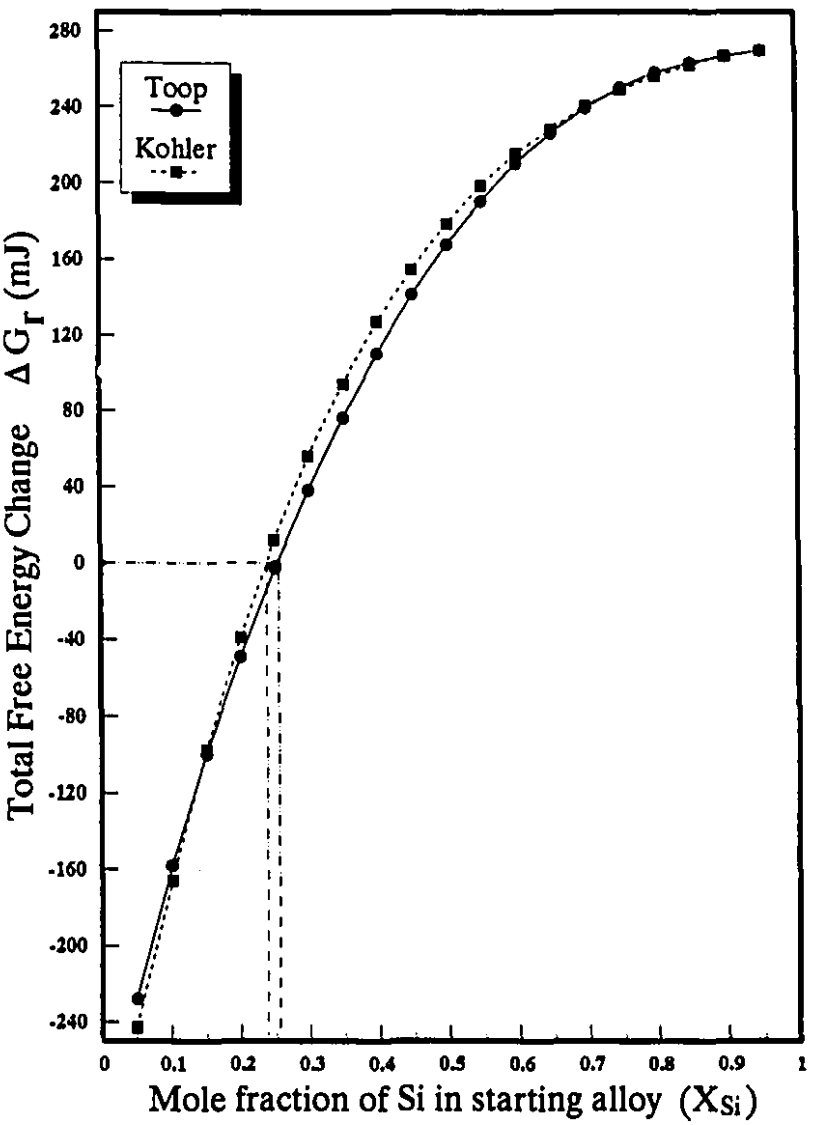

Figure 6.4 Variation of ΔG_r vs X_{Si} in the starting alloy.

alloy with a composition of 57.95 Ni-16.55Cr-25.5Si will be in thermodynamic equilibrium with Si_3N_4 and the Kohler equation predicted that the equilibrium composition would be 59.1Ni-16.9Cr-24Si.

6.2 Results of Wetting Experiments

To verify the predictions of the wetting model, wettability experiments were performed using the sessile-drop method. Figure 6.5 shows the liquid Ni-Cr-Si alloy

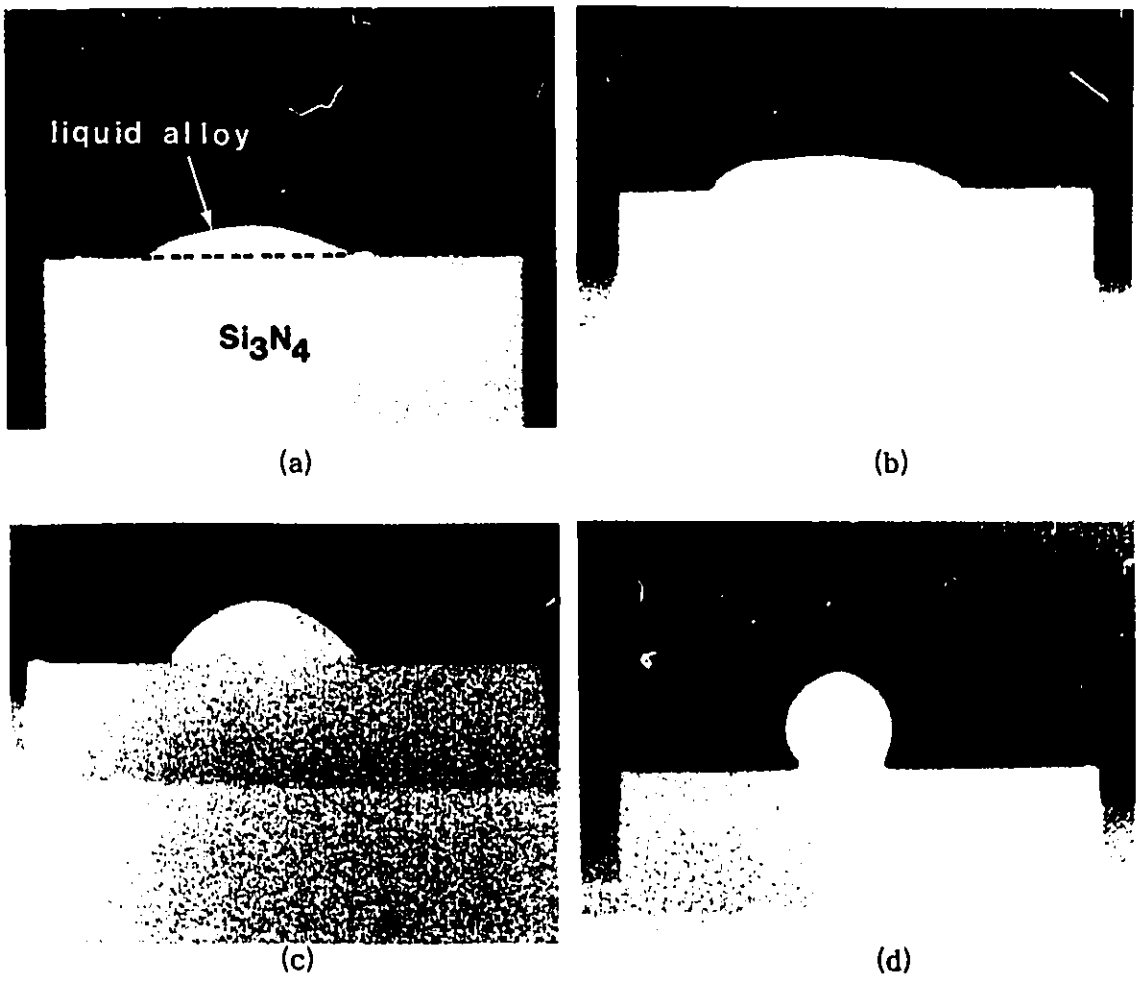

Figure 6.5 Photographs of liquid Ni-Cr-Si alloys after 10 min. contact with Si_3N_4 substrates at 1220°C, a) S10, b) S19, c) S25, and d) S30 alloy.

droplets with different compositions, in terms of Si contents (See Table 5.3), on the Si_3N_4 substrate. These photographs were taken after 10 min. contact between the liquid alloys and Si_3N_4 at 1220°C under a N_2 partial pressure of 15 Pa. which is the same condition as used in the thermodynamic calculations. It is quite obvious from Figure 6.5 that the alloys containing X_{Si}<0.3 will wet Si_3N_4, which conforms to the wetting model prediction particularly when using the Toop equation. This also confirms the assumption made concerning the influence of the Gibbs excess surface energy. This effect can be more clearly seen in Figure 6.6. Curve 1 in the Figure

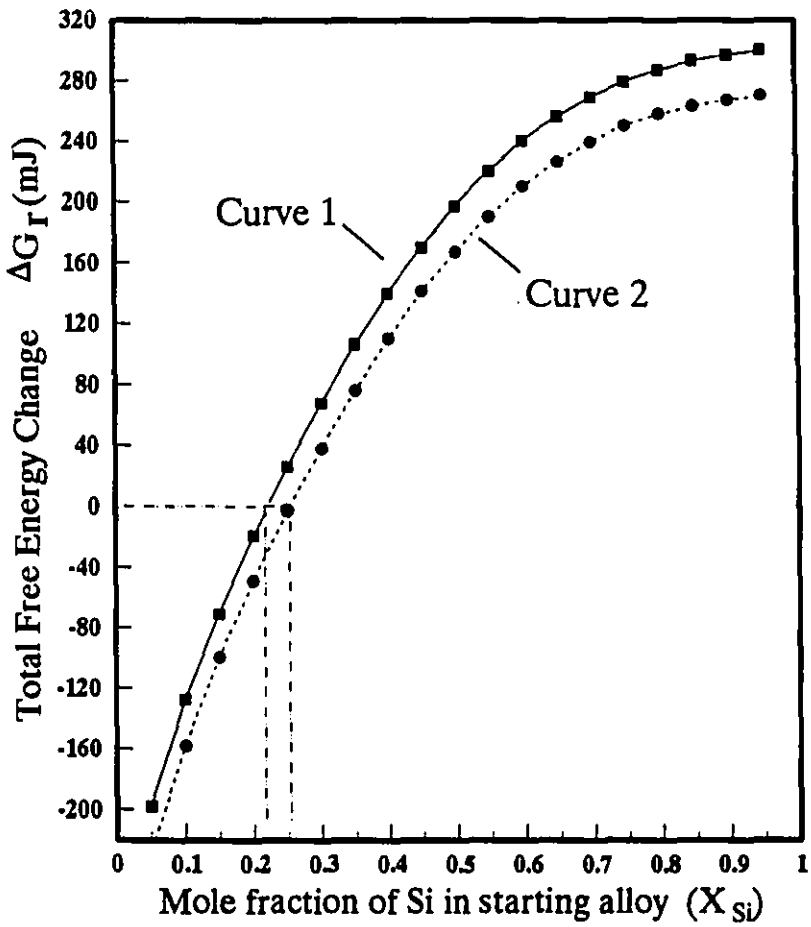

Figure 6.6 Variation of ΔG_r vs X_{Si}, showing the effect of surface excess energy on equilibrium Si content.

shows ΔG_r vs X_{Si} without taking into account the excess surface energy effect and curve 2 is the same as that illustrated in Figure 6.4 (when using Toop equation). Curve 1 in Figure 6.6 indicates that the Ni-Cr-Si alloy of X_{Si}=0.22 will be in thermodynamic equilibrium with Si_3N_4. In other words, alloys of X_{Si}>0.22 will not react with and wet Si_3N_4, which is not in agreement with the results of the wetting experiments.

6.2.2 Effect of N_2 Partial pressure

Another important factor in determining the degree to which a liquid Ni-Cr-Si alloy wets Si_3N_4, and reacts chemically with it, is the N_2 partial pressure (P_{N2}) in the environment. According to Equation 6.6, the higher the P_{N2}, the higher is the free energy change of dissociation of Si_3N_4. Therefore, at high P_{N2} the reaction between Si_3N_4 and the liquid alloy will be less viable and, for a given alloy composition the wetting of Si_3N_4 will be less likely to occur at higher N_2 partial pressure. The P_{N2} dependence of ΔG_r is illustrated in Figure 6.7. From the Figure it can be seen that a wetting-to-nonwetting transition occurs when the P_{N2} is increased. For instance, at $P_{N2}=10^5$ Pa for an alloy of X_{Si}=0.19, the value of ΔG_r will be +160 mJ, thus, this alloy is not expected to react with and wet Si_3N_4. The change of wettability with local atmospheric conditions around the drop was verified experimentally. The results demonstrate that S19 alloy which is able to adequately wet Si_3N_4 at a P_{N2} of 15 Pa (Figure 6.5), could not wet the ceramic when the P_{N2} raised to atmospheric pressure (Figure 6.8).

6.2.3 Effect of Alloy Composition

One of the major assumptions made in the wetting model was the dissolution of Si from Si_3N_4 into the liquid alloy to achieve a state of thermodynamic equilibrium. In fact this assumption explains the situation where the liquid is the active participant in the system as it changes to equilibrium composition. Based on this assumption, it is expected that the alloy compositions with low Si concentration

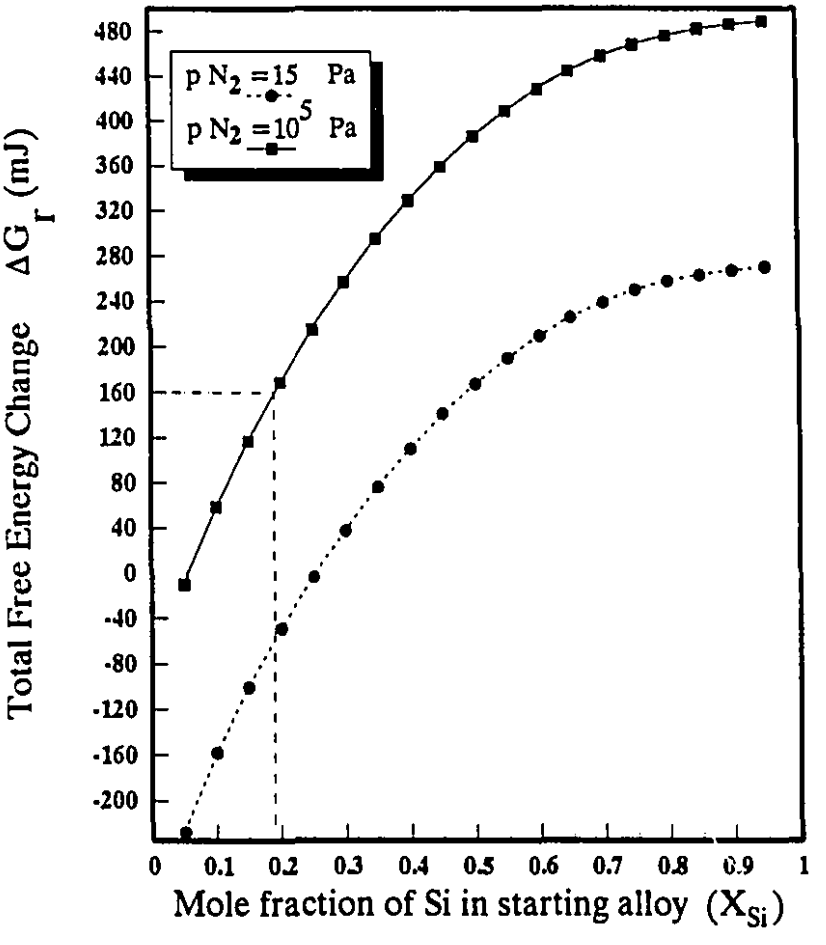

Figure 6.7 Variation of ΔG_r vs X_{Si}, showing the effect of N_2 partial pressure on equilibrium Si content.

will react to a higher degree with Si_3N_4 compared to an alloy whose Si content is close to the equilibrium value. To support this assumption, a Ni-20%Cr alloy with no Si was placed in contact with Si_3N_4. Figure 6.9 shows a SEM micrograph of the cross section through the middle of the solid drop. From the figure it is obvious that the alloy has extensively decomposed Si_3N_4 ($X_{Si\ (in\ the\ final\ alloy)}$=0.24). Hence, the depth of decomposition of Si_3N_4 is controlled by the Si content of the alloy.

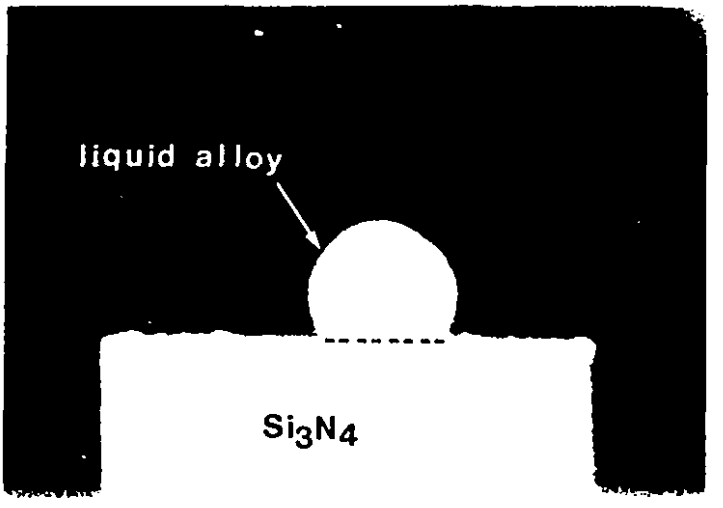

Figure 6.8 Photograph of S19 alloy on Si_3N_4 substrate at 1220°C and $P_{N2}=10^5$ Pa.

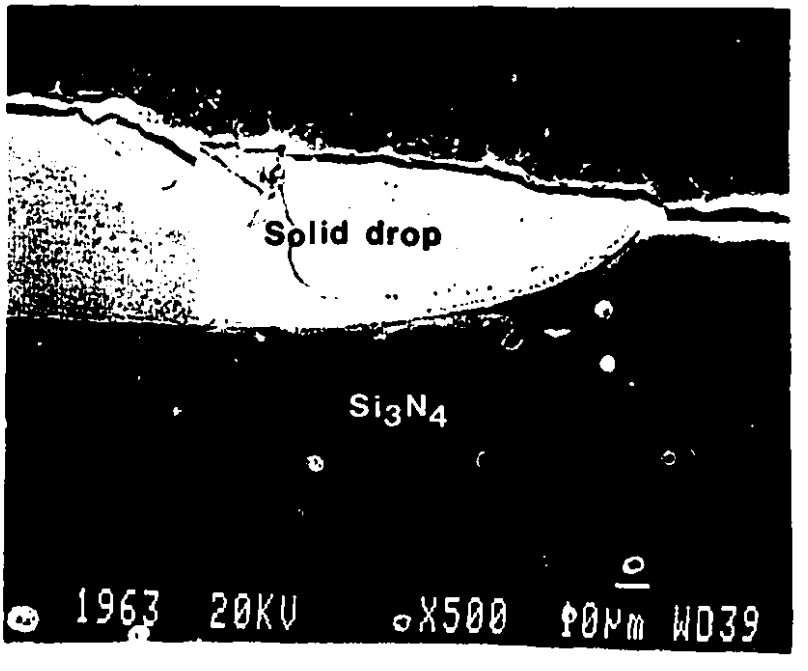

Figure 6.9 SEM image of a solidified Ni-20%Cr alloy on Si_3N_4 substrate.

6.2.4 Effect of Temperature

Variations of ΔG_r vs X_{Si} at two different temperatures, 1220 and 1300°C, are shown in Figure 6.10. From the figure, it can be seen that the a composition of X_{Si}=0.3 will be in thermodynamic equilibrium with Si_3N_4 at 1300°C. This indicates that, increasing the temperature, causes ΔG_r=0 to be shifted towards higher values of X_{Si}.

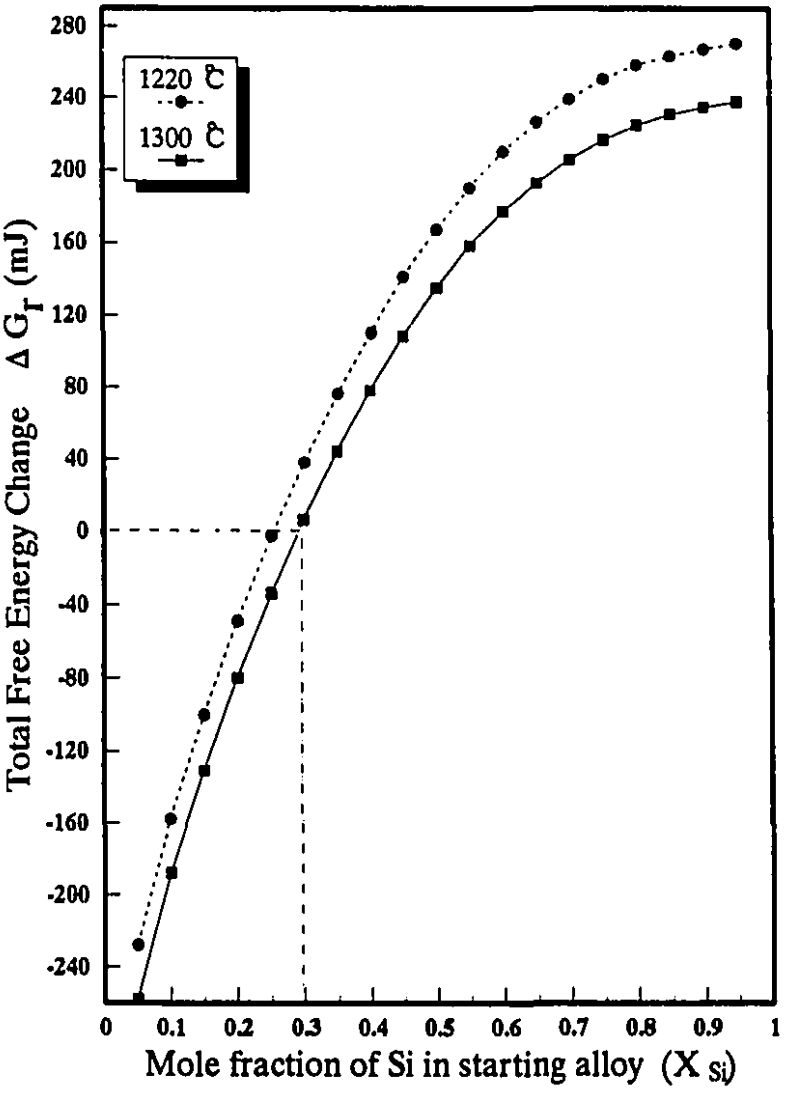

Figure 6.10 Variation of ΔG_r vs X_{Si}, showing the effect of temperature on equilibrium Si content.

A partial explanation of the variation of equilibrium composition with temperature is provided by Eq. 6.6. This equation indicates that the free energy change for the decomposition of Si_3N_4 decreases as the temperature is increased. Therefore, at higher temperatures, Si_3N_4 requires less energy to dissociate. This energy can then be supplied by a variation of Si content in the alloys with higher Si concentrations.

The experimental results showed that Si_3N_4 was wetted by an alloy of X_{Si}=0.3 at 1300°C (Figure 6.11), whereas, no wetting was observed at 1220°C (Figure 6.5).

6.2.5 Effect of Time

As mentioned previously, when a reaction occurs at the solid-liquid interface the free energy change per unit area per unit time will enhance wetting; in this case wetting is a time dependent phenomenon. The change of wettability with time is common in ceramic-liquid metal systems because several kinetic processes are often involved[249]. Although the present thermodynamic analysis does not include any discussion on the kinetics of wetting, experimental examinations showed that the wetting angle decreases with increasing time. The variation of contact angle (θ) with time from the sessile drop experiments for different alloy compositions is presented in Figure 6.12. The points on the graph result from measurements made

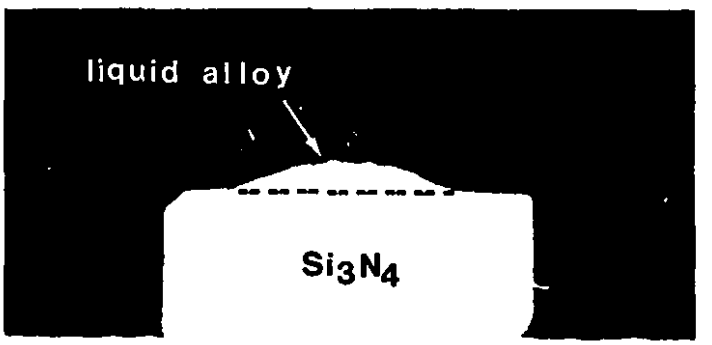

Figure 6.11 Photograph of S30 alloy on Si_3N_4 substrate at 1300°C and P_{N2}=15 Pa.

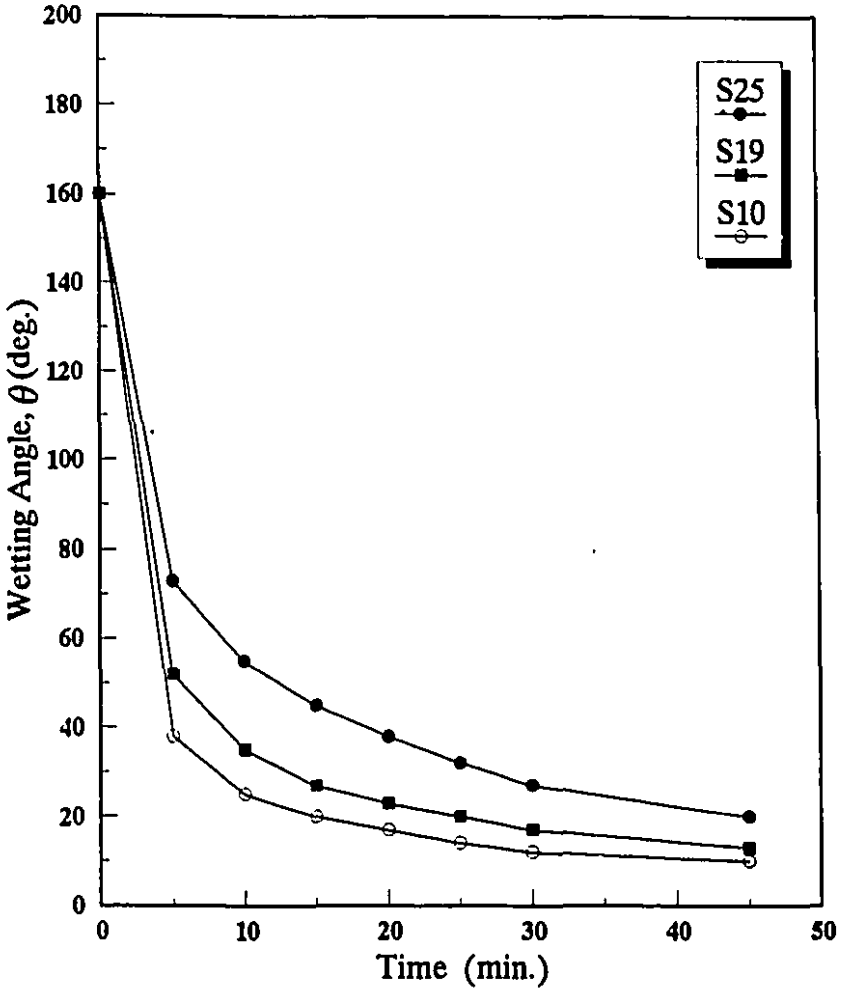

Figure 6.12 Time dependence of the wetting of silicon nitride by Ni-Cr-Si alloys at 1220°C.

at 5 min. time intervals. As was extensively discussed in Chapter 3, a variation of one of the three interfacial energies (γ_{lv}, γ_{sv}, and γ_{sl}) could, in principle cause a change of wetting angle. According to Young's equation (Eq. 3.10), under nonreactive conditions, wetting always occurs when $\gamma_{sv}>\gamma_{sl}>\gamma_{lv}$ and the driving force for wetting is thus $\gamma_{sv}-\gamma_{sl}$. When a reaction occurs between a solid and a liquid (Eq. 3.18), whether γ_{sv} is greater than γ_{lv} or not, the enhanced driving force for wetting by a reaction exceeds γ_{lv} and spreading occurs. This indicates that, in

reactive systems, the variation of γ_{lv} with composition will not significantly affect the wetting angle. Furthermore, in the present study, γ_{sv}, the surface energy of Si_3N_4, would remain practically constant. It is due to the fact that the surrounding atmosphere, particularly the oxygen partial pressure that may affect the γ_{sv} [238]is essentially fixed during the process. From the above, it can be concluded that the variation of θ in Figure 6.12 is due to the reduction of γ_{sl}, being directly linked to the solid/liquid interfacial reactions.

The change of wetting angle with time may be explained in terms of reaction kinetics in ceramic/metal system. For highly reactive systems the interfacial reactions proceed quickly after physical contact between the ceramic and the molten metal. In such instances, the contact angle drops rapidly in a short time. Further reductions of wetting angle will proceed at a slower rate until equilibrium wetting is achieved[250]. Figure 6.11 shows a strong reduction of wetting angle in the Si_3N_4/S10 system from ≈160° to 40° after 5 minutes and represents a state of a high interfacial reactivity due to the low concentration of Si in the alloy. For less reactive ceramic/metal systems, wettability is usually poor and the wetting process will advance at a slower rate and takes longer to reach equilibrium wetting[250,251].

6.3 Summary of Wetting at Si_3N_4/Ni-Cr-Si Alloys

A thermodynamic calculation has been performed to predict wetting at the Si_3N_4/Ni-Cr-Si alloy interfaces. The model was based on the assumption that wetting occurs when the change in total free energy of the reactions at the ceramic/metal interface is negative. It is due to the fact that metals are known to wet ceramics according to chemical wetting [194].

1. By using some simplifying assumptions and suitable scaling of the reaction, the model predicted that Ni-Cr-Si alloys with Ni/Cr=3.5 and X_{Si}<0.25 would react chemically with and wet Si_3N_4 ceramic. The equilibrium Si content, calculated using the Toop equation was found to be slightly different from the value using the Kohler

equation.

2. The predictions of the thermodynamic calculations were verified experimentally at 1220°C using different Ni-Cr-Si alloy compositions with Si contents ranging from X_{Si}=0.1 to X_{Si}=0.30. Good agreement was found between the theoretical calculations and experimental data.

3. The calculations showed that raising the temperature to 1300°C results in the equilibrium X_{Si} being increased to about 0.3. It was also found that the N_2 partial pressure under which the reactions take place would affect the wetting behaviour of Si_3N_4.

4. The results of the wetting experiments also confirmed the validity of the concept of treating wetting as a reaction between the liquid metal and the surface phase (instead of bulk phase).

From the above, it can be concluded that the theoretical approach based on chemical and solution thermodynamic principles, demonstrated here, is a useful analytical tool for predicting wetting at Si_3N_4/liquid metal interface.

Chapter 7

Si_3N_4/ Si_3N_4 Joining Experiments

In this chapter, the effect of brazing alloy composition on joint microstructure and microchemistry will be discussed for Si_3N_4-Si_3N_4 joining experiments. Strength testing and fractographic examination of experimental joints will also be presented.

7.1 Microstructural and Chemical Analysis of Experimental Si_3N_4-Si_3N_4 Joints.

This section includes the results of microstructural and microchemical examinations of Si_3N_4/Si_3N_4 joints formed with different Ni-Cr-Si alloy compositions in terms of the Si content ranging from 10 to 25 atom%. However, the emphasis will be on the joints made with X_{Si}=0.10 alloy, since they exhibited the highest strength relative to the joints made with other alloy compositions (See § 7.1.4).

7.1.1 Selection of the filler metals

Based on the prediction of the wetting model and wettability experiments,

Si_3N_4-Si_3N_4 brazing experiments were performed using different Ni-Cr-Si brazing alloys. Some of the alloys listed in Table 5.2, namely, S25, S19, and S10 were selected as filler metals for joining experiments (the numbers given in the alloy designations refer to their Si contents). The following criteria were considered in selecting these alloys:

a) Ni-Cr-Si alloys with $X_{Si}>0.25$ are not suitable for direct brazing, since these alloys do not wet Si_3N_4 under the experimental brazing conditions.

b) Based on wetting theory, angles of less than 90°are taken to represent a state of wetting. However, in practice, an angle of $\theta<15°$ to 20° is essential to ensure complete penetration of the brazing alloy into the joint. Better penetration of the filler metal into the joint is expected to reduce interfacial voids and thereby lead to stronger joints[252]. On the basis of the wettability studies, the above mentioned alloys, especially S10 exhibited lower contact angles.

Prior to any discussion on Si_3N_4/Si_3N_4 joint microstructure, it is preferable to examine the microstructure of the alloys located in the Ni-rich part of the Ni-Cr-Si ternary system. This examination will promote better understanding of experimental joint microstructure.

Figure 7.1 shows an isothermal section of the Ni-Cr-rich part of the Ni-Cr-Si system at 850°C[232,253]. Selection of this part of the system was due to the fact that all the experimental alloy compositions are located in this region along the line presented in Fig. 7.1. According to the phase diagram, the S19 composition consists of three phases, α-Ni_5Si_2, π, and γ which is a Ni-Cr-Si solid solution.

An optical micrograph of a sample with S19 composition is given in Figure 7.2. The sample was melted at 1200°C (which is about 65°C above the liquidus temperature of S19), and cooled at a rate of 1°C min^{-1} to 500°C, and then furnace cooled to room temperature. From Figure 7.2, three distinct phases can be identified. These phases are α (darker phase), γ (lighter phase), and the needle-

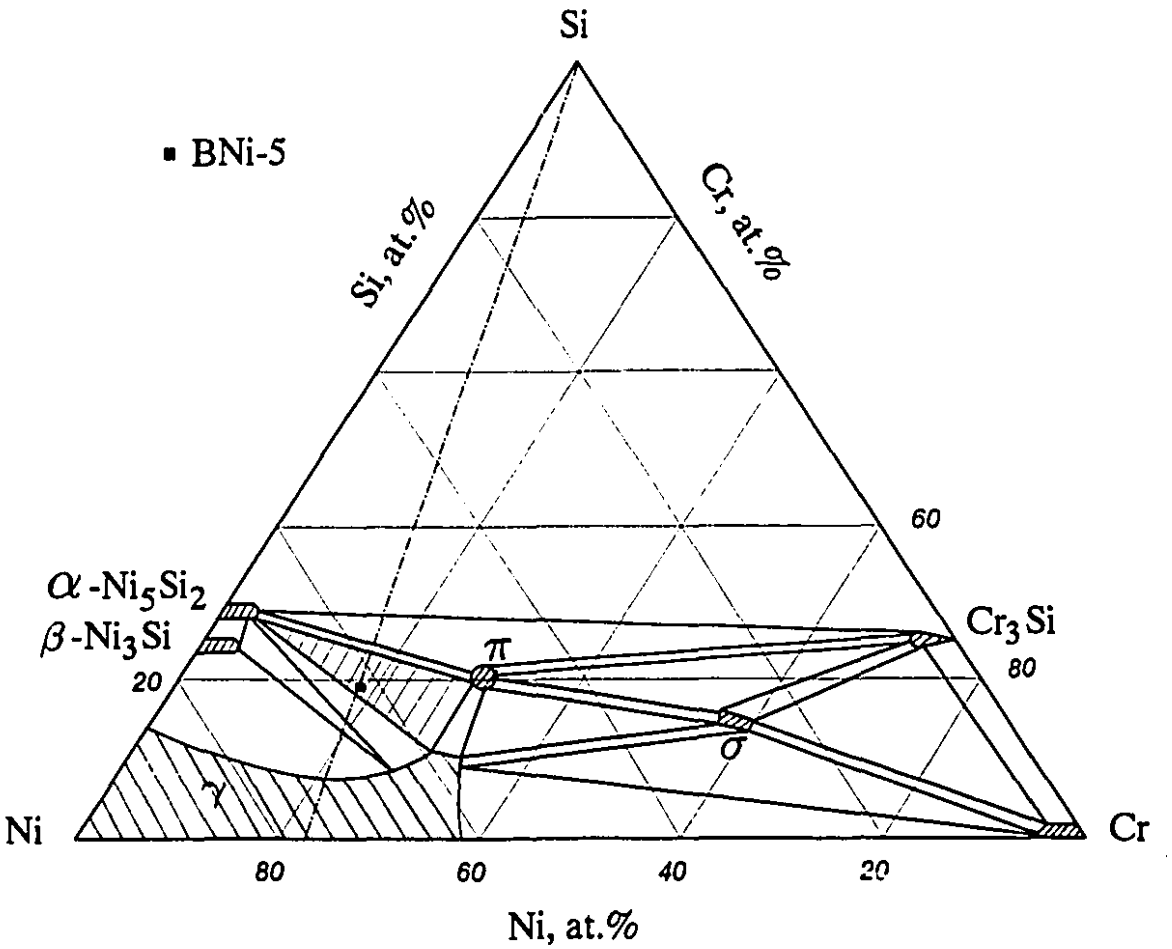

Figure 7.1 Subsolidus phase equilibrium for the Ni-rich region of the Ni-Cr-Si ternary system at 850°C.[234]

shaped π. Using EDS, the chemical analysis of the phases presented in Fig. 7.2 were found to be 69Ni-3Cr-28Si atom% (α) and 63Ni-24Cr-13Si atom% (γ). It should be mentioned that phase π was too fine to allow for quantitative analysis.

7.1.2 Microstructural and microchemical analysis of Si_3N_4/S19/Si_3N_4 joints.

Before any further discussion, it should be mentioned that the main reason

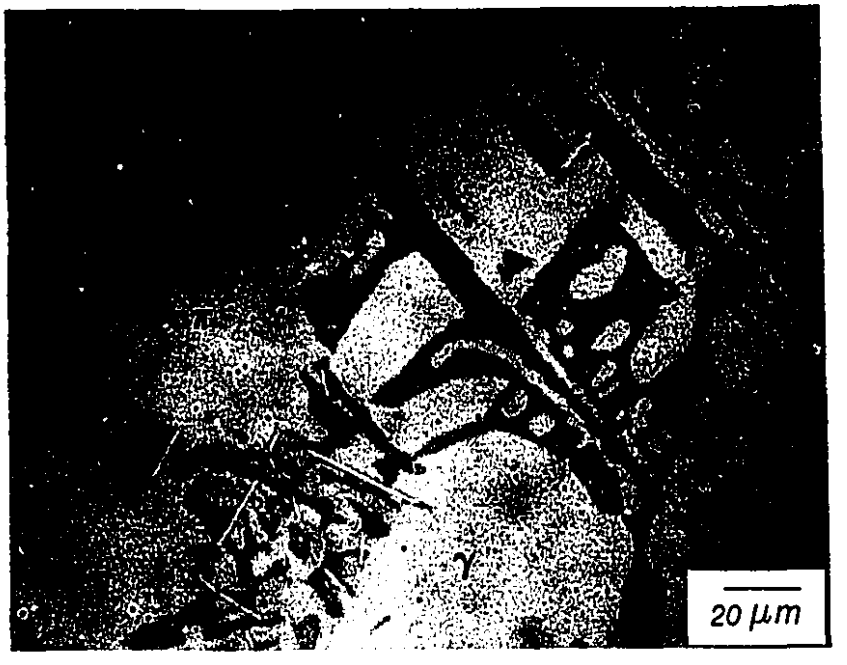

Figure 7.2 Optical micrograph of S19 alloy.

for starting with Si_3N_4/S19/Si_3N_4 joints was to first examine the joinability of commercial S19 brazing alloy and then to compare it with other modified alloys developed from the thermodynamic analysis.

Figure 7.3 depicts cross-sectional secondary electron image (SEI) micrographs of experimental joints brazed for 5, 10, and 15 min. using S19 brazing alloys. These joints were brazed at 1220°C and cooled at a rate of 10°C min^{-1} to room temperature. Figure 7.3 shows that all the silicon nitride couples have joined with no severe interfacial cracking and porosity. However, some transverse cracks due to the shrinkage of the filler metal are observed within the braze layer. From Figure 7.3, it can be seen that the joints formed using S19 exhibit almost identical microstructures consisting of a dark phase labelled "A" and a light phase labelled "B" irrespective of the brazing time. The concentration of phase A in all the joints is

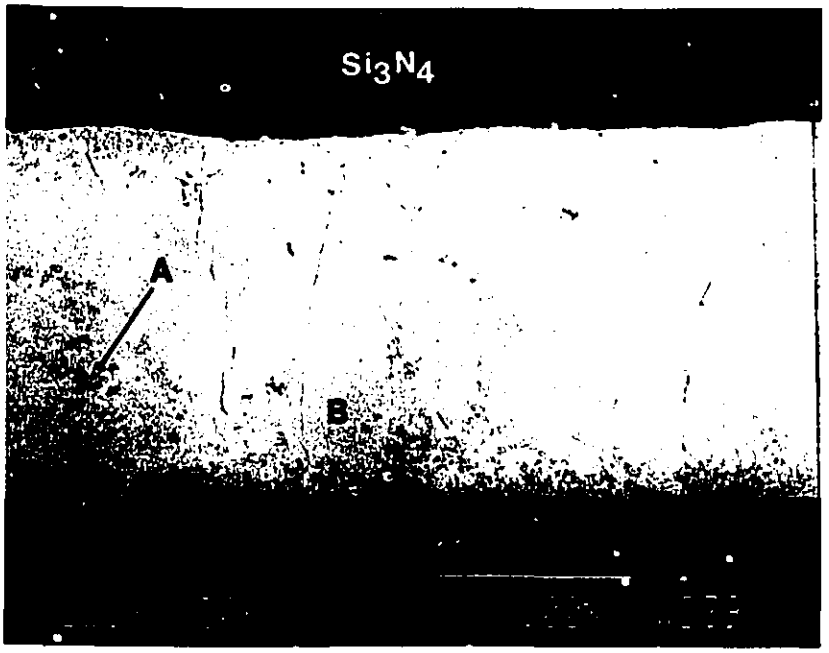

(a)

(b)

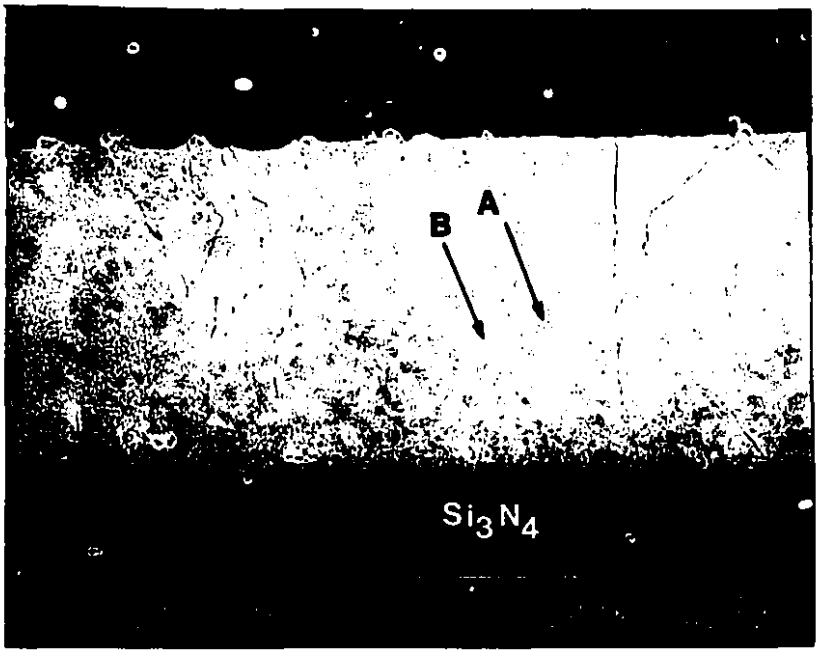

(c)

Figure 7.3 SEM micrographs of Si_3N_4/S19/Si_3N_4 joints, brazed for (a) 5 min, (b) 10 min., and (c) 15 min. at 1220°C.

higher in the area adjacent to the Si_3N_4/braze layer interface. The only detectable difference between them is the dispersion and concentration of the phase A and some variation in their microchemistries that will be discussed later.

It is obvious that the SEM micrographs of the braze layers presented in Figure 7.3 do not agree with the S19 microstructure given in Figure 7.2. Furthermore, optical examination of these joints revealed that the braze layer microstructure consists of four phases, three of which have already been identified in S19 microstructure (Figure 7.2) and the fourth one is phase A (Figure 7.4). In fact, the light phase labelled B in Figure 7.3, has a similar microstructure to S19 in which γ, α, and π (labelled as C, D, and E respectively) can clearly be identified (Fig. 7.4). However, because of the poor atomic contrast between α and γ (Fig. 7.3), these two

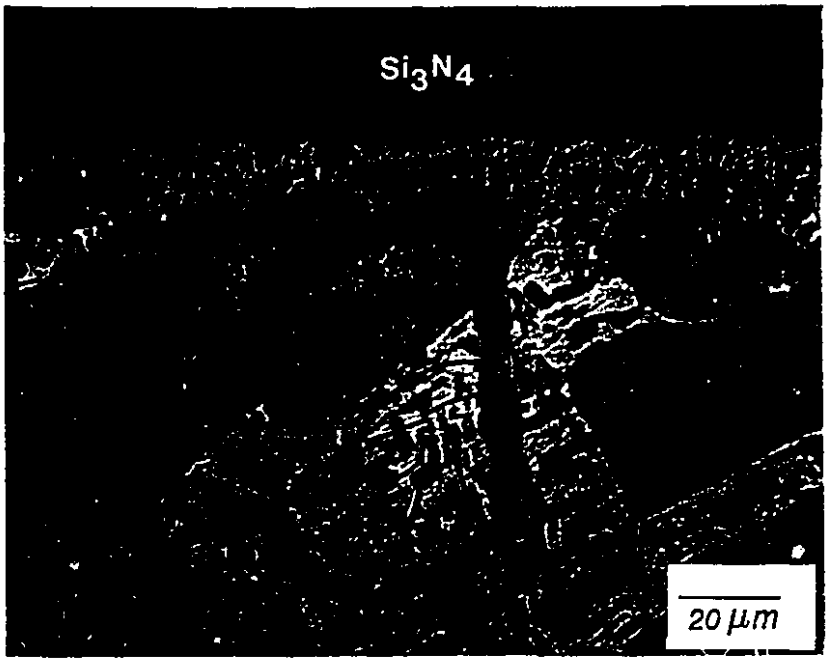

Figure 7.4 Optical micrograph of Fig. 7.3a

phases may not be clearly distinguished using scanning electron microscopy.

Table 7.1 summarizes the results of chemical analysis of the phases present in the joint microstructures given in Figures 7.3a and 7.4. The data presented in the table are the mean values of at least ten spot analysis on each phase in different locations within the braze layer (except for zone B, where area analysis was performed). It should be mentioned that phase E, which has the microstructure of π in S19, was too fine to analyze.

The overall composition of the braze layers in Figure 7.3 showed an increase in the Si from 20 to 23 atom% in going from 5 min. to 15 min. brazing time, whereas, the Ni/Cr ratio remained constant. These results, would tend to confirm the validity of the assumption made in the thermodynamic calculations in that there is a driving force for the reactant alloy to achieve the equilibrium composition of X_{Si}=0.25. However, the maximum brazing time of 15 min. appears to be insufficient

Table 7.1 WDS analysis of phases in Fig. 7.3a and 7.4 (all data are presented in atom%).

Phase	Ni	Cr	Si	N	Other	Remarks
A	27.8±0.4	42.5±1	13.2±0.6	16.7±0.7	0.3Al	
B	70.3±1.2	6.3±0.7	23.2±0.9	-	-	
C	64.0±0.5	23.4±0.3	12.6±0.3	-	-	γ
D	68.2±0.5	3.5±0.2	28.2±0.4	-	-	α-Ni_5Si_2 +{Cr}

for the alloy to attain a state of complete thermodynamic equilibrium. An examination of Fig. 6.12 shows that an equilibrium contact angle, which is also an indication of chemical equilibrium in the system, is not achieved within 15 min.

From the overall chemical analysis of Si_3N_4/S19/Si_3N_4 joints and examination of the Ni-Cr-Si phase diagram, it was found that the product alloy compositions lie within the shaded triangle shown in Figure 7.1. This indicates that all the product alloys must exhibit the same phase assemblage, which is in good agreement with the joint microstructure shown in Figure 7.3.

7.1.3 Microstructural and microchemical analysis of Si_3N_4/S25/Si_3N_4 joints.

Figure 7.5 illustrates that the SEI and optical micrographs of a Si_3N_4/Si_3N_4 joint brazed with the S25 alloy show a somewhat different joining behaviour. Unlike the former joints, the ceramic is debonded at the Si_3N_4/braze layer interface. The SEM micrograph (Fig. 7.5a) indicates that the braze layer microstructure is almost identical to that of the Si_3N_4/S19 joints brazed for the same time. However, some porosity was observed close to the ceramic/filler metal interface which is believed to be due to poor solidification. One possible explanation for this problem is that the brazing temperature of 1220°C might have been in the semi solid state particularly

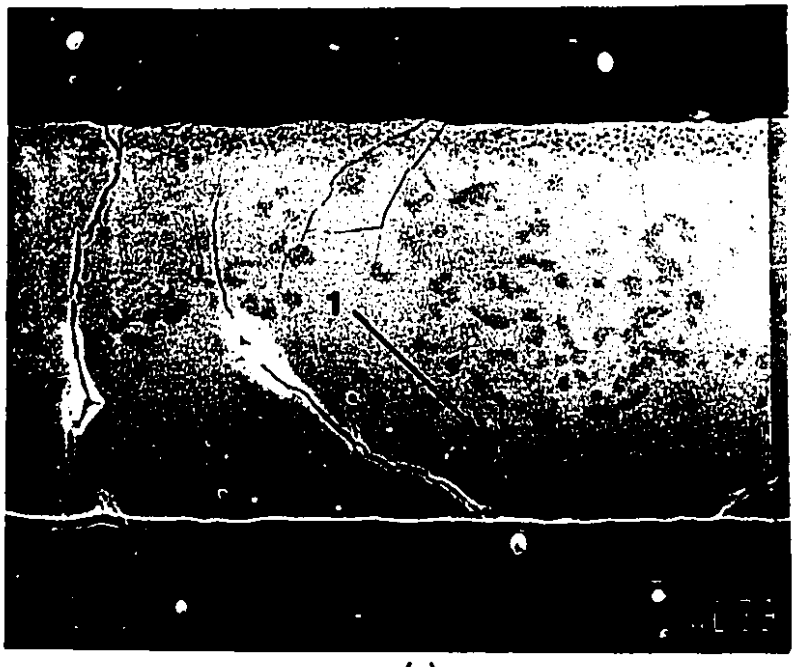

(a)

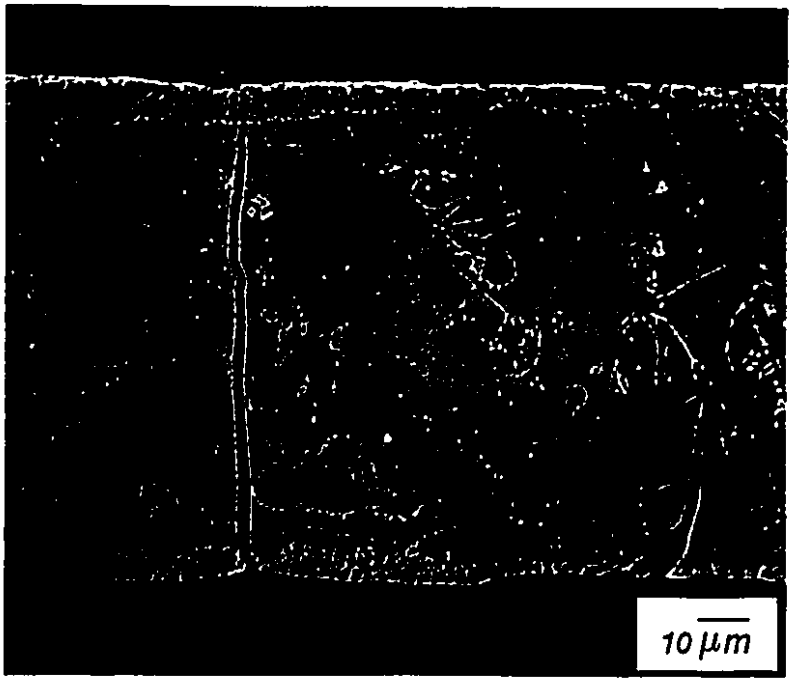

(b)

Figure 7.5 SEM (a) and optical (b) micrograph of Si_3N_4/S25/Si_3N_4 joint, brazed for 10 min. at 1220°C.

in the area close to the ceramic/filler metal interface, which has a different chemical composition from the centre of the braze layer. Another potential cause for the formation of this porous layer might be the evolution of N_2 gas which had not been dissolved into the brazing alloy. The optical image taken from the same sample (Fig. 7.5b) shows a different microstructure compared to Si_3N_4/S19 joints. As can be seen from Table 7.2, in this case, the braze layer consisted of a Ni-Cr-Si-N phase (labelled 1) with the same composition as phase A in the Si_3N_4/S19/Si_3N_4 joints, α-Ni_5Si_2 (labelled 2), a Cr_3Si phase (labelled 3), and phase π (labelled 4). From the overall composition of the braze layer and recalling the Ni-Cr-Si phase diagram, it is apparent that the phase assemblage in the braze layer conforms to the phase diagram.

The overall composition of the braze layer indicates that the product alloy composition is almost the same as the starting S25 alloy. However, a slight increase in the Si content of the product alloy from 25 to 26 atom% can be detected. Recalling the results of thermodynamic calculations, the Ni-Cr-Si alloy with $X_{Si}\approx25$ is in near equilibrium with Si_3N_4 at the brazing temperature. Therefore, it is not surprising that the alloy has not reacted extensively with the ceramic.

Although the mechanical properties of the joints will be discussed later in § 7.2, the primary source of the weak bonding at the interface of Si_3N_4/S25 alloy is the near-zero total Gibbs free energy of the reaction between the ceramic and the

Table 7.2 WDS analysis of phases presented in Fig. 7.5.

Phase	Composition (atom%)*	Remarks
1	Ni-42Cr-13Si-17N	
2	Ni-4Cr-27Si	α-Ni_5Si_2
3	Ni-71Cr-24Si	Cr_3Si
Overal braze layer	Ni-16Cr-26Si	

* Experimental error ± 0.4 atom%

metal, which can be translated into a low driving force for the S25 alloy to react and bond with Si_3N_4.

7.1.4 Microstructural and microchemical analysis of Si_3N_4/S10/Si_3N_4 joints.

Figure 7.6 illustrates the SEI images of Si_3N_4/Si_3N_4 joints brazed for 5, 10, and 15 min. at 1220°C using S10 composition. The overall appearance of the joints is somewhat similar to the joints produced using S19 brazing alloy (Fig. 7.3). The figure shows that the braze layers in all three cases consist of the dark phase denoted as "A" and the matrix phase denoted "B". However, some differences are observed. First, the concentration of the phase A is low in the centre of the braze and is high close to the Si_3N_4/braze interface especially for the joint brazed for 5 min. (Fig. 7.6a). Second, a reaction layer close to the Si_3N_4/braze interface is observed. This layer which is denoted as "RL" becomes thinner in going from 5 to 10 min. brazing time and disappears after the longer brazing time of 15 min.

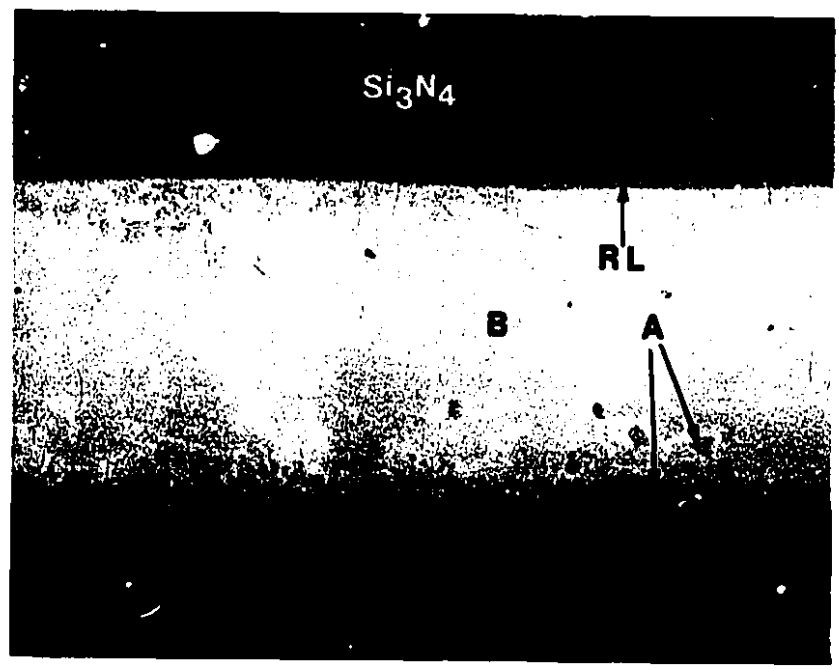

(a)

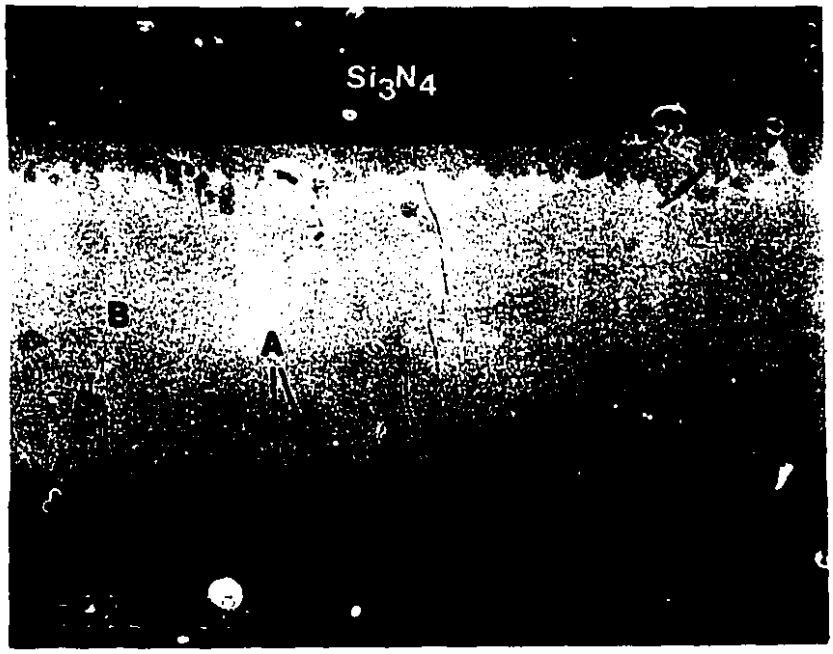

(b)

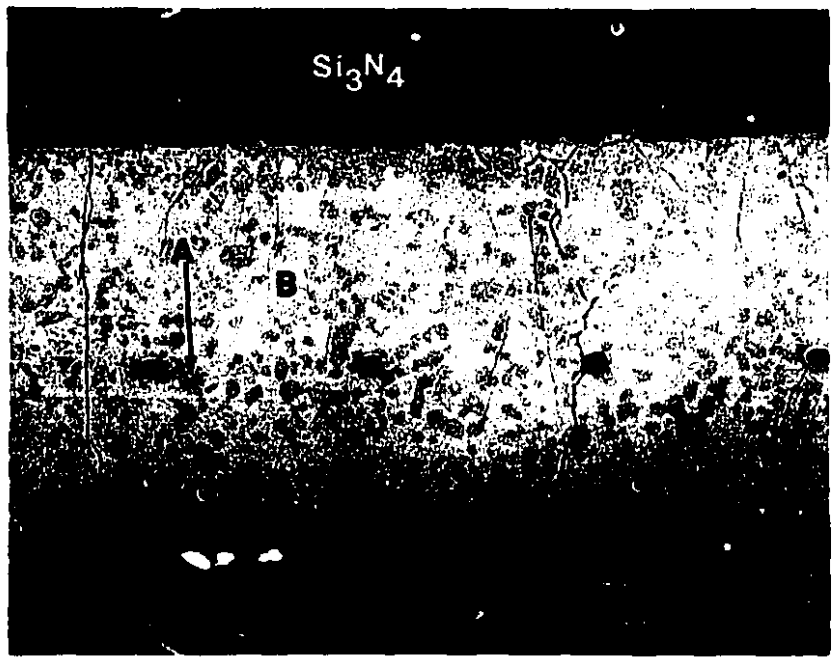

(c)

Figure 7.6 SEM micrographs of Si_3N_4/S10/Si_3N_4 joints, brazed for (a) 5 min, (b) 10 min., and (c) 15 min. at 1220°C.

Figures 7.6a and b also show that the centre of the braze layer was not notably affected by the brazing process. However, a significant amount of phase A, such as that identified in Si_3N_4/S19 joint (Fig. 7.3), had formed within the braze layer of the joints obtained after 15 min. brazing time (Fig. 7.6c). As given in Table 7.3, and will be discussed later, the composition of this phase was found to be Ni-42Cr-13Si-17N-0.7Al atom%. This indicated that almost all of the nitrogen from decomposition of Si_3N_4 had concentrated in the area close to the interface in the 5 min. brazed joints, whereas, in the 15 min. joints, there was sufficient time for the N to migrate into the braze to form phase A throughout the microstructure.

Figure 7.7 illustrates a SEI and an optical micrograph from the joint brazed for 5 min. (Fig. 7.6 a), showing the Si_3N_4/braze interface at higher magnification. Figure 7.7a clearly shows the presence of a reaction layer which had formed on the Si_3N_4 side of the original Si_3N_4/filler metal interface.

Table 7.3 presents the results of wavelength dispersive spectrometry (WDS) microchemical analysis of the phases shown in Figures 7.6a and 7.7. The table shows that the reaction layer (RL) is rich in N and Cr with a trace of Al and Y, resulting from the decomposition of Si_3N_4. In addition, the reaction layer contains about 3 atom% Ni and 4 atom% Si which may be due to the overlapping of the spot with the braze layer and Si_3N_4 during the analysis. The composition of the reaction layer can be written as $(Cr_{0.42}Ni_{0.03}Si_{0.04})N_{0.47}$ which may be considered as a quasi-stoichiometric CrN.

The electron probe micro analyzer (EPMA) scan across the Si_3N_4/braze joint (presented in Figure 7.7) is given in Figure 7.8. The lines were generated using a scanning step of 1 μm. Figure 7.8 suggests a high concentration of Cr and N in the reaction layer. It also contains some Ni and Si. The concentration of Al and Y in the reaction layer is almost the same as the base Si_3N_4 ceramic, and decreases to zero upon reaching the braze. As can be seen in Figure 7.8, the Cr level in the reaction layer is similar to that in the adjacent phase (A), and then decreases sharply to about 15% which is the mean concentration of Cr in zone B. The low concentration

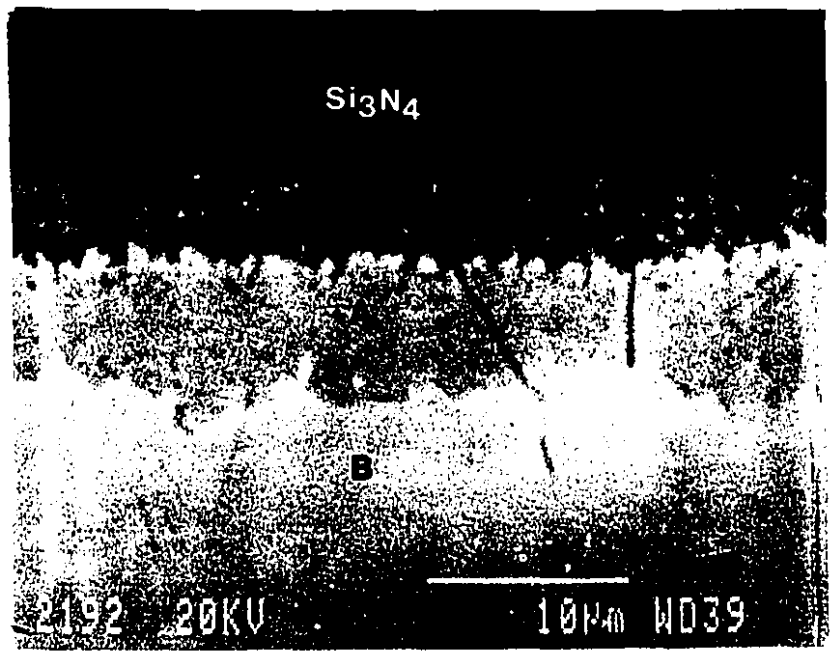

(a)

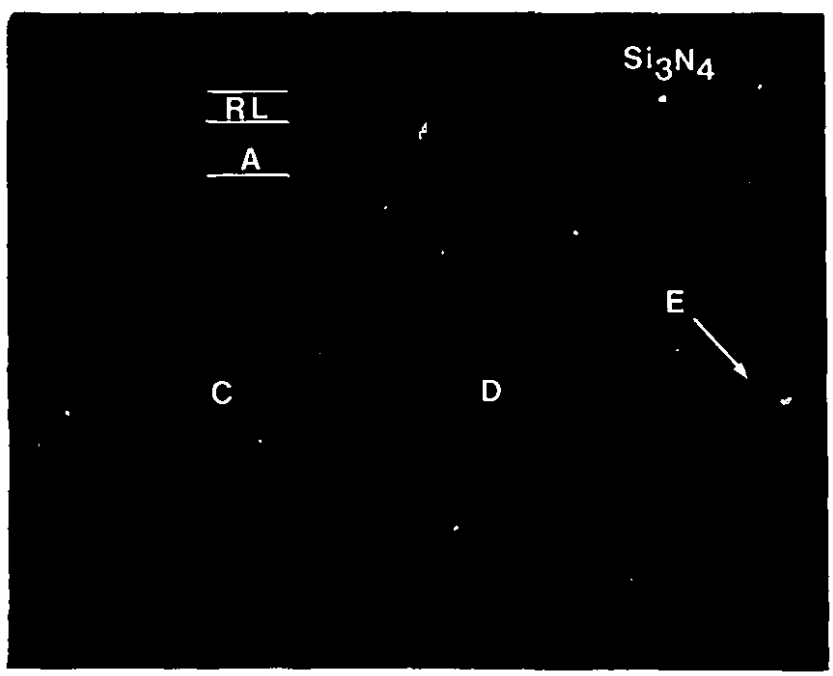

(b)

Figure 7.7 Higher magnification SEM (a) and optical (b) micrographs of Figure 7.6a.

Table 7.3 Chemical analysis of the phases in Si_3N_4/S10/Si_3N_4 joints brazed for 5 min.

Phase	Composition (atom%)
A	Ni-42Cr-13Si-17N-0.7Al
B	Ni-15Cr-19Si
C	Ni-23Cr-13Si
D	Ni-4Cr-27Si
E	N/A
RL	Ni-42Cr-4Si-47N-2.5Al-0.7Y
Overall braze Layer	Ni-17Cr-17Si-7N-0.2Al

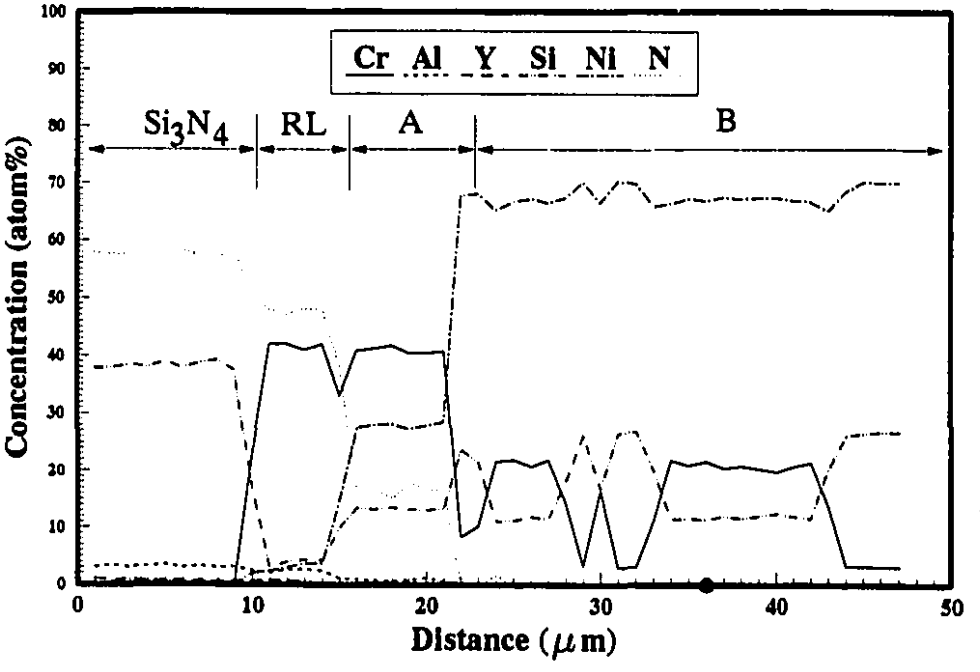

Figure 7.8 EPMA microanalysis line profiles across the joint area given in Fig. 7.7a.

of Si, and particularly Ni in phase A indicates that these elements have been rejected away from this zone. As per Si_3N_4/S19/Si_3N_4 joints, formation of phase A is due to the diffusion of N from ceramic side into the braze. From Figure 7.8, no detectable diffusion of Ni and Cr into Si_3N_4 was observed.

The WDS dot mapping of the region shown in Figure 7.7a (Fig. 7.9), provides an overview of the elemental distribution within the joint area. Again, it demonstrates the high concentration of Cr and N in the reaction layer adjacent to the Si_3N_4, as well as in phase A. Figure 7.9 also presents additional evidence of the low concentration of Ni and Si in the reaction layer and phase A. The formation of CrN was also supported by microhardness measurement on the reaction layer as well as other phases present in Figure 7.7. As shown in Table 7.4 the hardness of the reaction layer was found to be HV≈1200 which conforms to the published value for CrN.[254]

In summary, the main observations are: (a) the formation of a CrN reaction layer at the ceramic/braze interface for short brazing times, and (b) the dissociation of the reaction layer after longer brazing time of 15 min. In order to achieve a better understanding of this behaviour, one must consider the reactivity of Si_3N_4 with both Ni and Cr. The following reactions are considered between the Si_3N_4 and Cr:[181]

Table 7.4 Microhardness values of the phases in Fig. 7.7.

Phase	Load (g)	HV	Standard deviation*
Reaction layer	10	1200	100
A	25	860	40
C	25	490	25
D	25	960	25

* For at list five measurement on each phase.

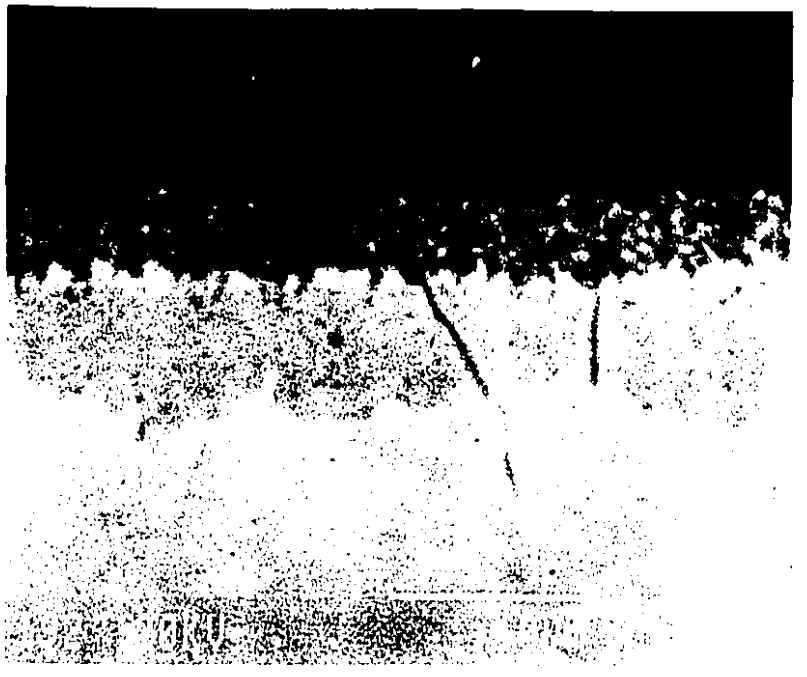

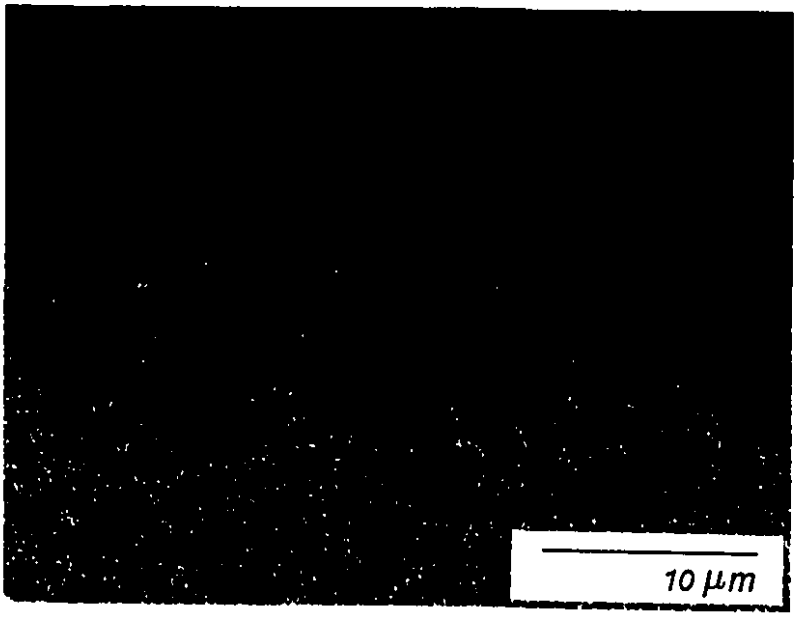

(Ni)

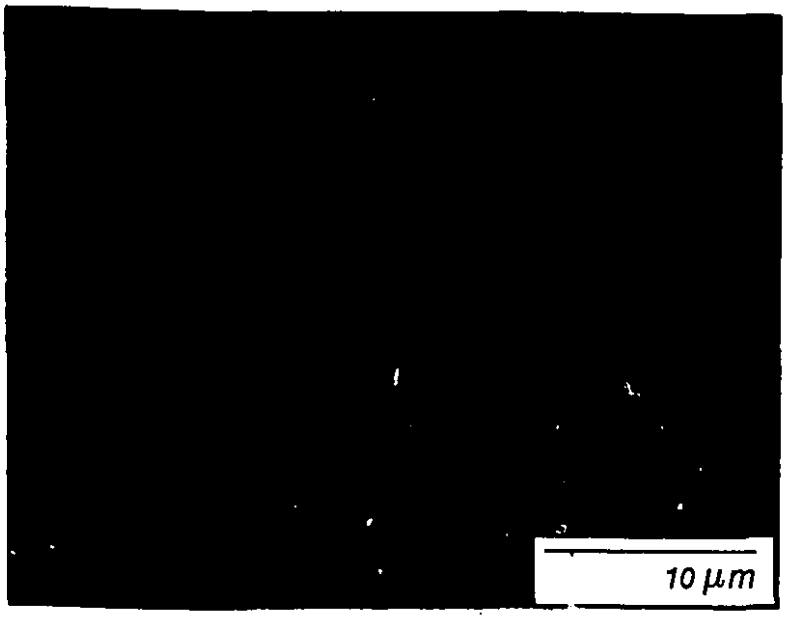

(Cr)

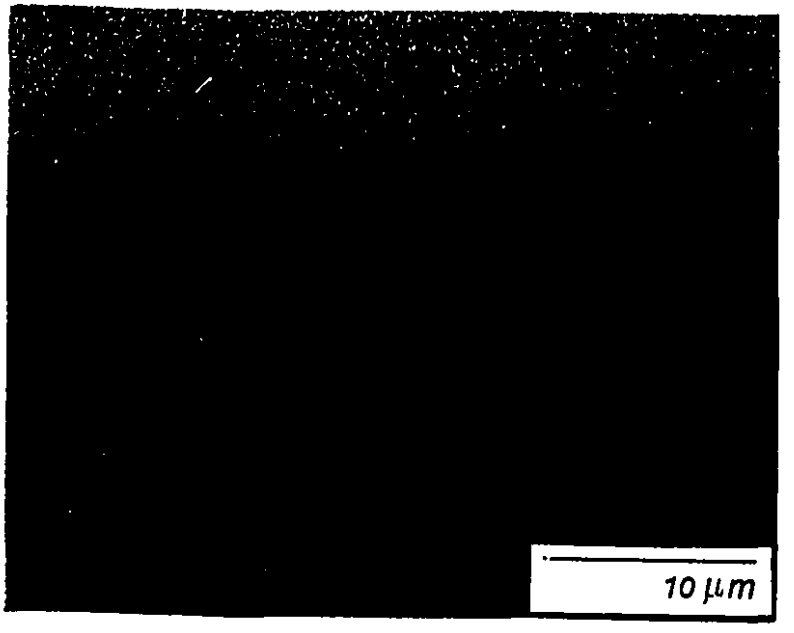

(Si)

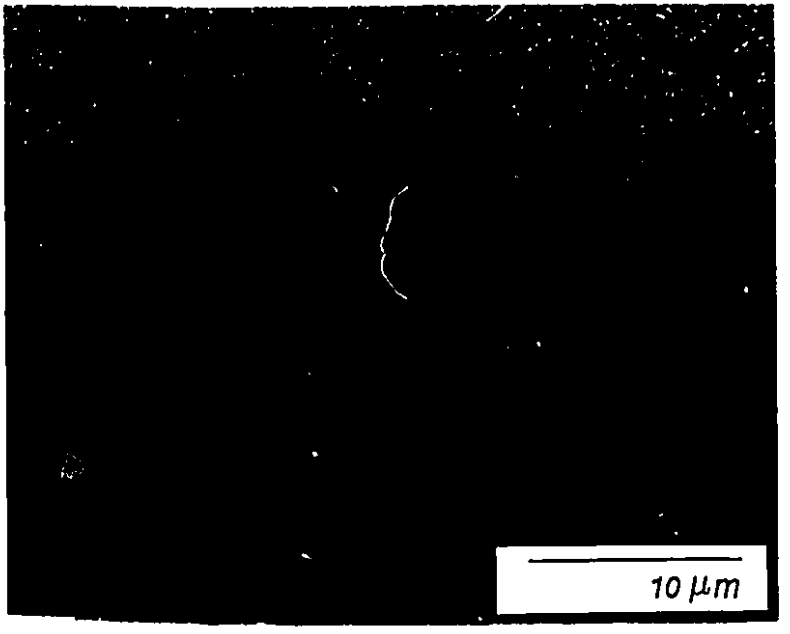

(N)

Figure 7.9 WDS compositional dot maps within the area in Fig. 7.7a.

$$Si_3N_4 + 4Cr = 4CrN + 3Si \quad \text{(a)}$$

$$2Si_3N_4 + 11Cr = 8CrN + 3CrSi_2 \quad \text{(b)}$$

$$2Si_3N_4 + 19Cr = 8Cr_2N + 3CrSi_2 \quad \text{(c)}$$

$$Si_3N_4 + 17Cr = 4Cr_2N + 3Cr_3Si \quad \text{(d)}$$

$$Si_3N_4 + 13Cr = 4CrN + 3Cr_3Si \quad \text{(e)}$$

The free energy changes for the reactions (a) through (e) with temperature are given in Figure 7.10. The figure was generated using the (F*A*C*T) system. From Figure 7.10, it can be seen that under atmospheric pressure, and when the activity of all the species has been taken to be unity, only the reaction "d" can

1220°C. However, the stability of Cr_2N and CrN depends on both N_2 pressure and the activity of Cr; when the Cr activity is high, the more stable phase at atmospheric pressure or lower is Cr_2N. On the other hand, when the Cr activity is low, at high P_{N2}, the more stable phase would be CrN and therefore reaction (e) would be more favourable.[182]

As mentioned previously, all the brazing experiments have been performed under a N_2 pressure of 15 Pa. Thus, from the above discussion and respecting the low P_{N2} pressure in the experimental environment, even at a_{Cr}=1 the formation of CrN is theoretically unlikely to occur. However, the experimental observations confirmed the formation of CrN at the interface.

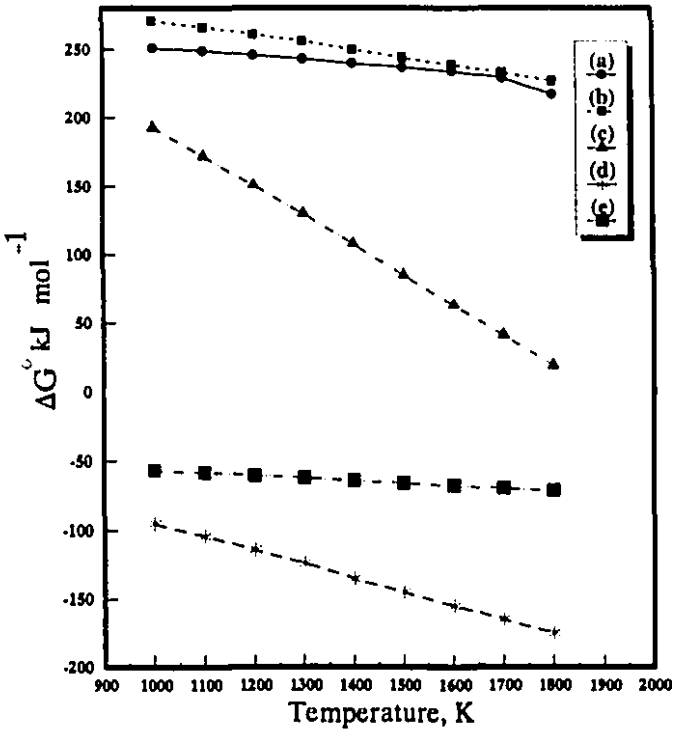

Figure 7.10 Free energy change for reactions (a) through (e) as a function of temperature.

In understanding why CrN forms when vacuum brazing, one must consider both the Cr activity and the environmental change that occurs during the dissociation of Si_3N_4. It is therefore necessary that the Cr activity be estimated in the brazing filler metal. Using solution thermodynamics theory, the Cr activity in the ternary S10 alloy was calculated to be a_{Cr}=0.26 (Appendix III). For better understanding of the effect of a_{Cr} and P_{N2} on the formation of CrN at the brazing temperature Figure 7.11 was generated using the F*A*C*T system. From Figure 7.11, when a_{Cr}=0.26, formation of CrN requires a N_2 pressure of about 0.8 MPa, which is orders of magnitude higher than the N_2 pressure in the joining atmosphere. However, the reaction between the liquid alloy and the ceramic that results in dissociation of Si_3N_4 into Si and N, could increase the local N_2 pressure at the Si_3N_4/braze interface. Although the pressure of liberated nitrogen at the interface

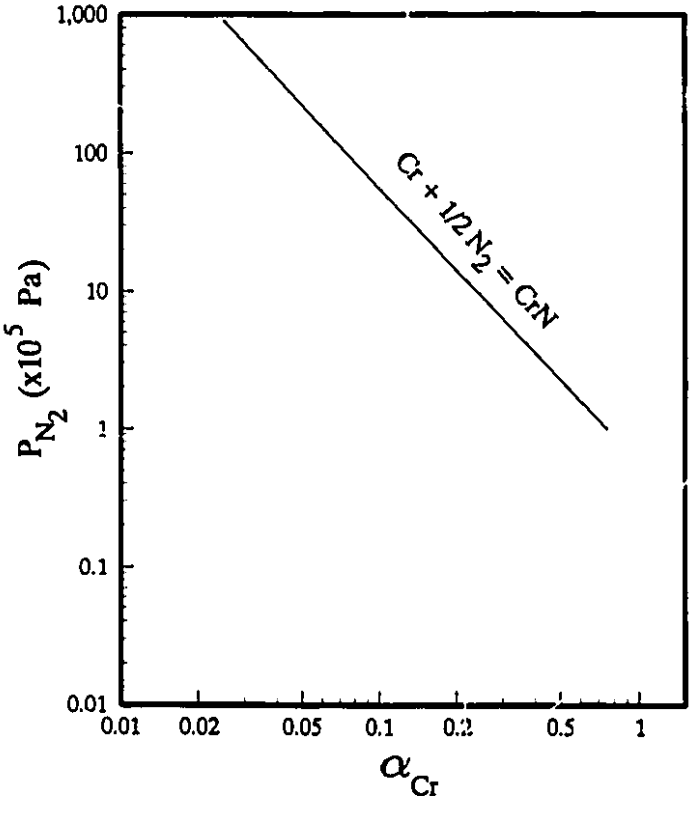

Figure 7.11 Effect of Cr activity and P_{N2} on stability of CrN at 1220°C.

cannot be measured, the local N_2 that became trapped in the interface must have been so high that there was sufficient pressure to stabilize CrN. It should be mentioned that in generation of Figure 7.11, the activity of CrN was taken to be unity. However, according to Equation 7.2, the presence of any impurities in CrN would lower its activity, hence, lowering the required P_{N2} to stabilize CrN.

$$Cr + \frac{1}{2}N_2 = CrN \tag{7.1}$$

$$\Delta G^\circ = -PT \ln \frac{a_{CrN}}{a_{Cr} \cdot P_{N_2}^{\frac{1}{2}}} \tag{7.2}$$

Once CrN forms, in other words, when the reaction between the ceramic and filler metal proceeds towards the equilibrium composition in terms of the Si content, the local N_2 pressure will drop to lower a value. Under this condition, the preformed CrN reaction layer is no longer thermodynamically stable. The investigation of Schuster[178] showed that in Cr-N system in the absence of external N_2 pressure (even if it is as low as 1 Pa) chromium nitride is not stable above 1000°C. Thus, as the brazing process continues, the reaction layer starts to decompose to N_2 +(Cr). This phenomena is clearly evident in Figure 7.6 where the reaction layer becomes thinner after 10 min. and began to disappear after a longer brazing time of 15 min.

Although the kinetics of the interfacial reaction has not been studied, the time dependency of the wetting angle (Fig. 6.12) may provide further information in order to gain a better understanding of the interfacial reactions. From Fig. 6.12, the sharp decrease of the wetting angle in Si_3N_4/S10 system indicates that severe reactions take place at the ceramic/metal interface in a short contact time of 5 min. It may also be explained by examination of the chemical composition of the product alloy in terms of Si content for the different brazing times shown in Figure

7.12. The figure indicates the severity of the reaction between the ceramic and the filler metal during the first minutes of the brazing process, leading to the enrichment of Si in the product alloy. Figure 7.12 also presents additional evidence that the brazing alloy is driving towards the equilibrium Si content of 25 atom%, predicted by the wetting model.

The formation of CrN in the Si_3N_4/Ni-Cr alloy joints has been observed in other studies. The investigation of Peteves *et al.*[182] in solid-state bonding of Si_3N_4-to-Si_3N_4 using a Ni-20%Cr alloy showed that a reaction layer of CrN had formed between the Cr-precoated or uncoated ceramic and the alloy at 1150°C when applying 100 MPa for 1 hour. In another investigation by Nakamura and Peteves,[181] Cr nitrides were identified as the interfacial reaction products.

The microchemical and phase analysis of all the Si_3N_4/Ni-Cr-Si/Si_3N_4 joints revealed that no Ni nitride had formed within the joint area. An examination of Ni-N system shows that N_2 is insoluble in and does not react with Ni at temperatures up to 1400°C. However, there is some evidence for a slight solid solubility of N in Ni of up to 0.3 at%[236].

The solubility of N in liquid Cr is about 4 wt% (12-13 at%),[236] whereas, solid chromium at 900°C absorbs 13.7 wt% (≈37 atom%) nitrogen.[255] It is therefore not surprising that a value of about 16 atom% nitrogen was found in phase A.

From all the above, it can be stated that Cr was found to be the most reactive element in the Ni-Cr-Si brazing alloys used for the brazing experiments.

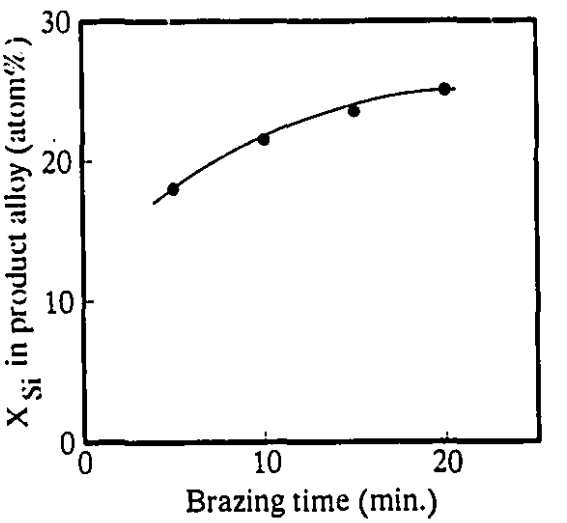

Figure 7.12 Variation of X_{Si} in product alloy vs brazing time in Si_3N_4/S10/Si_3N_4 joints.

7.2 Four-point Bend Strength of Si_3N_4-Si_3N_4 Joints.

7.2.1 Room-temperature MOR bars.

The room-temperature four-point bend values of the Si_3N_4-Si_3N_4 joints brazed at 1220 °C for 5 and 10 min. using S10, S19, and S25 alloys are presented in Table 7.5. The values given in the table are the average of at least six measurements.

As depicted in Table 7.5, the brazing alloy composition has a significant influence on joint strength. The table shows that as the Si content of the brazing alloy increases, the joint strength decreases. It can be seen that the average strength of Si_3N_4 brazements made with the S10 alloy for 10 min. brazing time is almost ten times that of the joints made with S25 alloy. The data also points to the brazing time dependency, since the S19 joints brazed for 10 min. exhibited a marginally higher strength in comparison to those joints brazed for shorter times. However, the strength of S10 joints brazed for 5 min. were found to be significantly

Table 7.5 Room-temperature four-point bend strength of Si_3N_4/Ni-Cr-Si/Si_3N_4 joints.

Brazing alloy composition	Brazing time (min.)	Joint strength (MPa)
S10	5	118±31
	10	95±22
	15	55±18
S19	5	18±7
	10	25±10
S25	5	No bonding
	10	10±6

higher than those joints brazed for longer times. These observations give rise to the following questions:

a) Why do the joint strengths decrease as the Si content of the brazing alloys increase?

b) What is the source of increase in joint strength as a result of shorter brazing time for Si_3N_4\S10\Si_3N_4 joints?

Although discussed in the next section, the most plausible explanation for (a) is the higher driving force for the alloys of low Si content to react with Si_3N_4, and for (b) is the formation of a CrN reaction layer at the ceramic/filler metal interface for the 5 min. brazed S10 joints. This layer, which is believed to be responsible for the high strength between Si_3N_4 and the alloy disappeared in going from 5 to 15 min. brazing time.

7.2.1.1 Effect of brazing alloy composition on joint strength.

From the prediction of the thermodynamic model (Figure 6.5) it is evident that as the Si content of experimental Ni-Cr-Si alloys decrease the ΔG_r increases. Therefore, in going from S25 alloy to S10 alloy the driving force for the alloy to react with Si_3N_4 increases. The more severe reaction between the alloy and the ceramic is the most probable justification for the increase in joint strength. However, in most ceramic joining processes, severe reactions between ceramics and metals are not recommended[139,148]. This is mainly due to the potential formation of low melting intermetallics or undesirable phases at the ceramic/metal interface. Thus, in such systems, the joining processes should be controlled in terms of joining temperature, time, and chemical composition of metallic medium in order to minimize the degree of reaction between the joining members.

In the case of the Si_3N_4/Ni-Cr-Si/Si_3N_4 system, as discussed in § 7.1, no low melting intermetallics were identified at the ceramic/filler metal interface. Joint microstructural examination also revealed that no porous reaction layer, which can

be found in many highly reactive ceramic/metal systems, formed at Si_3N_4/filler metal interfaces. From the above, we may conclude that in the present system being investigated, the severity of the reaction between Si_3N_4 and the Ni-Cr-Si alloys is not a detrimental phenomena. Indeed it is beneficial due to the formation of CrN reaction layer at the ceramic/filler metal interface and its influence on enhancing the joint strength, as will be discussed a bit later.

Another possible explanation for the effect of low Si content Ni-Cr-Si filler metals on enhancing the joint strength, is their contribution to eliminating the microcracks on ceramic surface through severe reaction between the alloy and Si_3N_4. The microcracks that are introduced on ceramic surfaces as a result of machining and grinding processes, will significantly reduce the joint strength[256]. The weakening effect is due to the fact that the deep scratches and surface cracks might act as failure origins because of large stress concentrations. In many cases, even the polishing process may not thoroughly eliminate the surface flaws. However, when excess reactions occur between the joining materials, a relatively thick Si_3N_4 layer will be eaten away, resulting in the removal of the machine damaged layer at the bond interface.

There is however, a basic limitation in reducing the silicon level of the filler metal which is due to the increase in the amount of nitrogen gas evolved as a result of the reaction between Si_3N_4 and the alloy. The excessive liberated N_2 gas may become trapped in the joint gap, leaving some unjoined areas, and as its pressure increases, it will tend to force the liquid filler metal away from the joining surface. An evidence of this condition is presented in Figure 7.13.

As shown in Table 7.5, the Si_3N_4/Si_3N_4 joints brazed with S25 alloy exhibited the lowest strength. There are two explanations for the low strength values of such joints. As mentioned previously, the near-equilibrium composition of the S25 alloy in contact with Si_3N_4 does not allow for the alloy to react with the ceramic as much as other compositions. Another factor affecting the joint strength is the presence of binary and ternary intermetallic phases such as α-Ni_5Si_2, Cr_3Si, and π. Because

Figure 7.13 Outer surface of a Si_3N_4/S10/Si_3N_4 joints showing the effect of N_2 pressure on forcing the alloy out of the interface.

of the lack of γ solid solution phase in the braze layer, the alloy has lost much of its capability to accommodate and deform under the residual stresses, resulting in debonding at the ceramic/metal interface.

The most probable explanation for the high strength of Si_3N_4/S10/Si_3N_4 joints brazed for 5 min. is the existence of the CrN reaction layer at the ceramic/metal interface. This layer has a two fold effect on enhancing the joint's mechanical properties. First, although the study of crystallographic relationship between the reaction layer and Si_3N_4 is not included in the present investigation, certain crystallographic planes of hexagonal ß-Si_3N_4 and CrN (NaCl structure[257]) must have been oriented such that the interface has little or no lattice spacing mismatch. This will provide strong bonding through the minimized lattice strain at their mutual interface. For instance, (611) plane (0.9492 Å) of Si_3N_4 coincides well with (331) plane (0.9496 Å) of CrN. Good lattice matching can also form between (111) (2.310

Å) and (501) (1.1998 Å) planes of Si_3N_4 with (111) (2.394 Å) and (222) (1.197 Å) planes of CrN respectively.

Second, the coefficient of thermal expansion of CrN is almost the same as that of the Si_3N_4 ($2.3x10^{-6}K^{-1}$)[258], therefore this would minimize the residual thermal stresses at the Si_3N_4/reaction layer interface on cooling from the braze solidification temperature. Moreover, the CrN reaction layer will act as an intermediate layer between the ceramic and the braze, thus alleviating the mismatch stresses between the braze ($\alpha \approx 12x10^{-6}K^{-1}$) and Si_3N_4 ($\alpha \approx 2.3x10^{-6}K^{-1}$).

It is interesting to note that the solidification shrinkage stresses within the braze layer (Fig. 7.7b) were accommodated by the γ phase (solid solution of Ni-Cr-Si), while several shrinkage cracks are observed in the α-Ni_5Si_2 phase which have been arrested by both the γ and A phases .

In understanding the effect of brazing time on joint strength with S19, note must be taken of reactions at Si_3N_4/S19 interface. For longer brazing times, more Cr will have diffused from the bulk of the braze layer to the interface resulting in enrichment of phase A at the interface and this is believed to be responsible for the strong bonding between Si_3N_4 and the alloy.

7.2.1.2 Effect of joint thickness and flaws on joint strength

In general, the scatter of results given in Table 7.5 is relatively large. There seem to be several reasons for this. One, is the influence of surface flaws particularly those near and at the braze layer. It is also due to the variation of filler metal thickness and its influence on mechanical properties of the joints. Usually, thin filler metal joints (<100 μm thick) exhibited lower bond strength. In contrast, the strength with a joint thickness between 100 and 200 μm is optimal, with a decrease being observed in excess of 200 μm. This result is in good agreement with the investigation of Mizuhara *et al.*[79] in brazing Si_3N_4 ceramic using active filler metals. They found that when the filler metal thickness was increased from 50 μm to 100 μm, an increase in the joint strength was observed. One possible explanation

for these results is that thicker filler metals undergo more plastic deformation during cooling cycle to result in lower thermal stress at the joint, hence, higher joint strength.

It is to be mentioned that, although the amount of brazing alloy used in all the joining experiments was kept constant and sufficient to produce a 100 μ thick layer upon solidification, small inconsistencies in the braze layer thicknesses were observed. This was mainly due to the loss of the filler metals to the outer surface of joints during brazing, commonly known as blushing. Therefore, often times the thickness of the braze layer after solidification was not uniform and varied slightly from one sample to another. The effect of joint thickness on the strength of Si_3N_4/S10/Si_3N_4 5 min. joints is given in Table 7.6. There is another possible explanation for the relatively scattered strength values. In some of the brazements, particularly those brazed with low Si content filler metals, some partially bonded areas were observed at the joining surfaces. Considering equation 4.1 for the bend strength calculation, the effect of reduced cross-sectional area on lowering the

Table 7.6 Four-point bend strength of Si_3N_4/S10/Si_3N_4 5 min. joints.

Sample No.	joint Thickness (μm)	strength (MPa)
1	75	98
2	90	90
3	100	117
4	120	125
5	120	145
6	150	140
7	230	108

strength is quite obvious.

As stated in § 2.3.3 and listed in Table 1.1, ceramics are generally more brittle, stiffer, and have lower thermal expansion coefficients than metals. Thus, the interface between the ceramic and the braze will be stressed when cooled from the joining temperature.

If the braze undergoes plastic deformation during the cooling cycle, some of the interfacial stresses will be relieved, resulting in an increased joint strength. The amount of the plastic deformation depends on the yield strength of the filler metal. The lower the yield strength, the more plastic deformation will occur and consequently this will lower the residual stresses. One possible approach to increasing the joint strength, is post-fabrication heat treatment such as annealing and slow cooling. It will allow the braze to undergo more plastic deformation which, in turn, will alleviate the residual stresses.

In general, attempts to reduce thermal stresses by lowering the cooling rate failed to increase the joints strength. A slow cooling rate of 3°C min^{-1} was employed after solidification of the filler metal, but no distinct difference in the bend strength between the two cooling rates (3°C and 10°C min^{-1}) was observed. A mean strength of 125 MPa for four Si_3N_4/S10/Si_3N_4 5 min. joints was obtained when applying a cooling rate of 3°C min^{-1}. This value was not too different from the strength value of the similar joints when cooled at a rate of 10°C min^{-1} (Table 7.5). Similar observations were reported by Mizuhara *et al.*[79] and Nicholas.[259]

To obtain information about the stresses present in joints of various braze layer thickness and different compositions, one can use previously mentioned techniques outlined in §2.3.3. A meaningful calculation requires sufficient information about the elastic-plastic behaviour of joining materials, i.e., the ceramic and the filler metal for a specified composition. For instance, the following equation has been used for the calculation of the residual stresses in bonded strips of thickness, t, to ceramics:

$$\sigma_m^c = \frac{\left[(\alpha_m - \alpha_c)\Delta T + \left(\frac{\sigma_y}{H}\right)\right]}{\left(\frac{1}{E_m} + \frac{t_m}{t_c}\frac{1}{E_c} + \frac{1}{H}\right)} \qquad (7.3)$$

and:

$$\sigma_c^c = -\sigma_m^c t_m / t_c \qquad (7.4)$$

where:

σ^c_m and σ^c_c= cooling stress in metal and ceramic respectively

α_m and α_c= coefficient of thermal expansion of metal and ceramic

σ_y= the yield strength of the metal

E_m and E_c= the Young's moduli of metal and ceramic

H= linear work hardening coefficient of the metal

ΔT= temperature range

Application of Equations 7.3 and 7.4 to evaluate the stresses that develop in Si_3N_4 and the filler metal near the interface, requires the values of mechanical and thermo-mechanical properties of the ceramic and the metal. For the ceramic, all the data are readily available, but not for the filler metal. Calculation of σ^c_m and consequently, σ^c_c, requires such properties of the filler metal as α, E, σ_y, and H that are not available in the literature. It would be of interest to experimentally measure these properties to study the effect of cool-down stresses on joint quality. Since such measurements were beyond the scope of this thesis, the stress analysis was not conducted. Instead, high-temperature four-point bend tests were performed and this was able to provide some insight with respect to the residual stresses within the joint (see the following section).

7.2.2 High-temperature strength of Si_3N_4/Si_3N_4 joints.

The successful production of a joint with high room-temperature strength, however, does not in itself guarantee the stability of the component at elevated temperatures. It is therefore important that the joint maintains its high-temperature strength in such applications as heat engines.

The main objectives of high-temperature joint strength evaluation were:
a) To study the mechanical stability of the joints at elevated temperatures, and
b) To study the effect of reheating temperature on residual stress relaxation.

The Si_3N_4/S10/Si_3N_4 joints, which exhibited the highest room-temperature strength, were selected for testing at 500°C, 700°C, and 900°C in air. The high temperature strength of Si_3N_4/S10/Si_3N_4 joints brazed for 5 min. at 1220°C is given in Table 7.7 and its variation with temperature is shown graphically in Figure 7.14.

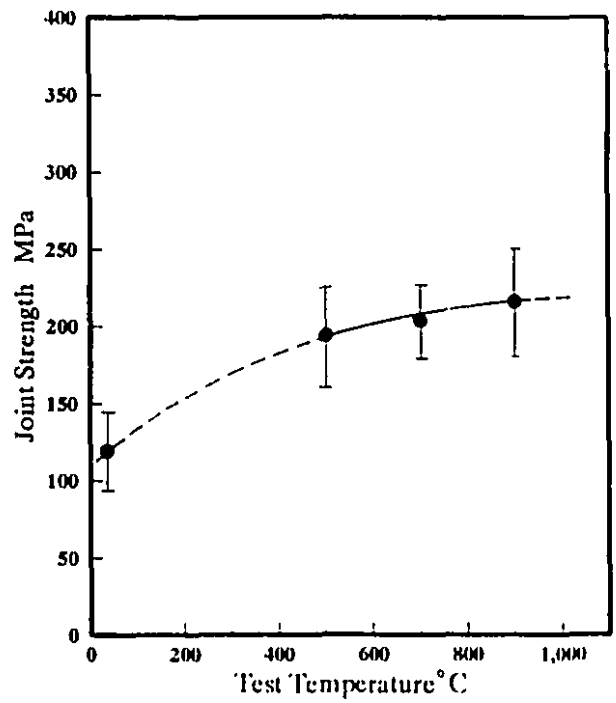

Figure 7.14 High-temperature four-point bend strength of Si_3N_4/S10/Si_3N_4 joints brazed at 1220°C for 5 min.

Table 7.7 High temperature four-point bend strength of $Si_3N_4/S10/Si_3N_4$ joints.

Test temperature (°C)	Strength (MPa)
500	200
	195
	190
	160
	145
700	220
	212
	210
	198
	180
900	250
	230*
	225
	205
	195
	180*

* These joints fractured within the ceramic.

At least five joints were tested to evaluate the average strength at each temperature. As will be discussed in § 7.3 some joints fractured within the ceramic; the strength of such joints was not taken into account for the calculation of the mean strength values. As can be seen from Figure 7.14 the strength gradually increases from ≈185 MPa at 500°C to ≈200 MPa at 700°C and to ≈220 MPa at 900°C.

The results of this set of experiments were surprising because of the

achievement of a 220 MPa strength at 900°C, under optimized brazing conditions. They demonstrate that the thermal stresses, which are believed to be responsible for lowe · joint strength at room-temperature, can be alleviated through reheating the joints, thereby resulting in high strength at elevated temperatures.

In order to study the effect of reheating temperature on the stability of the braze microstructure, one of the bend samples which fractured through the ceramic was examined by SEM. Figure 7.15 represents the microstructure of a Si_3N_4/S10/ Si_3N_4 joint after testing at 900°C. From the comparison of figures 7.15 and 7.7a it is evident that the braze microstructure had not been significantly influenced by the reheating temperature. However, some cracking due to the bend stresses can be observed within the braze layer. It is interesting to note that in Figure 7.15, under

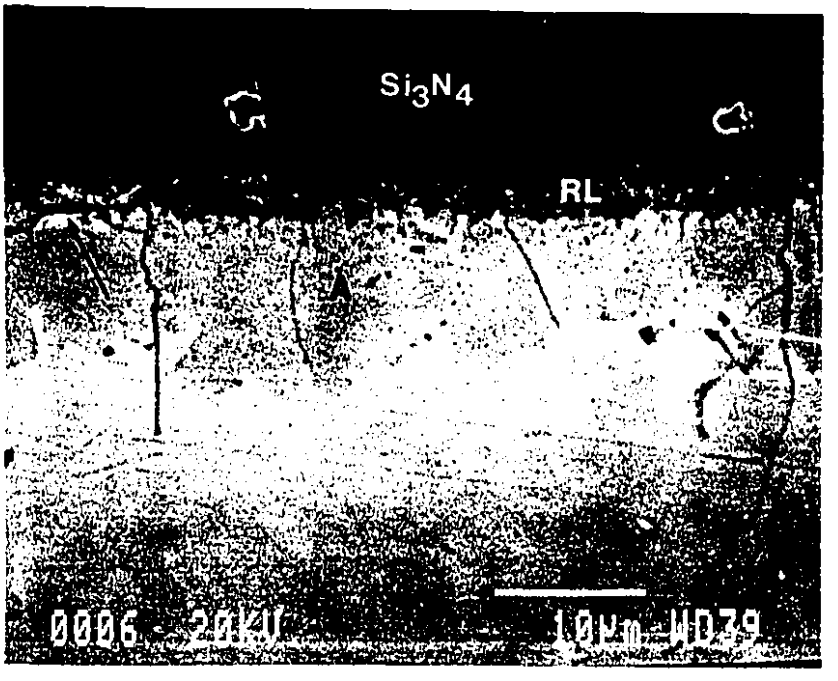

Figure 7.15 SEM micrograph of Si_3N_4/S10/Si_3N_4 joint after reheating at 900°C.

such stresses, some debonding of phase A from the reaction layer (RL) had occurred in some areas (see arrow). However, the Si_3N_4/RL interface remained intact. This would tend to confirm the strong bond between Si_3N_4 and the CrN reaction layer. This also indicates that the presence of CrN phase at the Si_3N_4/filler metal interface is attributable to the maintenance of the joint's strength at elevated temperatures.

From the strength values at room and high-temperature, the amount of residual stresses at the ceramic/metal interfaces can be estimated. For instance, Si_3N_4/S10/Si_3N_4 joints brazed for 5 min. exhibited strength values of 115 and 220 MPa at room-temperature and 900°C respectively. Thus, the amount of residual stresses can be simply calculated as:

$$\sigma_{residual} \geq \sigma_{T_{max}} - \sigma_{RT} \geq 220-115=105 \quad MPa$$

$$\text{with } T_{max} < T_{solidus}$$

When the T_{max} is at the temperature where all the residual stresses are relieved, then:

$$\sigma_{residual} = \sigma_{T_{high}} - \sigma_{RT}$$

7.2.3 Comparison of strength values

From the comparison of room-temperature strength values obtained in the present study with those presented in literature it was revealed that:

a) There are very few reports available on joining Si_3N_4/Si_3N_4 using Ni-based alloys and little or no studies have been made of joint strength. Nearly all the available data centre around the application of solid-state bonding techniques rather than brazing for joint fabrication. Nakamura and Peteves[260] reported four-point bend strength of ≈300 MPa for Si_3N_4/Si_3N_4 joints made with Ni-20Cr wt% alloy. Peteves *et al.*[261] also used the same alloy for diffusion bonding of silicon nitride. They found that depending on the joining environment, the joint strengths were between

100-384 MPa. As stated in § 2.3.2.1, although this method provides relatively high joints strength, it is a costly method and is restricted to joining very simple geometries. So far, there is no joint strength data available on Si_3N_4 ceramics brazed using Ni-based filler metals.

In general, the four-point bend strength of Si_3N_4/Ni-Cr-Si/Si_3N_4 joints, were found to be lower than that of the Si_3N_4 ceramic (≈600 MPa). Even the strongest joints exhibited a strength of ≈1/6 that of the ceramics. One of the main reasons for the low bond strength values relative to that of the Si_3N_4, is the presence of thermal stresses at the ceramic/filler metal interface.

b) Most of the Si_3N_4 brazements with high room-temperature strength have been fabricated using Ag-based filler metals. The most widely used being Cusil, Tcusil and Cusil ABA. As mentioned in § 2.3.5.2, strength values ranging from 300 to 770 MPa for Si_3N_4/Si_3N_4 joints have been reported[152]. In spite of relatively good mechanical properties, the application of such joints is limited to temperatures below 600°C, due to the low melting point of the brazing alloys. Furthermore, because of the Ti addition, such alloys exhibit low oxidation resistance.

c) Perhaps the highest melting point alloys yet reported for brazing Si_3N_4 ceramics, are those based on binary Cu-Ti with different Ti additions. Application of $Cu_{66}Ti_{34}$ and $Cu_{50}Ti_{50}$ for brazing Si_3N_4 at brazing temperature of 1100°C have been investigated by a number of researchers [100,105,160]. Depending on brazing conditions, they reported room-temperature strength values ranging from 19 to 313 MPa.

From the above, it can be stated that no data on the mechanical properties of Si_3N_4/Si_3N_4 joints using high melting point filler metals (i.e. alloys with melting point of >1000°C) have yet been reported.

Although there are many reports available on room-temperature joint strength measurement, the study of testing temperature dependency of joint

strength, particularly at temperatures exceeding 500°C, has been very limited. Some investigators who attempted to quantify the high-temperature joint strengths have reported similar results to those obtained in the present investigation. Most notable, is the study of Gyarmati *et al.*[132] who measured the strength of hot-pressed SiC/Ti/SiC joints at room-temperature and 1000°C. They found the bond strength to be relatively low at room-temperature (76±13 MPa), but nearly tripled at elevated temperatures (≈ 200 MPa). They concluded that the difference between the strength values obtained at room-temperature and 1000°C was attributable to the relaxation of the CTE mismatch stresses. The study of Naka *et al.*[160,173] on the variation of joint strength showed a different behaviour. The strength of $Si_3N_4/Al/Si_3N_4$ joints showed a maximum of 210 MPa at 100°C and then decreased to about 30 MPa at 500°C due to the weakening of the bonding phase. The authors found the same behaviour in studying the high-temperature strength of Si_3N_4/Si_3N_4 joints brazed with $Cu_{50}Ti_{50}$ filler metal. The strength of the joints increased to 200 MPa at 100°C and gradually decreased to 105 MPa at 700°C.

Other investigations have shown a decrease in bond strength at higher temperatures. Morozumi and co-workers[101] observed that the strength of hot-pressed Al_2O_3/Nb joints decreased from 120 MPa at room-temperature to about 30 MPa at 1000°C, at which temperature Nb becomes soft and very ductile. In the study of Iseki *et al.*[102], the four-point bend strength of pressureless sintered and reaction sintered SiC joints which were about 240 and 110 MPa, respectively at room-temperature, decreased to about 20 MPa at 500°C. The authors observed the same behaviour in another investigation[142]. The reduction of strength at higher temperatures was also observed by Santella *et al.*[129] and Nagano and Kato[262].

In all the above investigations, the authors concluded that the lower high-temperature joint strength was either due to the changes in joint chemistry or the loss of mechanical properties of metallic constituents at elevated temperatures.

A comparison of the present high-temperature strength results with those that have been reported in literature will show that the mean strength of 220 MPa

at 900°C is the highest elevated temperature strength value so far reported for Si_3N_4/Si_3N_4 brazed joints.

7.3 Fractography Examination of Si_3N_4/Si_3N_4 MOR Bars.

Scanning electron microscopy examination of the fracture surfaces of the experimental samples showed that fracture occurred via different fracture modes, influenced by:

i) brazing alloy composition
ii) brazing time, and
iv) testing temperature

a) Room-temperature Four-point bend samples

Figure 7.16 shows typical fracture surfaces of the samples brazed with S10 and S19 alloys at 1220°C for 10 min. The fracture surface in Figure 7.16a illustrates the brittle nature of the failure for the joint. The figure also gives clear evidence of weak bonding between the ceramic and the filler metal, since the filler metal has been easily separated from the ceramic. This would explain the fairly low strength of S19 joints given in Table 7.5. The fracture surfaces of S25 joints were also similar to that shown in Figure 7.16a.

Fractographic examination of the S10 joints showed a different fracture mode. In this case, as depicted in Figure 7.16b, crack initiated near the interface and propagated inwards until complete rupture occurred. The figure also shows that in some areas the crack propagated within the Si_3N_4, indicating a) a stronger bond between the ceramic and the braze than the bulk strength of the ceramic, and b) the effect of residual stresses in weakening the ceramic. The fracture mode observed in experimental Si_3N_4 joints brazed with S10 alloy is directly related to their higher bend strength compared to that of other joints (Table 7.5).

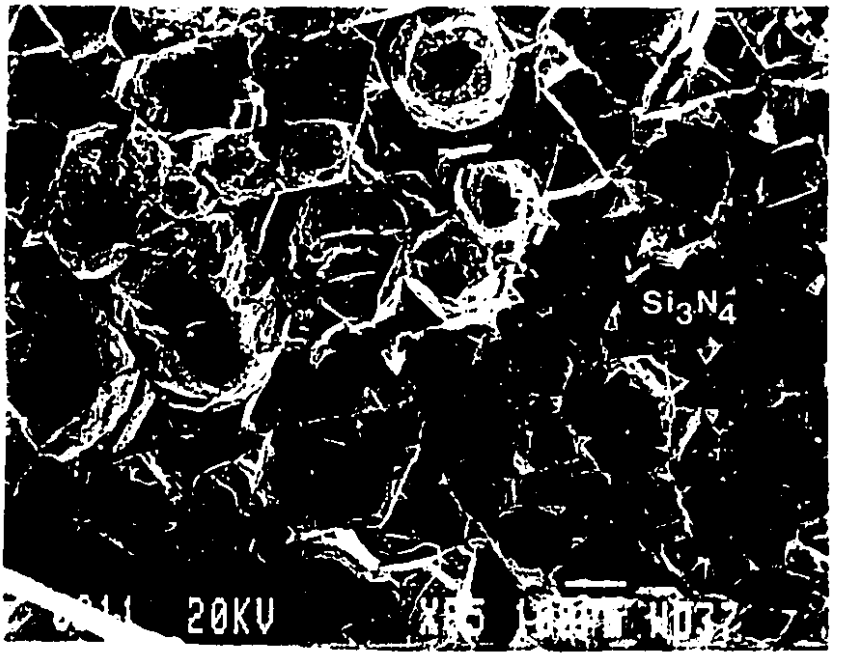

(a)

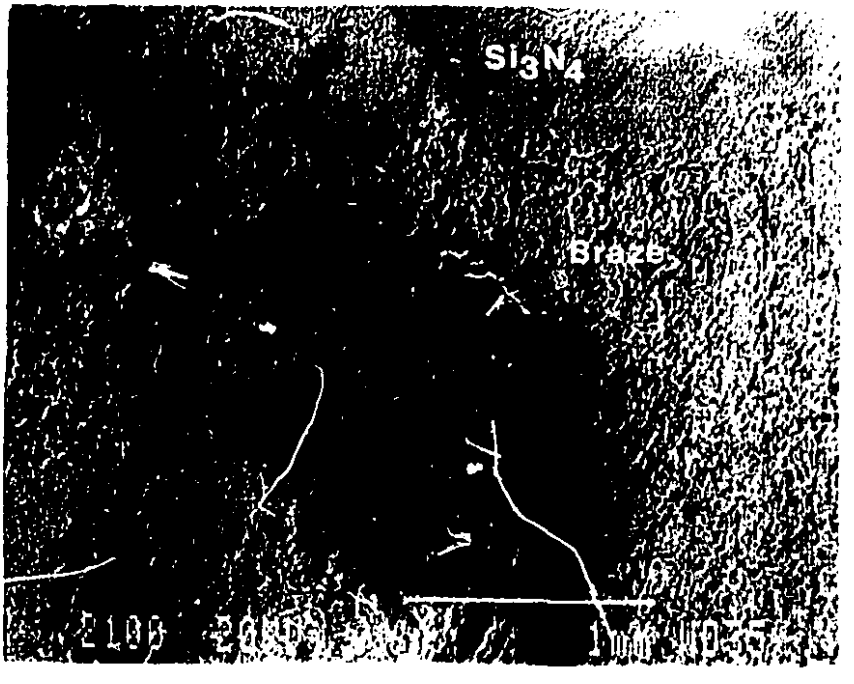

(b)

Figure 7.16 Fracture surfaces of (a) S19 and (b) S10 brazing alloy MOR bars.

b) High-temperature four-point bend samples

The high-temperature bend samples exhibited different fracture modes. Figure 7.17 shows three Si_3N_4/S10/Si_3N_4 samples after testing at 900°C. For some specimens as "A", fracture occurred in the ceramic instead of the joint. This type of fracture mode first indicates a strong bonding between the ceramic and braze, and second, the effect of surface flaws on lowering the strength of the ceramic, since further examinations revealed that fracture had occurred near a surface flaw (Fig. 7.18). The fracture strength of 230 MPa for this specimen is much lower than the strength of the parent Si_3N_4 which is about 600 MPa at room-temperature. It should be mentioned that, although, the high-temperature strength of experimental Si_3N_4 samples was not measured, the literature values[263,264] of high-temperature strength of Si_3N_4 showed no significant reduction in the strength of various types of Si_3N_4 ceramics at temperatures up to 1000°C, which exceeds the upper limit of the present measurements.

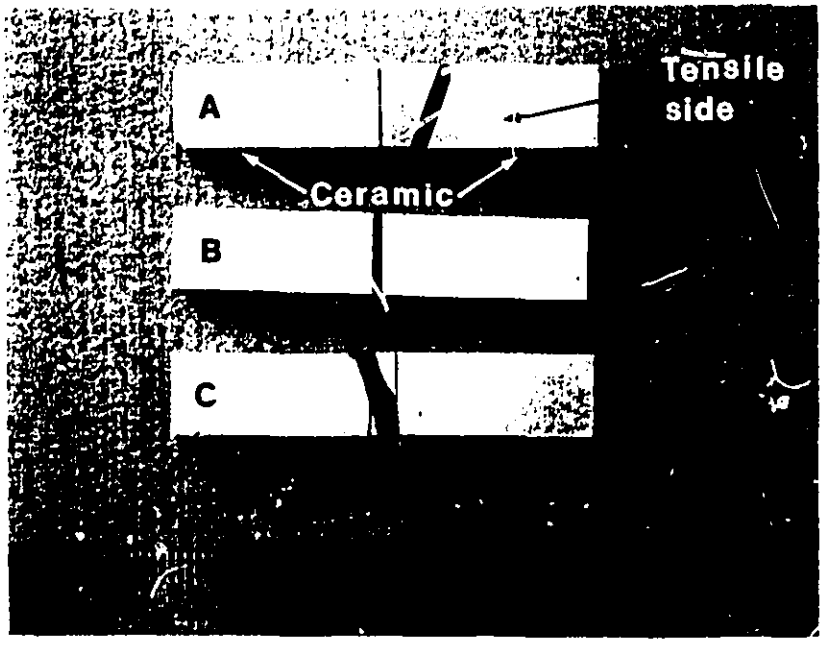

Figure 7.17 Four-point bend samples after testing at 900°C.

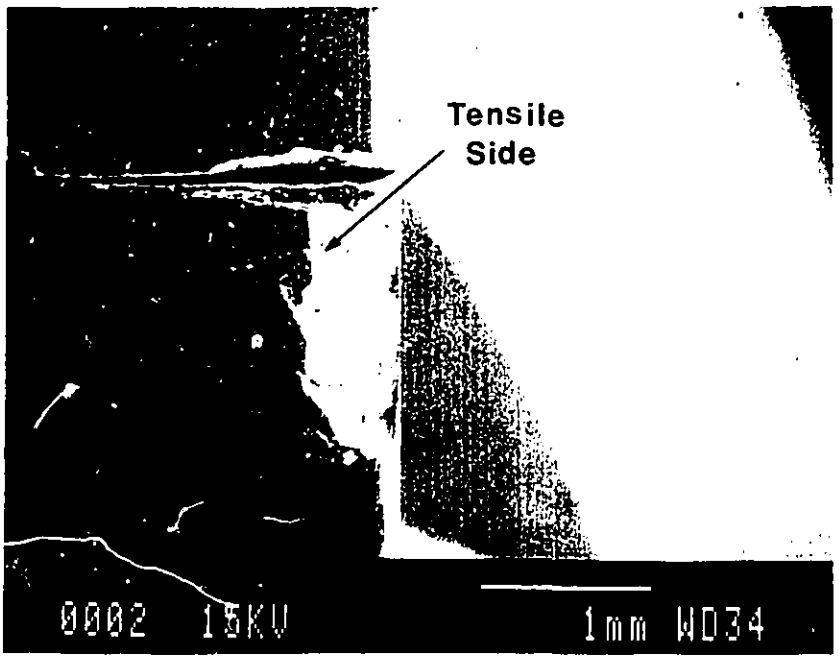

Figure 7.18 Effect of surface flaw on crack initiation in high temperature MOR bars.

Specimen B showed a different fracture mode, in this case the fracture path was through the joint area. The crack initiated and propagated at the joint interface.

For specimen C, the crack which had initiated at the tensile side of the sample, propagated along the joint interface then changed direction into the ceramic until complete rupture. Unfortunately for the samples which fractured along the interface, the precise location where crack had initiated could not be determined from the fractographic observation. In this case all the fracture surfaces contained a brittle fracture plane within the CrN reaction layer formed between the S10 alloy and Si_3N_4. Figure 7.19 illustrates the fracture surface of specimen C on the Si_3N_4 side. The figure also shows the region where the crack has changed direction into the ceramic. From the Figure 7.19, it is evident that, even at a temperature as high as 900°C, the alloy had not shown any detectable plastic deformation, emphasizing

the high-temperature mechanical stability of the filler metal. The XRD pattern taken from the fracture surface on the ceramic side showed the presence of CrN in that area.

The relatively large deviation presented in Figure 7.14 is mainly due to the distinct fracture modes exhibited by the bend specimens. In summary, the main parameters which induced different fracture behaviour were found to be as follows:

a) presence of some unjoined area observed within the braze layer of those samples that exhibited lower strength.
b) variation of joint thickness. Samples with 100 μm>t>200 μm (where t is the braze layer thickness), fractured along the interface and exhibited low strength values.
c) presence of flaws on the ceramic surface caused fracture away from the joint area. As was already mentioned, the strength of such joints was not taken into account for the calculation of the mean strength.

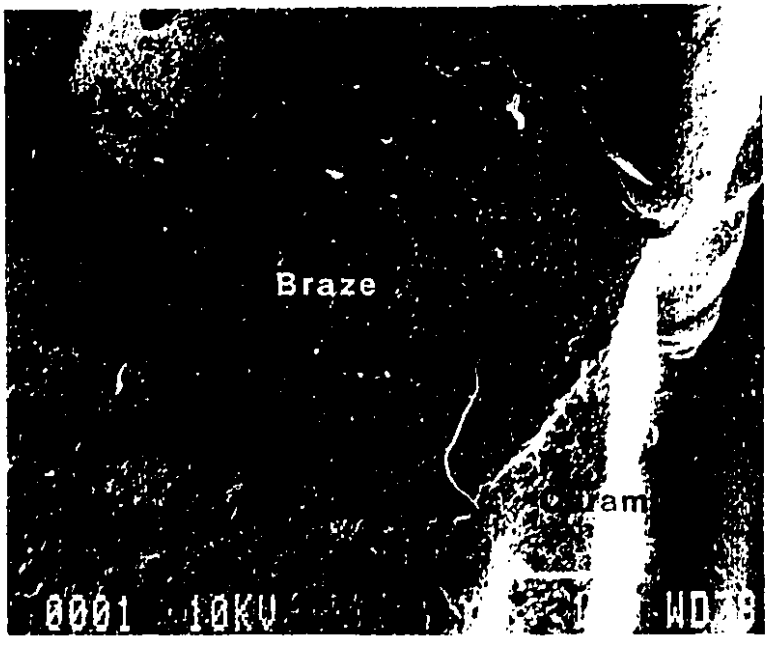

Figure 7.19 Fracture surface of specimen "C" in Fig. 7.17.

Although the above discussion concerns the samples which were tested at 900°C, almost the same fracture modes were observed for the samples tested at 500 and 700°C, except that in most cases fracture occurred along the interface. These results, along with the data presented in Figure 7.14, again emphasise the effect of reheating temperature on residual stress relaxation at the ceramic/filler metal interface.

From the fractographic examinations and the strength measurement at high temperature, it can be concluded that the strength of the ceramic at high temperatures was poorer than the joints themselves, since it was shown that some joints fractured within the ceramic. It is therefore important that all the processing parameters are carefully controlled in order to minimize the presence of any defects in the ceramic parts to be joined. It is believed that a higher joint strength would have been achieved if no flaws had been present in the experimental Si_3N_4 specimens.

7.4 Shear Strength Measurement

The room-temperature shear strength values of single brazed Si_3N_4/Si_3N_4 joints brazed with S10 and S19 filler metals are presented in Table 7.8. From the table, it can be seen that the effect of compositional variation on the shear strength of the interface is similar to that obtained for the four-point bend tests. Decreasing the Si content of the filler metal produces joints with higher shear strength. It is also demonstrated in Table 7.8 that all the joints exhibited lower shear than bend strengths, the main reasons of which will be discussed in § 7.5.

Table 7.8 Room-temperature shear strength of Si_3N_4/Ni-Cr-Si/Si_3N_4 joints.

Brazing alloy composition	Brazing time (min.)	Joint shear strength (MPa)
S10	5	55±15
S19	10	15±5

7.4.1 Fractography examination of shear samples

The fracture modes of shear samples were distinct from that of the bend samples. One of the features common to all of the experimental Si_3N_4/S10/Si_3N_4 shear samples was a mixed fracture mode that was observed in the joint area. In this system, as shown in Figure 7.20, cracks, which initiated at the ceramic/filler metal interface, propagated along the interface to a distance of about half the specimen thickness. The cracks then changed direction and propagated into the Si_3N_4 where the final fracture occurred.

As mentioned above, generally, the shear strength of experimental joints, regardless of the filler metal composition, was found to be lower than their bend strength. However, it should be noted that, although the results of shear testing showed lower strength values, the test will provide important data on the mechanical performance of the joints in shear. In a practical sense, this information can be utilized by proper engineering design when the joint is subjected to shear loading.

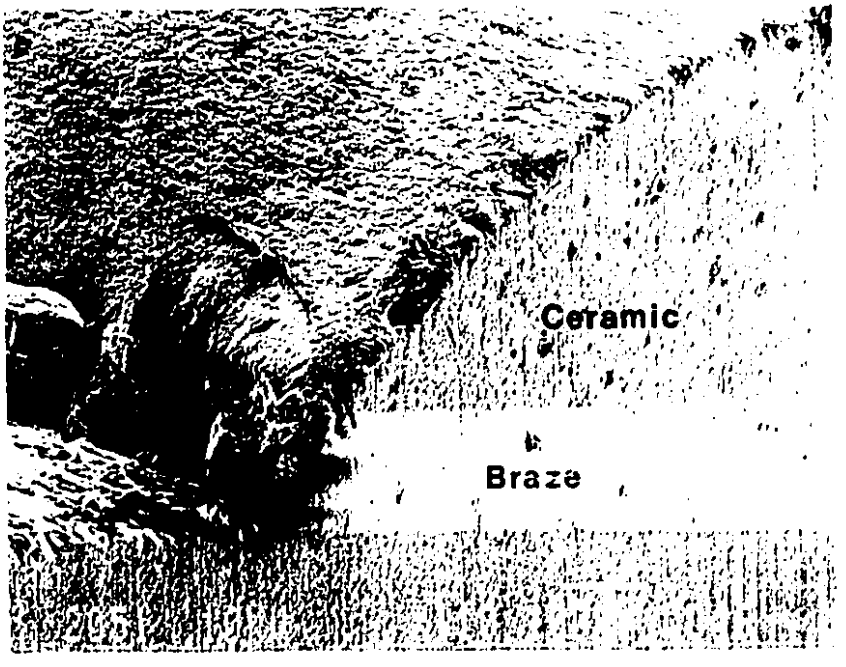

Figure 7.20 Typical fracture surface of shear samples for Si_3N_4/S10/Si_3N_4 joints.

7.5 Comparison of Results of Shear and Four-point Bending Tests.

As discussed in previous sections, the values of the joints strength obtained using shear or four-point bend tests were quite different. The fractographic examinations also showed different fracture paths the for shear and bend samples. These results emphasize the fact that the joint strength is strongly dependant on the method of evaluation. Therefore, it is of interest to study the joint behaviour under different loading conditions for a better understanding of the potential joint performance and design.

This section will focus on the residual stress distribution in the joint area to explain how these stresses will influence joint failure under different loading conditions.

There have been many useful theoretical investigations on the concentration and location of residual stresses around the bond between dissimilar materials. Although these investigations have been carried out for joints of various dimensions and prepared from various combinations of materials, they have presented many common results. This may aid in the interpretation of the different mechanical properties of joints and behaviour under different loading conditions.

It has been demonstrated that when a ceramic is bonded to a metal, large stresses appear near the free edges. An FEM study on residual stresses in the Si_3N_4/Mo joint system showed the presence of high stresses at the interface and free surfaces. This investigation, presented in Appendix V was primarily aimed at understanding the effect of joint geometry and joining materials on the peak stresses.

Figure 7.21 graphically represents the distribution of the residual stresses at the ceramic-metal interface near the free edges when the thermal expansion of metal is larger than that of the ceramic. It should be noted that because of the symmetry only one half of the joint has been shown. The figure is based on the investigations of Kirchner and Zdaniewski *et al.*[265]. Figure 7.21 indicates the presence of a large stress normal to the interface (σ_y). This stress is believed to be

due to the lateral shrinkage of the metal. The stress parallel to the interface (σ_x) is always maximum in the interior of the joint and decreases sharply to zero at the free surface. These stresses are compressive in the ceramic and tensile in the metal near the interface for a negative coefficient of thermal expansion mismatch (α_C-α_M <0) and become tensile in the ceramic when $\alpha_C > \alpha_M$. The shear stresses (γ_{xy}) are greatest at the edges and decrease sharply in the x direction. As presented in Figure 7.21, a negative thermal expansion mismatch will result in a negative residual shear stress at the free surface. In contrast, when αC > αM, a positive shear stress will

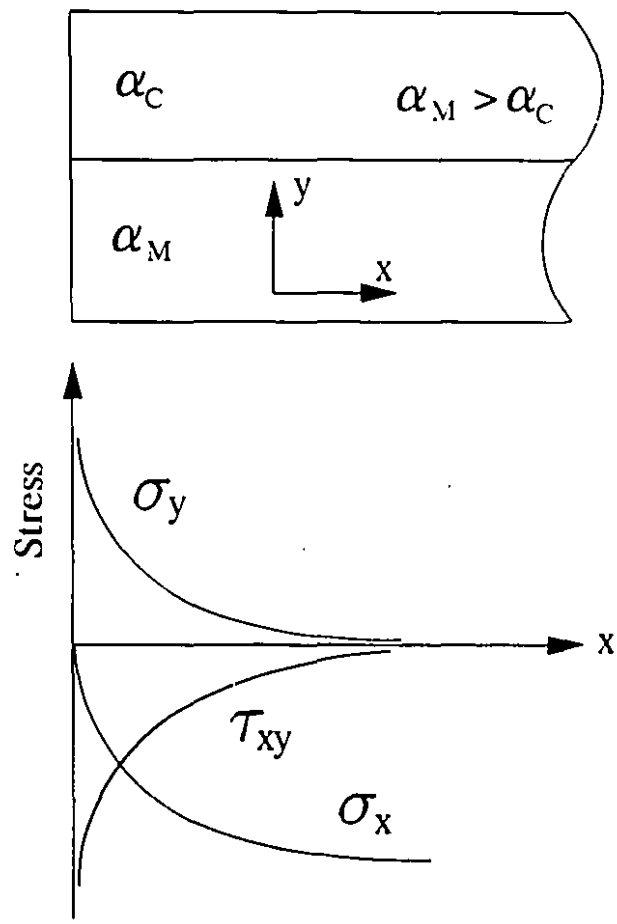

Figure 7.21 Schematic illustration of stress distribution at the ceramic/metal interface near the free surfaces when $\alpha_M > \alpha_C$.

appear at the edge of the joint.

The information given in Figure 7.21 together with the loading condition can be used to explain the fracture behaviour observed in experimental shear samples.

As showed in § 7.4.1, fractography examination of the shear samples revealed that the samples exhibited almost consistent fracture path. Under shear loading, the crack, which initiated at point A (Fig. 5.7), grew along the interface then changed direction depthwise into the ceramic until final fracture occurred (Fig. 7.20).

In understanding why the crack starts at point A in shear samples (see Fig. 5.7) both the residual stresses and loading condition must be considered. Although, in designing and application of the shear jig it was intended to avoid a bending moment at the joint interface, the sample geometry contributed to the presence of a small bending moment within the joint area. This is due to the fact that the shear loading was applied on either side of the braze layer, therefore, a gap of about 0.7 mm was left between the upper and lower part of the jig causing a small bending moment at the interface.

The bending moment applied on the sample produces a tensile stress at the edge of the sample. This stress will be intensified by the tensile residual stresses perpendicular to the interface (σ_y). On the other hand, the bending moment will introduce a compressive stress on point B (Fig. 5.7) that will suppress σ_y. Thus, an asymmetric condition for the stresses perpendicular to the interface will be presented at points A and B. It is therefore expected that the crack will initiate at point A, which was the case in almost all the shear samples.

Explanation of the fracture path in terms of initial crack propagation along the interface and then into the ceramic that was observed in fractured shear samples is somewhat more complex. It is influenced by several factors related to the residual stresses at the interface, interfacial bond strength, and loading conditions which translate into different stress intensity factors at the tip of the crack. Situations like this where a crack, lying at the interface between two brittle elastic solids, grows at the interface and then changes direction into one of the adjacent

materials have been treated as "kinking" in fracture mechanics[266,267,268]. According to the investigations of Hutchison and co-workers[268] the tendency of a crack in an interface to either remain at the interface or kink out into one of the materials depends on the ratio of:

$$\frac{G_i}{G_s} \quad \text{and} \quad \frac{\Gamma_i}{\Gamma_s}$$

where:

G_i= energy release rate for crack advanced in the interface

G_s= energy release rate for the crack kinking into the substrate

Γ_i and Γ_s= interface and substrate toughness, respectively.

Whether the ratio of energy release rate is greater or less than the toughness ratio will determine the condition of interface cracking or kinking, respectively.

Figure 7.22 shows schematically an interface crack leaving the interface under a mixed Mode I and Mode II loading condition. The figure indicates that for the substrate crack to propagate continuously, K_{II} must be positive[266]. Since in the experimental shear samples both loading conditions are present, kinking is expected to occur. On the other hand the positive K_{II} will facilitate the crack to grow into the Si_3N_4 ceramic.

It has been remarked that once the interface crack has grown into the substrate, the axial residual stress σ_x (or applied load in the x direction) becomes a driving force for the crack propagation into the substrate[266,267, 268].

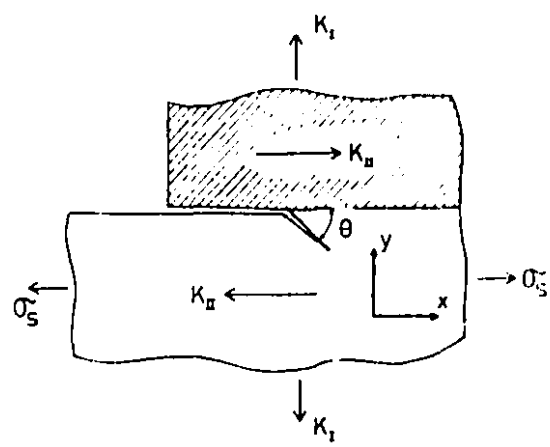

Figure 7.22 Schematic illustration of a kinked crack, and related stress intensity factors.[266]

The kinking angle (the angle by which the crack propagates into one of the adjacent materials) depends on whether σ_x is positive or negative. A positive σ_x will increase the kinking angle and vice versa. Therefore, the kinking angle may determine to a certain extent the magnitude of axial residual stresses. In the experimental Si_3N_4/Si_3N_4 brazed joints, because of the lower coefficient of thermal expansion of Si_3N_4 compared to that of the braze, the ceramic should be under a negative residual stress in the x direction. Hence, a low kinking angle is expected to be seen in fractured samples. The moderate kinking angle of ≈45° observed in experimental shear samples indicates that a high compressive axial residual stress did not exist within the joint area.

In the case of the bend test, the high tensile stress on one side of the sample together with the residual stress in y direction will contribute to crack initiation at the edge of the bend samples. When the crack has propagated well along the interface (where the residual γ_{xy} is zero) a criterion based on $K_{II}=0$ is expected to hold and the crack will continue to grow at the interface. As mentioned previously, an interfacial fracture path was observed in most of the bend samples.

From the above discussion, it can be stated that different fracture modes of the shear and bend specimens are not only related to the different loading conditions, but also on the complex stress conditions around the joint before and during loading which will determine the condition of interfacial or kinking fracture mode.

It should be mentioned that the purpose of the above discussion was mainly to point out some of the major factors involved in the competition between kinking and interfacial cracking. Investigation of conditions which have led to kinking in shear samples and determination of kinking angle requires data concerning the values of G, Γ, and K that must be discussed elsewhere.

7.6 Summary of Si_3N_4/Ni-Cr-Si/Si_3N_4 Joining

Brazing experiments were carried out to study the joinability of Si_3N_4 with

various Ni-Cr-Si filler metals which had already shown good wetting characteristics on Si_3N_4. The brazing filler metals consisted of Ni-Cr-Si alloys with the same Ni/Cr ratio of 3.5 and different Si contents, namely 10, 19, and 25 atom%, designated as S10, S19, and S25 respectively. The results of joining experiments showed that Si_3N_4/Si_3N_4 joints can form using all of these alloys. However, each alloy resulted in different joint strengths and microstructures. In summary:

1. The joints made with S19, S25 and the S10 alloys for 5, 10, and 15 min. at 1220°C exhibited quite different microstructures. The microchemical analysis of the braze layer showed an increase in the Si content of S10 and S19 alloys, while the S25 alloy composition was not significantly affected by the brazing process. This indicates the validity of thermodynamic calculations on predicting a state of thermodynamic equilibrium between Si_3N_4 and S25 alloy under the experimental condition.

2. The microstructural examinations revealed the presence of a CrN reaction layer at the ceramic/filler metal interfaces of the joints brazed with S10 alloy for 5 min. This layer disappeared after a longer brazing time of 15 min. It is believed that the local high nitrogen pressure from the decomposition of Si_3N_4 contributed to the formation of CrN reaction layer.

3. The study showed that Si and N, produced by the decomposition of Si_3N_4, were taken up totally (Si) or partially (N) by the brazing alloy. The results of microchemical analysis of Si_3N_4/Ni-Cr-Si/Si_3N_4 joints suggest the formation of either CrN or N/Ni-Cr-Si solid solution rather than Cr silicide at the Si_3N_4/braze interface.

4. Joints formed with the alloy of X_{Si}=0.25 were found to exhibit the lowest strength. This was mainly due to the different joint microstructures and the lack of reactivity between the ceramic and the S25 alloy.

5. The Si_3N_4/S10/Si_3N_4 joints were found to present the highest strength among all the Si_3N_4/Ni-Cr-Si/Si_3N_4 joints. The strength of such joints decreased as the brazing time increased. The high strength of the joints, especially those which were brazed for 5 min., was mainly due to the presence of a CrN layer at the interface which provided a strong interface between the ceramic and the braze.

6. The room-temperature shear strengths of the joints were found to be significantly lower than the four-point bend strength of the same joints. The difference between the shear and four-point bend values is basically due to the fact that these tests present different features in strength evaluation. In general, regardless of the strength measurement method, it was found that the strength of Si_3N_4/Ni-Cr-Si/Si_3N_4 joints was strongly dependant on the Si content of the alloy and the brazing time, particularly for the joints brazed with S10 alloy.

7. The high-temperature four-point bend strength of the joints brazed with S10 alloy for 5 min. was significantly higher than their corresponding room-temperature strength values. It was demonstrated that a test temperature of 900°C was effective in improving the joints performance through the elastic stress relaxation between the mating surfaces.

8. Fractographic examination of the experimental Si_3N_4/Ni-Cr-Si/Si_3N_4 four-point bend bars, tested at room-temperature revealed that in most of the cases the crack propagated along the ceramic/filler metal interface. The high-temperature four-point bend bars showed that, in many cases, the fracture path was through the ceramic, indicating a high bond strength at the interface.

9. The results of the present investigations showed that the joint strength values correlate well with the sessile drop wetting angles between the ceramic and the filler metal. The S10 alloy, which exhibited the lowest wetting angle on Si_3N_4

ceramic, produced the strongest joints, and vice versa for the S25 alloy.

Based on all the above observations, it was concluded that the S10 alloy was the most promising in the series of alloys studied.

Chapter 8

Si_3N_4 / Mo Joining Experiments

In this chapter the effect of brazing alloy composition and brazing time and temperature on the microstructure and microchemistry of Si_3N_4/Mo joints will be discussed. The discussion is divided into two sections: a) the effect of joining variables on Si_3N_4/Mo joints using commercially available S19 (BNi-5) brazing alloy and b) on Si_3N_4/Mo joints using the modified S10 composition, for which the high strength Si_3N_4/Si_3N_4 joints were obtained. This also includes the results of strength testing and fractographic examination of Si_3N_4/Mo joints.

8.1 Microstructural and Chemical Analysis of Experimental Si_3N_4/S19/Mo Joints.

Secondary electron image (SEI) micrograph of a typical Si_3N_4/S19/Mo joint brazed for 10 min. at 1220°C is shown in Figure 8.1. From the figure, it can be seen that the braze layer microstructure has been significantly affected by the presence of Mo on the other side of the joint, since no similarity between the braze layer microstructure in this case and that of the Si_3N_4/Si_3N_4 joints was observed. Figure 8.1 shows that no significant porosity exists within the braze layer. However, due to CTE mismatch cracking, the braze layer has been debonded at the ceramic/filler metal interface.

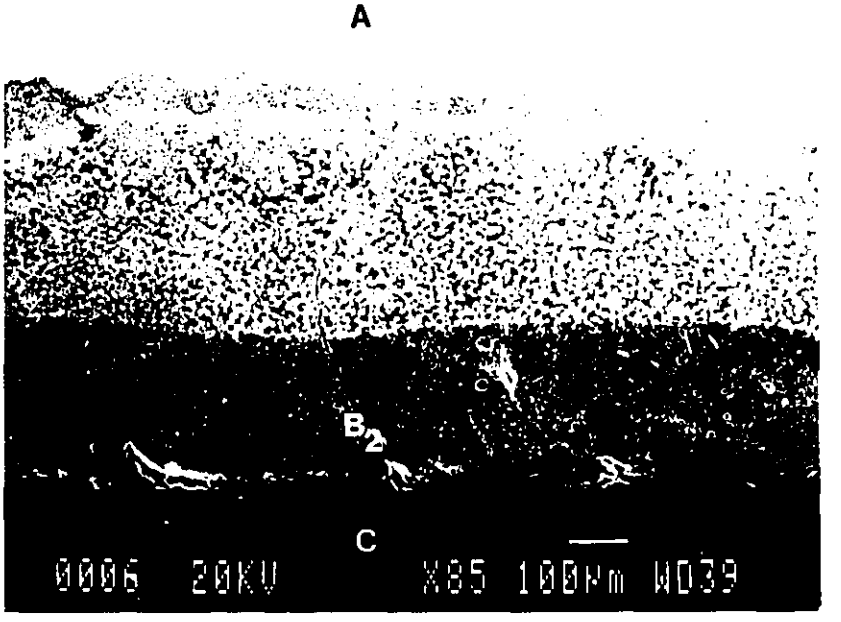

Figure 8.1 SEI micrograph of a Si_3N_4/S19/Mo joint brazed for 10 min. at 1220°C.

Figure 8.1 can be divided into four distinct zones labelled, A, B_1, B_2 and C. The composition of each zone is given in Table 8.1. The values given in the table are the mean of ten measurements. Zone A is molybdenum with almost 5 atom% Si, Ni, and Cr to a distance of about 30 μm from the Mo/filler metal interface. From the

Table 8.1 Chemical composition of different zones of Fig. 8.1.

Zone	Composition (atom%)
A	Mo + <5% Ni, Cr, and Si
B_1	Ni-11Cr-19Si-20Mo
B_2	Ni-20Cr-11Si-10Mo-15N
C	Si_3N_4

Mo-Ni, Cr, and Si phase diagrams, no eutectic occurs at this composition level, therefore, the refractoriness of the Mo would not have been significantly affected by the joining process. Zone B_1 extends from the Mo/filler metal interface to a distance which is approximately half the thickness of the braze layer. Zone B_2 extends the remaining distance between the zone B_1 and the Si_3N_4/filler metal interface. These two zones are distinguished from each other by their microstructures and chemical compositions (Table 8.1).

The overall composition of zone B_1 is Ni-11Cr-19Si-20Mo (atom%). The micrograph shown in Figure 8.2(a) indicates that zone B_1 consists of two phases denoted as α and ß. The α phase was found to be Ni-8.5Cr-20Si-26Mo(atom%), while ß was determined as Ni-19Cr-11Si (Table 8.2). The microscopic appearance of zone B_1 indicates a normal solidification with α as the primary solid phase. Although it

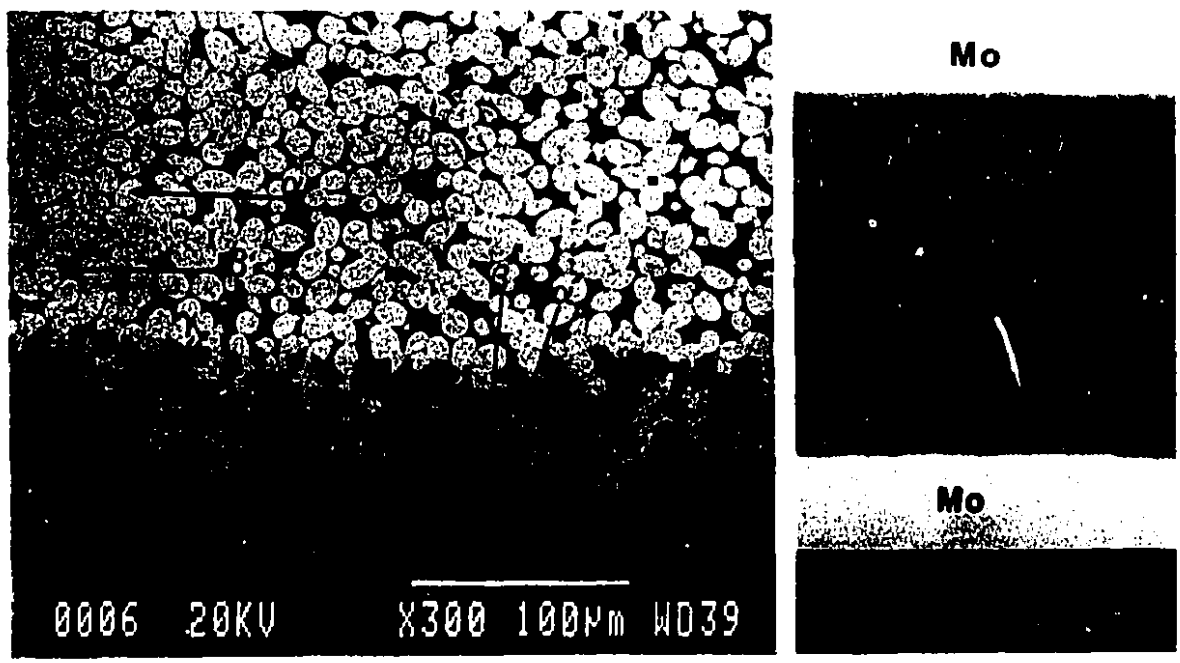

(a) (b)

Figure 8.2 BEI micrograph of zone B_1 and B_2 (a) and (b) SEI micrograph of a Mo/S19/Mo joint.

Table 8.2 Composition of different phases of Fig. 8.2a.

Phase	Composition (atom%)
α	Ni-8.5Cr-20Si-26Mo
α'	Ni-8Cr-19Si-26Mo-1N
ß	Ni-19Cr-11Si
ß'	Ni-15Cr-9Si-8N
γ	Ni-22Cr-13Si-12Mo-15N

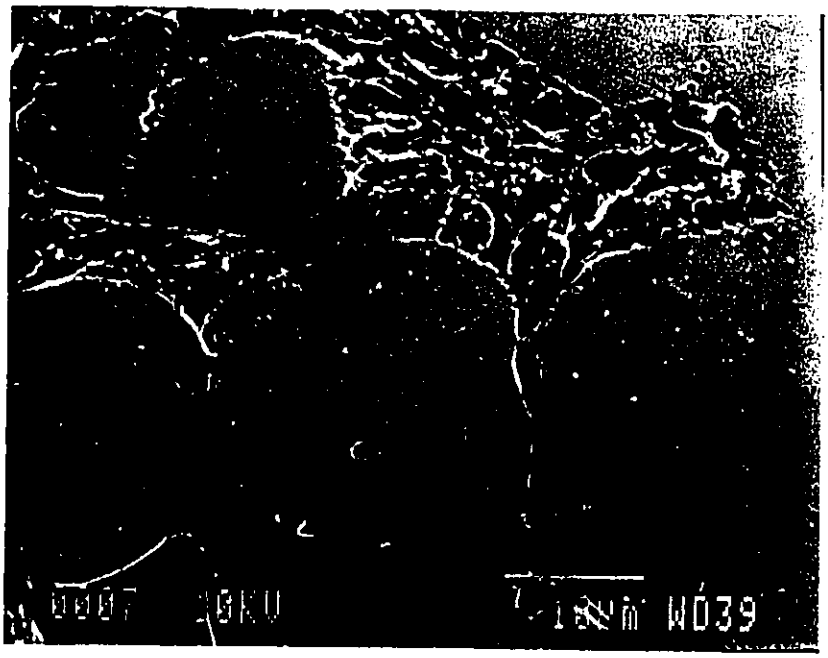

Figure 8.3 SEI micrograph of phases α and ß in zone B_1.

is not distinguished in Figure 8.2 (a), further examinations revealed that ß had a eutectic type structure. Figure 8.3 shows a high magnification SEI image of zone B_1 after etching the sample*. Unfortunately, the fine structure of the eutectic phases did not allow for chemical analysis of the individual phases.

* Etchant: 90 ml HCl, 5 ml H_2SO_4, 5 ml HNO_3, 1 ml HF.

Zone B_2 was found to have an overall composition of Ni-20Cr-11Si-10Mo-15N(atom%). The overall compositions of zone B_1 and B_2 indicate that zone B_1 is rich in Mo, while the concentrations of Cr and N are higher in zone B_2. The chemical analysis of the phases in this zone showed that zone B_2 consisted of three phases. The light phase (α') had almost the same composition as the α phase in zone B_1 with a small amount of nitrogen ($\approx$ 1 atom%). The dark phase was found to be Ni-15Cr-9Si-8N (β'). A comparison between the composition of this phase and that of β in zone B_1 reveals that both phases have almost identical compositions in terms of Ni, Cr, and Si. However, some nitrogen have been dissolved in β' in zone B_2. The higher concentration of N in β' than in α' is due to the presence of more Cr in this phase which has a higher solubility for N than any other constituent in those phases[236]. The study of zone B_2 demonstrated the presence of a third phase, denoted γ, which contains more Cr and N than any other phases present in the braze layer. This phase is observed as grey spots on Figure 8.2(a).

The two-zone microstructure observed in the braze layer has been formed as a result of competition between the migration of Mo from the metal side and Si and N from decomposition of Si_3N_4 on the ceramic side. As a comparison, a SEI micrograph of a Mo/Mo joint brazed with S19 is given in Figure 8.2(b). It can be seen from the figure that braze layer microstructure is very similar to that of the zone B_1 which formed as a result of diffusion of Mo into the filler metal.

From Table 8.1, it can be concluded that the compositional changes observed in going from the Mo side to the Si_3N_4 side causes the alloy to cross a phase boundary from a two phase ($\alpha+\beta$) region in the quaternary Ni-Cr-Si-Mo system to a three phase ($\alpha'+\beta'+\gamma$) region, in the Ni-Cr-Si-Mo-N system.

The overall composition of the braze layer (B_1+B_2) was determined as Ni-14Cr-16Si-15Mo-7N (atom%). By performing a mass balance on the filler metal, a slight increase in Si content was observed. This observation along with the presence of nitrogen in the braze indicated that the filler metal had reacted and decomposed the Si_3N_4.

The most interesting finding was that, as can be seen from the overall composition of the braze layer, the Mo content of the filler metal had increased from zero (starting alloy) to 15 atom% (product alloy). Unfortunately there is no phase diagram available for the quaternary Mo-Ni-Cr-Si system; the presence of 15 atom% Mo with melting temperature of about 2600°C would have certainly increased the melting point of the braze alloy. In order to evaluate the approximate liquidus temperature of the braze, samples with the same composition of the product alloy (without taking into account the N) were prepared and heated up in the brazing furnace until melting occurred; the melting point was found to be 1270±10°C.

From the above, it can be stated that at a brazing temperature of 1220°C, the alloy was no longer in the liquid state to react with Si_3N_4. The diffusion path of nitrogen in the braze layer also indicates that the migration of N into the braze stopped after the alloy had solidified. To confirm that the solidification of the filler metal (as a result of diffusion of Mo) takes place during the brazing process, the concentration of Mo in the product alloy was measured as a function of brazing time (Fig. 8.4). The figure shows that the filler metal becomes saturated with Mo at the very beginning of the brazing process. Although there is no data available concerning the diffusion coefficient of Mo in the Ni-Cr-Si alloys, the study of Jacobson and Martin[269] in induction brazing of Mo in vacuum with Inconel 600 (80Ni-14Cr-6Fe) showed considerable diffusion of Mo into the braze in a short brazing time of 5 sec.

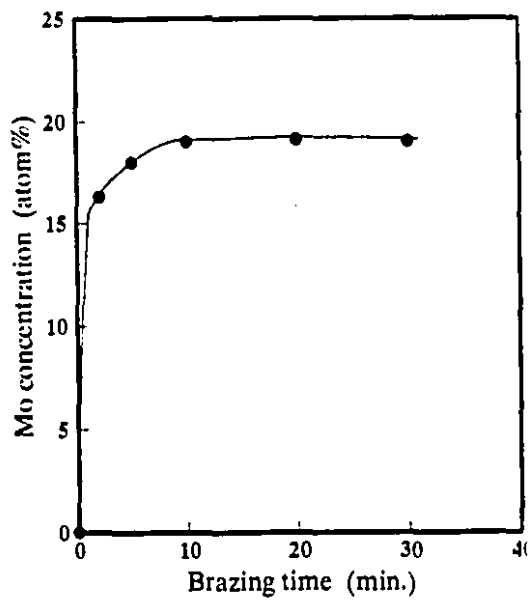

Figure 8.4 Variation of the Mo concentration with the brazing time.

This result was surprising in the sense that the brazing temperature of 1220°C, although about 80°C higher than the liquidus temperature of S19 filler metal, was not suitable for this system, mainly due to the higher liquidus temperature of the product alloy. Thus, further joining experiments were performed at a higher brazing temperature of 1300°C.

Figure 8.5a illustrates SEI images of Si_3N_4/S19/Si_3N_4 joints brazed at 1300°C for 10 min. A comparison of Figures 8.1 and 8.5a shows that the braze layer microstructure has been altered by the higher brazing temperature. Figure 8.5a shows a uniform two-phase microstructure consisting of a light phase with composition of α' (in Fig. 8.2) and a dark phase with composition of ß' within the braze layer. The micrograph shown in Figure 8.5 again indicates that no bonding occurred at the ceramic/filler metal interface. Most of the joints brazed under this condition were debonded after removal from the furnace.

A comparison of Si_3N_4/Si_3N_4 and Si_3N_4/Mo joints so far discussed indicates that the poor joining of Si_3N_4 to Mo is due mainly to the presence of Mo in the product alloy and the reaction of this element with the ceramic at the Si_3N_4/filler metal interface.

The reaction between Si_3N_4 and Mo has been investigated by some researchers[178,270,271]. Figure 8.6 presents the phases which are in equilibrium with Si_3N_4 in the Mo-Si-N system as a function of nitrogen partial pressure and temperature. From the figure, it can be seen that in the absence of external nitrogen pressure, at 1300°C(1573 K), Si_3N_4 can coexist with Mo_5Si_3[270]. At lower nitrogen partial pressure, say 10^{-4} bar (≈10 Pa, which is almost equal to the experimental N_2 pressure), $MoSi_2$ would be the stable phase. The figure also shows that no ternary phase forms in the Mo-Si-N system.

The investigation of Heikinheimo *et al.*[270] in the study of Mo-Si_3N_4 diffusion couples at 1300°C showed that independent of the nitrogen external pressure, only one phase, Mo_3Si, was formed at the interface. The reaction layer was very irregular and contained many cracks. At a N_2 partial pressure of 2 Pa they found layers of

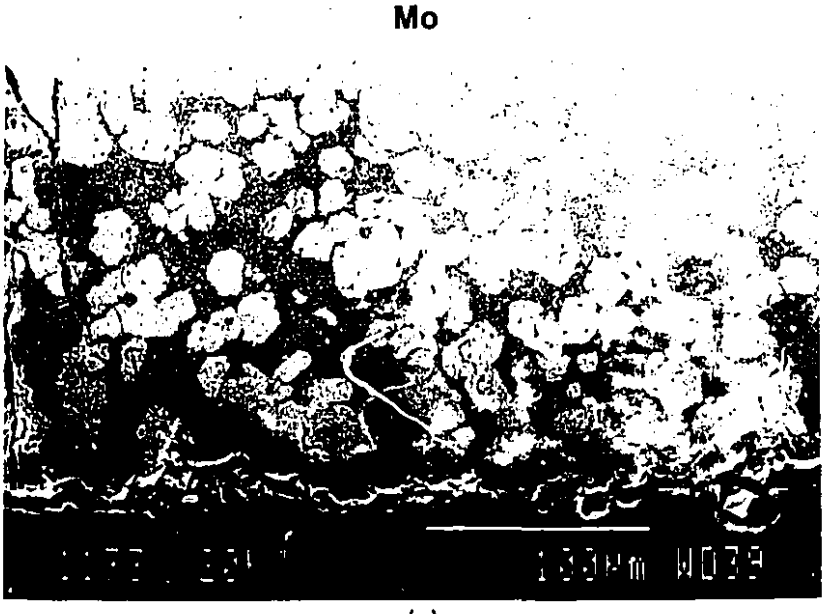

(a)

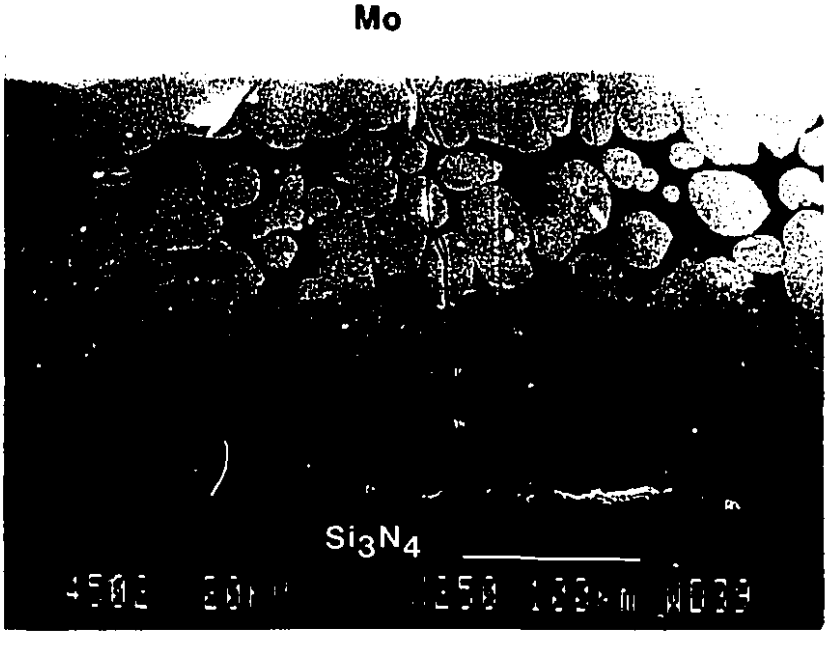

(b)

Figure 8.5 SEI micrographs of Si_3N_4/S19/Mo joints brazed for (a) 10 min. and (b) 1 min. at 1300°C.

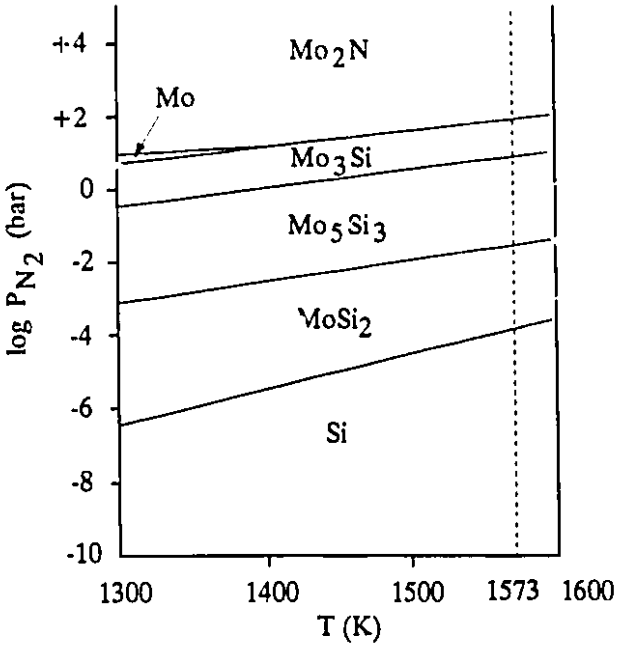

Figure 8.6 Solid phases in equilibrium with solid Si_3N_4 in the Mo-Si-N system.[270]

$MoSi_2$, Mo_5Si_3 and Mo_3Si in the Mo side of the joint.

The XRD pattern taken from the fracture surface of the joints brazed at 1300°C for 10 min., on both the Si_3N_4 and the braze sides, showed no known spectra of the phases expected in Mo-Si-N system. This is mainly due to the presence of Ni and Cr which makes the system far more complex. Although, information exists concerning the ternary Ni-Cr-Mo[272] and Ni-Si-Mo[273] systems, unfortunately no phase relationships about the quaternary Ni-Cr-Si-Mo system (without taking into account the N) can be found in the literature.

In order to alleviate the reactions at the ceramic/metal interface another set of experiments was conducted to join Si_3N_4 to Mo using the same brazing alloy, at 1300°C, but for shorter times (Figure 8.5b). A comparison of Figures 8.5a and b will show that there are less voids at the interface. However, some cracks were observed close to the ceramic/braze interface due to the thermal expansion mismatch between the joint materials ($\alpha_{Mo} = 5.5x10^{-6}\ C^{-1}$, $\alpha_{Si3N4} = 3.2x10^{-6}\ C^{-1}$, and α_{Si9}

$\approx 10x10^{-6}\ C^{-1}$). These cracks are very important because joint failure is likely to occur at this location during stressing of the joint.

It must be pointed out that the interfacial microstructure of the Si_3N_4/Mo joints presented in Figure 8.5b is superior to that of the joint brazed for 10 min. (Fig. 8.5a), due to the fact that the degree of interfacial reaction was significantly lower in the later, resulting in a bond formation at the ceramic/filler metal interface.

The strengths of these joints were measured using the four-point bend test and were found to be 25 MPa with a deviation of about 10 MPa. Most of the joints fracture at the ceramic/filler metal interface, however, in case of the stronger joints, fracture occurred within the ceramic body near the interface. This was mainly due to the edge cracking in the ceramic. This effect, which is presented in Figure 8.7 emphasizes first the presence of high residual stresses in that region and second, it shows a fairly considerable bond strength at the ceramic/braze layer interface.

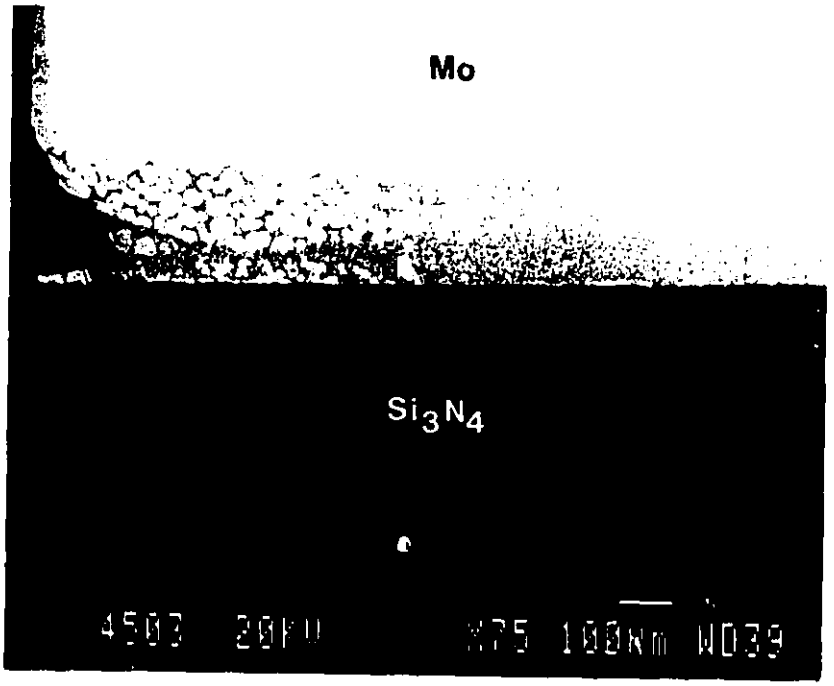

Figure 8.7 Edge cracking in the Si_3N_4/Mo joint presented in Fig. 8.5b.

The magnitude of residual CTE mismatch stresses in this case must be more severe relative to the Si_3N_4/Si_3N_4 joints, due to the presence of Mo with its higher coefficient of thermal expansion and also due to the higher brazing temperature.

8.2 Microstructural and Chemical Analysis of Experimental Si_3N_4/S10/Mo Joints.

Based on the results of Si_3N_4/S19/Mo joining experiments, the joining of Si_3N_4 to Mo using S10 filler metal was conducted at 1300°C. Selection of this brazing temperature was mainly due to the fact that the previous set of experiments showed that no bonding occurred at 1220°C, the temperature used in Si_3N_4/Si_3N_4 joining experiments. Figure 8.8a illustrates an SEI micrograph of a Si_3N_4/S10/Mo joint brazed for 10 min at 1300°C. As was the case for S19 joints brazed for the same time at the same temperature, no bonding occurred at the ceramic/braze layer interface. The lack of cracking in the braze layer indicates that debonding had occurred prior to the complete solidification of the filler metal.

The morphology of the braze layer in Figure 8.8a is somewhat similar to that of zone B_2 of Figure 8.2a. However, the γ phase was difficult to identify in this case. The microchemical analysis of the phases in Figure 8.8a are presented in Table 8.3. From the table, it can be seen that these phases have almost identical compositions as α' and ß' in Table 8.2. However, in this case about 4% nitrogen and 3% Mo was found in α' and ß' respectively. Small amounts of Al (≈0.3%) from decomposition of Si_3N_4 were detected in the area close to the ceramic/metal interface. As was the case for the S19 joints, the XRD pattern taken from the fracture samples at both the ceramic and braze layer sides showed no identifiable peaks of any known compounds. With respect to the overall composition of the braze layer given in Table 8.3 , by performing a mass balance on the product alloy composition, it was found that the Si content of the filler metal had increased from 10 atom% to about 19 atom%. This again indicates that the product alloy is driving towards the equilibrium composition in terms of the Si concentration. However, due to the presence of Mo in the system, the equilibrium Si content must be different

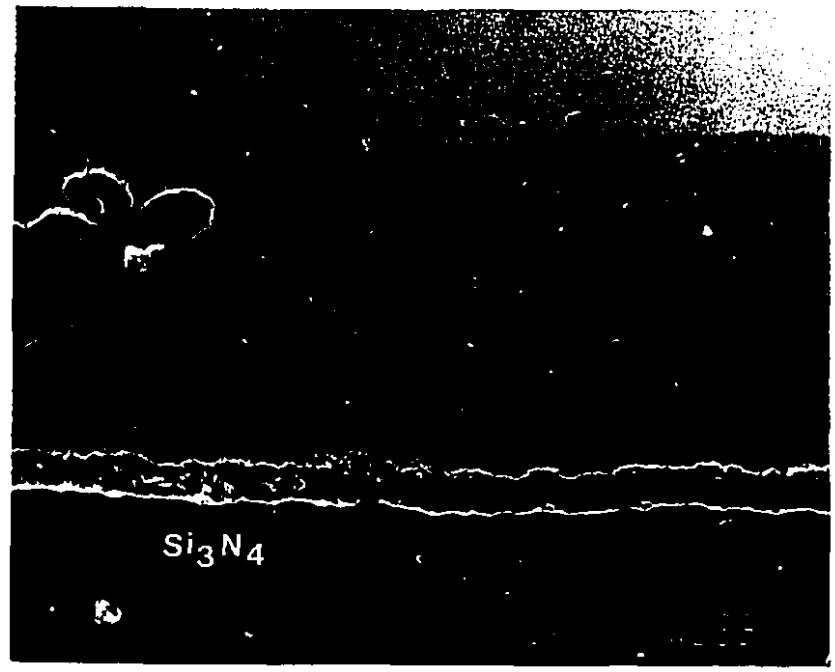

(a)

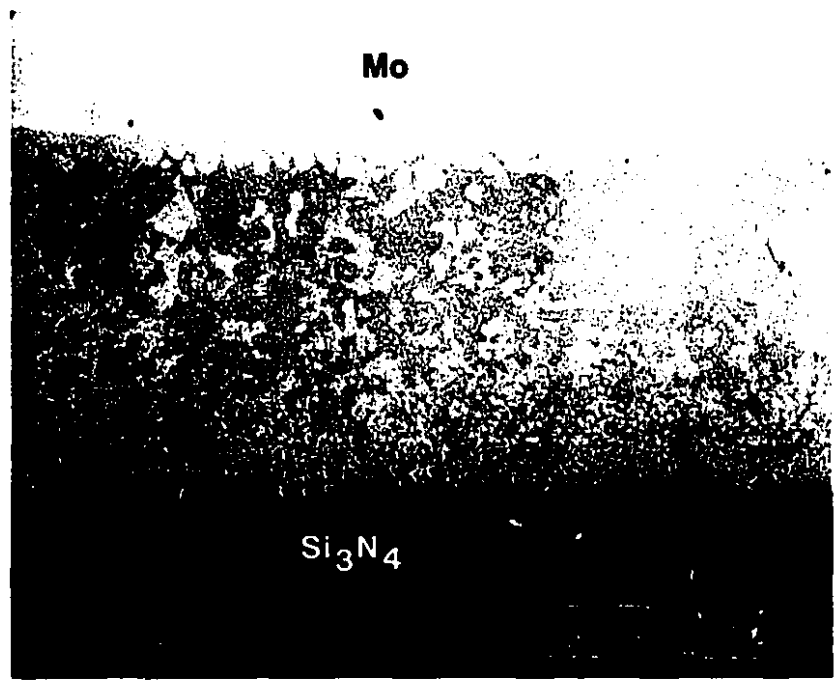

(b)

Figure 8.8 SEI micrographs of Si_3N_4/S10/Mo joints brazed for (a) 10 min. and (b) 1 min. at 1300°C.

Table 8.3 Chemical analysis of Si_3N_4/S10/Mo joints brazed for 10 min. at 1300°C.

Phase	Composition (atom%)
α'	Ni-8Cr-18Si-26Mo-4N
ß'	Ni-15Cr-9Si-3Mo-9N
Braze layer	Ni-13Cr-15Si-16Mo-8N

from that of Ni-Cr-Si alloys in contact with Si_3N_4.

Since debonding at the ceramic/braze layer interface was believed to be a result of extensive reactions between the ceramic and the filler metal, the brazing time was reduced to shorter times to alleviate these reactions. The joints brazed for 5 min. showed almost the same microstructure as the 10 min.-brazed joints, with no bonding at the ceramic/filler metal interface. Figure 8.8b shows a SEI micrograph of a Si_3N_4/S10/Mo joint brazed for 1 min. at 1300°C. The figure provides evidence of bond formation at the ceramic/metal interface with no cracking in the braze layer. However, some minor porosity exists within the braze layer in the area close to Si_3N_4/braze interface. This may indicate that at the brazing temperature, the alloy near the interface was not completely liquid. Another possibility for the formation of the porosity is N_2 gas evolution at the interface. Figure 8.8b also shows that the brazing time has a strong influence on reducing the interfacial reactions and consequently the joint quality.

Further examination of Figure 8.8b reveals that the braze layer microstructure is similar to that of the joint brazed for 10 min. at the same temperature. The microchemical analysis (Table 8.4) showed that the product alloy consisted of two phases, α' and ß', with almost identical composition as the phases in Figure 8.8a. However, from the overall composition of the braze layer, it was found that the product alloy contained less Si, Mo and N, due to the shorter brazing time.

Table 8.4 Chemical analysis of Si_3N_4/S10/Mo joints brazed for 1 min. at 1300°C.

Phase	Composition (atom%)
α'	Ni-8Cr-18Si-26Mo-4N
ß'	Ni-15Cr-9Si-2.5Mo-8N
Braze layer	Ni-14Cr-13Si-14Mo-7N

Figure 8.9 illustrates the X-ray elemental dot mapping within the braze layer. As can be seen from the figure, unlike the Si_3N_4/S10/Si_3N_4 joints, the distribution of Ni, Cr, Si, and N is fairly uniform within the braze layer. However, Mo is more concentrated in α' and the area close to the ceramic/braze layer interface. The EPMA results across the joint area, presented in Figure 8.10, provide additional information on the elemental distribution within the braze layer. The figure repeatedly indicates that there is no concentration gradient for Ni, Si, and particularly Cr and N in the braze layer and in the area close to the ceramic/filler metal interface.

From Figures 8.9 and 8.10, it is apparent that no CrN or a Cr-rich phase (like A in Fig. 7.3) formed at the interface, as was the case for the Si_3N_4/Ni-Cr-Si/Si_3N_4 joints. This can be better explained by reference to Table 8.5. The table, generated using the F*A*C*T system, represents the free energy change of the possible reactions between Si_3N_4 and Mo or Cr under the experimental brazing condition (T=1300°C and P=15 Pa). It can be seen from Table 8.5 that the formation of Mo silicides, particularly $MoSi_2$ is more likely to occur than Cr nitride or Cr silicides at the interface.

8.3 Strength Measurement and Fractographic Examinations

The strength of the Si_3N_4/S10/Mo joints brazed for 1 min. at 1300°C were measured using both four-point bend and shear tests. For each set of experiments

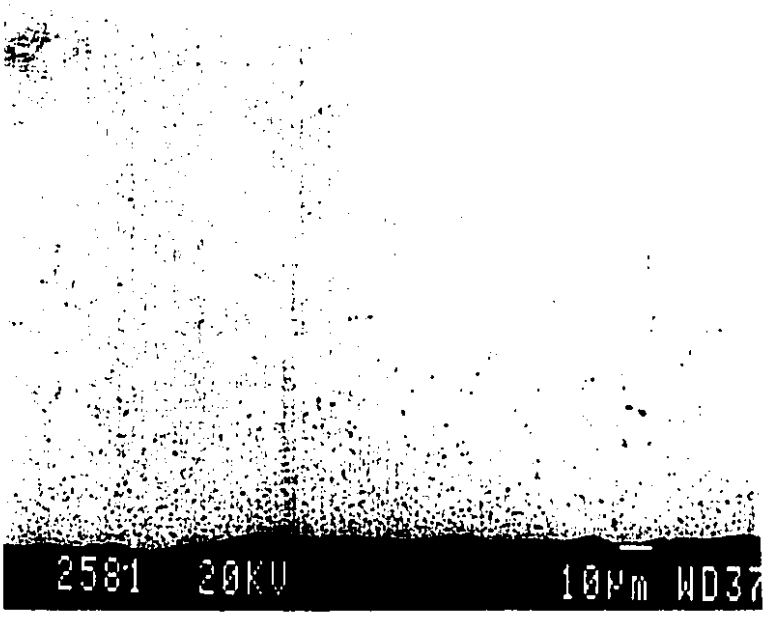

Figure 8.8b

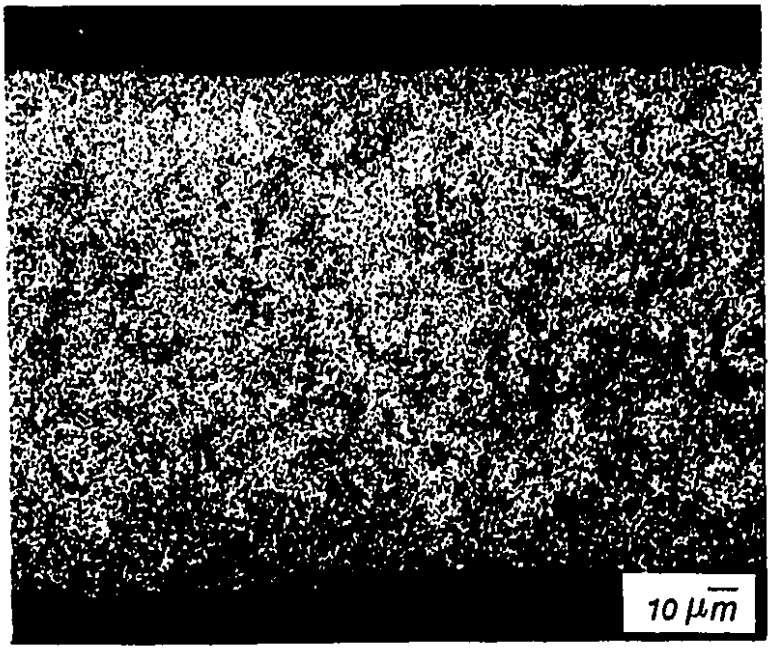

(Ni)

(Cr)

(Si)

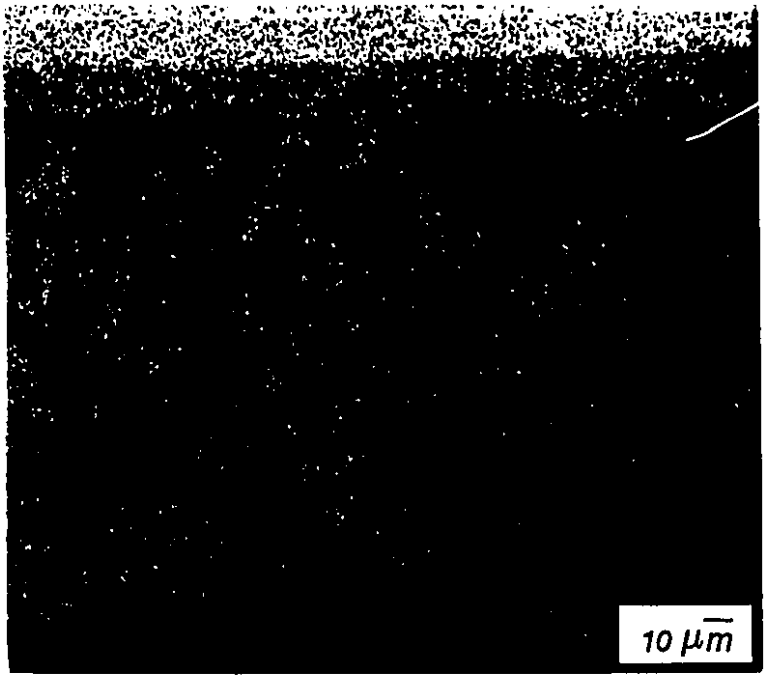

(Mo)

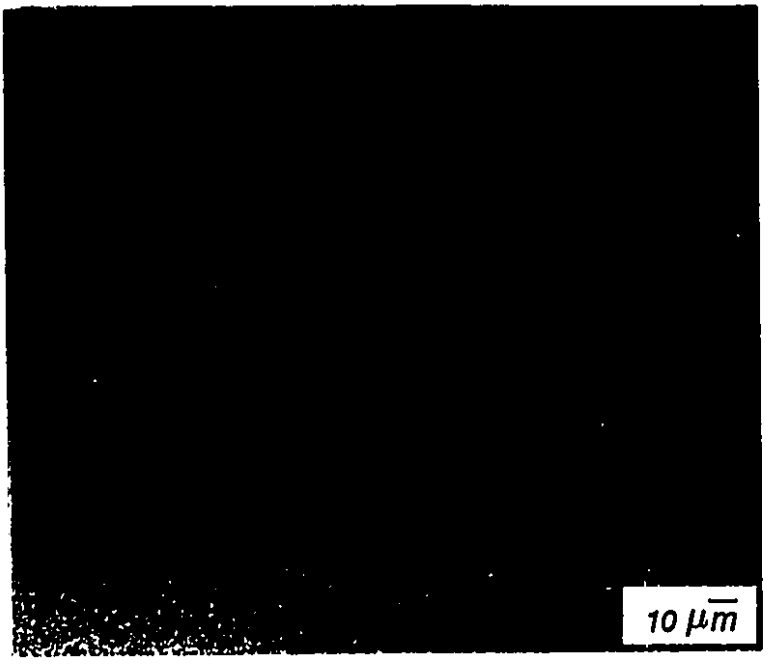

(N)

Figure 8.9 WDS compositional dot maps within the joint area in Fig. 8.8b.

Table 8.5 Free energy change for the reactions between Si_3N_4 and Mo or Cr at T=1573 K and P=15 Pa.

Reaction	ΔG KJ
$2Si_3N_4 + 3Mo = 3MoSi_2 + 4N_2$	-393.3
$Si_3N_4 + 9Mo = 3Mo_3Si + 2N_2$	-349.6
$Si_3N_4 + 5Mo = Mo_5Si_3 + 2N_2$	-322.8
$2Si_3N_4 + 3Cr = 3CrSi_2 + 4N_2$	-239.3
$Si_3N_4 + 9Cr = 3Cr_3Si + 2N_2$	-307.6
$Si_3N_4 + 17Cr = 4Cr_2N + 3Cr_3Si$	-152.6

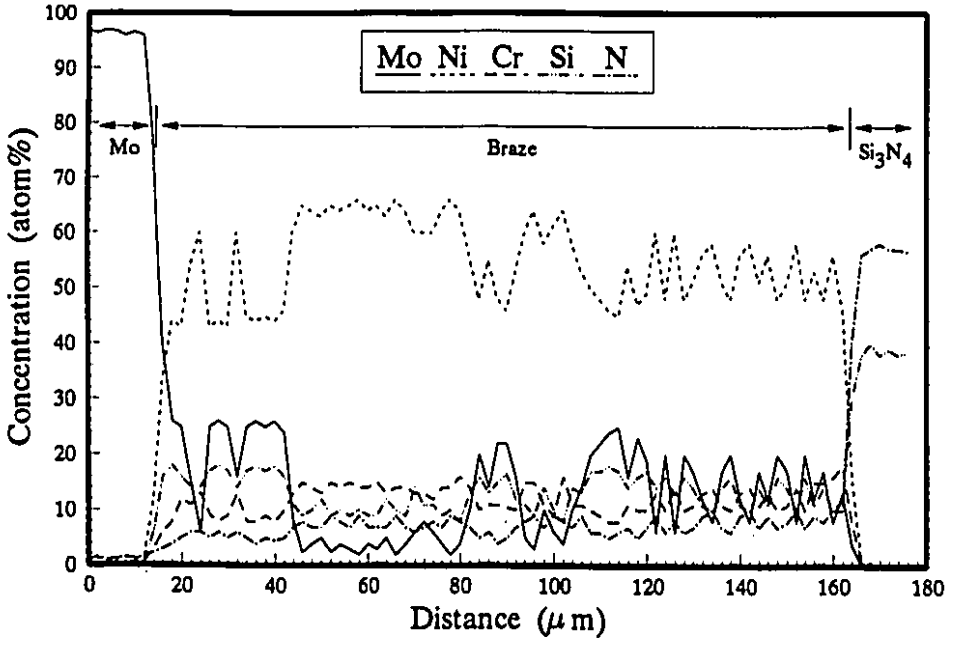

Figure 8.10 EPMA microanalysis line profiles across the joint area in Fig. 8.8b.

at list six samples were tested. The shear strength of the joints was found to be 28±8 MPa, whereas, the joints exhibited a higher four-point bend strength of 55±10 MPa. These results conform to the results of strength measurements on Si_3N_4/Si_3N_4 joints where a higher strength was achieved by using the four-point bend test.

The fractography examination of the Si_3N_4/Mo MOR bars revealed that most

of the bars fractured through the braze layer at the ceramic/braze layer interface that is apparently the weakest plane in the joints. In some cases the cracks, which had initiated at the edge of the sample due to the residual CTE mismatch stresses, propagated under the bending load and fracture occurred in Si_3N_4 near the interface. In fact the influence of edge cracks in determining the joint quality is stronger than the interfacial bond strength by itself. The FEM study (Appendix V) which was primarily aimed towards the effect of joint geometry on the residual stresses in Si_3N_4/Mo joints showed that high tensile CTE mismatch stresses exist in the ceramic near the free edges (Fig. 2, Appendix V) which may explain the edge cracking observed in the experimental joints (Fig. 8.7)

Shear samples exhibited a different fracture mode. As was the case for the Si_3N_4/Si_3N_4 shear samples, the crack which had initiated at the interface changed direction into the Si_3N_4 (Figure 8.11). Since the interfacial strength in this case was

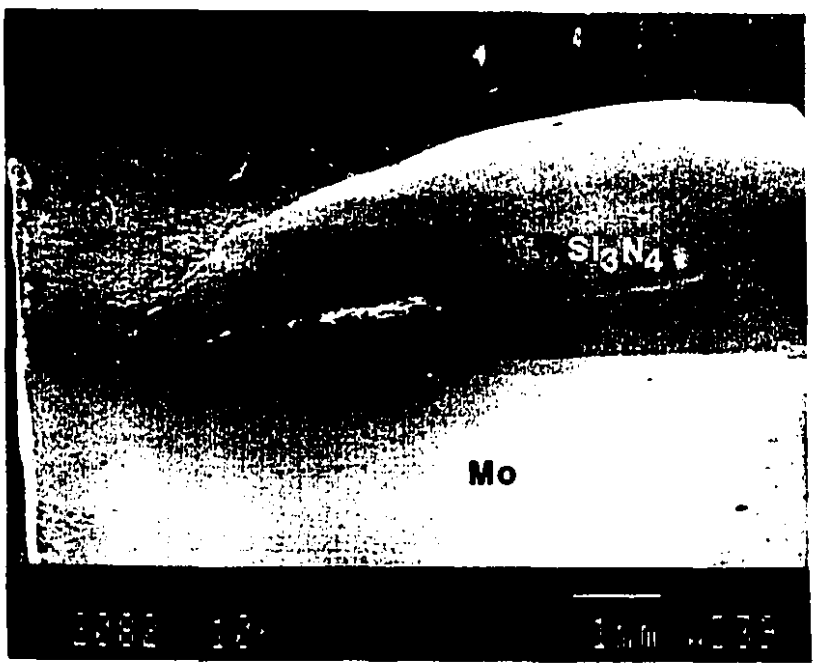

Figure 8.11 Typical fracture surface of Si_3N_4/S10/Mo shear samples.

not as high as the Si_3N_4/Si_3N_4 joints and because of the presence of cracks at the edge of the samples, it is believed that this type of fracture path was due to the edge cracking rather than kinking.

It is worth mentioning that one of the problems observed in all the joining experiments was blushing of Mo by the filler metals, mainly due to the high reactivity between them. This problem, in many cases, resulted in the depletion of the joint gap from the filler metal. An attempt to paint the Mo sides with a so-called "stop-off" agent* (a suspension of fine ZrO_2 powder in a lacquer) failed to prevent the Mo from blushing and the filler metal crept beneath the coated layer.

8.4 Summary of the Si_3N_4/Ni-Cr-Si/Mo Joints.

Brazing experiments were carried out to investigate the brazeability of Si_3N_4 to Mo using a commercially available brazing alloy S19 (AWS BNi-5) and a modified Ni-Cr-Si, S10 alloy, having the same Ni/Cr ratio as that of S19. The selection of the S10 alloy was based on the results of Si_3N_4/Si_3N_4 joining experiments in which strong joints were fabricated using this alloy. In summary:

1. A brazing temperature of 1220°C used in Si_3N_4/Si_3N_4 joining experiments was not suitable for fabrication of Si_3N_4/Mo joints. This was mainly due to the rapid diffusion of Mo into the filler metal, resulting in an increased alloy liquidus temperature; therefore, the brazing temperature was raised to 1300°C.

2. Because of the severe reaction at the ceramic/filler metal interface no bonding occurred at the Si_3N_4/braze layer interfaces of the joints brazed for 10 min. at 1300°C. However, when the brazing time was reduced to 1 min. the interfacial strength increased in the case of both S19 and S10 brazing alloys.

3. The microchemical analysis revealed that the joint microstructures were strongly influenced by the competition between the diffusion of Mo, Si and N from the parent materials. Unlike the Si_3N_4/Si_3N_4 joints in which Cr was the most

* Wall Colmonoy Co., MI, USA.

reactive element in the system and contributed to the interfacial bond formation, Mo was found to be more effective in determining the interfacial strength and chemistry.

4. From these results it was found that the joint quality was strongly influenced by the composition of the filler metal and such brazing variables as brazing time and temperature. In addition, the effect of CTE mismatch cracking in reducing the joint strength needs to be further addressed.

5. The four-point bend strength of the joint was found to be higher than their shear strength. A strength value of ≈55 MPa was achieved for the Si_3N_4/Mo joints brazed for 1 min. at 1300°C using S10 alloy, whereas, the shear strength of the same joints were found to be about 28 MPa. The lower strength of the Si_3N_4/Mo joints compared to that of the Si_3N_4/Si_3N_4 joints was due to (a) different interfacial chemistry which can be translated into different bond strengths, and (b) the presence of Mo, with different mechanical and thermo-mechanical properties compared to Si_3N_4. In addition, the higher brazing temperature magnifies the residual CTE mismatch stresses.

Chapter 9

Conclusions and Recommendations

This chapter includes conclusions that have been drawn from the above thermodynamic approach in predicting wetting of Si_3N_4 by a series of Ni-Cr-Si alloys to be used as brazing filler metals for joining of Si_3N_4 to Si_3N_4 and to Mo, and also the conclusions on the thermodynamic calculations and joining studies on Si_3N_4/Si_3N_4 and Si_3N_4/Mo.

9.1 Thermodynamic Calculations

1. A thermodynamic method was developed to predict wetting at the ceramic/liquid brazing alloy interface. The technique was based on the free energy change of the system as a result of decomposition of the Si_3N_4 and variation of composition of the candidate alloys. The alloys studied were based on the AWS BNi-5 with the same Ni/Cr ratio, but different Si contents. The solution thermodynamic properties of the ternary alloys were calculated from the data of the binary systems using the Toop and Kohler equations.

2. The method showed that under the experimental condition of T=1493 K (1220°C) and P_{N2}=15 Pa, an Ni-Cr-Si alloy with Ni/Cr ratio of 3.5 and X_{Si}=0.25 would be in

thermodynamic equilibrium with Si_3N_4 using the Toop equation. The equilibrium Si content using the Kohler equation were found to be 0.24, slightly different from that using the Toop equation.

3. Experimental verifications confirmed the validity of the calculations, as it showed that the alloys with Si content of less than the equilibrium concentration reacted with and wetted Si_3N_4 ceramic. The degree of wetting increased as the Si content decreased. The results of wetting experiments showed that no wetting occurred between Si_3N_4 and the alloy with X_{Si}=0.3.

4- Both the thermodynamic calculations and experimental verifications showed that the degree to which Si_3N_4 will react with the alloys is strongly influenced by the environmental N_2 partial pressure and temperature. An increase of temperature to 1300°C resulted in an increase of the equilibrium Si content to about 0.3. Under a N_2 partial pressure of 10^5 Pa, no wetting was observed between the ceramic and the experimental Ni-Cr-Si alloys.

5- The study showed the validity of the concept of treating wetting as a reaction between the liquid metal and the surface of the ceramic.

9.2 Effect of the Filler Metal Composition and Brazing Time on the Quality and Microstructure of Si_3N_4/Ni-Cr-Si/Si_3N_4 Joints.

1- Based on the results of the wetting model three different Ni-Cr-Si alloys in terms of their Si content were selected as the brazing filler metals. The alloys consisted of Ni-16.7Cr-25Si, Ni-18Cr-19Si and Ni-20Cr-10Si designated as S25, S19, and S10 respectively. The Si_3N_4/Si_3N_4 brazing experiments were performed at 1220°C under a N_2 partial pressure of 15 Pa for different brazing times ranging from 5 to 15 min..

2- The use of S25 brazing alloy resulted in a weak bonding at the ceramic/filler metal interface. This was due to a) a near-equilibrium composition of S25 alloy in contact with Si_3N_4 under the experimental brazing conditions, and b) the microstructure of the braze layer, consisting mainly of intermetallic phases, which could not accommodate the CTE mismatch stresses during cooling of the joints from the brazing temperature.

3- Joints formed with S19 brazing alloy exhibited a somewhat different braze microstructure and higher strength than that of the S25 joints. The joint microstructures, regardless of the brazing time, were similar to those of the base filler metal, consisting of a γ solid solution, α-Ni_5Si_2 and an intermetallic (π). However, a new phase with a composition of Ni-42Cr-13Si-17N was identified within the braze layer close to the Si_3N_4/braze layer interface. The overall microchemical analysis revealed that the composition of the product alloys was driven towards the equilibrium Si content of 25 atom% predicted by the thermodynamic calculations.

4- The Si_3N_4/Si_3N_4 joints formed with S10 brazing alloy exhibited the highest strength compared to the joints formed with S25 and S19 alloys. The strength of the S10 joints decreased as the brazing time increased from 5 to 15 min.; a high four-point bend strength of ≈120 MPa was achieved for the 5 min.-brazed joints. The formation of a CrN reaction layer at the ceramic/filler metal interface contributed to the high strength of such joints. This layer disappeared after longer brazing times, due to the decrease in the local N_2 partial pressure.

5- The four-point bend strengths of the S10 joints increased as the testing temperature was raised in the range of 500-900°C. A mean strength value of ≈220 MPa was achieved when the joints were tested at 900°C. These results demonstrate the effect of reheating temperature on improving the joints mechanical strength through residual stress relaxation within the joint area.

6- The shear strengths of the Si_3N_4/Si_3N_4 joints were found to be lower than the four-point bend strength of the same joints. The shear samples also presented different fracture mode compared to the MOR measurements. Fractographic examinations of the shear samples revealed that the crack, which initiated at the edge of the samples propagated along the interface and then changed direction into the ceramic until final fracture occurred. Thus, it can be concluded that in spite of the simplicity of the shear test, this method is not recommended for strength evaluation.

7- In general, the strength of the Si_3N_4/Si_3N_4 joints was found to be strongly dependent on the brazing time and to a greater degree on the composition of the brazing filler metal in terms of the Si content. The deviation in the strength values was mainly due to the variation of braze layer thickness and to the unjoined areas at the interface.

9.3 Effect of the Brazing Variables on the Si_3N_4/Ni-Cr-Si/Mo Joints.

Brazing experiments were carried out to study the use of Ni-Cr-Si brazing alloys for joining Si_3N_4 to Mo. Two different compositions, mainly S19 and S10 were selected as the joining vehicles. The S25 composition was not studied since Si_3N_4/Si_3N_4 joining experiments showed that this alloy did not produce strong joints.

1- For the Si_3N_4/Mo joints formed with S19 at 1220°C, no bonding occurred at the ceramic/filler metal interface. The braze layer showed a two zone microstructure as a result of the competition between the diffusion of Mo from the metal side and Si and N from the ceramic side. The microchemical analysis of the product alloy revealed that diffusion of Mo into the liquid brazing alloy altered its chemistry. Thus, at the brazing temperature, the alloy was no longer entirely liquid and therefore inadequately reacted and wet the ceramic.

2- Brazing at a higher temperature (1300°C) resulted in a more uniform microstructure. However, after brazing for 10 min., again no bonding occurred at the ceramic/filler metal interface which was due to the severe reaction between the mating materials. Reducing the brazing time to 1 min. resulted in adequate bond formation at the interface.

3- The Si_3N_4/S10/Mo joints exhibited the same behaviour as the joints formed with the S19 alloy. For the joints formed with S10 alloy at 1300°C for 1 min. brazing time, strong bonding was observed at the ceramic/filler metal interface, whereas the 10 min.-brazed joints showed no bonding or mechanical strength.

4- Unlike the Si_3N_4/Si_3N_4 joints in which Cr was the most reactive element in the system, in this case Mo was found to be the most effective element in determining the joint quality and microstructures. Although no known reaction products were identified at the interface, it is believed that the formation of complex Mo compounds was responsible for debonding at the ceramic/filler metal interface for the 10 min.-brazed joints.

5- As was the case for Si_3N_4/Si_3N_4 joints, reduction of the Si content of the filler metal resulted in higher joint strength. The highest four-point bend strengths achieved for Si_3N_4/Mo joints was ≈ 55 MPa, when these materials were brazed at 1300°C for 1 min. using the S10 alloy. One of the main parameters that contributed in the lower strength of these joints relative to those of the Si_3N_4/Si_3N_4 joints, was the edge cracking observed in nearly all of the joints.

OVERALL CONCLUSIONS

From the overall results of this study, the following conclusions may be drawn:

- The principles of solution thermodynamics provide a strong analytical technique

that can be used for successfully modelling the wetting of liquid brazing alloys at the ceramic/metal interfaces.

- The brazing technique can be used for joining Si_3N_4 to Si_3N_4 and to Mo using Ni-based brazing alloys with well-defined compositions and under controlled brazing conditions.

- Joining of ceramics to metals is a more difficult task than joining of ceramics to ceramics. Firstly, because of the greater chemical complexity of the systems and secondly, because of the presence of higher residual stresses within the joint area due to the differences between the mechanical and thermo-mechanical behaviour of the mating materials.

9.4 Recommendations for Further Investigations

1- Verification of the assumptions made in the thermodynamic calculations by taking into account the dissolution of N_2 from decomposition of Si_3N_4 into the liquid alloy.

2- Extending the solution thermodynamic modelling of wetting to other oxide and non-oxide ceramics such as Al_2O_3, ZrO_2, and AlN for a better evaluation of the calculations methods.

3-Study the influence of variation of Cr and Ni content of the filler metals on both wetting behaviour of the ceramic and the quality and microstructure of Si_3N_4/Si_3N_4 and Si_3N_4/Mo joints.

4- Preparation of TEM samples from the interfacial area of Si_3N_4/SIO/Si_3N_4 joints to study the crystallographic relationships between the CrN reaction layer and the Si_3N_4 ceramic.

5- Study the effect of the ceramic surface roughness and the additive contents of Si_3N_4 (e.g. Al and Y) on the joints strength.

6- Further study of the interfacial reaction products in Si_3N_4/Ni-Cr-Si/Mo joints for better understanding of the bonding mechanisms in such joints.

7- Since the migration of Mo into the liquid filler metal and its reaction with Si_3N_4 were found to be detrimental in the joints quality, a diffusion barrier might be found that restricts the Mo migration. The barrier must be stable at the brazing temperature and not react with either the ceramic or the filler metal.

Contributions to Original Knowledge

This thesis has been the first work to investigate the critical process parameters involved in the application of Ni-based alloys for the joining of Si_3N_4 to Si_3N_4 and to Mo using a brazing technique.

This work has demonstrated the following contributions to original knowledge:

1. The development of a method based on a combination of the principles of solution thermodynamics and surface science to predict the wettability of Si_3N_4 ceramic by the candidate brazing alloys.

2. The application of commercially available BNi-5 brazing alloy and two other modified alloys based on BNi-5 to form Si_3N_4/Si_3N_4 and Si_3N_4/Mo brazed joints.

3. Evaluation of joint quality through microstructural and microchemical analysis and strength testing; establishment of a link between the Si content of the filler metals and the joint mechanical properties. This can be translated into a link between the free energy of wetting and joint quality.

4. Assessing the optimum brazing conditions in terms of brazing time, temperature, and atmosphere under which strong Si_3N_4/Si_3N_4 and Si_3N_4/Mo joints could form.

5. Modification of the BNi-5 alloy, through the results of the thermodynamics calculations into an alloy by which Si_3N_4/Si_3N_4 brazed joints of high strength can be formed.

6. Achievement of the highest strength yet reported for Si_3N_4/Si_3N_4 brazed joints at 900°C.

This work has also confirmed:

-The link between the presence of a CrN reaction layer and joint strength for Si_3N_4/Ni-Cr-Si/Si_3N_4 brazed joints.

- The effect of reheating temperatures on the residual stress relaxation at the interfaces of ceramic/metal joints.

- The validity of the Ni and Cr-rich part of the Ni-Cr-Si system.

and finally:

- Diffusion of parent materials into the brazing alloy can strongly alter the braze chemistry resulting in an increase of the recommended brazing temperature.

References

1. M.K. Murthy, "*Advanced Ceramics*", Report No. 3/86, Office of Industrial Innovation, Dept. of Regional Industrial Expansion, Ottawa, Ont., K1A 0H1, Canada.

2. M.M. Schwartz, "*Ceramic Joining*", American Society for Metals, Metals Park (1990) pp. 1-10.

3. R.R. Tummala, "Ceramics in Microelectronic Packaging", *Am. Ceram. Soc. Bull.*, 67[4] 752-758 (1988).

4. S.T. Buljan and V.K. Sarin, "Improved Productibility Though Application of Silicon Nitride Cutting Tools", Carbide Tool J., May-June (1982).

5. F.F. Lange, "Structural Ceramics: A Question of Fabrication Reliability", J. Mater. for Energy system, 6[2], 107-113 (1984).

6. R.N. Katz, "Applications of High Performance Ceramics in Heat Engine Design", Engineering Ceramics 1984, M.I. Shalmon and D.G. Brandon Eds., Elsiever Applied Science Publishers (1985) pp. 227-249.

7. M.R. Pascucci, "The Role of Ceramics in Engines - An Assessment", Engineering Applications of Ceramic Materials, M.M. Schwartz Ed., American Society for Metals, Metals Park (1985) pp.15-18.

8. W.D. Carruthers and G.L. Boyd, "Automotive Gas Turbine Ceramic Component Testing", Proceeding of the Third International Symposium on Ceramic Materials and Components for Engines, V.J. Tennery, Ed., Am. Ceram. Soc., Las Vegas, NV, Nov. 27-30(1988)pp.32-38.

9. H.E. Helms and S.R. Thrasher, "Ceramic Applications in Turbine Engines (CATE) Development Testing", ibid. pp. 25-31.

10. D.W. Richerson, "*Modern Ceramic Engineering*", Marcel Dekker Inc., New York (1992) pp. 123-203.

11. C.R. Tottle, "An Encyclopedia of Metallurgy and Materials", The Metals Society, Macdonald and Evans Pub., U.K. (1984).

12. D. Carruthers, "Critical Issues for Ceramics for Gas Turbines", Proceeding of the Third International Symposium on Ceramic Materials and Components for Engines, V.J. Tennery, Ed., Am. Ceram. Soc., Las Vegas, NV, Nov. 27-30 (1988)pp. 1258-1272.

13. E.J Nubel, Jr., "Good Opportunities for Advanced Ceramics", Adv. Mater.& Proc., [illegible] 55-60 (1989).

14. M.M. Schwartz, "*Ceramic Joining*", American Society for Metals, Metals Park (1990) pp. 165-170.

15. D.C. Larsen et al, "*Ceramic Materials for Advanced Heat Engines*", Noyes Publications, Park Ridge, New Jersey (1985) pp. 314-347.

16. Charles River Associates, Inc., "Advanced Ceramic Materials", Noyes Publications, Park Ridge, New Jersey (1985) pp. 10-15.

17. L.M. Sheppard, Ed., " Cost-Effective Manufacturing of Advanced Ceramics", *Amer. Ceram. Soc. Bull.*, 70[4] 692-701 (1991).

18. R.N. Penny, "Gas Turbines for Land Transport", Sci. Journal, 54-59, April (1970).

19. C. Suh, Y. Sato, and T. Kojima, "Gas Pressure Sintered Si_3N_4 Components in Spark Ignition (SI) Engines", Proceeding of the Third International Symposium on Ceramic Materials and Components for Engines, V.J. Tennery, Ed., Amer. Ceram. Soc., Las Vegas, NV, Nov. 27-30 (1988) pp. 1320-1333.

20. G.L. White and P.J. Oakly, " Industrial Ceramics - A Survey of Materials Applications and Joining Processes", *Weld. Inst. Res. Bull.*, 9444,1/85/476.3, June (1986) pp. 1-24.

21. J.M. Schoenung, "Markets for advanced Ceramics in Internal Combustion Engines", Proceeding of the Third International Symposium on Ceramic Materials and Components for Engines, V.J. Tennery, Ed., Amer. Ceram. Soc., Las Vegas, NV, Nov. 27-30 (1988) pp. 1246-1258.

22. E. Butler, M.H. Lewis, A. Hey and R.V. Sharples, "Ceramic Joining in Japan", Department of Trade and Industry, U.K. June (1986).

23. M.J. Edirisinghe and J.R.G. Evans, "Review: Fabrication of Engineering Ceramics by Injection Moulding. II. Techniques", *Int. J. High Technology Ceramics*, 2, 249-278 (1986).

24. G.R. Van Houten,"A Survey of Ceramic-to-Metal Bonding", Am. Ceram. Soc. Bull., 38[6] 301-307 (1959).

25. M.M. Schwartz, "*Ceramic Joining*", American Society for Metals, Metals Park (1990) pp. 100-106.

26. A.J. Moorhead, "Direct Brazing of Alumina Ceramics", Advanced Ceramic Materials, 2[2] 159-166 (1987).

27. D.C. Larsen et al, "*Ceramic Materials for Advanced Heat Engines*", Noyes Publications, Park Ridge, New Jersey (1985) pp 4-7.

28. R.L. Tallman, J.C. Mittl, J.G. Jolley and P.V. Kelsey, Jr., , "Joining of Silicon Nitride-Based Ceramics", Strategic and Critical Materials Program Annual Report, May (1985).

29. G. Ziegler, " Thermo-Mechanical Properties of Silicon Nitride and Their Dependence on Microstructure", Materials Science Forum - Preparation and Properties of Silicon Nitride Based Materials", D.A. Bonnell Ed.,Trans Tech Publications Ltd., Switzerland (1989) pp. 162-203.

30. D.W. Richerson, "Modern Ceramic Engineering", Marcel Dekker, Inc., New York (1982) pp. 152-153.

31. H.S.C. Deville, F. Wohler, Liebeg's Ann., Vol. 104 (1857) pp. 256.

32. G. Ziegl, J. Hienrich, and G. Wotting, "Review; Relationships Between Processing, Microstructure and Properties of Dense and Reaction-Bonded Silicon Nitride", *J. Mater. Sci.*, 22, 3041-3086 (1987).

33. K.H. Jack, "Review: Sialons and Related Nitrogen Ceramics", *J. Mater. Sci.*, **11**, 1135-1158 (1976).

34. R.A.L. Drew, "Silicon Nitride and Sialons Ceramics- A Review", Can. Metal. Quater., 27[1], 59-64 (1988).

35. T.B. Troczynski, D. Ghosh, and S.D. Gupta, "Advanced Ceramic Materials for Metal Cutting", Proceed. of the Inter. Symp. on Adv. Struc. Mater., Montreal, Canada, D.S. Wilkinson Ed., Pergamon Press, 157-168 (1988).

36. R. Wertheim, "Improved Tool Life With Silicon Nitride", Machine and Tool Blue Book, 81[1], 66-68 (1986).

37. S. Natansohn, "Silicon Nitride, A Material for Tommorow's Engines?", Proceed. of the ACS, Div. of Polymeric Sci. and Eng., Vol. 53, Pub. by ACS, 297 (1985).

38. M.D. Pugh and R.A.L. Drew, "Fabrication of Si_3N_4 Valve Discs", Proceed. of the Inter. Symp. on Adv. Struc. Mater., Montreal, Canada, D.S. Wilkinson Ed., Pergamon Press, 139-148 (1988).

39. R.F. Coe, R.T. Lumby, and M.F. Pawson, "Some Properties of Hot-Pressed Silicon Nitride", Proceed. 5^{th} Symp. Special Ceram., BCRA, P. Popper Ed., 361- 376 (1972).

40. J. Greim, K. Hunold, K.A. Schwetz, and A. Lipp, "Injection Moulded Sintered Turbocharger Rotors; A Comparison of SSIC with SSN and SRBSN", Proceeding of the Third International Symposium on Ceramic Materials and Components for

Engines, V.J. Tennery, Ed., Amer. Ceram. Soc., Las Vegas, NV, Nov. (1988) pp.1365-1375.

41. D.W. Richerson and P.M. Stephan, "Evolution of Application of Si_3N_4-Based Materials", *Materials Science Forum - Preparation and Properties of Silicon Nitride Based Materials*, D.A. Bonnell Ed.,Trans Tech Publications Ltd., Switzerland (1989) pp. 282-307.

42. B. Vassiliou and F.G. Wild, "A Hexagonal Form of Silicon Nitride", Nature, Vol. 179, 435 (1957).

43.S.N. Ruddlesden and P.Popper, "On the Crystal Structure of the Nitrides of Silicon and Germanium", Acta. Cryst., Vol. 11, 296 (1958).

44. D.S. Thompson and P.L. Pratt, "The Structure of Silicon Nitride", In Science of Ceramics, G.H. Stewart, Ed., Vol. 3, Academic Press (1967) pp. 33-51.

45. G. Schwier, G. Nietfeld, and G. Franz, "Production and Characterization of Silicon Nitride powders", Materials Science Forum - Preparation and Properties of Silicon Nitride Based Materials", D.A. Bonnell Ed.,Trans Tech Publications Ltd., Switzerland (1989) pp. 1-20.

46. W.M. Shen and R.V. Sara, "Characteristics and Processability of Gas Phase Synthesized and Direct Nitridation Si_3N_4 Powders", Conf. Paper Pres. at 1St Int'l Conf. on Ceram. Powder Process. Sci., Orlando, Florida, Nov. 1-4, 1-12 (1987).

47. J.M. Schoenung, "Silicon Nitride Powders: Investigating the Cost of Production", Int'l Symp. Fine Particles, Montreal, 1-11 (1988).

48. D. Segal, "Chemical Synthesis of Advanced Ceramic Materials", Cambridge University Press (1989) p. 129.

49. K.S. Mazdiyasni and C.M. Cooke, "Synthesis, Characterization, and Consolidation of Si_3N_4 Obtained from Ammonolysis of $SiCl_4$", J. Am. Ceram. Soc., 56[12], 628-633 (1973).

50. S. Grenier, "Large Scale Carbothermal Synthesis Submicron Silicon Nitride Powder", M.Sc. Thesis, McGill University, Montreal, Canada, May (1992).

51. J. Weiss and W.A. Kaysser, " Liqui Phase Sintering", Progress in Nitrogen Ceramics, F.L. Riley, Ed., Martinus Nijhoff Publishers (1983) pp. 169-186.

52. M.H. Leipold, "Treatise on Materials Science and Technology", Ceramic Fabrication Processes, Vol. 9, F.F.Y. Wang Ed., Academic Press, Inc., New York (1976) p. 361.

53. D.W. Richerson, "Modern Ceramic Engineering", Marchel Dekker, Inc., New York (1982) pp. 244-248.

54. CRC Handbook of Chemistry and Physics, 72ND Edition, D.R. Lide, Ed., CRC Press (1991-1992) p. 4-18.

55. Volume 2, Metals Handbook, 10th Ed. American Society for Metals, Metals Park (1990) pp. 1140-1142.

56. A. Sutulov, "Molybdenum and Rhenium", University of Conception Press, Chile, (1976) pp. 13-17.

57. A. Sutulov, "International Molybdenum Encyclopedia", Vol III, Alexander Sutulov Intermet Publication, Santiago, Chile (1980) pp. 40-63.

58. J.J. Harwood, "The Metal Molybdenum", Symposium Proceeding, Sept. 18&19, 1956, Published by Amer. Soc. for Metals, Cleveland, Ohio (1956) pp. 420-459.

59. R. Syre, "Handbook on the Properties of Niobium, Molybdenum, Tantalum, Tungsten and Some of Their Alloys" ,Report prepared for Advisory Group for Aerospace Research and Development, NATO, May (1965) pp. 126-128.

60. Volume 13, Metals Handbook, 9th Ed. American Society for Metals, Metals Park (1980) p. 1169.

61. J.J. Harwood, "The Metal Molybdenum", Symposium Proceeding, Sept. 18&19, 1956, Published by Amer. Soc. for Metals, Cleveland, Ohio (1956) pp. 241-261.

62. Volume 6, Metals Handbook, 9th Ed. American Society for Metals, Metals Park (1980) pp. 1049-1060.

63. J.J. Harwood, "The Metal Molybdenum", Symposium Proceeding, Sept. 18&19, 1956, Published by Amer. Soc. for Metals, Cleveland, Ohio (1956) pp. 192-198.

64. R.L. Tallman, R.M. Neilson,Jr., J.C. Mittl, S.P. Henslee, and P.V. Kelsey, Jr., "Joining Silicon Nitride Based Ceramics: A Technical Assessment", Report Prepared for the U.S. Bureau of Mines, EG&G Idaho, Inc., March (1984).

65. S.S. Cole, G. Sommer, "Glass-Migration Mechanism at Ceramic-to-Metal Seal Adherence", J. Am. Ceram. Soc., 44[6], 265-271 (1961).

66. S.H. Chang, "Characterization of Interfacial Reactions in Silver-to-Alumina Bonding,- with a Supplement: A General Model for Metal-to-Ceramic", Ph.D. Thesis, Rutgers University The State U. of New Jersy (New Brunswick) (1981) p. 13.

67. M.M. Schwartz, "Ceramic Joining", American Society for Metals, Metals Park (1990) pp. 17-40.

68. ibid, p. 77.

69. G.R. Van Houten,"A Survey of Ceramic-to-Metal Bonding", *Am. Ceram. Soc. Bull.*, **38**[6] 301-307 (1959).

70. M.G. Nicholas and D.A. Mortimer, "Ceramic/Metal Joining for Structural Application", Mater. Sci. and Tech., Vol.1, 657-665, Sept. (1985).

71. E. Butler, M.H. Lewis, A. Hey, and R.V. Sharples, "Ceramic Joining in Japan", Department of Trade and Industry, U.K., June (1986).

72. R.E. Loehman, "Joining Engineering Ceramics", Proceeding of the International Conference on Advances in Joining Newer Structural Materials, International Institute of Welding, Montreal, July 1990, Pergamon Press, Toronto (1990) pp. 83-98.

73. R.E. Loehman and A.P. Tomsia, "Joining of Ceramics", Am. Ceram. Soc. Bull., **67**[2] 375-380 (1988).

74. F.P. Bailey and W.E. Borbidge, "Solid State Metal-Ceramic Bonding", Mater. Sci. Res., Vol. 14, V.A. Pask and A.G. Evans Ed., Plenum Press, NY (1981) 525-533.

75. M.G. Nicholas and R.M. Crispin, "Diffusion Bonding Stainless Steel to Alumina using Aluminium Interlayers," J. Mater. Sci., **17**, 3347-3360 (1982).

76. J.T. Klomp, "Bonding of Metals to Ceramics and Glasses" Am. Ceram. Soc. Bull., **51**, 683-688 (1972).

77. J.A. Pask, "From Technology to the Science of Glass/Metal and Ceramic/Metal and Sealing", Am. Ceram. Soc. Bull., **66**[11], 1587-1592 (1987).

78. F. Hatakeyama, K. Suganuma, and T. Okamoto, "Solid-State Bonding of Alumina to Austenitic Stainless Steel", J. Mater. Sci., **21**, 2455-2461 (1986).

79. H. Mizuhara, E. Huebel, and T. Oyama, "High-Reliability Joining of Ceramic to Metal", Am. Ceram. Soc. Bull., **68**[9] 1591-1599 (1989).

80. K. Suganuma, T. Okamoto, M. Koizumi, and M. Shimada, "Solid-State Bonding of Oxide Ceramic to Steel", J. Nuclear Mater., **133&134**, 773-777 (1985).

81. H.E. Eaton and R.C. Novak, "Alumina-CoCrAlY Material as an Improved intermediate Layer for Graded Ceramic Gas-Path Sealing in Aeroturbine Engine", Ceram. Eng. Sci. Proc.,7[7-8] 727-735 (1986).

82. K. Suganuma, T. Okamoto, M. Shimada, and M. Koizumi, "New Method for Solid-State Bonding Between Ceramics and Metals", J. Am. Ceram. Soc., 66[7] C117-C118 (1983).

83. M. Ruhle, M. Backhaus-Ricoult, K. Burger, and W. Mader, "Diffusion Bonding of Metal/Ceramic Interfaces- A Model Study at the Nb/Al_2O_3 Interfaces", Mater. Sci. Res., J.A. Pask and A.G. Evans Eds., Vol. 21, 295-305, Plenum Press, NY, (1987).

84. T. Yamada, H. Sekiguchi, H. Okamoto, S. Azuma, A. Kitamura, and K. Fukaya,"Diffusion Bonding SiC or Si_3N_4 to Nimonic 80A", High Temp. Tech., 4[4] 193-200 (1987).

85. M.M. Schwartz, "Ceramic Joining", American Society for Metals, Metals Park (1990) pp. 100-106.

86. E.O. Ballard, E.A. Meyer, and G.M. Brennan, "Brazing of large-Diameter Ceramic Rings to Niobium Using an Active Metal Ticusil Process", Welding Journal, 37-42, Oct. (1985).

87. D.M. Mattox and H.D. Smith, "Role of Manganese in the Metallization of High Alumina Ceramics", Am. Ceram. Soc. Bull., 64[10] 1363-1367 (1985).

88. J. van Esdonk and H.H. van der Sluis, "Ceramic to Metal Seals by Metallising and/or Active Brazing", Engineering applications of Ceramic Materials, M.M. Schwartz Ed., Am. Soc. For Metals (ASM), 227-230 (1985).

89. D.A. Canonico, N.C. Cole, and G.M. Slaughter, "Direct Brazing of Ceramics, Graphite and Refractory Metals", Welding Journal, 31-38, August (1977).

90. M. Naka, M. Kubo, and I. Okamoto, "Metallizing of Silicon Nitride with Amorphous Filler Metal", J. Mater. Sci. Letter, 5, 855-856 (1986).

91. J.P. Hammond, S.A. David, and J.J. Woodhouse, "Indirect Brazing of Structural Ceramics for Uncooled Diesels", Brazing of Structural ceramics for uncooled Diesels, Proc. of 22nd Automotive Technology Contractor Coordination Meeting (1984) pp.523-520.

92. M.L. Santella, "Brazing of Titanium-Vapour-Coated Silicon Nitride", Adv. Ceram. Mater., 3[5] 457-462 (1988).

93. H. Mizuhara and K. Mally, "Ceramic-to-Metal Joining with Active Brazing Filler Metals", Welding Journal, **64**[10] 27-32 (1985).

94. W. Weise, W. Malikowski, and W. Bohm, "Active Brazing Alloys Make Strong, Economical joints", Ceram. Industry, 38-39, Feb.(1990).

95. H. Mizuhara and E. Huebel, "Joining Ceramic to Metal with Ductile Active Filler Metals", Welding Journal, 43-51, Oct.(1986).

96. E. Lugscheider and M. Boretius, "Active brazing of Silicon-Carbide and Silicon-Nitride to Steel Usin[illegible] Thermal-Stress Reducing Metallic Interlayer", In Joining Ceramics, Glass and Metal, W. Kraft Ed., DGM Informationsgesellschaft, FRG (1989) pp. 25-32.

97. K. Suganuma, "New Process for Brazing Ceramics Utilizing Squeeze Casting", J. Mater. Sci., **26**, 5093-5100 (1991).

98. D. Palaith and R. Silberglitt, "Microwave Joining of Ceramics", Am. Ceram. Soc. Bull., **64**[9] 1601-1606 (1989).

99. J.T. Klomp, "Ceramic-Metal Reactions and Their Effect on the Interface Microstructure", In Ceramic Microstructure '86: Role of Interface, Mat. Sci. Res., Vol 21, J.A. Pask and A.G. Evans Eds., Plenum Press, New York (1987) pp. 307-317.

100. S. Morozumi, M. Endo, and M. Kikuchi, "Bonding Mechanism Between Silicon Carbide and Thin Foils of Reactive Metals", J. Mater. Sci., **20**, 3976-3982 (1985).

101. S. Morozumi, M. Kikuchi, and T. Nishino, "Bonding Mechanism Between Alumina and Niobium", J. Mater. Sci.,**16**, 2137-2144 (1981).

102. T. Iseki, T Kameda, and T. Maruyama, "Interfacial Reaction Between SiC and Aluminium During Joining", J. Mater. Sci., **19**, 1692-1698 (1984).

103. Y. Zhou, K. Ikeuchi, T.H. North, and Z. Wang, "Effect of Plastic Deformation on Residual Stress in Ceramic/Metal Interfaces", Metal. Trans., **22A**[11] 2822-2825 (1991).

104. C.H. Hsueh and A.G. Evans, "Residual Stresses in Metal/Ceramic Bonded Strips", J. Am. Ceram. Soc., **68**[5] 241-248 (1985).

105. B.J. Dalgleish, M.C. Lu, and A.G. Evans, "The Strength of Ceramics Bonded with Metals", Acta Metall., **36**[8] 2029-2035 (1988).

106. K. Kokini, "Interfacial Cracks in Ceramic-to-Metal Bonds Under Transient Thermal Loads", J. Am. Ceram. Soc., **70**[12] 855-859 (1987).

107. S.C. Kunz and R.L. Loehman, "Thermal Expansion Mismatch Produced by Interfacial Reaction in Glass-Ceramic to Metal Seals", Adv. Ceram. Mater., 2[1] 69-73 (1987).

108. T. Yamada, K. Yokoi, and A. Kohno, "Effect of Residual Stress on the Strength of Alumina-Steel Joints with Al-Si Interlayer", J. Mater. Sci., 25, 2188-2192 (1990).

109. A. Levy, "Thermal Residual Stresses in Ceramic-to-Metal Brazed Joints", J. Am. Ceram. Soc., 74[9] 2141-2147 (1991).

110. F. Taheri and J.G. Murphy, "Modelling of Ceramic to Metal Brazed Joints- A Fracture Mechanics Finite Element Approach", In proc. of Int. Sym. Processing and Applications of Ceramics and Metal-Matrix Composites, H. Mostaghaci Ed., Pergamon Press, Toronto (1989) pp. 281-29.

111. H.P. Kirchner, J.C. Conway, JR., and A.E. Segall, "Effect of Joint Thickness and Residual Stresses on the Properties of Ceramic Adhesive Joints: I, Finite Element Analysis of Stresses in Joints", J. Am. Ceram. Soc., 70[2] 104-109 (1987).

112. M.D. Drory, M.D. Thouless, and A.G. Evans, "On the Decohision of Residually Stressed Thin Films", Acta Metall., 36[8] 2019-2028 (1988).

113. K. Suganuma, T. Okamoto, and M. Koizumi, "Effect of Thickness on Direct Bonding of Silicon Nitride to Steel", J. Am. Ceram. Soc., 68[12] C_334-C_335 (1985).

114. K. Suganuma, T. Okamoto, and M. Koizumi, "Effect of Interlayers in Ceramic-Metal Joints with Thermal Expansion Mismatch", J. Am. Ceram. Soc., 67[12] C_256-C_257 (1984).

115. T. Yada and H. Koguchi, "Reliability Evaluation of Joints of Ceramics and Metals (Consideration of Thermoelastic-Plastic Stress around the Interface of Joined dissimilar Materials)", JSME Inter. J., Series 1, 34[2] 163-170 (1990).

116. Y. Zhou, F.H. Bao, J.L. Ren, and T.H. North, "Interlayer Selection and Thermal Stresses in Brazed Si_3N_4-Steel Joints", Mat. Sci. Tech., 7[9] 863-868 (1991).

117. T. Tanaka, H. Morimoto, H. Homma, "Joining of Ceramics to Metals," Nippon Steel Technical Report No. 37, April (1988).

118. M. Naka, K. Sampath, I. Okamoto, and Y. Arata, "Influence of Brazing Condition on Shear Strength of Alumina-Kovar Joint Made with Amorphous $Cu_{50}Ti_{50}$ Filler Metal", Trans. JWRI, 12[2] 181-183 (1983).

119. M. Ruhle and W. Mader, "Structure and Chemistry of Metal/Ceramic Interfaces" In Designing Interfaces for Technological Applications: Ceramic-Ceramic and Ceramic-Metal Joining, S.D. Peteves Ed., Elsevier Applied Science NY. (1988) 145-196.

120. I. Okamoto and M. Naka, "Joining of Steels to Alumina with Copper Filler Metal", Engineering Applications of Ceramic Materials, M.M. Schwartz Ed., Am. Soc. for Metals (ASM) (1985) pp. 210-215.

121. M. Naka, K. Sampath, I. Okamoto, and Y. Arata, "Joining of alumina Ceramics to Fe-Ni-Co (Kovar) Alloy Using Amorphous Cu-Ti Filler Metal", Engineering Applications of Ceramic Materials, M.M. Schwartz Ed., Am. Soc. for Metals (ASM) (1985) 205-208.

122. S.V. Pepper, "Shear Strength of Metal-Sapphire Contacts", J. App. Phy., **47**[3] 801-808 (1976)

123. K. Sakata, K. Honma, K. Ogawa, O. Watanabe, and K. Nii, "Interface Chemistry and Bonding Strength for Diffusion-bonded Fe/Fe-FeO/Al_2O_3 Systems", J. Mater. Sci., **21**, 4463-4467 (1986).

124. A.J. Moorhead, H.M. Henson, and T.J. Henson, "The Role of Interfacial Reactions on the Mechanical Properties of Ceramic Brazements", In Ceramic Microstructure '86: Role of Interfaces, J.A. Pask and A.G. Evans Eds., Plenum Press, NY (1987) pp. 949-958.

125. M.M. Schwartz, "Ceramic Joining", American Society for Metals, Metals Park (1990) pp. 53-72.

126. A.J. Moorhead and H. Keating, "Joining of Ceramics for Advanced Heavy-Duty Diesels", Report Prepared for National Aeronautics and Space Administration, US Department of Energy, Document No. ORNL-6262, Oak Ridge National Laboratory, March (1986).

127. A.J. Moorhead, "Direct Brazing of Structural Ceramics for Uncooled Diesels", Oak Ridge National Laboratory Report under contract No. DOE C-74184-D (1985).

128. R.C. Rathner and D.J. Green, "Joining of Yttria-Tetragonal Zirconia Polycrystal with an Aluminum-Zirconium Alloy", J. Am. Ceram. Soc., **73**[4] 1103-1105 (1990).

129. M.L. Santella, J.P. Hammond, S.A. David, and W.A. Simpson, "Ceramic-to-Metal Brazing for Uncooled Diesel Engines", Presented at the 23rd Automotive Technology Contractors Coordination Meeting, Dearborn, Michigan, October (1985).

130. M.A. DeLuca, J.W. Swain, Jr., and L.R. Swank, "An Advanced Ceramic-to-Metal Joining Process", Ceram, Eng. Sci. Proc., 8[7-8] 602-610 (1987).

131. N. Iwamoto, Y. Makino, and H. Miyata, "Joining Silicon Carbide Using Nickel-Active Metal (or Hydride) Powder Mixtures", Ceram. Eng. Sci. Proc., 10[11-12] 1761-1767 (1989).

132. E. Gyarmati, W. Kesternich, and R. Forthmann, "Joining Silicon Carbide with the Aid of Thin Ti-Layer", cfi/Ber. DKG 66, No.7/8, 292-297 (1989).

133. M.R. Jackson, R.L. Mehan, A.M. Davis, and E.L. Hall, "Solid State SiC/Ni Alloy Reaction", Met.Trans. A, 14A[3] 355-364 (1983).

134. R.L. Mehan and R.B. Bolon, "Interaction Between Silicon Carbide and a Nickel-Based Superalloy at Elevated Temperatures", J. Mater. Sci. 14[10] 2471-2481 (1979).

135. R.L. Mehan and D.W. Mckee, "Interaction of Metals and Alloys with Silicon-Based Ceramics", J. Mater. Sci., 11[6] 1009-1018 (1976).

136. M.E. Brito, J. Matsumoto, Y. Hirotsu, Y. Fukuzawa, and K. Tanaka, "Solid State Reaction of Nickel on Silicon Carbide Single Crystal", In Joining Ceramics, Glass and Metal, W. Kraft Ed., DGM Informationsgesellschaft, Germany (1989) pp. 305-312.

137. S.K. Choi, L. Froyen, and M.J. Brabers, "Interfacial Reaction between SiC and Transition Metals, Ti, Cr, Fe, Ni", ibid, pp. 297-304.

138. R.C.J. Schiepers, J.A. Van Beek, E. De Giacomoni, B. Valla, F.J.J. Van Loo, and G. De With, "The Interaction Between SiC and Ni or Fe and their Alloys", to be published in *Scripta Metall. Mat.* (1990).

139. R.L. Mehan and M.R. Jackson, "A Study of solid Metal/Ceramic Reactions", In Surfaces and Interfaces in Ceramic and Ceramic-Metal Systems, J. Pask and A. Evans Eds., Mater. Sci. Res., Vol. 14, Plenum Press, NY (1981) pp. 513-523.

140. R.C.J. Schiepers, F.J.J. Van Loo, and G. De With, "Reaction Between α-Silicon Carbide Ceramic and Nickel or Iron", J. Am. Ceram. Soc., 71[6] C284-C87 (1988).

141. T. Nishino, S. Urai, I. Okamoto, and M. Naka, "Ti_3SiC_2 phase in SiC/SiC Joint Brazed with $Cu_{43}Ti_{57}$ Alloy", J. Mater. Sci. Letter, 9, 1417-1418 (1990).

142. T. Iseki, H. Matsuzaki, and J.K. Boadi, "Brazing of Silicon Carbide to Stainless Steel", Am. Ceram. Soc. Bull., 64[2] 322-324 (1985).

143. H. Okamura, T. Shida, and T. Funamoto, "Brazing of High Thermal Conductivity Ceramics", In Advanced Technology in Welding, Materials Processing and Evaluation, Proceedings of the 5th International Symposium of the Japan Welding Society, Makuhari, Tokyo, Japan, April 17-19 (1990).

144. J.K. Boadi, T. Yano, and T. Iseki, "Brazing of Pressureless-Sintered SiC Using Ag-Cu-Ti Alloy", J. Mater. Sci., 22, 2431-2434 (1987).

145. H. Mizuhara, "Vacuum Brazing Ceramics to Metals", Adv. Mater.& Proc. Metal Progress, 53-55, Feb. (1987).

146. T.J. Moore, "Feasibility Study of the Welding of SiC", J. Am. Ceram. Soc., 68[6] C-151-C-153 (1985).

147. J.R. McDermid, "A Thermodynamic Approach to Brazing SiC", Ph.D. Thesis, Dept. of Mining and Metallurgical Engineering, McGill University, Montreal, Canada (1992).

148. J.R. McDermid and R.A.L. Drew, "Thermodynamic Brazing alloy Design for Brazing Silicon Carbide", J. Am. Ceram. Soc., 74[8] 1855-1860 (1991).

149. R.E. Loehman, "Interfacial Reaction in Ceramic-Metal Systems", Am. Ceramic. Soc. Bull., 68[4] 891-896 (1989).

150. W.E. Hauth III, "Ceramic-to-Ceramic Sealing for Large Shapes", Am. Ceram. Soc. Bull.,58[6] 584-586 (1979).

151. A.P. Xian and Z.Y. Si, "Joining of Si_3N_4 Using $Ag_{57}Cu_{38}Ti_5$ Brazing filler Metal", J. Mater. Sci., 25, 4483-4487 (1990).

152. R.E. Loehman, A.P. Tomsia, J.A. Pask, and S.M. Johnson, "Bonding Mechanism in Silicon Nitride Brazing", J. Am. Ceram. Soc., 73[3] 552-558 (1990).

153. R.K. Brow and R.E. Loehman, "Interfacial Reactions in Metal-Si_3N_4 Bonding", Ceram. Eng. Sci. Proc., 10[11-12] 1685-1695 (1989).

154. A.P. Tomsia, J.A. Pask, and R.E. Loehman, "Joining Nitride Ceramics", Ceram. Eng. Sci. Proc. 10[11-12] 1631-1654 (1989).

155. S.M. Johnson, "The Formation of High Strength Silicon Nitride Joints by Brazing", SRI International, D88-1208 (1988).

156. A.H. Carim, "Transitional Phases at Ceramic-Metal Interface: Orthorhombic, Cubic, and Hexagonal Ti-Si-Cu-N Compounds", J. Am. Ceram. Soc., 73[9] 2764-2766 (1990).

157. S.C. Hsu. E.M. Dunn, K. Ostreicher, and T. Emma, "An Investigation of Interfacial Microstructure and Bonding in Brazed Silicon Nitride-Silicon Nitride and Silicon Nitride-Ni-Cr-Fe Alloy 600 Joints", Ceram. Eng. Sci. Proc., 10[11-12] 1667-1684 (1989).

158. R.R. Kapoor and T.W. Eagar, "Oxidation Behaviour of Silver- and Copper-Based Brazing Filler Metals for Silicon Nitride/Metal Joints", J. Am. Ceram. Soc., 72[3] 448-454 (1989).

159. M. Naka, T. Tanaka, and I. Okamoto, "Joining of Silicon Nitride Using Amorphous Cu-Ti Metal", Trans. JWRI, 16[1] 83-90 (1987).

160. M. Naka, T. Tanaka, I. Okamoto, and Y. Arata, "Non-oxide Ceramics (Si_3N_4, SiC) joints Made with Amorphous $Cu_{50}Ti_{50}$ and $Ni_{24.5}Ti_{75.5}$ Filler Metals", Trans. JWRI, 12[2] 177-180 (1983).

161. H. Sueyoshi, M. Tabata, Y. Nakamura, and R. Tanaka, "Joining of silicon Nitride to SUS304 Stainless Steel Using a Sputtering Method", J. Mater. Sci., 27, 1926-1932 (1992).

162. M. Morita, K. Suganuma, and T. Okamoto, "Fracture of Silicon Nitride Joined with an Aluminium Braze", J. Mater. Sci., 22, 2778-2782 (1987).

163. K. Suganuma, T. Okamoto, M. Koizumi, and M. Shimada, "Method for Preventing Thermal Expansion Mismatch Effect in Ceramic-Metal Joining", J. Mater. Sci. Lett., 4, 648-650 (1985).

164. M.G. Nicholas, D.A. Mortimer, L.M. Jones, and R.M. Crispin, "Some Observations on the Wetting and Bonding of Nitride Ceramics", J. Mater. Sci., 25, 2679-2689 (1990).

165. M. Morita, K. Suganuma, and T. Okamoto, "Effect of Pre-heat-treatment on Silicon Nitride Joining with Aluminium Braze", J. Mater. Sci. Lett., 6, 474-476 (1987).

166. M. Naka, M. Kubo, and I. Okamoto, "Joining of Silicon Nitride with Al-Cu Alloys", J. Mater. Sci., 22, 4417-4421 (1987).

167. S.M. Johnson, "Mechanical Behaviour of Brazed Silicon Nitride" Ceram. Eng. Sci. Proc. 10[11-12] 1846-1853 (1989).

168. F. Edelman, E. Gutmanas, and R. Brener, "Interfacial Reactions in the Al/Si_3N_4/Si and Au/Si_3N_4/Si Systems", Mat. Res. Soc. Symp. Proc., 153, 77-81 (1989).

169. M. Naka, H. Mori, M. Kubo, I. Okamoto, and H. Fujita, "Observation of Al/Si_3N_4 Interface", J. Mater. Sci. Letter, 5, 696-698 (1986).

170. X.S. Ning, K. Suganuma, M. Morita, and T.Okamoto, "Interfacial Reaction Between Silicon Nitride and Aluminium", Phil. Mag. Lett., 55[3] 93-97 (1987).

171. X.S. Ning, K. Suganuma, T. Okamoto, A. Koreeda, and Y. Miyamoto, "Interfacial Strength And Chemistry of Additive-Free Silicon Nitride Ceramics Brazed with Aluminium", J. Mater. Sci., 24, 2879-2883 (1989).

172. X.S. Ning, T. Okamoto, Y. Miyamoto, A. Koreeda, and K. Suganuma, "Reaction Chemistry at Joined Interfaces Between Silicon Nitride and Aluminium", J. Mater. Sci., 26, 4142-4149 (1991).

173. M. Naka, M. Kubo, and I. Okamoto, "Brazing of Si_3N_4 to Metals with Al Filler (Report I)", Trans. JWRI, 18[1] 81-86 (1989).

174. M. Naka, M. Kubo, and I. Okamoto, "Brazing of Si_3N_4 to Metals with Al Filler (Report II)", ibid, 18[2] 33-36 (1989).

175. K. Suganuma, T. Okamoto, and M. Koizumi, "Joining of Silicon Nitride to Silicon Nitride and to Invar Alloy Using an Aluminium Interlayer", J. Mater. Sci., 22, 1359-1364 (1987).

176. A. Wicker, P. Darbon, and F. Grivon, "Solid State Bonding of Metal to Ceramic", Proc. Int. Sym. on Ceramic Components for Engines, Japan (1983).

177. J.T. Klomp,"Thermodynamic of Ceramic-Metal Interfaces," In Designing Interfaces for Technological Applications: Ceramic-Ceramic and Ceramic-Metal Joining, S.D. Peteves, Ed., Elsevier Applied Science, New York (1989) pp. 127-145.

178. J.C. Schuster, "Silicon Nitride-Metal Joints: Phase Equilibria in the Systems Si_3N_4-Cr,Mo,W and Re", J. Mater. Sci., 23[8] 2792-2796 (1988).

179. E. H. Andrews, W. Bonfield, C.K.L. Davies, and A.J. Markham, "Silicon Nitride-Nickel Compatibility: the Effect of Environment", ibid, 7, 1003-1010 (1972).

180. T.W. Orent and R.A. Wagner, "Investigation of the Chemical Bonding of Cr and Ti to Silicon Nitride", J. Vac. Sci. Technol., B 1(3), 844-849, July-Sept. (1983).

181. M. Nakamura and S.D. Peteves, "Solid-State Bonding of Silicon Nitride Ceramics with Nickel-Chromium Alloy Interlayers", J. Am. Ceram. Soc., 73[5] 1221-1227 (1990).

182. S.D. Peteves, M. Moulaert, and M.G. Nicholas, "Interface Microchemistry of Silicon Nitride/Nickel-Chromium Alloy Joints", Metal. Trans., **23A**[6] 1773-1781 (1992).

183. R.L. Mehan, M.R. Jackson, M.D. McConnell, and N. Lewis, "The Solid State Reaction of Silicon Nitride with an Ni-Base Alloy", J. Mater. Sci., **18**, 508-514 (1983).

184. M.J. Bennett and M.R. Houlton, "The Interaction Between Silicon Nitride and Several Iron, Nickel and Molybdenum-Based Alloys", J. Mater. Sci., **14**, 184-196 (1979).

185. K. Suganuma, T. Okamoto, Y. Miyamoto, M. Shimada, and M. Koizumi, " Joining Si_3N_4 to Type 405 Steel with Soft Metal Interlayers", Mater. Sci. Technol., 2[11] 1156-1161 (1986).

186. A.J. Moorhead and P.F. Becher, "Development of a Test for Determining Fracture Toughness of Brazed Joints in Ceramic Materials", Weld. J., **66**[1] 26-32 (1987).

187. R.F. Pabst and G. Elssner, "Adherence Properties of Metal-to-Ceramic Joints", J. Mater. Sci., **15**, 188-196 (1980).

188. P.F. Becher, W.L. Newell, and S.A. Halen, "Application of Fracture Mechanics to the Adherence of Thick Films and Ceramic Brazed Joints", In Fracture Mechanics for Ceramics, Vol. 3, R.C. Bradt, D.P.H. Hasselman and F.F. Lange, Eds., Plenum Press, New York (1978) pp. 463-471.

189. G.D. Quinn and R. Morrell, "Design Data for Engineering Ceramics: A Review of the Flexure Test", J. Am. Ceram. Soc., **74**[9] 2037-2066 (1991).

190. M.L. Santella, "A Review of Techniques for Joining Advanced Ceramics", Am. Cera. Soc. Bull., 71[6] 947-954 (1992).

191. "Flexural Strength of High Performance Ceramics at Ambient Temperature", MIL-STD-1942A (1990).

192. B. C. Allen, W. D. Kingery, "Surface Tension and Contact Angles in Some Liquid Metal-Solid Ceramic Systems at Elevated Temperatures", Trans. Metal. Sci. of AIME, **215**[2], 30, (1959).

193. L. E. Murr, "Interfacial Energies in Metal-Metal, Metal-Ceramic, Metal-Semiconductor, and Related Solid-Solid and Liquid-Solid Systems", in Surfaces and

Interfaces in Ceramic and Ceramic-Metal Systems, Mat. Sci. Res. vol. 14, J.A. Pask and A.G. Evans Eds., Plenum Press, New York (1981) pp. 107-119.

194. M.G. Nicholas, "Interaction at Oxide-Metal Interfaces", Mater. Sci. Forum, vol. 29 (1988) pp. 127-150.

195. D. Mayers," *Surfaces, Interfaces, and Colloids*", VCH Publishers,Inc., New York(1991) pp. 7-14.

196. D.A. Porter and K.E. Easterling, "*Phase Transformations in Metals and Alloys*", Van Nostrand Reinhold (UK) Co. Ltd.(1981) pp. 110-111.

197. M.J. Jaycock and G.D. Parfitt, " *Chemistry of Interfaces*", Ellis Horwood Limited (1981) pp. 136-141.

198. E.T. Turkdogan, "*Physical Chemistry of High Temperature Technology*", Academic Press, New York, NY.(1980) p. 93.

199. P.R. Chidambaram, G.R. Edwards, and D.L. Olson, "A Thermodynamic Criterion to Predict Wetting at Metal-Alumina Interface", Metal. Trans., 23B[4] 215-222 (1992).

200. J.V. Naidich, "The wettability of solids by liquid metals", *Progress in Surface and Membrane Science*, vol 14, D.A. Cadenhead and J.F. Danielli Ed., Academic Press, New York, NY.(1981) p. 353-458.

201. D.K. Chattoraj and K.S. Birdi, "*Adsorption and the Gibbs Surface Excess*", Plenum Press, New York, NY.(1984) pp. 233-235.

202. W. D. Kingery, "Role of Surface Energies and Wetting in Metal-Ceramic Sealing", Am. Ceram. Soc. Bull., 35, 108, (1956).

203. M.M. Schwartz, "*Ceramic Joining*", American Society for Metals, Materials Park, Ohio (1990) pp. 17-24.

204. J.A. Pask, "From Technology to the Science of Glass/Metal and Ceramic/Metal Sealing", Am. Ceram. Soc. Bull., 66[11] 1587-1592(1987).

205. L.E. Murr,"*Interfacial Phenomena in Metals and Alloys*", Addison-Wesley, (1975) pp. 87-162.

206. A.S. Skapski, "A Theory of Surface Tension of Solids-I. Application to Metals," Acta Met., 4, 576-582 (1956).

207. W.R. Tyson, "Surface Energies of Solid Metals," Can. Metal. Quart., 14[4], 307-314 (1975).

208. W.D. Kingery,"*Introduction to Ceramics*", John Wiley & Sons Inc., New York (1960) pp. 191-217.

209. R.H. Bruce, "Aspects of the Surface Energy of Ceramics I-Calculation of Surface Free Energies", In Science of Ceramics, G.H. Stewart Ed. Academic Press, London, Vol. 2 (1965) pp. 359-381.

210. M.W. Barsoum and P.D. Ownby," The Effect of Oxygen Partial Pressure on the Wetting of SiC, AlN, and Si_3N_4 by Si and A Method for Calculating the Surface Energies Involved", in Surfaces and Interface in Ceramic and Ceramic-Metal Systems, Mat. Sci. Res. vol 14, J.A. Pask and A.G. Evans Eds., Plenum Press, New York (1981) pp. 457-466.

211. I.A. Aksay, C.E. Hoge, and J.A. Pask, " Wetting under Chemical Equilibrium and Nonequilibrium Conditions", J. Phys. Chem., 78[12] 1178-1183 (1974).

212. J.A. Pask and A.P. Tomsia, "Wetting, Spreading and Reaction at Liquid-Solid Interfaces", in *Surfaces and Interface in Ceramic and Ceramic-Metal Systems*, Mat. Sci. Res. vol 14, J.A. Pask and A.G. Evans Eds., Plenum Press, New York (1981) pp. 411-419.

213. F. Delanay, L. Froyen, and A. Deruyttere, " The Wetting of Solids by Molten Metals and its Relation to the Preparation of Metal-Matrix Composites", J. Mater. Sci., 22, 1-16(1987).

214. W.D. Kingery and M. Humenik,JR., "Surface Tension at Elevated Temperatures. I. Furnace and Method for Use of the Sessile Drop Method; Surface Tension of Silicon, Iron, and Nickel", J. Phy. Chem., Vol. 57, 359-363 (1953).

215. J.E. McDonald and J.G. Eberhart, "Adhesion in Aluminum Oxide-Metal Systems", Trans. Metal. Soc. AIME, 233[3] 512-517 (1965).

216. M.G. Nicholas & D.A. Mortimer, "Ceramic/Metal Joining for Structural Applications", Mater, Sci. and Tech., 1[9] 557-665 (1985).

217. K. Suganuma, "Joining of Ceramics and Metals", Ann. Rev. Mater. Sci., 18, (1988) pp 47-73.

218. A.J. Moorhead, "Direct Brazing of Alumina Ceramics," Adv. Ceram. Mater., 2[2] 159-166 (1987).

219. M.G. Nicholas, T.M. Valentine, and M.J. Waite, "The wetting of Alumina by Copper Alloyed with Titanium and other Elements", J. Mater. Sci., 15, 2197-2206 (1980).

220. L. L. Jungberg and R. Warren, "Wetting of Silicon Nitride With Selected Metals and Alloys", Ceram. Eng. Sci. Proc., 10[11-12] 1655-1666(1989).

221. M. Naka, M. Kubo, and I. Okamoto,"Brazing of Si_3N_4 to Metals with Al Filler (Report I) -Si_3N_4/Si_3N_4 and Si_3N_4/Ti or Nb Joints-," Trans, JWRI, 18[1] 81-86 (1989).

222. J.G. Li and H. Hausner,"Influence of Oxygen Partial Pressure on the Wetting Behaviour of Silicon Nitride by Molten Silicon", J. Eur. Ceram. Sci., 9, 101-105 (1992).

223. J.A. Champion, B.J. Keene, and S. Allen,"Wetting of Refractory Materials by Molten Metallides", J. Mater. Sci., 8, 423-426 (1973).

224. M.I. Ginsberg and R.H. Krock, US Patent No. 3 399 076 (1968).

225. M.D. Pugh and R.A.L. Drew, "Enhanced Processing of Sintered Silicon Nitride", J. Can. Ceram. Soc., 58[2] 45-49 (1989).

226. ASTM Specification C373,"Annual Book of ASTM Standards", Am. Soc. for Tes. and Mat's., Philadelphia (1982) pp. 145-146.

227. Norman L. Hecht, Steven M. Goodrich, Leon Chuck, and Dale E. McCullum," Mechanical Properties Characterization of One SiC and Two Si_3N_4 Commercially Available Ceramics", Am. Ceram. Soc. Bull., 71[4] 653-59 (1992).

228. H. Mizuhara, E. Huebel, and T. Oyama," High-Reliability Joining of Ceramic to Metal", Ceram. Bull., 68[9] 1591-1599 (1989).

229. J.L. Pouchou and F. Pichoir, "A New Model for Quantitative X-ray Microanalysis, Part I: Application to the Analysis of Homogeneous Samples", Rech. Aérosp., 3, 13-37 (1984).

230. Michael T. Postek, Karen S. Howard, Arthur H. Johnson, and Kathlyn L. McMichael," Scanning Electron Microscopy", Ladd Research Industries, Inc. (1980) pp. 87-89.

231. W.T. Thompson, A.D. Pelton and C.W. Bale, "Facility for the Analysis of Chemical Thermodynamics, Guide to Operations", Ecole Polytechnique Press, University of Montreal, Montreal, Quebec, H3C 3A7, May (1985).

232. E. Lugscheider, O. Knotek, and K. Klohn, "Melting Behaviour of Nickel-Chromium-Silicon System", Thermochem. Acta., **29**, 323-329 (1979).

233. I. Ansara, T.G. Chart, P.Y. Chevalier, K. Hack, G. McHugh, M.H. Rand and P.J. Spenser, "Phase Diagrams for Fe-Cr-Ni Based Alloys, Part I: Phase Diagrams for Binary and Ternary Alloys of Fe, Cr, and Ni with Si and C", Commission of the European Communities Report No. EUR 9657/I/EN (1985).

234. R.W. Guard and E.A. Smith, "Constitution of Nickel-Based Ternary Alloys: V Nickel-Chromium-Silicon System", J. Inst. Met., **88** 369-374 (1959-60).

235. D.A. Mortimer and M. Nicholas, "The Wetting of Carbon by Copper and Copper Alloys", J. Mater. Sci., **5**, 149-155 (1970).

236. P.M. Hansen, "Constitution of Binary Alloys", Second Ed. McGraw-Hill Book Co., New York (1958).

237. P.R. Chidambaram, G.R. Edwards, and D.L. Olson, "A Thermodynamic Criterion to Predict Wettability at Metal-Alumina Interfaces", Metall. Trans., **23B**[4] 215-222 (1992).

238. M.W. Barsoum and P.D. Ownby, "The Effect of Oxygen Partial Pressure on the Wetting of SiC, AlN, and Si_3N_4 by Si and a Method for Calculating the Surface Energies Involved", in *Surfaces and Interfaces in Ceramic and Ceramic-Metal Systems*, Mat. Sci. Res., Vol 14, J. Pask and A. Evans Eds., Plenum Press, New York (1981) pp. 457-466.

239. D.R. Gaskell, "*Introduction to Metallurgical Thermodynamics*", Second Ed., McGraw-Hill, New York (1981) pp. 319-337.

240. O. Kubaschewski and C.B. Alcock, "*Metallurgical Thermochemistry*", Fifth Ed., Pergamon Press, Toronto (1979) pp. 57-64.

241. I. Ansara, "Comparison of Methods for Thermodynamic Calculation of Phase Diagrams", Int. Met. Rev., **24**[1] 20-53 (1979).

242. O. Kubaschewski and C.B. Alcock, "*Metallurgical Thermochemistry*", Fifth Ed., Pergamon Press, Toronto (1979) p. 382.

243. E.T. Turkdogan, "*Physical Chemistry of High Temperature Technology*", Academic Press, New York (1980) p. 20.

244. P. Nash, "The Cr-Ni (Chromium-Nickel) System", Bull. Alloy Phase Diagram, 7[5] 466-476 (1986).

245. L. Kaufman and H. Nesor, "Calculation of the Binary Phase diagrams of Iron, Chromium, Nickel and Cobalt", Z. Metall., 64[4] 249-257 (1983).

246. J.P. Riegert, A. Vermande, and I. Ansara, "Thermodynamic Properties of Cr-Si Alloys at 1900°C", High temp.-High pressure, 5, 231-235 (1973)in French.

247. A.B. Gokhale and G.L. Abbaschian, "The Cr-Si (Chromium-Silicon) System", Bull. Alloy Phase Diagrams, 8[5] 474-484 (1987).

248. P. Nash and A. Nash, "The Ni-Si (Nickel-Silicon) System", Bull. Alloy Phase Diagram, 8[1] 6-14 (1987).

249. X.M. Xue, J.T. Wang, and M.X. Quan, "Wettability and Spreading Kinetics of Liquid Aluminium on Boron Nitride", J. Mater. Sci., 26, 6391-6395 (1991).

250. S.-Y. Oh, J.A. Cornie, and K.C. Russell, "Wetting of Ceramic Particulates with Liquid Aluminum Alloys: Part II. Study of Wettability", Metall. Trans., 20A[3] 533-541 (1989).

251. X.M. Xue, J.T. Wang, and M.X. Quan, "Wettability and Spreading Kinetics of Liquid Aluminium on Boron Nitride", J. Mater. Sci., 26, 6391-6395 (1991).

252. R.R. Kapoor and T.W. Eagar, "Oxidation Behaviour of Silver- and Copper-Based Brazing Filler Metals for Silicon Nitride/Metal Joints", J. Am. Ceram. Soc., 72[3] 448-454 (1989).

253. E.I. Gladyshevskii and L.K. Borusevich, "The Cr-Ni-Si Ternary System", Russ. J. Inorg. Chem., 8[8] 997-1000 (1963).

254. *Handbook of Refractory Compounds*, G.V. Samsonov and I.M. Vinitskii, Eds., Plenum Press, New York (1980) pp. 288-299.

255. R.M. Brick and J.A. Creevy, "Solubility of Nitrogen in Liquid Fe-Cr and Fe-V Alloys", AIME Metals Technol., 7, TP 1165 (1940).

256. K. Suganuma, T. Okamoto, M. Koizumi, and M. Shimada, "Effects of Surface Damage on Strength of Silicon Nitride Bonded with Aluminum", Adv. Ceram. Mater., 1[4] 356-360 (1986).

257. *Handbook of Refractory Compounds*, G.V. Samsonov and I.M. Vinitskii, Eds., Plenum Press, New York (1980) pp. 32-91.

258. ibid, pp. 198-207.

259. M.G. Nicholas, "Bonding Ceramic-Metal Interfaces and Joints", In *Ceramic Microstructures' 86: Role of Interfaces*, Mat. Sci. Res., Vol 21, J.A. Pask and A.G. Evans Eds., Plenum Press, New York (1987) pp. 349-357.

260. M. Nakamura and S.D. Peteves, "Solid-State Bonding of Silicon Nitride Ceramics with Nickel-Chromium Alloy Interlayers", J. Am. Ceram. Soc., 73[5] 1221-1227 (1990).

261. S.D. Peteves, M. Moulaert, and M.G. Nicholas, "Interface Microchemistry of Silicon Nitride/Nickel-Chromium Alloy Joints", Metall. Trans., 23A[6] 1773-1781 (1992).

262. T. Nagano and H. Kato, "Diffusion Bonding of Ceramics: Mullite, ZrO_2-toughened Mullite", J. Mater. Sci., 26, 4985-4990 (1991).

263. G. Ziegler, "Thermo-Mechanical Properties of Silicon Nitride and Their Dependence on Microstructure", *Materials Science Forum - Preparation and Properties of Silicon Nitride Based Materials*, D.A. Bonnell Ed., Trans Tech Publications Ltd., Switzerland (1989) pp. 162-204.

264. K. Yabuta, H. Nishio and H. Okamoto, "High Temperature Bending Strength and Oxidation Resistance of ß-Sialon Prepared with Minimal Grain Boundary Phase", Proceeding of the Third International Symposium on Ceramic Material and Components for Engines, V.J. Tennery, Ed., Amer. Ceram. Soc., Las Vegas, NV, Nov. (1988) pp. 622-630.

265. W.A. Zdaniewski, J.C. Conway, JR., and H.P. Kirchner, "Effect of Joint Thickness and Residual Stresses on the Properties of Ceramic Adhesive Joints: II, Experimental Results", J. Am. Ceram. Soc., 70[2] 110-118 (1987).

266. Y. Yoshino, H. Ohtsu, and T. Shibata, "Thermally Induced Failure of Copper-Bonded Alumina Substrates for Electronic Packaging", J. Am. Ceram. Soc., 75[12] 3353-57 (1992).

267. M-Y. He, A. Bartlett, and A.G. Evans, "Kinking of a Crack out of an Interface: Role of in-plane stress", J. Am. Ceram. Soc., 74[4] 767-771 (1991).

268. M-Y. He and J.W. Hutchinson, "Kinking of a Crack Out of an Interface", Trans. ASME, J. Appl. Mech., 56[6] 270-277 (1989).

269. M.I. Jacobson and D.C. Martin, "Brazing Molybdenum for High-Temperature Service", Weld. J., 34[2] 65s-74s (1955).

270. E. Heikinheimo, A. Kodentsov, J.A. Van Beek, J.T. Klomp and F.J.J. Van Loo, "Reaction in the Systems Mo-Si_3N_4 and Ni-Si_3N_4", Acta. Metall. Mater., 40, S111-S119 (1992).

271. K. Suganuma, M. Takagi, Y. Miyamoto, M. Koizumi, T. Okamoto, and H. Nakata, "Joining of Silicon Nitride to Molybdenum under High Pressure", Nippon-Seramikkusu-Kyokai-Gakujutsu-Ronbunishi, 96[11] 1051-56 (1988).

272. A.H. Sully and E.A. Brandes, "*Chromium*", Plenum Press, New York (1967) pp.346-348.

273. R.W. Guard and E.A. Smith, "Constitution of Nickel-Based Ternary Alloys: II. Nickel-Molybdenum-Silicon System", J. Inst. Met., 88, 285-287 (1959-60).

274. L.S. Darken, "Application of the Gibbs-Duhem Equation to ternary and Multicomponent Systems.", J. Am. Chem. Soc., 72[2A] 2909-2914 (1950).

275. G.W. Toop," Predicting Ternary Activities Using Binary Data", Trans. Met. Soc. AIME, 233[5] 850-855 (1965).

276. R.J. Fruehan, "The Activity of Cr in Liquid Ni-Cr Alloys", Trans. TMS-AIME, 242, 2007-08 (1968).

277. S.W. Gilby and G.R. St. Pierre, "Equilibrium Vapour Compositions and Activity of Components for Fe-Cr-Ni Alloys at 1600°C", Trans. TMS-AIME, 245, 1749-58 (1969).

278. J.P. Riegert, A. Vermande, and I. Ansara, "Thermodynamic Properties of Cr-Si Alloys at 1900°C", High-Temp.-High Pressures, 5, 231-235 (1973).

Appendix I

Thermodynamic properties of Ternary Solutions

In this appendix, the derivation of the Toop and Kohler equations will be briefly reviewed. All the subsequence discussion refers to the discussions of Darken[274], Toop[275], Gaskell[239], and Kubaschewski[240] on the subject. As a preliminary step, the partial molar aspect of the extensive thermodynamic properties will be briefly reviewed.

The value of any extensive thermodynamic properties of a species i in a mixture of i, j, k, .., per mole of that species is called the *partial molar value of that property* and is formally defined as:

$$\overline{Q_i} = \left(\frac{\partial Q'}{\partial n_i}\right)_{T,P,n_j n_k,\ldots} \qquad \text{(AI.1)}$$

where Q' is the value of the extensive property of the arbitrary quantity of the mixture. $\overline{Q}$ is thus defined as the change in the value of Q' of the mixture for an small addition of the component i, at constant temperature and pressure, and mole numbers of all other components, per mole of i added. Thus if $\overline{Q}_i$ is the value of Q per mole of i as it occurs in the solution, then the value of Q' for the solution itself is:

$$Q' = n_i\overline{Q_i} + n_j\overline{Q_j} + n_k\overline{Q_k} + \ldots. \qquad \text{(AI.2)}$$

API.1 The Gibbs-Duhem equation

It is frequently found that the extensive thermodynamic properties of only

one component (e.g. the activities) in a binary (or multicomponent) solution are amenable to experimental measurement. In such cases the corresponding properties of the other components can be obtained by means of a general relationship between the values of the property for the two components. This relationship, which is known as the Gibbs-Duhem relationship, was found independently in 1875 by J.W. Gibbs and in 1886 by Duhem.

An extensive thermodynamic property of a solution Q', can be written as:

$$Q' = Q'(T,P,n_i,n_j,n_k,\dots) \tag{AI.3}$$

Eq. (AI.3) express that Q' is a function of the temperature, the pressure, and the number of the various solution components. Thus, at constant T and P the variation of Q' with composition is given as:

$$dQ' = \left(\frac{\partial Q'}{\partial n_i}\right)_{T,P,n_j,n_k,\dots} dn_i + \left(\frac{\partial Q'}{\partial n_j}\right)_{T,P,n_i,n_k,\dots} dn_j + \left(\frac{\partial Q'}{\partial n_k}\right)_{T,P,n_i,n_j,\dots} dn_k + \dots \tag{AI.4}$$

with respect to the Eq. (AI.1), Eq. (AI.4) can be written as:

$$dQ' = \overline{Q_i} dn_i + \overline{Q_j} dn_j + \overline{Q_k} dn_k + \dots. \tag{AI.5}$$

differentiation from Eq. (AI.2) will give:

$$dQ' = n_i d\overline{Q_i} + n_j d\overline{Q_j} + n_k d\overline{Q_k} + \dots + \overline{Q_i} dn_i + \overline{Q_j} dn_j + \overline{Q_k} dn_k + \dots \tag{AI.6}$$

Comparison of Eq. (AI.5) and (AI.6) indicates that, at constant T and P:

$$n_i d\overline{Q_i} + n_j d\overline{Q_j} + n_k d\overline{Q_k} + \ldots = 0 \qquad \text{(AI.7)}$$

or, generally:

$$\sum_i n_i d\overline{Q_i} = 0 \qquad \text{(AI.8)}$$

Dividing by the total number of moles of all solution components (n), gives:

$$\sum_i X_i d\overline{Q_i} = 0 \qquad \text{(AI.9)}$$

Equations (AI.8) and (AI.9) are equivalent expressions of the Gibbs-Duhem equation.

AI.2 Darken's equation

Application of the Gibbs-Duhem equation to a binary system, in terms of the free energy will yield the relation:

$$\overline{G_i} = G + (1-X_i)\left(\frac{dG}{dX_i}\right) \qquad \text{(AI.10)}$$

For a ternary A-B-C system, at constant X_A/X_C, and when only the component B is allowed to vary, we may then write:

$$\overline{G_B} = G + (1+X_B)\left(\frac{\partial G}{\partial X_B}\right)_{\frac{X_A}{X_C}} \qquad \text{(AI.11)}$$

By rearranging terms and dividing by $(1-X_B)^2$, and integration from $X_B=1$ to X_B gives:

$$G - (1-X_B) \lim_{X_B \to 1} \left(\frac{G}{1-X_B} \right) = (1-X_B) \int_1^{X_B} \frac{\overline{G_B}}{(1-X_B)^2} dX_B \qquad \text{(AI.12)}$$

This relation can be applied to the excess molar free energy of mixing G^{xs} which is defined as:

$$G^{xs} = G - G^{id} \qquad \text{(AI.13)}$$

where G^{id} is the ideal contribution to the free energy. In terms of the partial molar excess free energy:

$$\overline{G}_B^{xs} = \overline{G}_B - \overline{G}_B^{id} = RT \ln \gamma_B \qquad \text{(AI.14)}$$

where γ_B is the activity coefficient of component B. Equation (AI.12) now becomes:

$$G^{xs} - (1-X_B) \lim_{X_B \to 1} \left(\frac{G^{xs}}{1-X_B} \right) = (1-X_B) \int_1^{X_B} \frac{\overline{G}_B^{xs}}{(1-X_B)^2} dX_B \qquad \text{(AI.15)}$$

Integration of Eq. AI.15 (details of the analysis can be found in the Darken's article[274]) will give the Darken's equations:

$$G^{xs} = (1-X_B) \left[\int_1^{X_B} \frac{\overline{G}_B^{xs}}{(1-X_B)^2} dX_B \right]_{\frac{X_A}{X_C}} - X_A \left[\int_1^{0} \frac{\overline{G}_B^{xs}}{(1-X_B)^2} dX_B \right]_{X_C=0} - X_C \left[\int_1^{0} \frac{\overline{G}_B^{xs}}{(1-X_B)^2} dX_B \right]_{X_A=0} \qquad \text{(AI.16)}$$

This is the final equation expressing the excess molar free energy of a ternary

solution in terms of the partial molar excess free energy of only one component.

Substituting Eq. (AI.14) into Eq. (AI.16) gives:

$$\frac{G^{xs}}{RT} = (1-X_B)\left[\int_1^{X_B} \frac{\ln\gamma_B(in\ ternaryABC)}{(1-X_B)^2}\,dX_B\right]_{\frac{X_A}{X_C}} - X_A\int_1^0 \frac{\ln\gamma_B(in\ binaryAB)}{(1-X_B)^2}\,dX_B - X_C\int_1^0 \frac{\ln\gamma_B(in\ binaryBC)}{(1-X_B)^2}\,dX_B \qquad \text{(AI.17)}$$

Equations (AI.16) express that if the activity coefficient of B in the ternary ABC system is known, then the right hand side of the equation would contain only binary terms which are more readily available than the ternary terms.

AI.3 The Toop and Kohler equations

The object of the Toop equation is to demonstrate the reverse of the Darken's equation, that is, if the thermodynamic properties of all three binaries of a ternary system are known, the thermodynamic properties of the ternary system can be predicted. The method is considered to be accurate only if all three binary systems are regular solutions, i.e., $ln\ \gamma_i = \alpha(1-X_i)^2$, where α is a constant.

Toop showed that a possible solution to Eq. (AI.17) can be given by:

$$\ln\gamma_{B(ABC)} = \left[\frac{X_A}{1-X_B}\ln\gamma_{B(AB)} + \frac{X_C}{1-X_B}\ln\gamma_{B(BC)}\right]_{X_B} -(1-X_B)^2\left[\frac{G^{xs}_{AC}}{RT}\right]_{\frac{X_A}{X_C}} \qquad \text{(AI.18)}$$

The final form of the Toop equation is given as (the details of the analysis can be find in the Toop article[275]):

$$G_{ABC}^{XS} = \left[\frac{X_A}{1-X_B} G_{AB}^{XS} + \frac{X_C}{1-X_B} G_{BC}^{XS} \right]_{X_B} + (1-X_B)^2 \left[G_{AC}^{XS} \right]_{\frac{X_A}{X_C}} \quad \text{(AI.19)}$$

the definition and location of the terms in Eq. (AI.19) is given in Figure 6.3a.

Kohler obtained another solution which can be obtained from the Darken equation by choosing different integration paths (Fig. 6.3b) but again assuming regular behaviour along these. The path of integration are now along constant ratios X_A/X_B, X_B/X_C, and X_C/X_A to yield the equation:

$$G_{ABC}^{XS} = (1-X_C)^2 \left[G_{AB}^{XS} \right]_{\frac{X_A}{X_B}} + (1-X_B)^2 \left[G_{AC}^{XS} \right]_{\frac{X_A}{X_C}} + (1-X_A)^2 \left[G_{BC}^{XS} \right]_{\frac{X_B}{X_C}} \quad \text{(AI.20)}$$

Although the Toop and Kohler equations have been derived for the excess Gibbs energy, these equations are also applicable to the enthalpy and excess entropy of mixing.

Appendix II

Thermodynamic Calculations

This appendix presents the programs written in "FORTRAN 77" for the calculation of the total free energy change of reaction between Si_3N_4 and Ni-Cr-Si alloys (ΔG_r) along with the samples of calculations. These calculations resulted in generation of the plots presented in § 6.1.1 of this thesis.

AII.1 Sample of the calculations

a) Using the Toop equation

The following calculations will determine the total free energy change of the reaction between Si_3N_4 and a Ni-20Cr-10Si atom% (i.e. S10) alloy at 1493K and pN_2=15 Pa ($\approx 1.5^{-4}$ atm), defined as E in the program. The following assumptions was made for the calculations and scaling up the reaction between the ceramic and the liquid alloy:

- 0.001 mol of the alloy (defined as X in the program) will react with 10^{-6} mol of the ceramic. This value which is defined as Y in the program was calculated based on the assumption that the reaction will occur between the alloy and a thickness of 2μ of the ceramic over a area of 0.2 cm^2. With respect to molar weight and theoretical density of Si_3N_4 (140 g mol^{-1} and 3.27 g cm^{-3} respectively) this value (Y) was calculated to be 9.37×10^{-7} mol ($\approx 10^{-6}$ mol).
- The standard state was taken to be the pure elemental liquid in the computation of Gibbs energy of Ni-Cr-Si ternary alloys.

To calculate the ΔG_r, one must calculate ΔG_1, ΔG_2, and ΔG_3 in Eq. 6.5. ΔG_1 which is free energy change of decomposition of 10^{-6} mol of Si_3N_4 on the surface,

with respect to Eqs. 6.6 to 6.10 and the to the following values was calculated as:

$\Delta G^{\circ}_{Si_3N_4} = 740{,}568+24.09TlogT-402.9T \quad J\ mol^{-1} \quad (Ref.\ 242)$

$a_{Si_3N_4} = 0.9$

$a_{Si} = 1$

$G^{xs}_{Si_3N_4} = 29698 \quad J\ mol^{-1} \quad (calculated\ from:\ V_{m\,Si_3N_4}=\frac{140}{3.27}=42.8\ and\ m=\frac{1}{4})$

thus:

$\Delta G_1 = 6.24 \quad mJ$

ΔG_2, which represents the free energy change of fusion of $3x10^{-6}$ mol Si (from decomposition of 10^{-6} mol of Si_3N_4) was determined to be:

$\Delta G_2 = (50530-29.99T)x3x10^{-6} = 17.26 \quad mJ$

The last term to be calculated in Eq. 6.5 for determining the total free energy change of the reaction is ΔG_3 which is free energy change of 10^{-3} mol of the liquid Ni-18Cr-20Si atom% alloy as a result of addition of $3x10^{-6}$ mol of liquid Si, which change the composition of the starting alloy. Thus, ΔG_3 will be the free energy change of the following reaction:

$(10^{-3})\ Ni\text{-}20Cr\text{-}10Si + (3x10^{-6})\ Si = (10^{-3}+3x10^{-6})\ Ni\text{-}19.94Cr\text{-}10.27Si$

The free energy change of the above reaction can be calculated by knowing the Gibbs energy of the ternary Ni-Cr-Si solutions with the above compositions. As mentioned previously, Toop and Kohler equations were used for determining the

Gibbs energy of the ternary Ni-Cr-Si system from the binary data; Ni-Cr, Ni-Si, and Cr-Si systems. The following formula was used to compute the binary system compositions from the ternary composition when using the "Toop" equation (see Figure 6.4a; taking A=Ni, B=Si, and C=Cr):
in Ni-Si and Cr-Si systems,

$$X_{Si_{binary}} = X_{Si_{ternary}}$$

$$X_{Ni_{binary}} = (1 - X_{Si_{binary}}) \quad and \quad X_{Cr_{binary}} = (1 - X_{Si_{binary}})$$

in Ni-Cr system,

$$X_{Ni_{binary}} = \frac{X_{Ni_{ternary}}}{X_{Ni_{ternary}} + X_{Cr_{ternary}}}$$

$$X_{Cr_{binary}} = (1 - X_{Ni_{binary}})$$

Using the Toop equation and with respect to the above formulae and the data given in Table 6.1, the free energy of the reaction AII.1, which represents the ΔG_3 was calculated to be:

$$\Delta G_3 = -182.1 \quad mJ$$

Finally, the total free energy of the reaction (ΔG_r) between Si_3N_4 and the Ni-20Cr-10Si alloy (denoted as GR in the program) will be the sum of ΔG_1, ΔG_2, and ΔG_3:

$$\Delta G_r = \Delta G_1 + \Delta G_2 + \Delta G_3 = 6.24 + 17.26 - 182.1 = -158.6 \quad mJ$$

This procedure was repeated by the program for $0.5 < X_{Si} < 0.95$ at intervals of $X_{Si}=0.05$. The output of the program consists of 6 columns. Columns 1 and 2 show the X_{Si} in the reactant alloys and product alloys, respectively, columns 3,4, and 5

represent the ΔG_1, ΔG_2, and ΔG_3 respectively, and column 6 shows the total free energy change of the reaction (ΔG_r).

Although it is not shown in the output of the program, by modifying just the "WRITE" command, the program will provide such information as G^{XS} of Ni-Si system (denoted as XNS), Cr-Si system (denoted as XCS), and Ni-Cr system (denoted as XNC), as a function of the alloy compositions. The G^{XS} of the ternary Ni-Cr-Si system with Ni/Cr=3.5, as a function of Si content (denoted as XNCS) can also be included in the output of the program if desired.

The following will show the program to calculate the ΔG_r as a function of Si content in the reactant alloy using the Toop equation. The input of the program will allow for the calculations under the conditions of T=1493K and pN_2=15 Pa. The output was then used to generate Figure 6.4.

```
c*********************************************************
c  This program will calculate the free energy change of the
c  reaction between silicon nitride and Ni-Cr-Si alloys with
c  Ni/Cr=3.5 as a function of Si content of the reactant alloys.
c*********************************************************

      IMPLICIT REAL*8(A-H,O-Z)

      COMMON /B2/ B,XO,T

      OPEN (3,FILE='TOOP.DAT',ACCESS='APPEND',FORM='FORMATTED')

c*********************************************************
c  The following part defines the input of the program
c  in which, B1=XSi of the reactant alloy, X=amount of the
c  alloy, Y=amount of the ceramic to react with the alloy,
c  T=temperature, and E= partial pressure of nitrogen.
c*********************************************************

            B1=0.05D0
```

```
      X=0.001D0
      Y=1.0D-6
      T=1493.0D0
      E=1.5D-4
      H=10D0


    WRITE(3,*) 'T=',T, 'K',    'pN2=',E,  'atm'
    WRITE(3,*)
    WRITE(3,*) 'XSi in   XSi in     DG1    DG2    DG3     DGr '
    WRITE(3,*) 'reactant  Product'
    WRITE(3,*) 'alloy     alloy'
    WRITE(3,*)
c*************************************************************
c  The following part will calculate the Gibbs energy of the
c  reactant alloys.
c*************************************************************
    DO 100 I=1,19
    B=B1
    CALL CALCUL
    U=XO
    R=U*X

c*************************************************************
c  In this part, first, the Si content of the product alloy,
c  and second the Gibbs energy of the product alloys will
c  be calculated.
c*************************************************************
    B=(X*B1+3.0D0*Y)/(X+3.0D0*Y)
    CALL CALCUL
    W=XO
    P=W*(X+3.0D0*Y)

c*************************************************************
c  In the following part, the free energy of dissociation of
c  silicon nitride on the surface (denoted as G1) and the free
```

```
c  energy change of fusion of Si (denoted as G2), the free
c  energy change as a result of addition of Si in the reactant
c  alloy (G3), and the total free energy change of the system
c  will be calculated.
c*************************************************************

      G1=((177000.0 +5.76*T*(LOG(T)/LOG(H))- 96.3*T)*4.184
     $    + 8.314D0*T*LOG((E*E)/0.9D0)-29698.0)*Y
      G2=((12080.-7.17*T)*4.184)*3.0D0*Y
      G3=P-(R-83085.0*3.0D0*Y)
      GR=G1+G2+G3
      WRITE(3,15) B1,B,G1,G2,G3,GR
 15   FORMAT(2(F5.4,6X),4(F7.5,4X))


      B1=B1+0.05D0
 100  CONTINUE
      STOP
      END

c*************************************************************
c  The following subroutine will first calculate the excess free
c  energy of the Ni-Si (XNS), Cr-Si (XCS), and Ni-Cr (XNC) systems
c  and then based on those values by using the Toop equation will
c  calculate the excess free energy of the ternary NI-Cr-Si alloys
c  (XNCS). The last step, is the calculation of the Gibbs energy
c  of the ternary alloys at the temperature of interest (XO).
c*************************************************************

      SUBROUTINE  CALCUL

      IMPLICIT REAL*8(A-H,O-Z)
      COMMON /B2/ B,XO,T

      C=(1.0D0-B)/4.5D0
      A=3.5*C
```

```
      XNS=-B*(A+C)*(259994.*(A+C)+133888.*B)+T*B*(A+C)
     $  *(62.01*(A+C)+22.01*B)

      XCS=-B*(A+C)*((36409.+223060.*B-177882*B**2)
     $  +   T*(28.73-26.56*B))
      XNC=-8368.*A*C/(A+C)**2
      XNCS=(A*XNS/(1.-B)+C*XCS/(1.-B))+XNC*(1-B)**2
      XO=XNCS+ T*8.314*(A*LOG(A)+B*LOG(B)+C*LOG(C))

      RETURN
      END
```

Output of the program to generate Fig. 6.4

T=1493.0K pN2=1.50D-004 atm

XSi in reactant alloy	XSi in Product alloy	DG1	DG2	DG3	DGr
.0500	.0528	0.00624	0.01726	-.25218	-.22868
.1000	.1027	0.00624	0.01726	-.18213	-.15863
.1500	.1525	0.00624	0.01726	-.12432	-.10082
.2000	.2024	0.00624	0.01726	-.07306	-.04956
.2500	.2522	0.00624	0.01726	-.02671	-.00321
.3000	.3021	0.00624	0.01726	0.01533	0.03883
.3500	.3519	0.00624	0.01726	0.05334	0.07684
.4000	.4018	0.00624	0.01726	0.08746	0.11096
.4500	.4516	0.00624	0.01726	0.11778	0.14128
.5000	.5015	0.00624	0.01726	0.14438	0.16788
.5500	.5513	0.00624	0.01726	0.16739	0.19089
.6000	.6012	0.00624	0.01726	0.18692	0.21042
.6500	.6510	0.00624	0.01726	0.20317	0.22668
.7000	.7009	0.00624	0.01726	0.21636	0.23986
.7500	.7507	0.00624	0.01726	0.22674	0.25024
.8000	.8006	0.00624	0.01726	0.23462	0.25812
.8500	.8504	0.00624	0.01726	0.24038	0.26388
.9000	.9003	0.00624	0.01726	0.24442	0.26792
.9500	.9501	0.00624	0.01726	0.24721	0.27071

Output of the program to generate Fig. 6.6

T=1493.0K pN2=1.50D-004 atm

XSi in reactant alloy	XSi in Product alloy	DG1	DG2	DG3	DGr
.0500	.0528	0.03594	0.01726	-.25218	-.19899
.1000	.1027	0.03594	0.01726	-.18213	-.12893
.1500	.1525	0.03594	0.01726	-.12432	-.07112
.2000	.2024	0.03594	0.01726	-.07306	-.01986
.2500	.2522	0.03594	0.01726	-.02671	0.02648
.3000	.3021	0.03594	0.01726	0.01533	0.06853
.3500	.3519	0.03594	0.01726	0.05334	0.10654
.4000	.4018	0.03594	0.01726	0.08746	0.14066
.4500	.4516	0.03594	0.01726	0.11778	0.17097
.5000	.5015	0.03594	0.01726	0.14438	0.19758
.5500	.5513	0.03594	0.01726	0.16739	0.22058
.6000	.6012	0.03594	0.01726	0.18692	0.24012
.6500	.6510	0.03594	0.01726	0.20317	0.25637
.7000	.7009	0.03594	0.01726	0.21636	0.26956
.7500	.7507	0.03594	0.01726	0.22674	0.27993
.8000	.8006	0.03594	0.01726	0.23462	0.28782
.8500	.8504	0.03594	0.01726	0.24038	0.29358
.9000	.9003	0.03594	0.01726	0.24442	0.29762
.9500	.9501	0.03594	0.01726	0.24721	0.30041

Output of the program to generate Fig. 6.7

T=1493.0K pN2=1.0 atm

XSi in reactant alloy	XSi in Product alloy	DG1	DG2	DG3	DGr
.0500	.0528	0.22483	0.01726	-.25218	-.01010
.1000	.1027	0.22483	0.01726	-.18213	0.05996
.1500	.1525	0.22483	0.01726	-.12432	0.11777
.2000	.2024	0.22483	0.01726	-.07306	0.16903
.2500	.2522	0.22483	0.01726	-.02671	0.21537
.3000	.3021	0.22483	0.01726	0.01533	0.25742
.3500	.3519	0.22483	0.01726	0.05334	0.29543
.4000	.4018	0.22483	0.01726	0.08746	0.32955
.4500	.4516	0.22483	0.01726	0.11778	0.35986
.5000	.5015	0.22483	0.01726	0.14438	0.38647
.5500	.5513	0.22483	0.01726	0.16739	0.40947
.6000	.6012	0.22483	0.01726	0.18692	0.42901
.6500	.6510	0.22483	0.01726	0.20317	0.44526
.7000	.7009	0.22483	0.01726	0.21636	0.45844
.7500	.7507	0.22483	0.01726	0.22674	0.46882
.8000	.8006	0.22483	0.01726	0.23462	0.47671
.8500	.8504	0.22483	0.01726	0.24038	0.48247
.9000	.9003	0.22483	0.01726	0.24442	0.48651
.9500	.9501	0.22483	0.01726	0.24721	0.48930

Output of the program to generate Fig. 6.10

T=1573.0K pN2=1.50D-004 atm

XSi in reactant alloy	XSi in Product alloy	DG1	DG2	DG3	DGr
.0500	.0528	-.03066	0.01006	-.24966	-.27026
.1000	.1027	-.03066	0.01006	-.17960	-.20020
.1500	.1525	-.03066	0.01006	-.12220	-.14279
.2000	.2024	-.03066	0.01006	-.07142	-.09202
.2500	.2522	-.03066	0.01006	-.02556	-.04616
.3000	.3021	-.03066	0.01006	0.01605	-.00455
.3500	.3519	-.03066	0.01006	0.05368	0.03309
.4000	.4018	-.03066	0.01006	0.08749	0.06690
.4500	.4516	-.03066	0.01006	0.11757	0.09697
.5000	.5015	-.03066	0.01006	0.14399	0.12340
.5500	.5513	-.03066	0.01006	0.16688	0.14628
.6000	.6012	-.03066	0.01006	0.18635	0.16575
.6500	.6510	-.03066	0.01006	0.20258	0.18199
.7000	.7009	-.03066	0.01006	0.21579	0.19519
.7500	.7507	-.03066	0.01006	0.22622	0.20563
.8000	.8006	-.03066	0.01006	0.23419	0.21360
.8500	.8504	-.03066	0.01006	0.24005	0.21946
.9000	.9003	-.03066	0.01006	0.24421	0.22361
.9500	.9501	-.03066	0.01006	0.24710	0.22651

b) Using the Kohler equation

The same procedure outlined in the previous section was used for the calculation of ΔG_r using the Kohler equation, except that, for the calculation of Gibbs energy of ternary Ni-Cr-Si alloys the Kohler equation was used instead.

The following formula was used to compute the binary system compositions from the ternary composition (see Figure 6.4b; taking A=Ni, B=Si, and C=Cr):
in Ni-Cr system:

$$X_{Ni_{binary}} = \frac{X_{Ni_{ternary}}}{X_{Ni_{ternary}} + X_{Cr_{ternary}}} \quad and \quad X_{Cr_{binary}} = 1 - X_{Ni_{binary}}$$

in Ni-Si system:

$$X_{Ni_{binary}} = \frac{X_{Ni_{ternary}}}{X_{Ni_{ternary}} + X_{Si_{ternary}}} \quad and \quad X_{Si_{binary}} = 1 - X_{Ni_{binary}}$$

and in Cr-Si system:

$$X_{Cr_{binary}} = \frac{X_{Cr_{ternary}}}{X_{Cr_{ternary}} + X_{Si_{ternary}}} \quad and \quad X_{Si_{binary}} = 1 - X_{Cr_{binary}}$$

Using the Kohler equation, the ΔG_3 and ΔG_r for the case when the Ni-20Cr-10Si is taken as the reactant alloy were calculated as:

$\Delta G_3 = -190.3 \quad mJ$

$\Delta G_r = \Delta G_1 + \Delta G_2 + \Delta G_3 = 6.24 + 17.26 - 190.3 = -166.8 \quad mJ$

It should be noted that ΔG_1 and ΔG_2 are the same as the previous calculations and are independent of the equations used for the computation of the Gibbs energy of the ternary alloys.

The program shown below, was then used to calculate the ΔG_r as a function

of Si content of the ternary alloys ranging from X_{Si}=0.05 to 0.95 at the interval of X_{Si}=0.05. All the arguments that was made for the Toop equation program are valid here as well.

```
c*********************************************************
c  This program will calculate the free energy change of the
c  reaction between silicon nitride and Ni-Cr-Si alloys with
c  Ni/Cr=3.5 as a function of Si content of the reactant alloys.
c*********************************************************

      IMPLICIT REAL*8(A-H,O-Z)

      COMMON /B2/ B,XO,T

      OPEN (3,FILE='KOHLER.DAT',Access='append',FORM='FORMATTED')

c*********************************************************
c  The following part defines the output of the program
c  in which, B1=XSi of the reactant alloy, X=amount of the
c  alloy, Y=amount of the ceramic to react with the alloy,
c  T=temperature, and E= partial pressure of nitrogen.
c*********************************************************

          B1=0.05D0
          X=0.001D0
          Y=1.0D-6
          T=1493.0D0
          E=1.5D-4
          H=10D0

      WRITE(3,*) 'T=',T, 'K',     'pN2=',E,  'atm'
      WRITE(3,*)
      WRITE(3,*) 'XSi in    XSi in      DG1     DG2     DG3      DGr '
      WRITE(3,*) 'reactant  Product'
```

```
      WRITE(3,*) 'alloy     alloy'
      WRITE(3,*)
c*************************************************************
c  The following part will calculate the Gibbs energy of the
c  reactant alloys.
c*************************************************************
      DO 100 I=1,19
      B=B1
      CALL CALCUL
      U=XO
      R=U*X

c*************************************************************
c  In this part, first, the Si content of the product alloy,
c  and second the Gibbs energy of the product alloys will
c  be calculated.
c*************************************************************
      B=(X*B1+3.0D0*Y)/(X+3.0D0*Y)
      CALL CALCUL
      W=XO
      P=W*(X+3.0D0*Y)

c*************************************************************
c  In the following part, the free energy of dissociation of
c  silicon nitride on the surface (denoted as G1) and the free
c  energy change of fusion of Si (denoted as G2), the free
c  energy change as a result of addition of Si in the reactant
c  alloy (G3), and the total free energy change of the system
c  will be calculated.
c*************************************************************

      G1=((177000.0 +5.76*T*(LOG(T)/LOG(H))- 96.3*T)*4.184
     $    + 8.314D0*T*LOG((E*E)/0.9D0)-29698.0)*Y
      G2=((12080.-7.17*T)*4.184)*3.0D0*Y
      G3=P-(R-83085.0*3.0D0*Y)
      GR=G1+G2+G3
```

```
      WRITE(3,15) B1,B,G1,G2,G3,GR
 15   FORMAT(2(F5.4,6X),4(F7.5,4X))


      B1=B1+0.05D0
 100  CONTINUE
      STOP
      END
c*************************************************************
c  The following subroutine will first calculate the excess free
c  energy of the Ni-Si (XNS), Cr-Si (XCS), and Ni-Cr (XNC) systems
c  and then based on those values by using the Kohler equation will
c  calculate the excess free energy of the ternary NI-Cr-Si alloys
c  (XNCS). The last step, is the calculation of the Gibbs energy
c  of the ternary alloys at the temperature of interest (XO).
c*************************************************************

      SUBROUTINE  CALCUL

      IMPLICIT REAL*8(A-H,O-Z)
      COMMON /B2/ B,XO,T

        C=(1.0D0-B)/4.5D0
        A=3.5*C

      XNS=-(A*B/(A+B)**2)*(259994.*A/(A+B)+133888.*B/(A+B))+(T*A*B/
     $(A+B)**2)*(62.01*A/(A+B)+22.01*B/(A+B))

      XCS=-(B*C/(B+C)**2)*(36409.+223060.*B/(B+C)-177882*B**2/(B+C)**2)
     $  -(T*B*C/(B+C)**2)*(28.73-26.56*B/(B+C))
      XNC=-8368.*A*C/(A+C)**2
      XNCS=((1-C)**2)*XNS+((1-B)**2)*XNC+((1-A)**2)*XCS
      XO=XNCS+T*8.314*(A*LOG(A)+B*LOG(B)+C*LOG(C))

      RETURN
      END
```

Output of the program to generate Fig. 6.4

T=1493.K pN2=1.50D-004 atm

XSi in reactant alloy	XSi in Product alloy	DG1	DG2	DG3	DGr
.0500	.0528	0.00624	0.01726	-.26718	-.24368
.1000	.1027	0.00624	0.01726	-.19031	-.16681
.1500	.1525	0.00624	0.01726	-.12246	-.09896
.2000	.2024	0.00624	0.01726	-.06298	-.03948
.2500	.2522	0.00624	0.01726	-.01143	0.01207
.3000	.3021	0.00624	0.01726	0.03298	0.05648
.3500	.3519	0.00624	0.01726	0.07109	0.09459
.4000	.4018	0.00624	0.01726	0.10367	0.12717
.4500	.4516	0.00624	0.01726	0.13144	0.15494
.5000	.5015	0.00624	0.01726	0.15500	0.17850
.5500	.5513	0.00624	0.01726	0.17488	0.19838
.6000	.6012	0.00624	0.01726	0.19155	0.21505
.6500	.6510	0.00624	0.01726	0.20540	0.22890
.7000	.7009	0.00624	0.01726	0.21681	0.24031
.7500	.7507	0.00624	0.01726	0.22607	0.24957
.8000	.8006	0.00624	0.01726	0.23347	0.25697
.8500	.8504	0.00624	0.01726	0.23928	0.26278
.9000	.9003	0.00624	0.01726	0.24370	0.26720
.9500	.9501	0.00624	0.01726	0.24697	0.27047

Appendix III

Calculation of the Cr Activity in a Ni-20Cr-10Si (atom%) Alloy

The activity coefficient of Cr (γ_{Cr}) in a liquid Ni-20Cr-10Si (i.e. S10) alloy can be calculated using the Eq (AI.18). Taking A=Ni, B=Cr, and C=Si, the following data are required for such a calculation:

- $\gamma_{B(AB)} = \gamma_{Cr\ (Ni-20Cr)}$
- $\gamma_{B(BC)} = \gamma_{Cr\ (Si-20Cr)}$
- $G^{XS}_{(AC)}$ (with the same X_A/X_C ratio as the ternary alloy) = $G^{XS}_{(Ni-14.3\ Si)}$

From the investigation of Fruehan [276] and Gilby and Pierre[277] the γ_{Cr} in Ni-20Cr liquid alloy is taken to be:

$$\gamma_{Cr(Ni-20Cr)} = 0.74 \qquad \text{(AIII.1)}$$

and from the investigation of Riegert *et al*:[278]

$$\gamma_{Cr(Si-20Cr)} = 0.031 \qquad \text{(AIII.2)}$$

From the data given in Table 6.1 and with respect to:

$$\frac{X_{Ni}}{X_{Si}} = \frac{0.7}{0.1} = 7 \qquad \text{(AIII.3)}$$

the $G^{XS}_{(Ni-14.3Si)}$ having the same Ni/Si ratio as that of the ternary composition was calculated as:

$$G^{XS}_{(Ni-14.3Si)} = -19353 \quad Jmol^{-1} \qquad \text{(AIII.4)}$$

Substituting the Eqs. (AIII.1, 2, and 4) into the Eq. (AI.18) will result in:

$$\ln\gamma_{Cr(Ni\text{-}20Cr\text{-}10Si)} = 0.3 \quad or \quad \gamma_{Cr} = 1.34 \tag{AIII.5}$$

and from the relation:

$$a_{Cr} = X_{Cr}\gamma_{Cr} \tag{AIII.6}$$

thus

$$a_{Cr(Ni\text{-}20Cr\text{-}10Si)} = 0.2 \times 1.3 = 0.26 \tag{AIII.7}$$

Appendix IV

A Comparison Between the Four-point Bend and Shear Strength of Si_3N_4/Cusil-ABA/Si_3N_4(or Mo) Joints.

The main objectives of this study were the following:

a) Designing a shear jig to evaluate the shear strength of double-brazed ceramic/ceramic and ceramic/metal joints and further comparison of the results with shear strength of single-brazed joints.

b) Evaluation of the four-point bend strength of the joints and establishing a possible correlation between the results of MOR and shear tests.

Materials

The ceramic used in this study consisted of sintered silicon nitride produced in house with the same composition as already described in Chapter 5 of this thesis. The metal used was Mo and a commercially available brazing alloy Cusil-ABA was selected as the filler metal. This filler metal was selected because the previous study by other investigators[151,152] had shown that strong and reliable Si_3N_4/Si_3N_4 and Si_3N_4/Mo joints which was needed for this study can form using Cusil-ABA alloy.

Preparation of the experimental samples

In order to make the experimental test bars three blocks of either ceramic or ceramic and metal with dimensions of the 20x9x6 mm^3 (side blocks) and 9x9x6 mm^3 (centre blocks) were brazed together. The side blocks were ceramics in all the cases. The brazing alloy used in form of foils of 0.2 mm thick. The alloy foils placed between the blocks. A BN brazing jig was used to hold the blocks together.

Specimens were brazed in a graphite element vacuum furnace with the previously mentioned specifications (Chapter 5). Brazing took placed at three

different temperatures, 890, 910, and 950°C for different brazing times of 10 and 20 min. under a vacuum of 15 Pa. After brazing, samples were prepared in the way described in § 5.1.3 for strength measurements.

Results

A summary of the results of strength testing is given in Table IV.1. The values given in the table are the mean of four measurements and the numbers in parentheses shows the standard deviations of the relevant values.

From the table, it can be seen that, generally, the shear test tends to give lower strengths than the MOR values. The table also shows higher deviations for shear values than that of the MOR bars. Moreover, the deviations for single-brazed joints is lower than for the double brazed joints. The latter was mainly due to

Table IV.1. Shear and four-point bend strength of Si_3N_4/Cusil-ABA/Si_3N_4 (or Mo) joints.

Materials	Brazing Condition	MOR (MPa)	$\sigma_{Shear(D.B.)}$* (MPa)	$\sigma_{Shear(S.B.)}$** (MPa)
Si_3N_4/Si_3N_4 Si_3N_4/Mo	890°C-10 min.	156 (25)*** 176 (30)	93 (25) 104 (31)	90 (15) 110 (14)
Si_3N_4/Si_3N_4 Si_3N_4/Mo	890°C-20 min.	215 (35) 260 (38)	N/A 161 (38)	N/A 150 (20)
Si_3N_4/Si_3N_4 Si_3N_4/Mo	910°C-10 min.	281 (32) 201 (30)	226 (45) 134 (39)	202 (34) 150 (28)
Si_3N_4/Si_3N_4 Si_3N_4/Mo	910°C-20 min.	121 (25) 134 (20)	N/A N/A	85 (25) N/A
Si_3N_4/Si_3N_4 Si_3N_4/Mo	950°C-10 min.	129 (30) 122 (31)	28 (14) 26 (6)	40 (15) N/A
Si_3N_4/Si_3N_4 Si_3N_4/Mo	950°C-20 min.	48 (18) 75 (20)	N/A 25 (12)	N/A N/A

* Double-brazed joints ** Single-brazed joints *** Standard deviation

problems associated with the sensitivity of the method to the specimen alignment. Another point to be noted is that, there is slight difference between the values obtained using single and double-brazed shear tests. From the overall results of this study, no obvious correlation was found between the strength values obtained by shear and four-point bend tests.

Appendix V

Finite Element Analysis in Si_3N_4 /Mo System

The principle objective of the finite element analysis was to evaluate the effects of variations in joint geometry on the magnitude and distribution of the residual stresses in Si_3N_4/Mo joints. The analysis performed using the "Algor Supersap" finite element program. A cylindrical butt joint model of 9 mm diameter was used. To assess the effect of the thickness of the parent materials on the stress distribution within the joint area, the thickness of one of the materials was assumed to be constant at 6 mm while that of the other was varied from 0.5 to 6 mm. Figure V.1 shows a typical FEM mesh consisting of rectangular elements. Because of symmetry, the finite element grid used in the calculations consisted of only half of the butt joint. In order to obtain a more realistic set of values from the FEM calculations, the mechanical and physical properties of the materials were selected at various temperatures between 25 and 1300°C. Table V.1 shows the values of the materials properties at 298 K. Bonding temperatures were assumed to be at 1100 and 1300°C; the joints were assumed to be cooled from the joining temperature to room temperature.

Some of the results of the FEM analysis are shown in Figures V.2, V.3, and V.4. Figure V.2 shows a contour map of the stress distribution and maximum principal stresses in a Si_3N_4/Mo joint. This joining model was assumed to be stress free at 1100°C. The figure shows that the ceramic is under compression while the metal is

Table V.1. Material properties at 298 K.

Material	E (GPa)	G (GPa)	α ($x10^6K^{-1}$)	ν
Si_3N_4	317	135	2.3	0.24
Mo	322	124	5.3	0.29

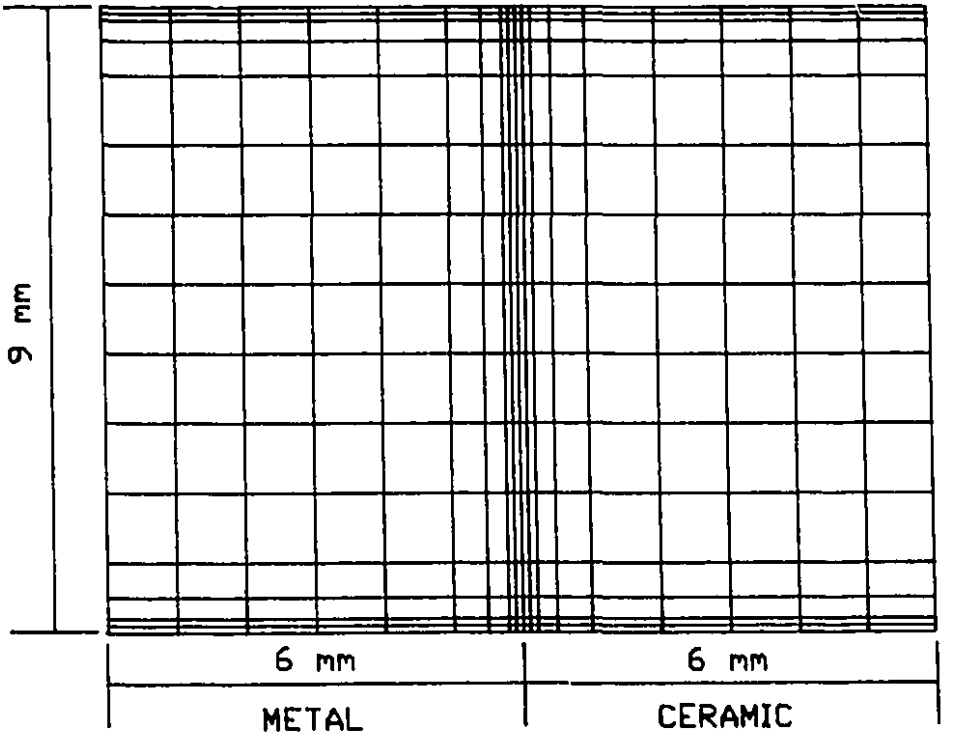

Figure V.1. FEM mesh for butt joint model

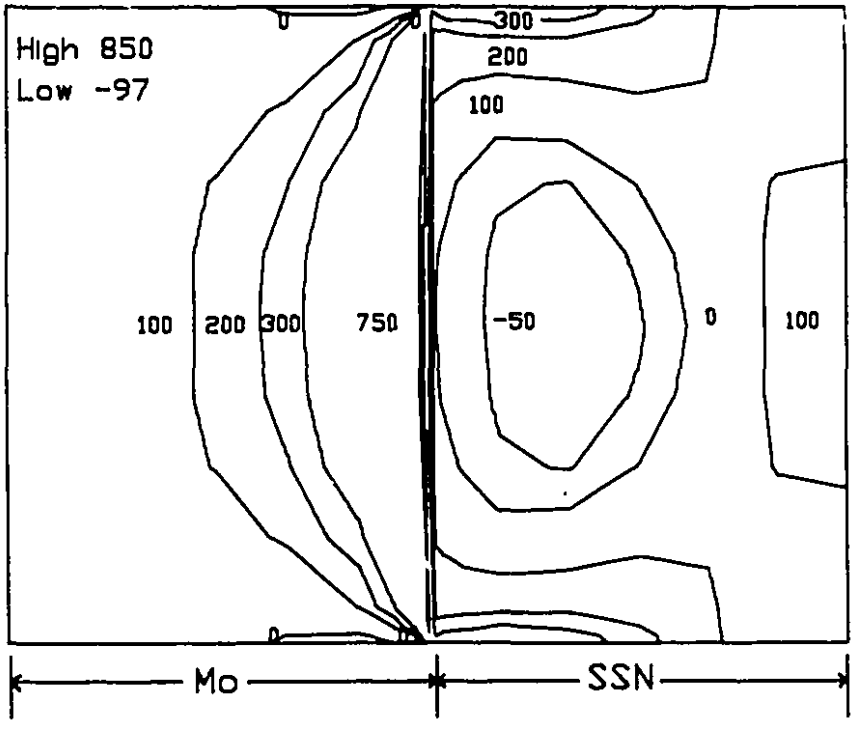

Figure V.2. Isostress contour map of internal stresses at 1100°C. (MPa)

under tension, particularly in the area close to ceramic/metal interface. Figure V.2 also indicates the presence of high tensile stress at the free edge of the sample in the ceramic part. These stresses are very significant because the crack initiation in the ceramic is likely to occur at this location.

Figure 3 shows the effect of ceramic thickness on the maximum tensile stress within the joint area, while the metal thickness was kept constant at 6 mm. Figure V.4 illustrate the same effect while the ceramic thickness was kept constant and the metal thicknesses varied from 0.5 to 6 mm. As a comparison the magnitude of the stresses when using Nb as the metal member is also given in these figures.

From Figure V.3 it can be seen that for the ceramic thicknesses above 3 mm the maximum stress is lower when using Mo and for the thicknesses below 3 mm it is lower when Nb is used as the metal member. In both cases when the ceramic

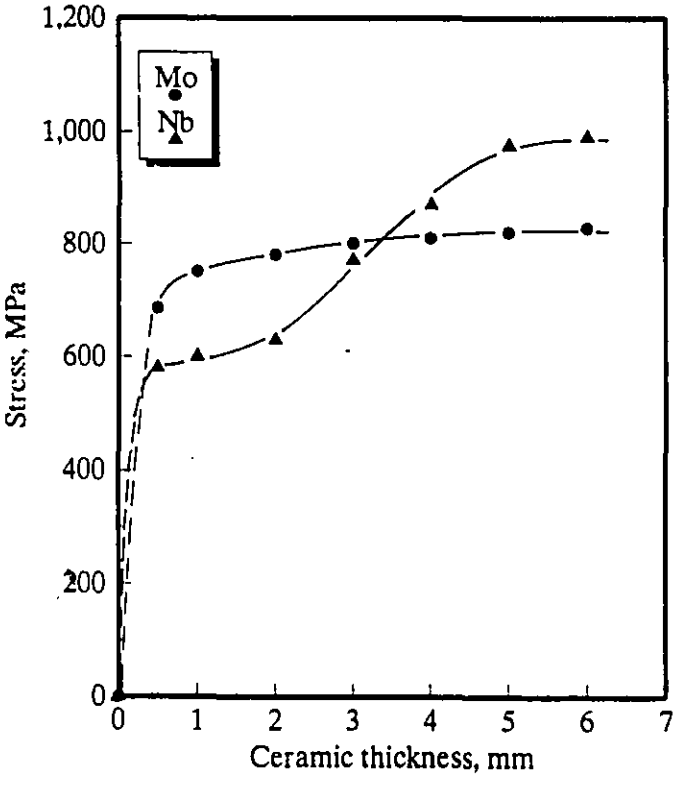

Figure V.3. Peak stress vs the ceramic thickness.

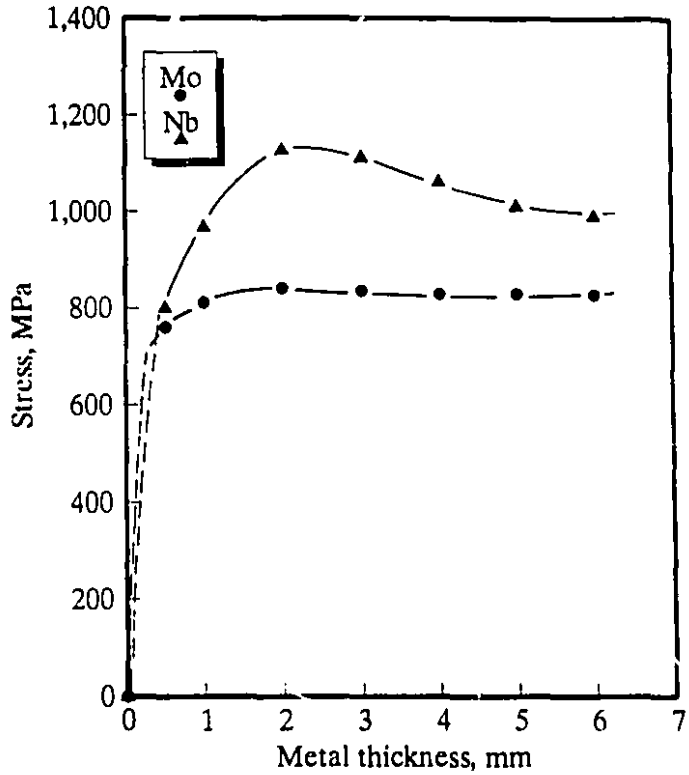

Figure V.4 Peak stress vs the metal thickness.

thickness is above 1 mm the level of residual stress is higher than the fracture stress of Si_3N_4 (700 to 800 MPa), therefore, it is expected that the ceramic would fracture under such stresses. It should be noted that when the ceramic thickness is below 1 mm, the maximum stress decreases to below the fracture stress of the ceramic, thus, such joints should be useable in service. This configuration is suitable for applications in which a thin ceramic layer is joined to a thick supporting metal. Cutting tools are an example of such applications.

Figure V.4 shows that for a constant ceramic thickness of 6 mm, the level of stress is lower for all the metal thicknesses when using Mo as the metal member. In both cases the magnitude of stresses is higher than the fracture stress of Si_3N_4 for all the metals thicknesses.

The finite element study was performed under the assumption that the

materials behave elastically and plastic deformation does not occur. However, the plastic deformation of the metal member, particularly the filler metal which has not been taken into account in the calculation will alleviate the residual stresses. Therefore, it is expected that the real value of the stresses would be less than the present calculations.